Cranfield University

Kelly Grant

Experimental Testing of Tip-Timing Methods used for Blade Vibration Measurement in the Aero-Engine

2004

School of Engineering

Ph.D. Thesis

Cranfield University

School of Engineering

Ph.D. Thesis

2000 - 2004

Kelly Grant

Experimental Testing of Tip-Timing Methods used for Blade Vibration Measurement in the Aero-Engine

Supervisor: Professor P. C. Ivey

October 2004

This thesis is submitted in fulfilment of the requirements for the Doctor of Philosophy.

Abstract

An important component within the jet engine in terms of vibration and high cycle fatigue (HCF) is the blade. This is the component where continuously higher demands on weight and loading are being made. As a consequence of this, there has been a growing interest in developing both numerical methods and instrument technology for blade HCF measurement. This growing interest has also been attributed to changing attitude within the military and aerospace industry, which has tended towards driving down costs and lengthening the engine's life span.

Many development technologies have been reported. One of which, is the development of a non-intrusive system for measuring blade vibratory stress. Research in non-intrusive techniques for the measurement of blade vibration has been ongoing since the early 1970's. The aim of which, has been to replace the conventional method, using strain gauges and slip rings, with an improved system based upon non-intrusive type instrumentation such as optical or capacitance probes. One such approach is known as tip-timing.

Tip-timing is a technique used to measure blade vibration using non-contact probes located around the engine casing. Many tip-timing techniques have been developed over the years, but there still remain significant problems associated with the approach. Such problems include sensitivity to noise and the high number of probes required. The development of two tip-timing methods known as the Autoregressive (AR) method and the Two Parameter Plot (2PP) method has recently been published in the open literature. This thesis describes the work done to experimentally test these two techniques.

During the course of this work, an experimental optical tip-timing test facility was built. This included purpose-built optical tip-timing instrumentation, a tip-timing data acquisition system, and a post processing system incorporated into the Cranfield University low speed compressor facility. Experimental testing of the Autoregressive method and the Two Parameter Plot method was carried out using a controlled test environment, representative of a real engine. An analysis of the two methods was conducted using data from a comprehensive range of frequencies and RPM speeds. The results were then compared with previously published numerical results and the two algorithms were evaluated in terms of replacing the conventional strain gauge method.

Testing of the AR method presented some interesting findings, with acceptable results produced at low rotational RPM speeds. However, as the rotational speed was increased, the accuracy of the results deteriorated. This type of result had not be highlighted in previous work. The 2PP method performed relatively well when using data sampled from the smaller 16 Engine Order (EO) response. However, this was not repeated when using the larger 72EO data. Additionally, this type of result had not been shown in previously published work.

Overall, it was concluded that the issues associated with the frequency measurements should be remedied and a technique for measuring Multiple-Degree-of-Freedom responses should be explored before tip-timing techniques can be considered as a replacement to the strain gauge approach.

Acknowledgements

Thanks go to Professor Paul Ivey for initiating this project and for the continual advice, support and encouragement provided throughout the course of this research.

I would like to acknowledge the United Kingdom Engineering and Physical Sciences Research Council for financially supporting this project. Rolls-Royce, Derby, UK are also acknowledged for financial support and for providing technical advice.

An extended thanks go to the Test House 3 team. In particular, I would like to thank Bernard Charnley, Brian Stapleton, and Pat Sweeney for their continual technical support and encouragement. Particular thanks to Brian who taught me the real meaning of 'no'. I would also like to thank Mark Erlund, who provided invaluable advice on instrumentation in his own special way.

I would like to thank Craig Lawson, a great friend who has gave me a great deal of support over the last two years. From whom, I have learnt a great deal.

A special thanks go to Marco Braglia, who has supported me over the last four years in achieving my goals.

Finally, I would like to thank my parents, Margaret and Neil for their continued support and encouragement throughout my period in full-time education.

Table of Contents

List of Figures

List of Tables

Nomenclature

EO	Engine Order
HCF	High Cycle Fatigue
OPR	Once Per Revolution
PSR	Probe Spacing on the Resonance
d_1	Distance blade tip travelled to probe 1 after OPR trigger
d_2	Distance blade tip travelled to probe 2 after OPR trigger
d_3	Distance blade tip travelled to probe 3 after OPR trigger
d_4	Distance blade tip travelled to probe 4 after OPR trigger
t_1	Blade tip time of arrival at probe 1 after OPR trigger
t_2	Blade tip time of arrival at probe 2 after OPR trigger
t_3	Blade tip time of arrival at probe 3 after OPR trigger
t_4	Blade tip time of arrival at probe 4 after OPR trigger
V	Blade tip velocity
R_T	Blade tip radius
t_{OPR}	Time of arrival at OPR probe
$\omega_{stationary}$	Bladed assembly frequency response in the stationary reference frame
$\omega_{resonant}$	Bladed assembly frequency response in the rotational reference frame
n	Resonance Order
N	Nodal diameter
Ω	Bladed assembly rotational frequency
x_A	Blade tip displacement measured at probe A
x_B	Blade tip displacement measured at probe B
$A(\omega)$	Blade tip response amplitude
θ_A	Probe A angular position on the casing
$\psi(\omega)$	Blade tip response phase
$\Delta\theta$	Angular spacing between probes A and B on the casing
C	Constant Offset
$A_{rel.}$	Relative resonance amplitude
A_{max}	Maximum resonance amplitude
x	Blade tip displacement
$\dot{x}$	Blade tip velocity
$\ddot{x}$	Blade tip acceleration
Δt	Time difference between tip timing probe positions
a	Autoregressive parameter
D	Blade DC offset
x_{ij}	Blade tip displacement measured at probe i during revolution j
P/D	Photodetector
A/D	Analogue to Digital
FEA	Finite Element Analysis
ESPI	Electronic Speckle Pattern Interferometry
LU	Lower Upper

FFT	Fast Fourier Transform
ω_n	The nth Resonant Frequency
A, B	Response Amplitude Components
SNR	Signal to Noise Ratio
AR	Autoregressive
ARIV	Autoregressive with Instrumental Variables
2PP	Two Parameter Plot
PSD	Power Spectral Density
SDOF	Single-Degree-of-Freedom
MDOF	Multiple-Degree-of-Freedom
GAR	Global Autoregressive
GARIV	Global Autoregressive with Instrumental Variables
PAS	The Probe Angular Spacing in degrees on the casing
VCA	The Vibration Cycle Angle in degrees on the casing
PS	Probe Separation
PR	Passage Radius

1. Introduction

1.1 Blade Vibration and High Cycle Fatigue

An important component within the jet engine in terms of vibration and high cycle fatigue (HCF) is the blade. This is the component where continuously higher demands on weight and loading are being made. As a consequence of this, there has been a growing demand for improved design and testing methodologies.

A jet engine blade can be subject to several types of excitation during its operation. The most common of these being those generated by inlet distortions, wakes, or pressure disturbances. A summarised descrption was provided in [1].

In general, a wake that is produced by an upstream vane, generates a velocity deficit within the flow through which the blade passes. Similarly, an obstruction in the flow can produce pressure disturbances in the flow. The blade normally experiences a combination of these forcing phenomena. Inlet distortions, which can be due to a lack of axial symmetry at the inlet or crosswinds during running, can also produce blade forces. All of these forces generate engine order type excitations, where the blade's frequency response is equal to the product of the bladed assembly's rotational speed and the number of disturbances. This type of vibration is known as synchronous vibration.

Other types are grouped under non-engine order forcing and are described as being asynchronous. These types of forces can include for example rotating stall, surge and flutter. A good description of each was provided in [2] and [3].

Generally speaking, rotating stall initiates from an increased angle of incidence of flow on the blade, which leads to boundary separation resulting in a stalled blade. A stalled blade results in the overloading of one blade and the unloading of another. The process of overloading one blade and unloading another is repeated so that a stall cell moves around the blade row at a velocity of around half the rotor speed. Surge on the other hand, involves the entire compressor experiencing stall and unstall. This can be so severe that the mass flow is reversed and compressed gas flow returns back out of the inlet. This results in large forces on the blade. The frequency of the surge cycle is set by the times for the storage volume to fill and empty. Finally, flutter is a self excited vibration, which can be associated with different regions of the compressor operating map. Flutter occurs where there is enough input energy from the gas stream to overcome the blade's damping force. This is commonly found during stall conditions where there are large amounts of separated flow on the blades.

The form of the forced response is determined by the dynamic characteristics of the blade, in terms of frequency and mode shape. The basic blade modes of vibration are described as flapwise, edgewise and torsional. Examples of these mode shapes are given in Figure 1.1,

Figure 1.2, and Figure 1.3. Flapwise, torsional, and edgewise modes can be abbreviated as 1F (first flap mode), 1T (first torsional mode), and 1E (first edgewise mode). The overall bladed assembly response is described differently and in terms of nodal diameters. Diagrams illustrating this type of response are shown in Figure 1.4 and Figure 1.5. This type of response depends on the degree of coupling between blades through the disc or shroud (if one is present). If the disc is rigid, the blades tend to vibrate independently of one another and at their individual cantilever blade frequencies. If however, the disc is flexible, both the blade and disc vibration characteristics coexist. At low nodal diameters, disc modes tend to dominate, whilst at higher nodal diameters, the individual cantilever blade modes dominate.

In order for an assembly mode to be excited, two conditions have to be met; the excitation frequency, which is a multiple of the engine order and the rotational frequency, must coincide with the assembly's natural frequency; and the excitation pattern must coincide with the nodal diameter shape. For example, a 5th engine order (EO) will only excite a mode with a 5 nodal diameter component in the mode shape. However, quite frequently, several modes will have n-diameter components in their mode shapes, which will all be susceptible to an nEO force. The relative strength of each will depend on how close the magnitude of the n-diameter frequency component is in that mode.

It is clear from this that compressor forces and blade and bladed assembly vibration response can be quite a complicated matter. During the design process, it is important that the assembly is constructed in such a manner that large vibration responses are avoided during running conditions, in order to insure that the limits dictated by the blade's material fatigue properties are not exceeded. An increased demand for higher thrust to weight ratio and reduced specific fuel consumption, has meant new engine designs have had to be employed. This lead to a deviation from the previous successful designs, upon which a lot of experience was based. The newer designs include fewer fan, compressor, and turbine stages, a higher pressure ratio per stage, integrally bladed assemblies, and minimal axial spacing between stages. This has resulted in highly stressed blade configurations, closely spaced and complex mode shapes, and an engine operating speed range with an increased level of aerodynamic excitation. As a consequence of this, the techniques used to evaluate the bladed assembly's HCF life expectancy have become increasingly important.

[4], [5], and [6] provide good descriptions of blade HCF and current methods used to predict the life span of the blade. Generally speaking, evaluation of the assembly's HCF life can involve a combination of approaches including numerical modelling, material assessment, and testing. In the past, forced response predictions were made from experience based interactions on a Campbell diagram. However, evolution in unsteady aerodynamic prediction capabilities, using state-of-the-art Computational Fluid Dynamics (CFD) have resulted in more numerically based forced response predictions. The availability of this type of information early on in the design process can reduce the number of design iterations in the later stages.

An assessment of the blade's material properties is conducted using a database containing data in the form of S-N (vibratory stress versus cycles to failure) diagrams. From this, and knowledge of the material's yield strength and ultimate strength, a Goodman Diagram is constructed, which provides a graph illustrating the safe stress region within which the blade can operate without failure due to HCF. There are however, problems associated with this simplistic approach. For example, this type of assessment does not incorporate complexities such as foreign object

damage (FOD), variability of stress states on the blade, multiple mode conditions, or fretting at the root attachment. Testing provides the final and essential part of the process. Testing is split into two main areas laboratory bench testing and engine testing. Laboratory testing generally involves clamping a blade to a shaker table and exciting the blade at its predicted resonant frequencies. The blade's response is recorded using both affixed strain gauges and an alternative non-contact method such as Electronic Speckle Pattern Interferometry (ESPI). The data provides frequencies, mode shapes, and stress ratios for the modes of interest. The final test takes place within an engine test cell. It is here that the blades are tested under actual running conditions. The blade response is measured using strain gauges and evaluated in terms of frequency and magnitude of the maximum stress response, whilst the engine is run through its entire operating range.

Over recent years, there has been a growing interest in developing both numerical methods and instrument technology for blade HCF measurement. This has been due to both the increased demand in modern engine design and associated complexities in the forced response. The growing interest has also been attributed to changing attitude within the military and aerospace industry, which has tended towards driving down costs and lengthening the engine's life span. An example of this was provided in [7], where the new military challenge of the United States Air Force to improve engine performance and availability was discussed.

Many development technologies have been reported. This has included for example, the design of damping into airfoils, improved blade forced response predictions, and blade surface treatments such as laser shock peening (which is used in order to strengthen the blade surface and prevent the formation of cracks). Finally, there has been the development of non-intrusive type instrumentation and algorithms, which would be used for the purpose of measuring blade vibration stress. It is the latter, the development of a non-intrusive system for measuring blade vibratory stress, that the work reported in this thesis is based upon.

1.2 Tip-Timing

Research in non-intrusive techniques for the measurement of blade vibration has been ongoing since the early 1970's. The aim of which, has been to replace the conventional method of vibration measurement, using strain gauges and slip rings, with an improved system based upon non-intrusive type instrumentation such as optical or capacitance probes. One such approach is known as tip-timing, where non-contact probes located around the engine's casing are used to measure the blade's dynamic characteristics. As part of the drive to improve HCF management technology, there has been an increased level of interest in using the tip-timing method to measure blade HCF.

Tip-timing is a technique used to measure blade tip vibration using non-contact probes located around the engine casing. A typical setup is shown in Figure 1.6. Two or more probes are located on the periphery of the engine casing in order to detect the passing of the blade tips. An additional once per revolution (OPR) probe is located on the disc, close to the blade root.

Blade tip deflection is calculated by measuring the blade tip time of arrival at each periphery probe relative to the OPR signal. Figure 1.7 illustrates one revolution window with the sequence of pulses, from which the blade tip deflection is calculated. It shows that the first pulse to occur is from the OPR, after which the time taken for the blade tip to pass under four periphery probes, t_1, t_2, t_3, and t_4 is recorded. The sequence is completed with another OPR pulse.

The OPR has two purposes; to provide a datum, from which the time taken for the blade tip to pass under each periphery probe is measured; and to calculate the blade tip velocity. The distance travelled by the blade tip upon arriving at each probe, is calculated using the formula shown by Equation 1.1. In this case, d_1 represents the distance travelled by the blade tip to probe 1.

$$d_1 = V * t_1 \tag{1.1}$$

The blade tip velocity, V, is shown in Equation 1.2 and is calculated using the time taken for the bladed assembly to complete one revolution ($t_{OPR2} - t_{OPR1}$) and the blade tip radius, R_T.

$$V = (2*\pi*R_T)/(t_{OPR2} - t_{OPR1}) \tag{1.2}$$

Combining these parameters, blade tip velocity and blade tip time of arrival, gives Equation 1.3.

$$d_1 = (2*\pi*R_T*t_1)/(t_{OPR2} - t_{OPR1}) \tag{1.3}$$

Reference distances are recorded at slow rotational speeds, ensuring the blade has minimal vibration. The distance travelled by the vibrating blade is measured during resonant conditions. The vibrating blade tip deflection is then calculated from the difference between the distance

travelled during blade vibration and the reference distance for each probe. This is illustrated in Figure 1.8 and Figure 1.9. Figure 1.8 shows the distance travelled by the original non-vibrating blade. Figure 1.9 shows the blade tip arriving early at the tip-timing probe due to its deflection. The difference in the calculated distance between the vibrating and non-vibrating blade represents the blade tip deflection.

To complete the process and in order to establish the dynamic characteristics of the blade, the blade tip deflection data, measured at each of the probes, is processed using tip-timing algorithms. It is the latter part of the tip-timing process, the tip-timing algorithms, that the work reported in this thesis is based upon.

1.3 Objectives

The main objective of this thesis was to experimentally validate two recently established tip-timing algorithms, the Autoregressive Method and the Two Parameter Plot Method. These algorithms were two recently published techniques taken from [8] and [9] respectively. These papers presented the two algorithms along with numerically based test results. This thesis looked to use these initial findings as a base upon which, the experimental test parameters and results would be compared. The results were then evaluated in terms of replacing the conventional strain gauge method for measuring blade vibration.

The main objective was divided into four smaller objectives:

1. Development of a test facility with tip-timing instrumentation and a data acquisition system.
2. Construction of the algorithm code and integration with the data acquisition system.
3. Test the algorithm code under real engine conditions, evaluate the results, and compare with previously published numerical results.
4. Evaluate the results in terms of their prospect as a replacement for the conventional technique using strain gauges.

1.4 Thesis Structure

This thesis presents the work undertaken in order to achieve the objectives set out in Section 1.3. Firstly, a review of tip-timing work is presented in Chapter 2. The review provides a historical account of tip-timing work over recent years, describing its evolution and associated issues. The purpose of the review was to evaluate the scope for original contribution by evaluating the type of work already done and understanding what the associated limitations were. This is followed by a description of the experimental facilities in Chapter 3, where a detailed account is given for each of the experimental components built in order to fulfil the first and second objectives in Section 1.3. The pre-experimental work is described in Chapter 4. In this case, the preliminary simulation work and test work carried out prior to testing the algorithms are described. The results from testing the two tip-timing algorithms are presented in Chapter 5, followed by a discussion and an analysis of the results in Chapter 6. Conclusions are drawn from the work in Chapter 7, where the aims set out in Section 1.3 are specifically answered.

2. Literature Review

2.1 Introduction

The purpose of the literature review was threefold. Firstly, to understand current practices used for measuring blade vibration during engine testing. Secondly, it was to provide a historical account of tip-timing, discussing its development in terms of application and highlighting associated issues. Finally, it was to discuss the development of two recently established tip-timing techniques, the Two Parameter Plot Method and the Autoregressive Method, evaluating the scope for continued work.

The review began by discussing the current practices employed to measure blade vibration during engine testing. The instrumentation used, its application, and associated issues were all discussed, illustrating the requirement for improved blade vibration measurement techniques. This was followed by a study into tip-timing, discussing the different tip-timing methods presented over the years. Development work and restrictions associated with these techniques were highlighted, illustrating the path taken to the eventual development of the two recently established tip-timing algorithms of interest, the Two Parameter Plot Method and the Autoregressive Method. The two tip-timing algorithms were then discussed in terms of theory and test and development work. The scope for continued work and original contribution was evaluated from this.

2.2 Current Measurement Practices

At the time of writing, current practices used to measure blade HCF life expectancy involved a strain gauge setup. Strain gauges were fixed to the surface of the blade at optimum locations, which were established through finite element analysis. Gauge positions tended to be towards the root of the blade, where surface strain was established to be greater in magnitude and where the rate of change of surface strain was minimal. Two gauge orientations were generally used; one parallel to the blade's neutral axis; and the other at 45^{o} to the neutral axis. These combined orientations were established as being sensitive to both pure bending and torsional modes. Gauge lead wires were fed through the inside of the rotor onto the slip ring. The slip ring provided a means of connecting the signal from the rotating strain gauge to the external data acquisition systems. The data acquisition system sampled the strain gauge output signal during engine testing and processed the data using fast fourier transform algorithms in order to establish the blade's frequency response components and amplitude. The frequency and amplitude components were then related back to the blade's failure criteria, which were established through off-rotor testing and finite element analysis.

A good description of the measurement process was provided in [10], where the most common approach was described. This involved the use of strain to tip deflection calibration factors in order to infer the blade tip deflection during resonance conditions. Since the measured blade strain was unlikely to be the peak strain, it could not be used as part of the failure criteria. The measured strain was therefore converted into a meaningful quantity such as blade tip deflection and then related back to the blade fatigue strength amplitude, which was measured during fatigue testing of the blades.

In order to calculate blade strain to tip deflection calibration factors, each instrumented blade underwent a bench test, whereby the blade was secured on a shaker table and excited at its important resonant frequencies. An additional non-contact device was used to measure the blade tip deflection during this process. From this, calibration factors, relating the strain and tip deflection, were calculated. During engine tests, strain signals were recorded whilst the engine was accelerated and decelerated through its entire operating range. The output was processed using fast fourier transforms, producing individual blade mode responses and then converted into blade tip response using the blade strain to tip deflection calibration factors. The expected HCF life of the blade was evaluated by comparing the measured blade tip amplitude with the amplitude associated with the blade's fatigue limits. These limits were established during fatigue testing of the blades.

Alternative methods of blade vibration measurement included the use of experimental strain to peak stress ratios and theoretical strain to peak stress / tip amplitude ratios. The use of experimental strain to peak stress ratios involved substantial preliminary strain gauge testing prior to the engine test. For example, tests could involve fitting the blade with up to 200 strain gauges and exciting it at all the important resonant frequencies. Two of the locations were selected for engine testing and the strain outputs would be used in conjunction with the output from the preliminary tests in order to establish maximum stress and therefore blade durability under running conditions. The use of theoretical strain to peak stress / tip amplitude ratios involved a theoretical analysis to calculate the blade's modal stress distribution for each of the resonant frequencies for a particular gauge location on the blade. This was used to calculate

strain to stress ratios, which were then used in a similar way as described for the previous methods.

According to [10] the first method, involving the use of experimental strain to tip deflection calibration factors, was the preferred and most frequently used method. This was because extensive testing associated with the second method (using experimental strain to peak stress ratios) was not required and errors associated with gauge location and orientation associated with the third method (using theoretical based strain to stress ratios) were apparently eliminated. However, the calibration factors associated with the first method were subject to experimental error, which was dependent on both the experimental facilities and the level of blade tip deflection. This was discussed more in Section 4.3, where some calibration factors calculated for the two experimental compressor test blades were presented. In addition to this, preliminary testing was also still both time consuming and costly.

The general disadvantages associated with the strain gauge method were also discussed in [10]. This included for example, reliability issues due to the regular occurrence of strain gauges breaking under severe engine running conditions. Replacing gauges proved to be quite expensive in terms of both time and money. Also, the number of instrumented blades was limited by the number of available channels on the slip ring. Therefore, not all blades were monitored and the engine designer could not be sure that the worst case blade vibration responses were shown. Additional effects such as blade mistuning could cause significant variations in blade tip displacement on the same assembly. With a limited number of channels, these response variations may not have been detected by the strain gauge setup.

As a consequence of such issues, there had been much research on the subject of replacing the strain gauge system at the time of writing this thesis. The majority of such work involved evaluating the prospect of measuring blade tip vibration using non-contact techniques. One such technique was known as tip-timing.

2.3 Tip-timing - A Historical Account

At the time of this work, research in tip-timing had been ongoing for many years, with the earliest work being recorded in 1967 by [11]. Here, the use of one optical probe to detect the passing of blade tips was discussed. Calculation of blade tip deflection only and not frequency was reported. A good summary of earlier tip-timing research work was provided in [12], where tip-timing work was grouped into two different approaches based upon the type of blade response being measured, asynchronous, or synchronous. Asynchronous and synchronous vibration responses were described in Section 1.1.

The asynchronous vibration response, since its frequency is equal to a non-integer multiple of the bladed assembly's rotational frequency, was easier to measure using tip-timing techniques. For example, in the case of one probe measuring tip deflection, the sampling location on the asynchronous vibration cycle would differ during each revolution. Therefore, with one probe, a picture of the blade's response could be formed. On the other hand, with synchronous vibration, the sampling location on the vibration cycle would not differ during each revolution. This is because the synchronous response is at a frequency equal to an integer multiple of the bladed assembly's rotational frequency. Thus, a picture of the vibration cycle could not be formed with just one probe. As discussed in [12], the earliest work tended to be based upon the measurement of the blade's asynchronous response, since asynchronous vibration was the easier of the two to measure. Asynchronous work was discussed in [13], [14], [15], [16], [17], and [18].

The work described in [13] and [14] was based upon the same method, whereby [13] presented the theory behind the work discussed in [14]. The papers looked at using a single tip-timing probe in conjunction with an OPR probe to measure asynchronous blade vibration. The method, as discussed in [13], was based upon spectral analysis of tip deflection data points sampled from each blade over a series of revolutions at a constant rotational speed. The sampled data was fourier transformed, from which the resulting spectrum contained a range of frequencies including the original data frequency and harmonics of the sampling frequency. The paper illustrated that if the sampling frequency was varied through altering the bladed assembly's rotational frequency, the integer representing the harmonic component of the sampled frequency could be established. From which, the actual frequency of response could be calculated, thus providing an individual blade spectra. The application of this theory was discussed in [14], where a tip-timing system was set up on a turbine test engine. The aim of the work was to acquire asynchronous blade response data and convert it into meaningful dynamic stress data in order to evaluate the technique's potential as an alternative to the conventional strain gauge setup.

An alternative way of measuring individual blade spectra was discussed in [15] and [16], where two probes were used to measure blade response. The blade tip deflections, sampled at both probes, were processed using the standard fourier transform technique, thus producing aliased frequency results. The second probe was used in order to evaluate the phase difference between the two sensors' data, which was then used to correct the aliased frequencies.

[12] suggested that the techniques used to measure the individual blade spectra were sensitive to noise, sensitive to multiple frequencies and therefore did not reliably identify blade spectra unless resonant frequencies were measured by another independent technique.

Another approach to measuring asynchronous vibration was based upon evaluating the all-blade spectra. Some theory and application were discussed in both [17] and [18]. The all-blade spectra approach used in both [17] and [18] was based upon two tip-timing measurement probes and one OPR probe, set up to measure the travelling wave response of the bladed assembly at a constant rotational speed. Using this method, blade tip deflection sampled at each probe was formed into an array of data. Blade frequency response was evaluated by processing the data array using a fast fourier transform algorithm from which, the calculated frequency corresponded to one viewed from a stationary reference frame. This measured frequency is illustrated by Equation 2.1, where the calculated stationary resonant frequency is equal to a combination of the assembly's actual resonant frequency and the product of the nodal diameter and bladed assembly's rotational frequency. The tip deflection phase angle calculated from the sampled data measured at the two probes was used to establish the magnitude of the nodal diameter. The resonant frequency was calculated from knowing the stationary frequency, nodal diameter and the rotational frequency of the assembly.

$$\omega_{stationary} = \omega_{resonant} + N\Omega \qquad 2.1$$

It was suggested in [12] that with the increased sample rate (equal to the product of the number of blades and the bladed assembly rotational frequency), problems associated with frequency aliasing were reduced or eliminated.

In [12], work involving the measurement of synchronous vibration was also summarised, describing the following two different approaches, the Single-Degree-of-Freedom (SDOF) oscillator technique and a four probe curve fitting technique. The theory and application of both methods were also discussed in [15], [16], [18], and [19].

[12] described the SDOF oscillator method as indirect, whereby one or two probes could be used to measure individual blade tip deflection as the resonance was traversed. Traversing a blade resonance involved accelerating or decelerating the rotational speed of the assembly through a region, where the excitation frequency was equal to the resonant frequency of the blade or bladed assembly. Plots in [12] showing tip deflection versus assembly rotational speed illustrated peaks in a blade's response at an assembly speed coinciding with blade's resonance. It was claimed that this alone provided blade tip amplitude at resonance, but not the resonant frequency. The second probe was used to determine the phase difference of the response between the two measurement probes. From this, the frequency of response was calculated. [19] discussed errors associated with the SDOF oscillator method, which included the blade's response phase not being tracked accurately by the measurement probe. This was due to the time of arrival varying with blade tip deflection changes, resulting in the probe's detection point varying on the blade's vibration cycle. This was found to be more of an issue associated with larger tip amplitudes.

The four probe curve fitting method was discussed briefly in the same papers, but no detailed description of the method, or results from its application were presented. [12] suggested that it was found through independent research carried out by the authors that such curve fitting methods were very sensitive to measurement noise. However, no results illustrating this were presented.

Later work was presented in [20], where methods for measuring both synchronous and asynchronous blade vibration were discussed. Three methods were presented. The first method used a combination of three and five probes to measure the synchronous single-blade spectrum. The data sampled at each of the probes was used to form an array, which was fourier transformed in order to establish the frequency content. A combination of probes were required so that all engine orders could be captured. [20] highlighted some problems with this approach, which included aliased frequencies in the response spectra. This was due to limitations of the sampling frequency associated with the individual blade spectra approach. The second method was similar to the SDOF oscillator approach previously described, where two probes were used to sample blade tip deflection, whilst the resonance was traversed. As with the SDOF oscillator technique, errors were incurred due to probe positioning on the blade vibration cycle, resulting in blade vibration phase changes not being accurately tracked. The final method involved measuring the asynchronous all-blade spectrum at a single probe. Several probes were located around the engine casing, from which the phase difference between spectral peaks were used to establish the frequency of response. This method was very similar to all-blade spectrum techniques described previously and appeared to work well when compared to the other two approaches.

2.4 Scope for Continued Tip-Timing Work

It is clear that a lot of the tip-timing work done was based upon the measurement of asynchronous blade vibration. The most successful of methods, appeared to be those based upon measurement of the all-blade spectra. In this case, the sampling frequency was high enough to capture the blade's resonant frequencies. Techniques for measuring synchronous blade vibration on the other hand, were not as well documented. Two methods were presented; the SDOF oscillator method, an indirect approach, which required the blade's resonance to be traversed; and a four probe curve fitting technique, a direct approach, where the bladed assembly's speed was kept constant. The SDOF oscillator method had problems associated with accurately tracking vibration phase changes. Both of which influenced the accuracy of the measured response amplitude. The four probe curve fitting technique was described by [12] as being very sensitive to noise. However, no results were published on this method.

As a consequence of the lack of research into measuring blade synchronous vibration, two methods were developed; the Two Parameter Plot Method; and the Autoregressive Method. These two methods were developed with the view of using a minimum number of probes, with minimum sensitivity to noise, to measure blade synchronous vibration.

The following sections of the literature review provide a description of each of the tip-timing algorithms and discuss published results, illustrating the requirement for continued work.

2.5 The Two Parameter Plot Method

The Two Parameter Plot Method was discussed in [9], where theory and some examples of its application were presented.

The method was indirect, requiring two tip-timing probes to sample blade tip deflection, whilst resonance was traversed. It was shown in [9] that blade tip displacement measured at each of the probes could be described by Equation 2.2 and Equation 2.3. In this case, the angular position on the blade vibration cycle is given by a combination of the resonance order, n, and the angular position of probe A on the casing, θ_A. The difference in probe positioning on the blade's vibration cycle between probe A and probe B is given by the product of the resonance order, n, and the probe spacing on the casing, $\Delta\theta$. The variable C, represents a constant offset and $\psi(\omega)$ represents the blade tip response phase angle.

$$x_A = A(\omega)\cos(n\theta_A + \psi(\omega)) + C \qquad 2.2$$

$$x_B = A(\omega)\cos(n\theta_A + \psi(\omega) + n\Delta\theta) + C \qquad 2.3$$

It was shown in [9] that an elliptical plot could be formed if the blade response, measured at each probe during the traverse of a resonance, was plotted against the other. The parameters of such a plot could then be related back to the blade engine order response using an empirically based formula. An example ellipse plot, illustrating the important parameters (major axis, minor axis, and major axis angle), is shown in Figure 2.1. Equation 2.4 presents the empirically based formula that was used to relate the axis ratio (which is the ratio of the major axis to the minor axis of the ellipse) to the sensor spacing on the blade's resonance, $n\Delta\theta$. Figure 2.2 illustrates this relationship graphically, where the 360 degree sensor spacing range is shown to be split into four different regions. The figure also shows that each region has a major axis angle of either positive or negative 45 degrees associated with it. [9] illustrated that the elliptical plot of the blade response data should have a +/- 45 degree major axis angle and that the deviation from this provided an indication of the quality of the data. The parameters P, Q, R, and S for each region are shown in Table 2.1.

$$\text{Sensor Spacing} = P * (\text{axis ratio})^3 + Q * (\text{axis ratio})^2 + R * (\text{axis ratio}) + S \qquad 2.4$$

In order to choose the correct parameters, both the sign of the major axis angle of the blade response plot and knowledge of the expected coverage of the blade's vibration cycle was required to ensure the correct parameters associated with each region were used. With the calculated sensor spacing on the resonance from Equation 2.4 and knowledge of the actual probe spacing on the casing, the resonance order could be calculated using the formula shown by Equation 2.5. $\Delta\psi$ represents the sensor spacing on the resonance, $\Delta\theta$ represents sensor spacing on the casing and n is the resonance order.

$$n = \Delta\psi / \Delta\theta \qquad 2.5$$

Issues associated with the method were also discussed in [9]. For example, the method was not fully automated, since prior knowledge of expected probe coverage of the blade response was required, in order that the correct polynomial coefficients could be used to calculate the resonance order. Another issue highlighted was the inaccuracies associated with the measured axis ratio. These types of errors were associated with the probe spacing, $n\Delta\theta$, changing whilst the blade's resonance was traversed. This was as a consequence of the blade tip amplitude influencing the probe's positioning on the blade vibration cycle. A similar issue was discussed for another indirect tip-timing technique, the SDOF oscillator method, in Section 2.3. It was shown in [9] that these types of errors were more significant for larger relative resonance amplitudes. The relative resonance amplitude is defined by Equation 2.6 where R_T represents the blade tip radius, A_{max} is the maximum tip response amplitude and A_{rel} is the relative tip response amplitude. The final issue discussed was the influence of mistuning on the elliptical plot. Mistuning is caused by slight manufacturing differences between blades, which cause the assembly double modes to split, producing close modes. The effect of these close modes was to distort the elliptical plot, producing smaller circles. An example of this is shown in Figure 2.3. The distortion of the elliptical plot resulted in inaccurate axis ratio calculations and thus, inaccurate resonance order calculations.

$$A_{rel.} = A_{max} / R_T \qquad 2.6$$

Application of the Two Parameter Plot Method was also discussed in [9], where a combination of three probes were used to measure blade response during commissioning of a low pressure steam turbine. Three resonances were present during the deceleration of the turbine, one 4EO and two 2EO resonances. The paper looked at using the Two Parameter Plot Method to measure the two 2EO resonant responses.

Probe spacings on the casing were described as being 5.625°, 16.875°, and 22.5°. These spacings translated into probe spacing on the resonance (PSR) values of 3%, 9%, and 13% respectively. PSR describes the percentage of the blade vibration cycle covered by the tip-timing probes. Tip deflection data sampled at each of the probes were plotted against one another and then fitted to an ellipse, using an ellipse fitting procedure. The EO was calculated from the fitted ellipse parameters using Equation 2.4 and Equation 2.5. The paper presented some EO results where the calculated EOs were shown to vary slightly about the correct value.

The results were not clear in terms of probe combinations and hence PSR used. In addition to this, both the PSR range and EO magnitude range were limited to very low values. It was clear from this paper that in order to establish the true potential of the method as a tip-timing technique, a fuller experimental investigation was required based upon a larger EO range, a larger PSR range and more test cases in general.

2.6 The Autoregressive Method

The Autoregressive (AR) Method was discussed in [8] and [21], where both theory and application were discussed. In [8], the AR Method was described as a curve fitting technique based upon the equation of motion of the blade tip displacement. Equation 2.7 represents a form of the equation of motion.

$$\ddot{x} + \omega^2 x = 0 \qquad 2.7$$

The AR Method was formulated by evaluating blade tip acceleration in terms of vibration deflection over a measured period of time, Δt. Figure 2.5 illustrates probe positioning on the blade's vibration cycle with equal spacings in time at positions j-1, j, and j+1. The following series of equations, Equation 2.8, Equation 2.9 and Equation 2.10 illustrate the relationship between sampled tip displacement, the time difference between each of the tip-timing probes, Δt, and the blade tip acceleration.

$$\ddot{x}_j = \frac{\dot{x}_{(j \to j+1)} - \dot{x}_{(j-1 \to j)}}{\Delta t} \qquad 2.8$$

$$\ddot{x}_j = \frac{\dfrac{x_{(j-1)} - x_j}{\Delta t} - \dfrac{x_j - x_{(j-1)}}{\Delta t}}{\Delta t} \qquad 2.9$$

$$\ddot{x}_j = \frac{x_{(j+1)} - 2x_j + x_{(j-1)}}{\Delta t^2} \qquad 2.10$$

Equation 2.10, represents the acceleration at point j, written in terms of measured displacement at positions j-1, j, and j+1. The acceleration term in Equation 2.7 was replaced with Equation 2.10, resulting in Equation 2.11 and Equation 2.12. Equation 2.12 is the blade tip equation of motion in terms of blade deflection measured at positions j-1, j, and j+1 on the blade vibration cycle and an autoregressive parameter, a. The autoregressive parameter, shown by Equation 2.14, was formulated from both the blade vibration frequency, ω and the time difference, Δt, between sampling probes.

$$x_{(j-1)} - (2 - \omega^2 \Delta t^2) x_j + x_{(j-1)} = 0 \qquad 2.11$$

$$x_{(j+1)} - a x_j + x_{(j-1)} = 0 \qquad 2.12$$

$$(x_{(j+1)} - D) - a(x_j - D) + (x_{(j-1)} - D) = 0 \qquad 2.13$$

$$a = -2\mathrm{COS}(\omega \Delta t) \qquad 2.14$$

In order to solve for the autoregressive parameter, Equation 2.12 was rewritten in matrix form in terms of four tip displacement measurements and a DC offset, D. Inclusion of the DC offset is illustrated in Equation 2.13, where it was assumed that the offset magnitude was constant for each probe measurement. The DC offset represented offsets in blade tip displacement caused by phenomena such as blade lean or twist and measurement errors associated with probe positioning and shaft movement. The autoregressive formulation for a four probe setup is represented by Equation 2.15, where x_1 is the tip displacement sampled at probe 1, x_2 is the tip displacement sampled at probe 2, x_3 is the tip displacement sampled at probe 3 and x_4 is the tip displacement sampled at probe 4. Each displacement should be acquired at a constant rotational speed coinciding with the blade's resonance.

$$\begin{bmatrix} x_1 + x_3 \\ x_2 + x_4 \end{bmatrix} = \begin{bmatrix} x_2 & 1 \\ x_3 & 1 \end{bmatrix} \begin{bmatrix} -a \\ D(2+a) \end{bmatrix} \qquad 2.15$$

An Autoregressive with Instrumental Variables (ARIV) method was also described in [8], which involved pre-multiplying the autoregressive formulation shown by Equation 2.15 by a matrix of delayed observations. This is illustrated by Equation 2.16. The theory behind the instrumental variables method was described in [27] and [28], where it was shown that by multiplying the autoregressive formulation by a matrix of delayed observations, the noise component in the signal could be reduced.

$$\begin{bmatrix} x_{22} & x_{32} \\ 1 & 1 \end{bmatrix} \begin{bmatrix} x_{11} + x_{31} \\ x_{21} + x_{41} \end{bmatrix} = \begin{bmatrix} x_{22} & x_{32} \\ 1 & 1 \end{bmatrix} \begin{bmatrix} x_{21} & 1 \\ x_{31} & 1 \end{bmatrix} \begin{bmatrix} -a \\ D(2+a) \end{bmatrix} \qquad 2.16$$

Testing of the Autoregressive Method was also discussed in [8], whereby three direct tip-timing analysis methods, two Global Autoregressive methods (the simple Global Autoregressive method and the Global Autoregressive method with Instrumental Variables) and another technique known as the Determinant Method were compared. The Global Autoregressive methods are similar to the simple Autoregressive approach, using the formulae shown by Equation 2.15 and Equation 2.16 to calculate the autoregressive parameters over a series of revolutions.

The theory associated with each method was discussed and tested using numerically generated data, which was corrupted with white noise of varying noise to signal ratios (SNR). The tip-timing data was generated from a single degree of freedom model, representing simplistic blade vibration. Test parameters included engine order (EO), PSR, probe 1 offset on the resonance, number of blades, number of revolutions and SNR. The two main results taken from [8] were that; the global autoregressive method with instrumental variables always gave significantly better results than the simple autoregressive approach for all the given test cases; and that significantly better results were achieved when the PSR was increased. The magnitude and range of EO and PSR were kept quite low.

[21] presented an extension to this work, discussing the development of a numerical model more representative of real engine conditions and using this to generate more representative data to test the algorithms. As discussed in Section 1.1, blade vibration response can be significantly more complex than the response generated by a single degree of freedom model. This was also discussed in [21], where such response conditions were summarised, including the effects of

blade coupling and mistuning, multiple mode conditions, and mixed synchronous and asynchronous responses.

Various case examples considering the effectiveness of the tip-timing approach under these conditions were discussed. The main conclusion taken from the discussion was that for most of the cases presented, a reasonable engine order of within +/- 1EO could be predicted when using the Autoregressive Method.

For example, [21] discussed the case where blade coupling was present. With the presence of blade coupling, the bladed disc vibrates as an entire assembly, with the number of modes in the assembly response corresponding with the number of blades. Increasing the number of blades results in an increased number of modes within a frequency range, such that during an engine acceleration, response peaks occur closer together and become less distinct. Such a case was illustrated in Figure 2.4, where multiple modes were generated during an engine acceleration due to a 4th EO excitation force. It was suggested in [21] that since the engine order remains the same for each of the close modes, the Autoregressive Method could be used. One approach would be to process data centred around a single peak of the vibration data.

Another case example presented, involved combining blade coupling with mistuning. Mistuning is a phenomenon that occurs when individual blades have slightly different vibrational characteristics. This mainly occurs because of slight blade manufacturing differences and differences in the blade root boundary conditions. The main effects of mistuning on the bladed assembly response include the splitting of double modes and an increase in the frequency range of the assembly's natural frequencies. In this case, [21] suggested that the autoregressive method could still provide EO information, using the same technique described for the multiple mode case. However, since with mistuning, slight differences in individual blade vibration characteristics are experienced, data from individual blades could only be used to calculate the EO. The consequence of this was described in [21] as being an increased sensitivity to noise and therefore, a reduced accuracy in the calculated results. The Global Autoregressive Method was found to provide the most accurate results in the presence of noise.

The only case where [21] found the Autoregressive Method would fail, was when two blade modes were excited at two different EOs simultaneously. In this case, all SDOF methods would fail. It was concluded also that other methods such as the two parameter plot method and the SDOF Oscillator method did not perform well when both blade coupling and mistuning were introduced.

The results presented in [8] were generated using data from a simple SDOF numerical model of a bladed assembly. The results suggested that PSR was the most important parameter when considering the accuracy of the EO prediction and sensitivity to noise. However, the range of both PSR and EO used during the validation work was limited. [21] extended this work by considering the use of the two tip-timing techniques, the Autoregressive Method and the Two Parameter Plot Method, when more realistic engine running conditions were applied. However, no results were presented and the different scenarios were limited to a discussion only.

2.7 Continued Work

Section 2.2 discussed the current measurement practices used to measure engine blade vibration. The strain gauge approach and its associated issues were described. Such issues included errors in the calibration factors, reliability issues associated with the strain gauges, the limited number of blades that could be monitored due to the restricted number of slip ring channels and build costs.

Section 2.3 discussed the ongoing research into alternative vibration measurement techniques. A historical account of the tip-timing method was presented, detailing the development of the method over recent years. Various tip-timing techniques were summarised. This included single probe and two probe methods for measuring asynchronous vibration. Some synchronous vibration measurement techniques, such as the SDOF Oscillator approach and some curve fitting techniques were also discussed. Concluded from the discussion was that the majority of research which was carried out, was focused around the measurement of asynchronous work. This led to the development of the two synchronous vibration measurement methods; the Two Parameter Plot Method; and the Autoregressive Method.

Section 2.5, and Section 2.6 described the two synchronous techniques; the Two Parameter Plot Method; and the Autoregressive Method. The theory associated with both methods and test results were discussed. The published results for the Two Parameter Plot Method in [9] were limited to a small combination of test parameters. The Autoregressive Method work, discussed in [8], although including a wider range of test parameters, was numerically based, using a simple single degree of freedom model. More realistic test cases were discussed in [21], but no test results were presented.

It was clear from the review of the earlier literature that further research into techniques for measuring synchronous vibration was required in order to successfully replace the conventional strain gauge approach. Two such methods were discussed, the Two Parameter Plot Method and the Autoregressive Method. However, it was clear from the published work on both methods presented in [8], [9], and [21], that further experimental based testing was required, which would have to include a wider range of more realistic test parameters.

3. Experimental Equipment

3.1 Introduction

Purpose built equipment was required in order to experimentally test the tip-timing algorithms. A rotating test facility and purpose built optical tip-timing instrumentation were used in order to generate real engine data. In this case, blade tip passing time variations due to phenomena associated with a rotating machine and instrumentation could be investigated. As a means of comparison, a strain gauge setup was used, which would provide both blade frequency response and blade deflection data. A data acquisition system was constructed for the purpose of acquiring time of arrival data at each of the tip-timing probes, for calculation of raw tip displacement data, and to arrange the data arrays in the correct format for the post processing algorithms. Post processing algorithms were also constructed, based upon the tip-timing theory presented in [8] and [9], in order to calculate the blade vibration response characteristics.

This chapter provides a detailed description of each experimental component. Section 3.2 describes the rotating test facility, Section 3.3 provides a detailed description of the measurement instrumentation used in the test facility, Section 3.4 discusses the data acquisition system used and Section 3.5 provides a description of the post processing algorithms used.

3.2 Test Facility

The test facility was a low speed, one and a half stage compressor with inlet guide vane, rotor, and stator stages. The rotor stage comprised of 79 oversized LM24 aluminium alloy blades, for the purpose of producing airflows similar to those found in high-speed engines. Each blade had a radial length of 90mm and chord length of 59mm. The stator and inlet guide vane stages comprised of 72 blades each. The hub diameter was approximately 1m and the overall flow passage diameter was approximately 1.2m. Figure 3.1 presents the front view of the compressor test rig. The intake is shown in Figure 3.2.

The compressor was driven by a 60kW electric motor and had a maximum operating speed of 1200RPM. The shaft torque was measured using a strain gauge based torque meter, which could be read from a LED display during operation. Flow pressure was measured at the inlet, the upstream position of the inlet guide vane, the upstream position of the rotor, the downstream position of the rotor, and the downstream position of the stator. Flow through the compressor was controlled using a back pressure valve, which was operated with a small electric motor. The back pressure valve is shown in Figure 3.3. The inlet temperature was measured using four PT100 platinum resistance probes positioned around the circumference of the inlet. A 24 channel slip ring was used to transfer on-rotor data to a data acquisition system.

Purpose built instrumentation was used in conjunction with the test facility in order to acquire tip-timing data. The following section provides a detailed description of the instrumentation used.

3.3 Instrumentation

3.3.1 The Optical Tip-Timing Probes

The optical tip-timing probes were purpose built and located around the circumference of the compressor casing, in order to measure blade tip time of arrival relative to a once per revolution pulse, as discussed in Section 1.2. The principle of measuring blade tip time of arrival was based upon the detection of light reflected by the blade tip as it passed under the probe.

Positioning of the tip-timing probes was achieved by using a purpose built cassette, which could be slotted into the casing. An engineering drawing of the cassette is shown in Figure 3.4. The cassette consisted of three rows of seven holes. The seven holes were equispaced at a distance of 13mm in order that the probes could be located over a range of positions on the blade vibration cycle. The length between the outer holes (the first hole and the seventh hole) was 78mm. The three rows provided access to the leading edge, mid chord and trailing edge positions on the blade tip.

The optical probe device comprised of three main components, which included the bifurcated optical cable, the light source and receiver circuit. The optical cable was a bifurcated miniature probe, with a glass fibre bundle of 1.2mm. The probe is shown in Figure 3.5. The bifurcated probe incorporated a bundle of low loss superflex glass fibres, which were used to carry the emitting and reflected light. A bundle of fibres was used in order to maximise the amount of reflected light captured at the probe tip, since no lens accessories were used.

The light source used was a high power 50mW GaAIAs IR emitter, which produced light at a wavelength of 880nm and was powered by a purpose built 500mA current source. Figure 3.6 provides a schematic of the circuit used to power the light source. The combination of voltage regulators, LM117 and KA350, and resistors were specially selected in order to supply the source with 1.65V and 500mA of current.

The receiver circuit comprised of a photodetector, amplifier, and purpose built digitiser circuit. The circuit diagram for the detector and digitiser is shown in Figure 3.7. The photodetector response bandwidth was selected by considering the rate at which light would be reflected off the blade tip as it passed under the probe head. It was approximated that at a rotational speed of 900RPM (blade tip speed of 57.4m/s) and using a 1.2mm diameter probe tip, the minimum reflected light rise time would be 21μsec. This was calculated by using the formula shown in Equation 3.1. In order to capture the variations in the blade tip reflected light, the photodetector used to receive the light signal had to have a response, which was at least an order of magnitude faster than 21μsec. The sensor used to detect the passing of the blade tip was a 230KHz photodetector with an integrated amplifier. The detector had a 2μs rise time and a peak response at a wavelength of 880nm. Figure 3.8 presents the actual photodetector signal at an assembly rotational speed of 900RPM and Figure 3.9 presents a magnified view of rise of the photodetector signal shown in Figure 3.8. The rise time of the reflected light signal is represented by the two vertical markers in Figure 3.9 and the magnitude is given by dx, which corresponded to 22μsec. This was in good agreement with the calculated rise time value of 21μsec.

$$t_{\text{rise time}} = \text{Probe tip diameter} / \text{Blade tip velocity} \quad 3.1$$

The output signal of the photodetector was connected to a purpose built digitiser circuit, which incorporated a high speed comparator and feedback components. A high speed comparator was used in order to minimise the time delay between triggering and acquiring the count value from the data acquisition card. The feedback components were a combination of resistors and capacitors, which were used to provide hysteresis and stability in the comparator signal. The input signal was connected to the positive pin of the comparator, whilst the threshold voltage was connected to the negative pin of the comparator. Using this setup, the output digital signal of the comparator was triggered on the rise of the photodetector signal, when it crossed the threshold voltage. Figure 3.10 illustrates the comparator output signal being triggered by the set threshold voltage on the rise of the photodetector signal. The digital output signal from the comparator was connected to a high speed counter, from which, the count values were latched. This is discussed further in Section 3.4.

3.3.2 The Once Per Revolution Probe

A once per revolution (OPR) probe was used to measure the rotational speed of the compressor and to provide a datum from which the distance travelled by each blade was measured. This was discussed in Section 1.2. The OPR probe was located at the rotor stage. A fin was fixed on the disc of the rotor bladed assembly, positioned in order that it pass through a slot type optical device once every revolution. The optical device was located at the furthest circumferential position on the disc radius, close to the blade root, maximising the tangential velocity of the fin for a given rotational speed.

The slot optical device comprised of a statically mounted laser and receiver, built up during the work described in [22]. Both the laser and receiver were integrated into a pigtail module, with fibres terminating in a SMA type connector. Fibre ends from both components were fixed 5mm apart on a purpose built mounting, through which the fin would pass. Figure 3.11 presents the OPR sensor arrangement, illustrating the termination of the pigtail fibres on the mounting and the fin path between the two fibre ends. The light source was a 655nm, 10mW laser, which required a +5V, 1A power supply unit. The detector had a 125MHz bandwidth, with a 3ns rise time. The response of the detector was selected for its suitability to follow variations in the reflected light signal from the passing of the fin through the slot detector. This concept was discussed in more detail in Section 3.3.1. The detector required a +5V supply and load resistor.

The laser and receiver setup provided a 400mV swing in voltage, which was fed through a Schmitt trigger setup (similar to the digitiser circuit described in Section 3.3.1). This setup produced a digital signal of 0V (low) to 4V (high) when the fin passed through the sensor mounting. The count values were latched off the digital signal using the high speed counter card.

3.3.3 The Strain Gauges

Strain gauges were used in order to monitor blade vibration response and to generate data with which, the tip-timing results could be compared. Two Nickel-Chromium Alloy strain gauges

were affixed to the two compressor test blades that were used to generate tip timing data. Figure 3.12 illustrates the positioning of the strain gauges, with one gauge parallel to the blade's neutral axis and the other being positioned at 45 degrees to the neutral axis. The combination of orientations was used to ensure that there was strain sensitivity to both the bending and torsional modes. This was discussed in Section 2.2.

Lead wires were routed from the blade surface, through the inside of the rotor shaft to the strain gauge power and amplification circuit boards mounted on the stub shaft. The signal from the circuit boards were connected to the data acquisition system through a slip ring. The strain gauge power and amplification circuit boards are shown in Figure 3.13. These circuit boards were built up during the course of work described in [22].

The strain gauges were powered using constant current sources. Amplification of the output signal was achieved using cascaded amplifier stages, which gave an overall gain of 2000. Pre-slip ring amplification was used in order to minimise the noise to signal ratio in the strain gauge signal, since the slip ring can introduce a significant amount of noise into the system. A full description of both the constant current sources and the amplifier circuitry was given in [22]. Each strain gauge was individually powered and amplified. Therefore, four power and amplifier boards were required, as shown in Figure 3.13. All four circuit boards were powered from a +/ - 17V mains power supply unit.

A frequency response graph for the strain gauge amplifier circuit was also provided in [22] and is illustrated in Figure 3.14. This strain gauge response characteristic was used to ensure that the appropriate blade strain frequency response could be sampled using the amplification circuitry. Figure 3.14 illustrates that a reasonably constant gain of just over 2000 could be achieved at a frequency of 400Hz and above.

The signal output from the gauge amplifier circuit was connected to a 100KHz A/D card with a user-interface available for on-line monitoring. This allowed the range of gauge frequency data to be safely sampled since the blade's resonant frequencies were well within this frequency bandwidth. The blade's resonant frequencies are shown in Table 4.3, Table 4.4, Table 4.6 and Table 4.7. The output data was then processed offline using the Matlab signal processing toolbox in order to evaluate the fast fourier spectrum of the data array.

3.4 Tip-Timing Data Acquisition

The purpose of the data acquisition system was to measure the blade tip time of arrival at each of the tip-timing probes relative to the OPR signal. The blade tip deflection was then calculated from this. The theory discussed in Section 1.2 was used.

A ten channel 80MHz counter/timer card and a purpose built Visual Basic user interface was used to acquire blade tip deflection data. Five channels were used. Four of these channels were for the tip-timing probes and one was for the OPR signal. The Buffered two-signal edge-separation measurement procedure was used to acquire the blade tip time of arrival data. An illustration of the process is given in Figure 3.15, where the signals are not to scale. The Aux_Line signal represents the OPR signal and the Gate signal represents one tip-timing probe signal. The source represents the on-board 80MHz counter signal. The active edge of the Aux_Line (OPR) signal initiated the counting of the rising edges on the source (80MHz counter). The active edge of the Gate (tip-timing probe) signal terminated the counting. The active edges are highlighted by the dashed arrows. On termination of the counting, the hardware save register latched the counter value. This count value was converted to time using the known frequency of the counter signal (80MHz). This is shown in Equation 3.2. From this, the blade tip time of arrival relative to the OPR pulse was calculated.

$$\text{Time of Arrival} = \text{No. of Counts} / \text{Counter Frequency} \qquad 3.2$$

Blade tip velocity had also to be measured in order to calculate the blade deflection. The Buffered period measurement procedure was used to calculate the tip velocity from the OPR signal. This procedure is illustrated in Figure 3.16, where the signals are not to scale. The Gate signal represents the OPR signal and the source represents the on-board 80MHz counter signal. The count value associated with the period between the active edges of the gate signal was latched by the hardware save register. The time for one revolution was calculated using Equation 3.2. Blade tip velocity was calculated using Equation 1.2 and blade tip deflection was calculated from the blade tip time of arrival and blade tip velocity using Equation 1.1.

Snapshots of the user interface are shown in Figure 3.17, Figure 3.18, and Figure 3.19. Figure 3.17 presents the main form. In this form, parameters such as the number of revolutions and the number of blades were set. These parameters determined the size of the buffer arrays and therefore, the acquisition time. Also in this form, there was the command to acquire. This command armed the relevant counters for measuring both the blade tip time of arrival and the OPR period.

The 'enable' button on the main form provided access to the counter selection form, which is shown in Figure 3.18. This form allowed the user to select the number of counters to be used during the acquisition process, to assign each probe signal to a specific counter and to select the type of measurement procedure (buffered two-signal edge-separation or buffered period measurement) used for each counter.

The 'Post Process' button on the main form provided access to the post processing form. This is shown in Figure 3.19. There were two main functions on this form. The first of which, was to calculate reference distances. The purpose of calculating reference distances was discussed in Section 1.2. The reference distance represented the distance travelled by the blade tip to each of the tip-timing probes during non-vibrating conditions. This was illustrated in Figure 1.7 and Figure 1.8. The second function was to calculate the blade tip deflection at each of the tip-timing probes. The blade tip deflection was calculated from the difference between the blade tip travelled distance during a resonance and the corresponding reference distance measured at the same probe. This is illustrated in Figure 1.9. The data for each probe and revolution were transferred into the same array in a format suitable for post processing with the tip-timing algorithms.

3.5 Post Processing Algorithms

3.5.1 The Autoregressive Method

The Autoregressive Method code is shown in Appendix A.1. The algorithm was constructed by using PV-Wave (Visual Numerics) code, according to the theory discussed in Section 2.6. The tip deflection data was read into user defined arrays and then arranged into autoregressive matrices similar to those shown in Equation 2.15. One revolution worth of data was required to solve for the autoregressive parameters. The matrices were then solved using a Lower Upper (LU) decomposition procedure to give the autoregressive parameter, a, and the DC offset. The vibration frequency was calculated from the autoregressive parameter, using Equation 2.14. The calculated frequency and DC offset were then inserted into a matrix representing the blade vibration response, as shown in Equation 3.3. Vibration amplitude, frequency, and phase were calculated for each revolution of probe data.

$$\begin{bmatrix} x_1 - D \\ x_2 - D \\ x_3 - D \\ x_4 - D \end{bmatrix} = \begin{bmatrix} \cos(\omega_n t_1) & \sin(\omega_n t_1) \\ \cos(\omega_n t_2) & \sin(\omega_n t_2) \\ \cos(\omega_n t_3) & \sin(\omega_n t_3) \\ \cos(\omega_n t_4) & \sin(\omega_n t_4) \end{bmatrix} \begin{bmatrix} A \\ B \end{bmatrix} \qquad 3.3$$

3.5.2 The Autoregressive Method with Instrumental Variables

The PV-Wave code for the Autoregressive Method with Instrumental Variables is shown in Appendix A.2. The theory was discussed in Section 2.6. As with the Autoregressive Method, the displacement data files were read into user defined arrays and then arranged into autoregressive matrices. However, in this case two revolutions of probe data were required to calculate the autoregressive parameter, a, and DC offset. The autoregressive matrix formulation is shown in Equation 2.16. The remainder of the process was similar to the Autoregressive method, where the LU decomposition procedure was used to calculate the autoregressive parameters and the blade vibration response was calculated using the matrix formulation shown by Equation 3.3.

3.5.3 The Two Parameter Plot Method

The PV-Wave code for the Two Parameter Plot Method is shown in Appendix A.3 and was based upon the theory discussed in Section 2.5. For this tip-timing technique, tip displacement data from two probes during a traverse of the blade's resonant frequency was required. The data corresponding to each probe was read into xdata and ydata arrays respectively. A least square ellipse fitting procedure was then used to fit the xdata and ydata to an ellipse. The ellipse fitting technique was taken from [23], where a full description of the method was presented. The elliptical parameters such as the axis ratio and major axis angle were calculated from the ellipse fit. The region associated with the ellipse was then established from the major axis angle and knowledge of the approximate probe coverage of the blade vibration cycle. The different regions are shown in Figure 2.2. The Two Parameter Plot coefficients corresponding with the established region were selected from Table 2.1. These coefficients were then substituted into

the Two Parameter Plot empirical based formula, shown by Equation 2.4, in order to give the sensor spacing in terms of degrees of resonance. The resonance order was calculated using Equation 2.5 with the knowledge of both the actual probe spacing on the casing (which was measured at non-vibrating speeds) and the calculated probe spacing on the resonance.

4. Pre-Experimental Work

4.1 Introduction

The pre-experimental work chapter describes the preliminary simulation and test work carried out prior to testing the tip-timing algorithms. This included numerical analysis of the test blades, blade bench tests, on-rotor testing, and evaluation of the instrumentation performance.

The numerical analysis involved evaluation of the dynamic properties of the test blades. This was carried out in the main to establish the suitability of the test blades for generating measurable tip displacement data. It was also useful for providing dynamic data with which, the results from the bench tests could be compared. Bench tests of the blades were carried out in order to establish the blade's natural frequencies and to calculate stress to tip deflection correlation factors. Knowledge of both the blade's natural frequencies and correlation factors was required in order to compare with the experimental tip-timing frequency and response amplitude results. On-rotor testing was carried out in order to establish the blade engine order response and consequently the critical operating speeds of the compressor. This determined the compressor speeds at which, the blade tip-timing data was measured. Finally, testing of the OPR probe and tip-timing probes was carried out in order to evaluate the individual performance of each probe and the combined accuracy of the tip deflection measurement system.

Section 4.2 discusses numerical modelling of the test blades, Section 4.3 describes the bench testing of the blades and Section 4.4 discusses the on-rotor testing. Testing of the OPR probe and tip-timing probes is discussed in Section 4.5 and Section 4.6 respectively.

4.2 Numerical Modelling

4.2.1 The Numerical Modelling Process

Finite element modelling of the compressor test blade was required in order to ascertain the dynamic characteristics of the test blade, to establish the expected level of blade excitation during running conditions and to establish the optimum strain gauge positions on the blade surface. The modelling of the blade was carried out using I-DEAS.

Firstly, the blade model was constructed and then meshed. Once meshed using the appropriate elements, material properties and boundary conditions, the natural frequencies, and mode shapes were calculated. With the modal characteristics of the blade established, the blade's forced response could be predicted and the blade surface strain could be evaluated.

The following subsections discuss the numerical modelling process and results. During this section, two sets of results are reported. One of which was associated with the original compressor test blade and the other corresponds to two flat blades, each with a different thickness of 2mm and 3mm. The requirement for the two flat blades is illustrated through the findings of the numerical modelling work and is discussed in the proceeding sections. The original test blade is referred to as the test blade, whilst the 2mm and 3mm thick blades are referred to as the flat blades.

4.2.2 The Blade Model

The finite element software package I-DEAS was used to generate the test blade model and carry out simulations. The original test blade geometry was provided as part of the compressor flow CFD grids. Using FORTRAN code, the blade surface points were read from the CFD grid data files into suitable output files for I-DEAS. The surface data points were read into an I-DEAS project. The data points were then joined using FORTRAN span-wise and stream-wise spline generation programs in order to create the blade frame. This process was taken from the work described in [22]. The 'Mesh of Curves' technique was then used to create the blade surfaces (the suction and pressure sides). The surfaces were then stitched together to create a blade shell. The solid model of the blade was completed by forming the blade tip and root surfaces using the 'Loft' technique. The blade solid model is shown in Figure 4.1.

Creating the flat blade models was more straightforward, as the design of the blade was relatively simple. The flat blades had the same height and width as the test blade, but consisted of a flat plate with the same root fixing. Therefore, simple drawing commands were used to construct the model in I-DEAS Master Modeller. An example of the 3mm thick blade solid model is shown in Figure 4.2.

4.2.3 Modal Analysis and Forced Response Predictions

The next step in the numerical modelling process involved meshing the blade volume. A free, solid, eight-node, tetrahedral mesh was generated for each of the three blade models. The free meshing method was used rather than the mapped meshing method for simplicity. Using the free meshing technique, the mesh was automatically generated using an algorithm, which minimised element distortion. Also, the use of this method meant that more complicated boundaries could be meshed. Mapped meshing was discussed in [26]. The material properties assigned to the elements are shown in Table 4.1. The aerodynamic critical damping ratio, taken from [1], was used since this is known to be the largest damping component. Other damping components include hysteretic damping and frictional damping, which are negligible in comparison. Displacement constraints were applied to the blade root in order to implement cantilever boundary conditions. The meshed test blade with displacement constraints fixed at the root is shown in Figure 4.3.

The Lanczos solver method was used to calculate the normal mode dynamics solution of the blade. This approach was used since it required minimum user input and was faster than the alternative methods (which were the Guyan reduction method and the Simultaneous vector iteration method). The Lanczos solver method, Guyan reduction method and Simultaneous vector iteration method were described in [24]. The calculated natural frequencies for the test blade and flat blades are shown in Table 4.2, Table 4.3, and Table 4.4. The corresponding modes shapes for the first and second modes are shown in Figure 4.4, Figure 4.5, Figure 4.6, Figure 4.7, Figure 4.8, and Figure 4.9.

The normal mode solution set was used to carry out further calculations, such as the forced response of the blade. It was important to establish the expected level of blade vibration in order to ensure that measurable blade tip deflection data could be generated using relatively low resolution optical probes. The optical probe resolution is discussed in Section 4.5 and Section 4.6. A forced response analysis of each blade was carried out using blade forces estimated from the shaft torque meter readings. The shaft torque meter readings were taken during run-up tests prior to the experimental work. The purpose of the forced response analysis was to approximate the effect of such forces on the level of blade tip deflection and to ascertain whether the level of blade tip deflection was measurable. The torque was measured to be 130Nm at a rotational speed of 850RPM. A blade force of 2.7N was approximated from this, since there were 79 blades with a blade tip radius of 0.609m. This calculation is shown by Equation 4.1.

$$\text{Force} = \frac{130}{0.609 \times 79} = 2.7\text{N} \qquad 4.1$$

The frequency forcing function was constructed so to generate a 2.7N force for a range of frequencies. The frequency range incorporated the first two resonant frequencies for each blade. The force was applied two thirds of the way up the blade and the forced response was calculated at the actual blade's resonant frequencies and at frequency intervals of 100Hz. The magnitude of the frequency interval was not important, since the off-resonance response result was presented to emphasise the peak at resonance only. Figure 4.10, Figure 4.11, and Figure 4.12 presents a graphical representation of the forced response for each blade. The results are shown in Table 4.5. The measured tip deflection values were not correct, since the real damping values associated with each blade were not known. The real damping values could not be established

since for blade vibration, the main source of damping is aerodynamic. This type of damping could only be measured during real engine tests, since bench tests would only give the hysteretic damping, which is known to be negligible in comparison. However, the results did provide an approximation of how the response would differ for each blade. It was clear from the results that the 2mm and 3mm blades would provide a significantly larger response than the original test blade, with peak responses of 2.1mm and 1.3mm respectively. The original test blade, on the other hand, had a peak response of 0.2mm. Therefore, the flat blades were used in place of the original test blade for further test work. Two of the original test blades were removed from the bladed assembly and replaced with the two flat blades.

4.2.4 Blade Surface Strain Analysis

Finally, the blade surface strain was evaluated in order to locate the strain gauges at the optimum locations. The optimum location was where surface strain was greatest and the rate of change of strain was minimal. This was discussed in Section 2.2. The blade's normalised modal strain response was calculated as part of the normal mode dynamics solution. The 2mm and 3mm flat blades were considered only, since it was established in Section 4.2.3 that the original test blade would be replaced with the 2mm and 3mm flat blades.

Figure 4.13 and Figure 4.14 presents the 3mm blade's normalised longitudinal and shear strain respectively. The 2mm Blade had a similar surface strain pattern. As anticipated, the magnitude of strain was largest towards the root of the blade. For the second mode (the torsional mode), the surface shear strain was found to be more sensitive than the longitudinal strain. As a result, the strain gauges were affixed to the blade surface as shown by Figure 4.15. Two gauges were used. The one closest to the blade root was parallel to the neutral axis of the blade and was therefore sensitive to the bending mode. The second gauge was located at 45^{o} to the neutral axis and was sensitive to the torsional mode.

4.3 Blade Bench Tests

The bench tests were carried out by Rolls Royce in order to evaluate the natural frequencies and mode shapes of the blades and to calculate the stress to blade tip deflection correlation factors for each strain gauge.

The flat blades were fixed in a crystal exciter and resonated at its first three modes. An Electronic Speckle Pattern Interferometry (ESPI) system was used to record the blade modal shapes, whilst the natural frequencies were recorded from the strain gauge output. Figure 4.16 presents the test setup.

The ESPI system is a well-known bench test technique for measuring the blade's resonant strain response. The blade surface is illuminated with laser light, resulting in a reflected speckle pattern, which is imaged onto a charge-coupled device (CCD) array. This image is saved on a PC. The blade is then deformed, resulting in a different speckle pattern. This second speckle pattern is saved to the PC and subtracted from, or added to, the previously stored pattern and the result is rectified. The resulting image is a pattern of dark and bright fringes, known as correlation fringes. Examples of this are shown in Figure 4.17 and Figure 4.18. The fringes represent contours of equal displacement along the viewing direction. The spacing of the fringes is inversely proportional to the displacement. Displacement between two points on the blade surface is calculated by counting the number of fringes between the two points and multiplying by a fringe sensitivity factor.

The natural frequencies recorded during the tests are shown in Table 4.6 and Table 4.7. The results, with the exception of the 3mm blade's third mode, were found to agree well with the FEA results shown in Table 4.3 and Table 4.4. In general, the higher modes become more difficult to evaluate using FEA as a consequence of the mode shape being more complex. The 3mm blade's third mode response provided the worst case result as a consequence of the blade's larger thickness, which required more finite element calculations. The third mode in this case was not important, since it was only the first two modes that would be used during the experimental test work. Figure 4.17 and Figure 4.18 represent the 2mm blade's first and second mode shapes, which were formed using the ESPI system.

Strain gauge correlation factors were also established. The correlation factors represented the blade tip deflection to stress ratio, for each mode shape. For each mode excited during the bench test, the blade stress was recorded using the attached strain gauges and the corresponding blade tip deflection was measured using the ESPI system. This provided conversion factors between blade stress and blade tip deflection. Using these correlation factors, the tip-timing displacement measurements could be directly compared to the strain gauge measurements during the experimental test work. The correlation factors and errors are shown in Table 4.8 and Table 4.9. Gauge A represents the gauge parallel to the blade's neutral axis and B represents the gauge, which is positioned at 45^{o} to the blade's neutral axis.

It is clear from the results shown in Table 4.8 and Table 4.9 that the errors associated with the calculated correlation factors were quite large. The errors were shown to range from 12% to 33%. These large errors were due to both the low level of excited strain (24 microstrain)

measured from the strain gauges during the bench tests and the low number of fringes visible in the ESPI images. The low level of strain resulted in a poor signal to noise ratio. This was reflected in the errors associated with the correlation factors. A proportion of the error was also due to the number of fringes in the ESPI images. Examples of the ESPI image fringes are shown in Figure 4.17 and Figure 4.18. Since the tip deflection measurement was discretised by the number of fringes, a lower number of fringes inferred a larger error in the calculation. As a consequence of these large errors, the strain gauge correlation factors could not be used to compare the tip-timing tip displacement measurements with the tip deflection inferred from the strain gauges. Therefore, the strain gauge measurements were used only to confirm the blade's frequency of response during the experimental test work.

4.4 On-Rotor Testing

On-rotor testing was carried out in order to establish the blade engine order response. This was done by evaluating the strain gauge output for the 2mm and 3mm blades whilst the compressor test rig was run through the entire operating speed range. The gauge output was viewed and processed using Matlab. The results are presented graphically in Figure 4.19 through to Figure 4.28.

Figure 4.19 represents the 2mm blade's strain response at 205RPM. The measurement was taken from the strain gauge parallel to the blade's neutral axis. The FFT of the signal is shown in Figure 4.20, where the peak is shown by marker 1 at a frequency of 244Hz. This frequency was in good agreement with the FEA calculated frequency shown in Table 4.3. Figure 4.21 and Figure 4.22 represent both the 2mm blade's 45° gauge output at 617RPM and the FFT of the signal respectively. The peak of the FFT signal is shown by marker 1 to be at 742Hz. This was in good agreement with the blade's first torsional mode frequency, which is also shown in Table 4.3. Finally, Figure 4.23 and Figure 4.24 present both the 2mm blade's parallel gauge output at 941RPM and the FFT of the gauge signal respectively. The peak of the FFT signal is shown by marker 1 to be at 254Hz. Although this result was in good agreement with the 2mm blade's first bending mode frequency, it was slightly higher than the value measured at the lower speed of 205RPM. This was believed to be due to the centrifugal stiffening effect of the assembly's high speed. Centrifugal stiffening effects were discussed in [25].

Figure 4.25 and Figure 4.26 represent both the 3mm blade's parallel gauge output and FFT of the signal respectively. The peak is illustrated by marker 1 to be 342Hz. This was in good agreement with the 3mm blade's first bending mode frequency shown in Table 4.4. Figure 4.27 and Figure 4.28 represent both the 3mm blade's 45° gauge output at 857RPM and the FFT of the signal respectively. The marker 1 highlights the peak frequency at 1025Hz. This corresponded with the 3mm blade's first torsional mode frequency shown in Table 4.4.

The results are summarised in Table 4.10 and Table 4.11, where the excited mode shape, the engine order, and the assembly's rotational speed are shown for each critical response. Table 4.10 presents the 2mm blade response. In this case, the three critical speeds, 205RPM, 617RPM, and 941RPM, are summarised. The first bending mode was excited at 205RPM and the first torsional mode was excited at 617RPM. Both modes represented a 72 EO response, which was generated by the 72 stator blades just upstream of the rotor blades. The EO response was discussed in Section 1.1. At the third critical speed of 941RPM, the first bending mode was excited again. This time the mode represented a 16 EO response, which was generated by the 16 struts on the engine face.

Table 4.11 summarises the 3mm blade response. In this case, the two critical speeds, 286RPM and 857RPM, are summarised. These two speeds corresponded with the first bending mode and the first torsional mode respectively. Both modes were excited by a 72EO force, which was generated by the 72 stator blades. All five of the critical speeds shown in Table 4.10 and Table 4.11 were used to generate tip-timing data.

4.5 Once Per Revolution Probe Testing

The tip-timing process was based upon the measurement of blade tip time of arrival at each peripheral probe relative to the OPR signal. This was discussed in Section 1.2. It was therefore important to evaluate the accuracy of both the OPR probe and tip-timing probe. From this, the accuracy of the blade tip deflection measurement was evaluated.

The OPR signal was evaluated at the three different speeds of 287RPM, 650RPM, and 938RPM. The position of the digital trigger between the 20% and 80% points on the detector signal slope was evaluated. The detector analog signal is shown in Figure 4.29 and the analog signal with the digital trigger is shown in Figure 4.30. The 20% and 80% values were used to define the upper and lower values of the signal slope. This was to ensure that the start and finish times were consistently located at the same positions on the signal slope. The variation of the trigger position between these two points was evaluated in order to establish the accuracy of the OPR probe timing measurement.

The digital signal position was measured in terms of percentage of the signal fall time. The percentage position of the digital signal was measured a number of times at each of the RPM speeds. A mean value was used to define the true trigger position on the slope of the signal and the deviation of the trigger point from the calculated mean was measured. The variation of the trigger position relative to the calculated mean was taken as the OPR timing error.

The results are shown in Table 4.12, where the trigger error in microseconds represents the variation of the trigger position on the detector signal in terms of time. The results are also shown in terms of millimetres, representing the error in the tip deflection measurement due to the trigger position variation. This was calculated from the blade tip velocity and the trigger time error using the formula shown in Equation 4.2. The results showed that the error in the measured tip deflection due to the variation of the OPR trigger position was as small as +/- 0.0018mm.

$$\text{Tip Deflection Error} = \text{Blade Tip Velocity} * \text{Trigger Time Error} \qquad 4.2$$

4.6 Tip-Timing Probe Testing

The tip-timing probe signal was evaluated at the three different speeds of 300RPM, 600RPM, and 900RPM. The accuracy of the timing measurement was evaluated applying the same method used for the OPR probes.

The position of the digital trigger was evaluated between the 20% and 80% points on the rise of the detector signal. As with the OPR probe, the variation of the trigger position from a calculated mean was used to evaluate the accuracy of the probe timing measurement. Figure 3.8, Figure 3.9, and Figure 3.10 present examples of the detector signal and the comparator digital signal being triggered at a threshold value on the rise of the detector signal.

The position of the digital signal was measured in terms of percentage of the signal rise time, which was measured a number of times at each of the RPM speeds. The deviation of the trigger position from the calculated mean was measured in the same way as the trigger deviation was measured for the OPR probe. The results are shown as displacement error in Table 4.13, Table 4.14, Table 4.15, and Table 4.16. The displacement errors were calculated using the formula shown by Equation 4.2.

With the exception of the first optical probe, the results presented the expected magnitude of displacement error, ranging from +/-0.011mm to +/-0.031mm. These results were found to be similar to error values quoted in other published work such as [16], where it was suggested that state-of-the-art sensors should detect blade tip arrival position within 0.03mm. The results shown for the first optical probe were less promising, with the worst case result measured at +/-0.052mm. The reason for this is not clear, but may have been due to an extra sensitivity to noise experienced by the electronic components for that particular optical probe.

The distance travelled by the two test blades between the OPR pulse, and each of the optical probes was measured also. These distances were measured at 300RPM only, since at this speed blade tip vibration was minimal. The purpose of this was to evaluate errors associated with the measurement system, which could be due to factors other than the accuracy of the trigger point. For example, one of these factors may have been shaft movement. Shaft movement would affect both the tip velocity measurement and blade tip time of arrival measurement as a consequence of the shaft physically shifting the OPR trigger fin and blade tips in position.

Equation 1.3 was used to calculate the distance travelled by each of the blades over a series of revolutions. Both the OPR pulse period and blade tip time of arrival at each of the probes were required for the calculation. Since, the actual distances were not known, the deviation of the measured distance from a calculated mean was used to evaluate the accuracy of the system. The results are shown in Table 4.18, where the worst case result for each optical probe is shown. The results show that the errors associated with the measured distances were similar to those due to the variation of the pretrigger position on the photodetector signal rise, as shown in Table 4.17. This verified that errors due to external factors such as shaft movement were negligible at the speed of 300RPM. Unfortunately, these tests could not be carried out at higher RPM speeds since blade tip vibration would influence the results.

The overall accuracy of the tip deflection measurement system was taken from the tip-timing probe trigger results since the error associated with the OPR probe was negligible. The worst case results were used to define the tip deflection measurement accuracy for each of the probes. The results are shown in Table 4.17.

5. Results

5.1 Introduction

The experimental methodology is presented in Section 5.2, where the approach used to sample the tip deflection data is outlined. Following this, the conditions under which, the data were sampled are discussed in Section 5.3.1, and Section 5.3.2. The conditions are presented in the form of test cases for the Autoregressive (AR) method, and the Two Parameter Plot (2PP) method. The experimental test results are then presented. Section 5.4.1 presents the tip deflection data for various probe setups on the cassette. The cassette was discussed in Section 3.3.1, and an engineering drawing was shown in Figure 3.4. Section 5.4.2 presents the AR results for each of the test cases discussed in Section 5.3.1, whilst Section 5.4.3 presents the 2PP results for each of the test cases discussed in Section 5.3.2.

5.2 The Experimental Methodology

5.2.1 The AR Method and ARIV Method

The AR method and ARIV method were described in Section 2.6. It was shown that the tip deflection data should be sampled using four tip-timing probes, whilst maintaining a constant rotational speed coinciding with the blade's resonant EO response. The on-rotor EO response for each of the test blades was discussed in Section 4.4, where it was shown that the first two modes for each of the test blades were detectable using the strain gauge instrumentation. This was summarised in Table 4.10 and Table 4.11.

The experimental test data was sampled at each of the resonant RPM speeds, using a range of probe positions on the cassette. The probe positioning is discussed in Section 5.3. Each resonant response was found by monitoring the online strain gauge data as the compressor's rotational speed was increased. The tip deflection data was sampled at each of the resonant speeds and processed using both the AR method and ARIV method in order to calculate the autoregressive parameter and response frequency. The autoregressive parameter was discussed in Section 2.6. The average error associated with the calculated autoregressive parameter and response frequency was evaluated from the data sampled at each resonant frequency.

The following sections present both the raw tip deflection data sampled by the four probes and the errors associated with the calculated autoregressive parameter and frequency for each EO response.

5.2.2 The 2PP Method

The 2PP method was described in Section 2.5. It was shown that two probes were required to sample tip deflection data as the blade's resonance was traversed in order to calculate the EO response. The EO response was discussed in Section 4.4, where it was shown that two EO responses, a 16EO response and a 72EO response, were available. This was summarised in Table 4.10 and Table 4.11.

The experimental test data was sampled during the traverse of each of the EO responses using a range of PSR settings. The test cases and corresponding PSR settings are discussed in Section 5.3.2. They are also summarised in Table 5.2. The compressor's rotational speed was incremented using intervals of 1RPM through each of the resonant speeds. Data was sampled at each PSR setting. The average error associated with the calculated EO for each PSR setting was evaluated.

The following sections present the raw tip deflection sampled during the traverse of each EO response, examples of the least square ellipse fit to the raw data and the errors associated with the calculated EO for each PSR setting and EO response combination.

5.3 Test Cases

5.3.1 Test Cases for the AR Method, and the ARIV Method

Nine different test cases were used to define the conditions under which the Autoregressive (AR) Method, and Autoregressive with Instrumental Variables (ARIV) Method were tested. The test cases are summarised in Table 5.1, where each case is described by the test blade, the critical RPM speed, the resonant frequency, the probe setup used, and the PSR.

The critical RPM speeds, and corresponding resonant frequencies were discussed in Section 4.4, and presented in Table 4.10, and Table 4.11. The probe setup describes the positions of the probes on the cassette. An illustration of the probe position numbering on the cassette is shown in Figure 5.1, where a cut-out section of the cassette is presented. Three probe setup positions were used: setup 1; setup 2; and setup 3. Setup 1 describes the first arrangement, where the entire length of the cassette was used with the probes located over the leading edge of the blade at positions 1, 3, 5, and 7. Setup 2 describes the second arrangement, where the probes covered the first half of the cassette length, on the blade's leading edge, in positions 1, 2, 3, and 4. Setup 3 describes the third arrangement, where the probes covered the second half of the cassette length, on the blade's leading edge, in positions 4, 5, 6, and 7.

The PSR represents the percentage of the blade vibration cycle covered by the tip-timing probes. This was discussed briefly in Section 2.5, and was calculated by considering both the angular spacing between the tip-timing probes, PAS, and the blade vibration cycle in terms of degrees on the casing circumference, VCA. Calculation of the PSR is shown by Equation 5.1. The VCA was defined in terms of degrees on the casing, and the PAS was measured between the first, and last probe used. Equation 5.2 presents the calculation of the VCA in terms of the EO.

$$PSR = PAS / VCA \tag{5.1}$$

$$VCA = 360 / EO \tag{5.2}$$

The range of PSR was restricted by both the size of the cassette, and the EO. For example, for case 1 in Table 5.1 a 16EO was excited. This translated into a VCA of 22.5 degrees on the casing, which was calculated using Equation 5.2. The maximum distance between the first and last probes, PS, was 78mm when using the setup 1 position. The spacing between probe positions is shown in Figure 3.4. The 78mm spacing translated into a PAS of 7.3 degrees on the casing circumference. This was calculated by using Equation 5.3, where the passage radius, PR, represented the distance from the centre of the shaft to the inside of the casing circumference and the probe spacing, PS, represented the circumferential distance between the first and last probes. Using Equation 5.1, the maximum achievable PSR was 32%.

$$PAS = (PS*180)/(\pi*PR) \tag{5.3}$$

On the other hand, case 2 represented a 72EO response, which gave a VCA of 5 degrees on the casing. The maximum PAS (using the setup 1 position) was established to be 7.3 degrees, so that the maximum PSR achievable, using Equation 5.2, was 146%. However, there were two criteria, which had to be adhered to whilst sampling tip-timing data for the Autoregressive method. These were the PSR, which had to be equal to or less than 100% and the spacing between each of the probes, which had to be equal in length.

The first of the two criteria meant that the probes could not be positioned over the entire length of the cassette, since a PSR of 146% could not be used. The second criterion, where the probe spacing had to be equal in length, meant that the probes could only be positioned on either half of the cassette using the setup 2 and setup 3 positions. The PS (between positions 1 and 4 and positions 4 and 7) was 39mm. This PAS was calculated as 3.7 degrees on the casing by using Equation 5.3. Since the VCA for the 72EO response was established as being 5 degrees on the casing circumference (using Equation 5.2), the only achievable PSR was calculated to be 70% (using Equation 5.1).

The range of PSR for each test case is presented in Table 5.1, showing that a PSR of 32% was achieved for the 16EO response and a PSR of 72%, was achieved for the 72EO response. Therefore, the test conditions were limited to these two PSR values.

5.3.2 Test Cases for the 2PP Method

Seven different test cases were used to define the conditions under which, the 2PP method was tested. These seven test cases are summarised in Table 5.2, where the true EO, the probe positions on the cassette and the PSR are presented for each case. Since in the case of the 2PP method the output parameter was EO and not frequency, the results generated from both of the test blade's data were combined and grouped according to the EO and PSR. The majority of the results were generated from both the 2mm and 3mm test blade's 72EO response data. A smaller proportion of the results were generated from the 2mm blade's 16EO response data. Therefore, the test cases shown in Table 5.2 correspond with either a 16EO or a 72EO.

The 16EO and 72EO test cases were grouped by PSR. Since only two probes were required, the range of PSR coverage was greater than that achieved for the AR and ARIV tests. For the 16EO response, three different PSR setups of 10%, 20%, and 30% were used. The 30% PSR was discussed in Section 5.3.1, where since the 16EO VCA was 22.5 degrees on the casing and the maximum PAS was 7.3 degrees (using setup 1), a PSR of 30% was calculated. The other two PSR values of 20% and 10% were achieved by moving the second probe closer to the first probe on the cassette, into positions 5 and 3 respectively and using the same calculations as those shown in Section 5.3.1 to calculate the corresponding PSR.

For the 72EO case the PSR ranged from 25% to 98%. The maximum PSR of 146% (calculated in Section 5.3.1 using setup 1) could not be used. As with the AR and ARIV methods, the PSR had to be equal to or less than 100%. However, the probe spacing did not have to be equal in length. The range of PSR values were achieved by positioning the probes using a variety of combinations other than the two outermost holes (positions 1 and 7). For example, the 98% PSR corresponded to probe positions 1 and 5. Whereas the 75% PSR corresponded with probe

positions 1 and 4, the 50% PSR corresponded with probe positions 1 and 3 and the 25% PSR corresponded with probe positions 1 and 2. Each PSR value was measured by using the same calculations shown in Section 5.3.1.

5.4 The Results

5.4.1 The Raw Tip Deflection Data

This section presents the raw tip deflection data measured at the four tip-timing probes for each of the critical operating speeds shown in Table 4.10 and Table 4.11. The three probe settings (setup 1, setup 2, and setup 3), which were used to define the test cases for the AR and ARIV methods in Section 5.3.1, were used again for the blade tip response measurements. The magnitude of each PSR corresponded with the values for each probe setup and critical RPM speed combination given in Table 5.1. Two sets of results are presented for each case. Firstly the blade tip deflection, sampled as the critical operating speed was traversed, is presented. In this case, the compressor's speed was increased by 1RPM at a time and the tip deflection was sampled at each of the four tip-timing probes. This plot represents the data used in the 2PP calculations and illustrates the blade's behaviour as the resonance was traversed. Following this, the tip deflection, which was sampled at the critical operating speed only, is presented. This plot represents the data used for the AR and ARIV calculations. It also illustrates the formation of the blade vibration cycle for each probe setup and PSR. The two plots are presented for each critical operating speed and probe setup combination and are shown in Figure 5.2 through to Figure 5.19. Finally, the response amplitude and SNR were evaluated for each tip deflection plot. The SNR represented the level of instrumentation noise relative to the output signal amplitude and was evaluated in order to understand its influence on the accuracy of the tip-timing algorithm calculations.

Figure 5.2 and Figure 5.3 represent the sampled 2mm blade tip deflection data at the critical speed of 941RPM with the probes located in the setup 1 position. The PSR is shown to be 32% in Table 5.1 for this critical speed and probe setting. Figure 5.2 represents the tip response sampled at each of the four probes as the RPM speed of the compressor was traversed through the resonant speed. Figure 5.3 represents the tip response at the critical speed of 941RPM with the data forming just under a third of the blade vibration cycle.

Figure 5.4, Figure 5.5, Figure 5.6, and Figure 5.7 represent the sampled 2mm blade tip deflection data at the critical speed of 205RPM. The data shown in Figure 5.4, and Figure 5.5 was acquired using the probe setup 2 position, whilst the data shown in Figure 5.6 and Figure 5.7 was acquired using the probe setup 3 position. Table 5.1 shows that the two positions covered 72% of the blade vibration cycle. Figure 5.4 and Figure 5.6 present the blade tip response as the critical speed was traversed, whilst Figure 5.5 and Figure 5.7 present 72% of the blade tip response at 205RPM. Figure 5.8, Figure 5.9, Figure 5.10, and Figure 5.11 present the 2mm blade tip response at the critical speed of 617RPM in the setup 2 and setup 3 positions. Again, both positions cover 72% of the vibration cycle. Figure 5.8 and Figure 5.10 present the response as the critical speed is traversed, whilst Figure 5.9 and Figure 5.11 represent 72% of the tip response at the critical speed of 617RPM.

The 3mm blade tip response is shown in Figure 5.12 through to Figure 5.19, where 72% of the blade tip response is covered for each probe setup. Figure 5.12 through to Figure 5.15 represent the tip response at the critical speed of 286RPM for setup 2 and setup3. Figure 5.12 and Figure 5.14 represent the blade tip response as the critical speed is traversed, whilst Figure 5.13 and

Figure 5.15 represent 72% of the blade tip response at the critical speed of 286RPM. Figure 5.16 through to Figure 5.19 represent the response at the critical speed of 857RPM for the setup 2 and setup 3 positions. Figure 5.16 and Figure 5.18 represent the blade tip response as the critical speed is traversed, whilst Figure 5.17 and Figure 5.19 represent 72% of the tip response at 857RPM.

From the tip response results shown in Figure 5.2 through to Figure 5.19, the SNR was approximated. The SNR, in the context of this work, represented the ratio of the tip-timing instrumentation error to the blade tip response amplitude. The tip-timing instrumentation error was taken from Table 4.17, where an average value of 0.03mm was calculated from all four probes. The response amplitude was evaluated from the tip deflection data sampled during the traverse of each of the resonant operating speeds. According to SDOF theory, the response amplitude can be measured from the overall change in tip deflection sampled at any position on the blade vibration cycle. The blade tip amplitude and SNR values were approximated from the response graphs and are shown in Table 5.3 for each test case.

5.4.2 The Autoregressive Results

This section presents the results from testing both the AR method and the ARIV method. The test cases are summarised in Table 5.1 and were discussed in Section 5.3.1. Figure 5.3, Figure 5.5, Figure 5.7, Figure 5.9, Figure 5.11, Figure 5.13, Figure 5.15, Figure 5.17, and Figure 5.19 represent the raw tip deflection data, which was used to generate the AR and ARIV frequency results. The data was acquired at each of the critical operating speeds for different probe settings, as detailed in Table 5.1.

The AR results are shown in Table 5.4 and Table 5.5. Table 5.4 presents the average AR parameter error versus SNR for each test case. The AR parameter, a, was described in Section 2.6 as the output solution from the AR and ARIV calculation. The AR parameter error was presented since this provided a true indication of the error in the AR and ARIV calculation. The true AR parameter value was taken from the most accurate frequency result for each test case.

Table 5.5 presents the average frequency error for each test case. The vibration frequency was calculated using Equation 2.14 from the AR parameter and the time difference between each of the tip-timing probes, Δt. Δt was dependant on the RPM speed and the probe spacing on the casing. The frequency error is presented alongside the average AR parameter error and Δt for each test case in Table 5.5 in order to evaluate the influence of such parameters on the accuracy of the frequency calculation.

Figure 5.20 through to Figure 5.28 present the calculated frequency for each test case. Figure 5.20 represents the calculated frequency for test case 1. The graph illustrates the deviation of the calculated frequency from the 2mm blade's true resonant frequency of 254Hz for the setup 1 position. 254Hz was the 2mm blade's first mode resonant frequency at the rotational speed of 941RPM. Figure 5.21 and Figure 5.22 represent the calculated frequency for test case 2 and test case 3 respectively. Both graphs illustrate the deviation of the calculated frequency from the 2mm blade's first mode resonant frequency of 244Hz for the two probe setups, setup 2 and setup 3. 244Hz was the 2mm blade's first mode resonant frequency at the rotational speed of

205RPM. The difference between the first mode resonant frequency measured at 941RPM and the first mode resonant frequency measured at 205RPM was discussed in Section 4.4. Figure 5.23 and Figure 5.24 represent the calculated frequency for test case 4 and test case 5. In this case, the graphs represent the deviation of the calculated frequency from the 2mm blade's second mode resonant frequency of 742Hz for the setup 2 and setup 3 positions. Figure 5.25 and Figure 5.26 represent the calculated frequency for test case 6 and test case 7. The two graphs represent the deviation of the calculated frequency from the 3mm blade's first mode resonant frequency of 342Hz for the setup 2 and setup 3 positions. Finally, Figure 5.27 and Figure 5.28 represent the calculated frequency for test case 8 and test case 9. The two graphs illustrate the deviation of the calculated frequency from the 3mm blade's second mode resonant frequency of 1025Hz for the setup 2 and setup 3 positions.

The ARIV results are shown in Table 5.6 and Table 5.7. Table 5.6 presents the average AR parameter error and SNR for each test case. Table 5.7 presents the average frequency error, AR parameter error, and Δt for each test case. Figure 5.29 through to Figure 5.37 present the calculated frequency for each test case using the ARIV method.

Figure 5.29 represents the calculated frequency for test case 1, where the deviation of the calculated frequency from the 2mm blade's first mode resonant frequency of 254Hz is shown. Figure 5.30 and Figure 5.31 represent the calculated frequency for test case 2 and test case 3, illustrating the deviation of the results from 244Hz for the two probe settings, setup 2 and setup 3. Figure 5.32 and Figure 5.33 represent the calculated frequency for test case 4 and test case 5, illustrating the deviation of the calculated frequency from 742Hz for the setup 2 and setup 3 positions. Figure 5.34 and Figure 5.35 represent the calculated frequency for test case 6 and test case 7, where the deviation from 342Hz is illustrated for setup 2 and setup 3. Finally, Figure 5.36 and Figure 5.37 represent the calculated frequency for test case 8 and test case 9, where the deviation from 1025Hz for the setup 2 and setup 3 positions is illustrated.

5.4.3 The Two Parameter Plot Results

This section presents the results from testing the Two Parameter Plot method. As discussed in Section 5.3.2, the results were grouped according to the EO and PSR since the output of the 2PP calculation was EO. The results were generated from the 16EO and 72EO response data for a range of PSR values. The test cases are summarised in Table 5.2 and were discussed in Section 5.3.2.

Figure 5.38 through to Figure 5.51 present the 2PP results graphically for each test case. Two different results are shown for each test case. Firstly, the probe deflection data plot is shown with the best fit ellipse illustrated. The data points represent the data acquired from the two tip-timing probes, whilst the elliptical solid line represents the least square ellipse fit to the data. Secondly, the calculated EO is presented for each test case, illustrating the deviation of the calculated results from the true value.

Figure 5.38 represents the least square ellipse fit to the data from the 2PP test case 1. The data corresponded with 10% of the 16EO vibration cycle. The ellipse presents a positive major axis angle, representing region 1 in the 2PP relationship. The 2PP relationship is shown in Figure 2.2

where each of the regions (regions 1 to 4) are illustrated. The 2PP relationship was also discussed in Section 2.5. Figure 5.39 represents the calculated EO for a number of samples taken for test case 1, illustrating the deviation of the calculated results from the true EO value of 16. Figure 5.40 represents the least square ellipse fit to the test case 2 data taken from 20% of the 16EO vibration cycle. Again, a positive major axis angle is shown, representing region 1 in the 2PP relationship. Figure 5.42 represents the least square ellipse fit to the test case 3 data taken from 30% of the 16EO vibration cycle. In this case, a negative major axis angle is shown, representing region 2 in the 2PP relationship. Figure 5.41 and Figure 5.43 illustrate the deviation of the calculated EO from the true value of 16 for both test case 2 and test case 3.

Figure 5.44 represents the least square ellipse fit to the test case 4 data taken from 25% of the 72EO vibration cycle. The ellipse has a positive major axis angle, representing region 1 in the 2PP relationship. Figure 5.46 and Figure 5.48 represent the ellipse fit to test case 5 data and test case 6 data taken from 50% and 70% of the vibration cycle respectively. Both ellipse fits produce a negative major axis angle, which correspond with regions 2 and 3 in the 2PP relationship respectively. Figure 5.50 represents the ellipse fit to the test case 7 data taken from 98% of the vibration cycle. The ellipse fit has a positive major axis angle, corresponding with region 4 in the 2PP relationship. Figure 5.45, Figure 5.47, Figure 5.49, and Figure 5.51 present the calculated EO for each of the 72EO test cases (test case 4 through to test case 7), illustrating the deviation of the calculated EO value from the true value of 72 for each PSR.

The overall results are shown in Table 5.8, where the average EO error, the true EO, and the PSR are presented for each test case.

6. Discussion

6.1 Introduction

This results presented in Chapter 5 are discussed here. Firstly, the raw tip deflection data results are discussed, with the view of evaluating characteristics, which were important for successful tip-timing calculations. This was not intended to be a detailed analysis, but was more a preliminary evaluation of the data prior to its use in the tip-timing algorithms. Following this, the use of the raw data in the tip-timing algorithms and the results from this are discussed. Finally, the tip-timing algorithms are discussed in the context of replacing the conventional strain gauge method.

The critical response plots are discussed in Section 6.2.1. The critical response plots represent the data sampled by the four tip-timing probes at the critical operating speed. This data was used in the AR and ARIV calculations. In this case, anomalies such as large errors or DC offsets, which were pertinent to the success of the AR calculation, were evaluated. The traversed resonance plots are discussed in Section 6.2.2. The traversed resonance plots represent the data sampled at each of the four tip-timing probes during the traverse of the critical operating speeds. This data was used in the 2PP calculations. In this case, the resonant characteristics and quality of the sampling were evaluated.

The AR results and the 2PP results are discussed in Section 6.3 and Section 6.4 respectively. The results are grouped and summarised according to the test cases discussed in Section 5.3.1 and Section 5.3.2, and then compared to numerical results published in previous work.

6.2 The Raw Tip Deflection Results

6.2.1 The Critical Response Plots

The raw tip deflection results were presented in Section 5.4.1 for each test case shown in Table 5.1. Each test case was defined by the critical speed, the PSR, and the response frequency. Two sets of results were presented for each case. The first set of plots, shown in Figure 5.2, Figure 5.4, Figure 5.6, Figure 5.8, Figure 5.10, Figure 5.12, Figure 5.14, Figure 5.16, and Figure 5.18, represented the tip deflection data sampled by each of the four tip-timing probes as the critical operating speeds were traversed. These traversed resonance plots represented the data used for the 2PP calculations. The second set of plots, shown in Figure 5.3, Figure 5.5, Figure 5.7, Figure 5.9, Figure 5.11, Figure 5.13, Figure 5.15, Figure 5.17, and Figure 5.19, represented the tip deflection data sampled by the four tip-timing probes at the critical operating speeds. These critical response plots represented the data used for the AR and ARIV calculations. Error bands are shown in all of the tip deflection data plots and represent the error associated with the tip-timing instrumentation. These errors were discussed in Section 4.6.

The critical response plots are discussed here. Each response plot was visually evaluated in terms of its formation of the vibration cycle and continuity over the length of the cassette. The continuity was evaluated in terms of how well the vibration cycle was continued over the length of the cassette when the setup 2 and setup 3 positions were used. The probe setup positions were discussed in Section 5.3.1, where setup 1 represented the probes positioned over the entire length of the cassette and setup 2 and setup 3 represented the positioning of the probes on either half of the cassette. This visual inspection of the tip-timing data ensured that the deflection data was representative of the blade vibration response and was required in order to look for the presence of large errors and DC offsets. A detailed analysis was not required, since this was the purpose of the tip-timing algorithms.

Each critical response plot illustrated the formation of the blade vibration cycle for each test case shown in Table 5.1. For example, Figure 5.3 represented the sampled tip deflection from the 2mm blade's 16EO first mode response at 941RPM. The probes were set in the setup 1 position with an expected PSR of 32%. The calculation of the PSR used to sample the 16EO response data was discussed in Section 5.3.1. Visual evaluation of the plot confirmed that the data could form 32% of the blade vibration cycle.

The remaining critical response plots represented the sampled tip deflection data from both the 2mm blade's and 3mm blade's 72EO response. The two probe setups, setup 2 and setup 3, were used. As shown in Table 5.1, a PSR of 72% corresponded with these two setups when sampling the 72EO response data. The calculation of the PSR used to sample the 72EO response data was discussed in Section 5.3.1. Visual evaluation of the plots confirmed that the data could form approximately 72% of the blade vibration cycle.

Figure 5.5 and Figure 5.7 represented the sampled tip deflection data from the 2mm blade's 72EO first mode response at 205RPM. The plots represented the data from either half of the cassette, sampled on separate occasions. Allowing for slight phase differences due to the data being sampled on different occasions, the data sampled on either half of the cassette showed

good continuity of the vibration cycle. Figure 5.9 and Figure 5.11 represented the sampled tip deflection data from the 2mm blade's 72EO second mode response at 617RPM. Again, the data sampled on either half of the cassette showed good continuity of the vibration cycle.

The 3mm tip deflection data was shown in Figure 5.13, Figure 5.15, Figure 5.17, and Figure 5.19. Figure 5.13 and Figure 5.15 represented the 3mm blade's 72EO first mode response at 286RPM in the setup 2 and setup 3 positions respectively. The data sampled on either half of the cassette showed good continuity. Figure 5.17 and Figure 5.19 represented the 3mm blade's 72EO second mode response at 857RPM, sampled in the setup 2 and setup 3 positions respectively. Again, the data showed good continuity over the length of the cassette.

The tip deflection data, sampled at each of the critical operating speeds was representative of the 2mm blade's and 3mm blade's vibration response with the data forming the expected percentage of the vibration response for each case. As expected, the largest response occurred at 941RPM, where the 2mm blade's first mode was excited. The 2mm blade's and 3mm blade's first mode response, excited at the lower rotating speed of 205RPM and 286RPM, produced a lower response as a result of the lower aerodynamic forcing at these slower rotational speeds. A larger response was shown at 617RPM, where the 2mm blade's second mode was excited. The 3mm blade's second mode response, which was excited at 857RPM, was also larger than its first mode response. Variations in the tip deflection, illustrated from the data sampled over successive revolutions, were experienced for all the responses. This was expected and was attributed mainly to fluctuations in the RPM speed.

The tip deflection results shown in the critical response plots could not be compared directly with the strain gauge results shown in Figure 4.19 through to Figure 4.28. This was because the errors associated with the strain to tip deflection conversion factors were too large. The errors associated with the strain gauges and the conversion factors were discussed in Section 4.3.

When evaluating both the 2mm blade's and 3mm blade's second mode response, it was clear that the sampled data occasionally appeared to be offset in the negative direction. From visual evaluation of the data plots, this appeared to be in the form of a DC offset. For example, Figure 5.19 presents the 3mm blade's torsional mode response at 857RPM, sampled using the setup 3 position. In this case, the sampled data appears to be offset for each individual revolution. However, the vibration cycle is still clear. Another example is shown by Figure 5.17, where the 3mm blade's torsional mode response, sampled using the setup 2 position, is shown. In this case, the data illustrates drifting in the blade's DC position over several revolutions.

The DC movement can be attributed to the high loading incurred by the blade at these higher RPM speeds. In this case, the frequency calculation was unaffected by the DC movements, since the waveform frequency was undisturbed. Also, both the AR and ARIV algorithms do have the capability to calculate the DC offset. However, this could not be evaluated in this instance, since there was no reference to compare the absolute magnitude of the tip deflection with.

6.2.2 The Traversed Resonance Plots

The traversed resonance plots, shown in Figure 5.2, Figure 5.4, Figure 5.6, Figure 5.8, Figure 5.10, Figure 5.12, Figure 5.14, Figure 5.16, and Figure 5.18, represented the data used in the 2PP calculations. Each plot presents the variation of the tip response as the blade's resonant frequency was traversed. The variation of the response was sampled at each of the four tip-timing probes for each of the test cases shown in Table 5.1. Each traversed resonance plot was visually evaluated in order to establish the position of the resonance, to evaluate how well the phase shift characteristics were sampled and to measure the magnitude of the overall response amplitude.

The position of the resonance, in terms of the compressor's operating speed, was characterised by either a peak or a phase shift in the blade tip deflection. The type of response was dependent on the probe's position on the blade's vibration cycle. Figure 6.1 presents some examples of this, where the first resonance curve corresponds with the probe located at the 0^o position on the blade vibration cycle. The second response curve corresponds with the probe located at the 90^o position, whilst the third response curve corresponds with the probe located at the 180^o position on the vibration cycle. The angular positions on the vibration cycle are illustrated in Figure 6.2.

The overall response amplitude was evaluated from each of the traversed plots. According to SDOF theory, the response amplitude corresponds with the overall change in tip deflection, sampled at any position on the blade vibration cycle. Examples of the change in tip deflection, sampled at the various positions on the cycle, are also illustrated in Figure 6.1.

Figure 5.2 represents the 2mm blade's tip response as its 16EO first mode frequency was traversed.Visual evaluation of the probe 4 sampled data confirms that a peak occurs from 940RPM to 945RPM. The data sampled at probe 1, probe 2, and probe 3 illustrate phase shift characteristics, similar to those shown in Figure 6.1. The response characteristics, such as the response peak and the phase shift, are represented well by the sampled data. The response amplitude, using SDOF theory, was 0.9mm.

Figure 5.4 represents the 2mm blade's tip response, sampled using the setup 2 position, as its 72EO first bending mode frequency was traversed. The plot shows that the data sampled at probe 1 and probe 3 have positive and negative peaks at the expected critical rotating speed of 205RPM. The data sampled by probe 2 and probe 4 alternate from one deflection level to another at 205RPM, representing the phase shift at resonance. Figure 5.6 represents the 2mm blade's tip response, sampled using the setup 3 position, as its 72EO first bending mode frequency was traversed. As expected, the plot was quite similar to Figure 5.4, with a response peak at 205RPM. The data sampled by probe 2 and probe 4 represent the response peak, whilst probe 1 and probe 3 sampled data represent the phase shift. The measured response amplitude was around 0.18mm for both cases.

Figure 5.8 represents the 2mm blade's tip response, sampled using the setup 2 position, as its 72EO first torsional mode frequency was traversed. The response peaks, from probe 1 and probe 3 sampled data, are shown to occur at 617RPM. The sampled data from probe 2 and probe 4 reflect phase shift characteristics during the resonance. Figure 5.10 represents the 2mm blade's tip response, sampled using the setup 3 position, as its 72EO first torsional mode frequency was

traversed. The data sampled from probe 4 appears to present a response peak at 617RPM, whilst the data sampled at probe 1 and at probe 3 reflect phase shift characteristics. In this case, there were larger changes in the measured off-resonance tip deflection. As a result, the resonant characteristics were less clear. The response amplitude was more difficult to evaluate in this case, but was approximated to be about 0.4mm.

Figure 5.12 and Figure 5.14 represent the 3mm blade's tip response as its 72EO first bending mode frequency was traversed. The plots represent the setup 2 and setup 3 positions respectively. The response peaks are clearly shown in both plots at 286RPM, with a combination of the peak and phase shift characteristics being reflected in the sampled data due to the positioning of the probes on the blade vibration cycle. The response amplitude was approximated to be 0.2mm from both cases.

Figure 5.16 represents the 3mm blade's tip response, sampled using the setup 2 position, as its 72EO first torsional mode frequency was traversed. In this case, the response peak is not clearly illustrated. The probe 2 and probe 4 sampled data appears to reflect some phase shift characteristics at 857RPM, but no real peak can be observed for any of the probes. Large changes in tip amplitude, as the operating speed was varied, can also be observed. Figure 5.18 represents the 3mm blade's tip response, sampled using the setup 3 position, as its 72EO first torsional mode frequency was traversed. The response peak, for this set of data, is more clearly shown at 857RPM. The probe 4 data represents the peak, whilst the probe 1 and probe 3 data reflect more the phase shift characteristics. However, as with the setup 2 position, large changes in tip amplitude were present. The response amplitude was difficult to evaluate in this case and was approximated to be between 0.2mm and 0.3mm.

Overall, good resonant characteristics are shown in the data plots, with peaks and phase shifts at the expected critical operating speeds. However, it was increasingly hard to evaluate the blade's resonant characteristics at the higher operating speeds of 617RPM and 857RPM, which coincided with the 2mm blade's torsional mode and the 3mm blade's torsional mode respectively. For example, the worst case is shown in Figure 5.16, where no clear peak response can be observed at all. The ambiguity of the resonant response at these operating speeds was due to the large changes in the off-resonance tip amplitude experienced at the higher speeds relative to the low torsional peak response. Such changes in the off-resonance tip amplitude can be attributed to the higher loading associated with increasing the RPM speed.

Another important observation is the difference in sampling quality between the 16EO response data and the 72EO response data. For example, Figure 5.2 represents the 2mm blade's 16EO first bending mode response at 941RPM. In this case, the resonant response is shown to have taken place over a large RPM range, from around 937RPM to 946RPM. As a result of this large resonance range, the resonant peak and phase shift were represented by several revolutions worth of data. However, this was not the case for the 72EO responses. An example of this is shown in Figure 5.4, where the data from the 2mm blade's 72EO first bending mode response is presented. In this case, the peak response and phase shift are represented by a very limited number of data points. A similar type of result is shown in the other 72EO response plots at 286RPM, 617RPM, and 857RPM. This lack of data was due to the limited RPM range associated with the 72EO responses. Control of the test rig speed was coarse and could only be varied by 1RPM at a time. Therefore, the sampled data during a resonance of this type was very limited. The implications of this are discussed later in Section 6.4.

6.3 The AR and ARIV Results

The results from the simple AR and the simple ARIV tests are discussed and compared to the numerical results published in [8] and [21]. [21] presented some results from a numerical analysis of the AR and ARIV methods, whilst [8] presented results from a numerical analysis of the Global AR method. The global approach was described in Section 2.6 as an extension of the AR method, where many revolutions of sampled data were required to calculate the autoregressive parameter. However, in this work, the simple AR method was considered, in order that the mechanics of the method and the parameters that mostly influenced the accuracy of the calculation could be evaluated.

The AR and ARIV test cases were discussed in Section 5.3.1 and are summarised in Table 5.1. In Table 5.1, each test case is described by the test blade, the critical operating speed, the resonant frequency response, and the PSR. The associated SNR is shown in Table 5.3 for each test case. The SNR was evaluated from both the response amplitude shown in the traversed resonance plots and the known tip-timing instrumentation error. This was discussed in Section 5.4.1. Initially, parameters such as PSR and SNR were used to evaluate the performance of the AR method. These parameters were chosen since they were described in [8] and [21] as being critical to the performance of the AR method. As discussed in Section 5.3.1, the PSR coverage was restricted to 32% and 72% by the size of the cassette and the response EO.

6.3.1 The AR Results

The output parameters of the AR method were frequency, amplitude, and phase, where the frequency was calculated from the autoregressive parameter and Δt. The parameter, Δt represents the time taken for the blade tip to pass between each of the four tip-timing probes. In this work, the autoregressive parameter and only the calculated frequency were evaluated. The response amplitude was not evaluated since there was not a system accurate enough to compare the amplitude results with. This was discussed in Section 4.3, where the blade tip deflection to stress correlation factors were shown to have errors up to 33%. The results for each of the test cases are shown in Table 5.4, Table 5.5, Table 5.6, and Table 5.7. The results for each revolution of sampled data are also presented in Figure 5.20 through to Figure 5.37.

Table 5.4 and Table 5.5 present the AR test results. In Table 5.4, the autoregressive parameter error is presented against the SNR and PSR for each test case. The autoregressive parameter, rather than the calculated frequency, was evaluated since it was considered to provide a true indication of the error in the AR calculation. From the results shown, it was clear that there was no correlation between the magnitude of the AR parameter error and the magnitude of the PSR or SNR.

This type of result was also shown in [8] and [21], where it was shown that the sensitivity of the calculated AR output to SNR was significantly reduced for a PSR of 30% and above. For example, the test results presented in [21] illustrated a trend of reduced sensitivity to noise with increased PSR. The results in that particular case showed that acceptable EO values were calculated for a PSR of 27% to 100%. Large errors were shown to occur outside this PSR range. The SNR was set at 30% in this case. Similar work in [8] showed that the calculated EO was

significantly more sensitive to SNR at a PSR of 15%. The same work also showed that a significant improvement in the results was achieved at the higher PSR value of 30%.

An important point to note is that the results in [8] and [21] were presented in terms of EO, whereas the results in this work were not. This was because a range of RPM speeds were used in this work, so that any error in the calculated frequency would be magnified by the magnitude of the RPM speed in the EO calculation (since the EO is equal to the vibration frequency divided by the rotational frequency). However, the trend of insensitivity to noise with increasing PSR, shown in [8] and [21], was still in good agreement with the results presented in Table 5.4.

Table 5.5 presents the average calculated frequency error against the autoregressive parameter error and Δt. The relationship between Δt, the autoregressive parameter, and the calculated frequency was shown by Equation 2.14. The parameter Δt was dependent on the blade tip velocity and the probe spacing.

The worst case result shown in Table 5.5 corresponds with test case 8, where an average frequency error of 88Hz is presented. However, it is clear from the results that the magnitude of the autoregressive parameter error was not the cause, since larger autoregressive parameter errors were calculated for some of the other test cases. There did however, seem to be a correlation between the magnitude of Δt and the average frequency error. For example, a similar autoregressive parameter of 0.202 and 0.235 is presented for test case 2 and test case 8 respectively. However, the average frequency error for test case 3 is 16Hz, whilst the average frequency error for test case 8 is significantly larger at 88Hz. This type of result is repeated for each of the test cases, with the calculated frequency error increasing with an increasing $1/\Delta t$ factor (which increased with larger blade tip velocities and smaller physical probe spacings). This $1/\Delta t$ factor was shown to be part of the frequency calculation, presented by Equation 2.14. Therefore, it was found that the parameter that was most critical, when evaluating the performance of the AR method, was Δt and not the PSR or SNR. This was the case for the range of PSR used in this work.

The AR calculated frequencies from each revolution of sampled data are shown in Figure 5.20 through to Figure 5.28. A large degree of scatter was presented for each test case, which increased with the larger RPM speeds as a consequence of the $1/\Delta t$ factor. It was clear from the results that calculating the blade frequency on a revolution by revolution basis would not be appropriate and that a better average result could be obtained (as reflected in the results shown in Table 5.5). This was particularly the case for the larger RPM speeds. For example, the test case 2 calculated frequency results are shown in Figure 5.21. The test case 2 represented the 2mm blade's 72EO first bending mode response at 205RPM. For this case, the maximum deviation in the calculated frequency was shown to be 18Hz. On the other hand, the maximum deviation shown in Figure 5.20 was 136Hz. This result corresponded with test case 1 data, which represented the 2mm blade's 16EO first bending mode response at 941RPM.

6.3.2 Comparison of the AR and ARIV Results

Table 5.6 and Table 5.7 present the ARIV results. The ARIV method was described in Section 2.6 and involved pre-multiplying the original autoregressive matrix formulation by a matrix of

delayed observations, as shown by Equation 2.16. The purpose of this was to reduce the bias associated with the results. In this case, the instrumental variables matrix was formulated from deflection data delayed by one revolution. The autoregressive parameter error is presented in Table 5.6 and the frequency error is presented against the autoregressive parameter error and Δt in Table 5.7.

The results shown in Table 5.6 are comparable with the AR results shown in Table 5.4, with no apparent improvement in the magnitude of the autoregressive parameter error. As a consequence, Table 5.7 presents similar results to those shown in Table 5.5, with no overall improvement in the accuracy of the calculated frequency. The ARIV calculated frequencies from each revolution of sampled data are shown in Figure 5.29 to Figure 5.37. As with the results shown in Table 5.6 and Table 5.7, there was no apparent improvement in the results.

The published numerical work in [21] evaluated the performance of the simple AR and simple ARIV algorithms. In this case, the calculated EO results were evaluated using a set SNR of 30% for a range of PSR settings from 0% to 200%. Although the EO was evaluated and not the frequency, the trend of the published results for the various PSR settings could be compared with the trend shown from the frequency results in this thesis. The results showed that for the PSR range of 40% to 100%, the AR and ARIV algorithms produced the same EO results. The magnitude of the calculated EO value was unknown, but appeared close to the correct value of 5EO. The published results also showed that at the PSR of 30% both the AR and ARIV methods produced incorrect EO values, but were within a +/-0.5EO band. The magnitude of the error is not relevant in this case though, since Δt was not known. Therefore, it would appear from the results in this work, and the results published in [21] that the simple ARIV method will produce similar results to those produced by the AR method.

6.3.3 The GARIV Method

The numerical based work in [8] presented a different result to the comparison shown in this work. In this case, the EO was calculated using both the Global Autoregressive (GAR) method and the Global Autoregressive with Instrumental Variables (GARIV) method. Both the GAR and the GARIV methods were described in Section 2.6 as an extension to the simple AR method and the simple ARIV method, utilising many revolutions worth of data to calculate the autoregressive parameter. The calculated EO was presented against the SNR, where the SNR was varied from 0% to 30% for a 3EO response.

The GARIV method was shown to provide better results than the GAR method. For example, at the SNR of 30%, the GAR calculated EO was shown to be 4.75, which corresponded with a frequency error of 58%. The GARIV calculated EO was shown to be 3.25, which corresponded with a frequency error of 8%. The difference in the results was quite significant, unlike the results shown in this work.

Therefore, it appeared from the results shown in [8] that significantly improved results could be achieved when using the GARIV method when compared to the GAR method. To understand why this was, the mechanics of the method should be understood. For example, the simple AR matrix formulation with an added noise component is shown in Equation 6.1. The right-hand

side of the simple ARIV formulation is shown in Equation 6.2 to illustrate the effect of multiplying the original matrix by a matrix of delayed observations. Equation 6.3 presents the simple ARIV formulation multiplied out. As shown by Equation 6.3, multiplying the original AR matrix by a matrix of delayed observations attempts to minimise the influence of noise by multiplying and summing uncorrelated noise components. The global form of Equation 6.3 is shown by Equation 6.4. It is clear from this, that by adding additional data from other revolutions, the noise component of the data can be minimised further by summing and multiplying a larger range of uncorrelated noise components. Therefore, the GARIV method may provide more accurate results than the simple AR and simple ARIV methods. However, the technique was not tested during this work.

$$\begin{bmatrix}(x_1+n_1)+(x_3+n_3)\\(x_2+n_2)+(x_4+n_4)\end{bmatrix} = \begin{bmatrix}(x_2+n_2) & 1\\(x_3+n_3) & 1\end{bmatrix}\begin{bmatrix}-a\\D(2+a)\end{bmatrix} \qquad 6.1$$

$$\begin{bmatrix}(x_{22}+n_{22}) & (x_{32}+n_{32})\\1 & 1\end{bmatrix}\begin{bmatrix}(x_{21}+n_{21}) & 1\\(x_{31}+n_{31}) & 1\end{bmatrix} \qquad 6.2$$

$$\begin{bmatrix}[(x_{22}+n_{22})(x_{21}+n_{21})+(x_{32}+n_{32})(x_{31}+n_{31})] & [(x_{22}+n_{22})+(x_{32}+n_{32})]\\[(x_{21}+n_{21})+(x_{31}+n_{31})] & 2\end{bmatrix} \qquad 6.3$$

$$\begin{bmatrix}\left[\sum_{i,j=2}^{\infty}(x_{ij}+n_{ij})(x_{ij-1}+n_{ij-1})\right] & \left[\sum_{i,j=2}^{\infty}x_{ij}+\sum_{i,j=2}^{\infty}n_{ij}\right]\\\left[\sum_{i,j=1}^{\infty}x_{ij}+\sum_{i,j=1}^{\infty}n_{ij}\right] & \sum_{1}^{\infty}1\end{bmatrix} \qquad 6.4$$

6.4 The 2PP Results

The results from the 2PP tests are described here. As discussed in Section 5.4.1, the 2PP data was sampled at RPM increments through each of the resonant operating speeds. The data was grouped under seven different test cases, which were discussed in Section 5.3.2 and were summarised in Table 5.2. The parameters used to define the test cases were EO and PSR. In Table 5.2, each test case corresponded with either a 16EO response, or a 72EO response. In the 16EO case, a PSR range of 10% to 30% was available, whilst for the 72EO response, a PSR range of 25% to 98% was achievable. The results are shown in Table 5.8 in the form of the average EO error and are graphically presented in Figure 5.38 to Figure 5.51, where both the ellipse fit to the sampled tip deflection data and the calculated EO for each sampled traverse is shown.

6.4.1 The 16EO Experimental Results

A summary of the 16EO results is shown in Table 5.8, with the largest average EO error equal to 2EO and the smallest average EO error equal to 1EO. The results are also shown graphically in Figure 5.39, Figure 5.41, and Figure 5.43, where the deviation of the calculated EO from the true EO for each PSR is illustrated. An improvement in the accuracy of the calculated EO with increasing PSR is shown clearly from comparing the graph results shown in the aforementioned three figures. For example, the data sampled at 32% PSR, shown in Figure 5.43, produced the most acceptable results with a maximum deviation of 1EO. However, there was a significantly larger degree of scatter in the results produced at the lower PSR values of 10% and 20%. For example, the 10% PSR results shown in Figure 5.39 varied from 11EO to 19EO, whilst the 20% PSR results, shown in Figure 5.41, varied from 11EO to 15EO.

The ellipse fit to the raw data is shown in Figure 5.38, Figure 5.40 and Figure 5.42. In each case, there appears to be a large degree of scatter of the data about the fitted ellipse. This scatter is due to the random blade response changes as a result of the high loading at 941RPM. These response changes are apparent in Figure 5.2, where the sampled blade tip response during the traverse of the 16EO response is shown. However, regardless of the degree of scatter shown in the ellipse fits, promising EO results were produced by the 30% PSR data.

The reason for the improved results at 30% PSR may be attributed to the physical probe spacing, $\Delta\theta$. In this work, the length of the minor axis of the ellipse was found to increase as the probe spacing was increased for the PSR range of 10% to 30%. The effect of the probe spacing on the axis ratio can be shown in some individual case results taken from the 16EO data shown in Table 6.1, where the axis ratio is shown to have increased with PSR for the 16EO data. It is possible that with an increased PSR, the influence of the deflection data scatter on the minor axis measurement error would be reduced. Any error associated with the measurement of the minor axis was transferred to the EO calculation through the 2PP relationship shown by Equation 2.4.

To understand why this is the case, the mechanics of the method should be understood. The method was described in [9], where it was shown that the basis of the 2PP method originated from the polar plot of the single-degree-of-freedom (SDOF) response during a resonance. It was

shown that the polar plot of a SDOF response has two components, shown by Equation 6.5 and Equation 6.6. $A(\omega)$ represents the vibration response amplitude and $\psi(\omega)$ represents the phase angle. An example of these two components is shown in Figure 6.3.

In [9] it was shown that the tip deflection, sampled by two probes during a traverse of a resonance, can be described in a similar way. For example, Equation 2.2 and Equation 2.3 represent two deflection data points; x_A and x_B, sampled by the tip-timing probes; probe A and probe B. The two probes were located within one vibration cycle, with a spacing of $n\Delta\theta$ degrees on the resonance. It was shown in [9] that if probe B is located 90 degrees from probe A on the resonance, then Equation 2.3 could be rewritten as Equation 6.7. Equation 2.2 and Equation 6.7 represent the components of the resonance polar plot shown in Figure 6.3. Therefore, at this spacing, the data sampled from each of the probes during the traverse of a resonance would represent the circular polar plot.

For other $n\Delta\theta$ probe spacings, elliptical polar plots were formed from the x_A and x_B components during the traverse of the resonance. It was shown in [9] that as $\Delta\theta$ is varied, both the position of the ellipse and its geometry would alter. Examples of this are shown in Figure 6.4, where the different ellipses are shown for a 10 degree sensor spacing and a 30 degree sensor spacing. Figure 6.4 illustrates that by reducing the probe spacing from 30 degrees to 10 degrees, the length of the minor axis is reduced. This can also be shown from Equation 2.2 and Equation 2.3, where it is clear that as $\Delta\theta$ tends to zero, x_B tends towards x_A, which would reduce the minor axis to zero.

$$A(\omega)\sin(\psi(\omega_1)) \tag{6.5}$$

$$A(\omega)\cos(\psi(\omega_1)) \tag{6.6}$$

$$x_B = -A(\omega)\sin(n\theta_A + \psi(\omega)) + C \tag{6.7}$$

6.4.2 Comparison of the 16EO Results with Previously Published Results

The 16EO results were comparable with the results published in [9] and [21]. In [9], the application of the 2PP method to some tip-timing data sampled from a low pressure steam turbine was discussed. Two 2EO responses were evaluated using a combination of three tip-timing probes, which provided a PSR coverage of 3%, 9%, and 12.5%. The calculated EO was presented for each of the responses. However, the corresponding probe combination used, and therefore the PSR, were not specified. The published results were compared with the 10% PSR results shown in this work, since 10% was the closest in magnitude to the three possible probe combinations specified. The first set of published results in [9] presented a maximum deviation of around 1EO, whilst the second set of results presented a maximum deviation of around 3EO. The second set of results were more comparable with the 10% PSR results shown in this work, where a maximum deviation of 5EO was shown in Figure 5.39. However, an important point to note is that the magnitude of the EO used in [9] was lower than the 16EO data used in this work. The possible implications of this are discussed later in this section.

Some 2PP results were also presented in [21], where numerically generated 5EO response tip deflection data was used. In this case, the calculated EO was evaluated for a range of PSR values. It was shown that a significantly improved EO result could be achieved above a PSR of 22%. This result was in good agreement with the 16EO results presented in this work, where an improved result was obtained when using the higher PSR setting of 30%. However, the results from this work were inconclusive since the PSR range was not large enough to evaluate fully the accuracy of the calculated EO versus PSR.

6.4.3 The 72EO Experimental Results

The results produced by the 72EO data had significantly larger errors. The average errors are presented in Table 5.8, where the largest average EO error is shown to be 21EO at a PSR of 25%, whilst the smallest average EO error is shown to be 4EO at a PSR of 98%. The calculated EO values are also shown graphically for each sampled traverse in Figure 5.45, Figure 5.47, Figure 5.49, and Figure 5.51. Figure 5.45 represents the 25% PSR calculated EO, where a maximum deviation of 34EO was shown. Figure 5.47 and Figure 5.49 present the 50% PSR and 70% PSR calculated EO respectively, where a maximum deviation of 24EO is shown for both cases. Figure 5.51 presents the 98% PSR calculated EO, where a maximum deviation of 11EO is shown.

The results are shown to improve with increasing PSR, with the worst case result corresponding with the 25% PSR and the best result corresponding with the 98% PSR. However, it is important to note that the 98% PSR results were extremely unreliable and frequently provided invalid results.

Overall, the 72EO results were poor. This may be attributed to two reasons. The first reason is the quality of the data and the range of RPM over which the 72EO resonance response was excited. Examples of this are shown in Figure 5.4, Figure 5.6, Figure 5.8, Figure 5.10, Figure 5.12, Figure 5.14, Figure 5.16, and Figure 5.18. For example, the traverse of the 2mm blade's 72EO first bending mode at 205RPM is shown in Figure 5.4. As discussed in Section 6.2.2, the 72EO resonance response was shown to have taken place over a small RPM range, from 203RPM to 206RPM. Since control of the test rig was coarse and could only be varied by 1RPM at a time, a minimal number of data points were sampled during the resonant phase shift of the 72EO response. As a consequence, the sampled response data sparsely covered the least squares ellipse fit. Examples of the least squares ellipse fits to the 72EO data are shown in Figure 5.44, Figure 5.46, Figure 5.48 and Figure 5.50.

Another example of a 72EO response is shown in Figure 5.8, where the traverse of the 2mm blade's 72EO first torsional mode at 617RPM is shown. The torsional mode inherently had a weaker response than the bending mode. As a consequence, the response was excited over a limited RPM range, even though in this case the RPM speed was higher than the previous example. In comparison to this, the traverse of the 16EO resonance, shown in Figure 5.2, was excited over a larger range of RPM speeds. As a consequence, significantly more data was sampled during the resonance phase shift. The corresponding ellipse fits are shown in Figure 5.38, Figure 5.40, and Figure 5.42, where it is clear that the data covered a larger proportion of the ellipse when compared to the 72EO ellipse plots shown in Figure 5.44, Figure 5.46, Figure 5.48 and Figure 5.50.

Another point to note is the quality of the data sampled during the traverse. For example, the traverse of the 3mm blade's first torsional mode is shown in Figure 5.16 and Figure 5.18. As discussed in Section 6.2.2, the resonant characteristics were not clearly illustrated. This was shown particularly in Figure 5.16. In this case, the change in amplitude sampled at each of the four probes did not coincide with one another. According to SDOF theory, the change in amplitude sampled at any point of the blade response cycle, during the traverse of a resonance, should be the same. This was clearly not the case with the sampled data shown in Figure 5.16. Also, the peak in the response was not clear for this example case. In Section 6.2.2, this was attributed to large changes in off-resonance tip amplitude due to the high aerodynamic loading on the blades at the higher RPM speeds. The torsional measurement was particularly sensitive to this since only one of the blade tip edges were covered by the tip-timing probe. A probe positioning setup less sensitive to random off-resonance deflection would have involved probes covering both the leading edge and trailing edge and using the difference in deflection to calculate the pure torsional component of the tip movement.

The second reason for the poor 72EO data results may be attributed to the impact of the tip-timing measurement error on the EO calculation. The tip-timing measurement in terms of SNR was discussed in Section 5.4.1 and summarised in Table 5.3 for each of the EO responses. Since the length of the major axis was effectively a measure of the blade vibration response amplitude, the SNR shown in Table 5.3 could be used to describe the percentage error associated with the axis ratio. The SNR represented the ratio of the tip-timing instrumentation error to the blade tip response amplitude. As discussed in [9], any percentage error associated with the axis ratio would result in the same percentage error in the calculated EO, as a result of their linear relationship. The linear relationship between the ellipse axis ratio and the calculated EO was shown by Equation 2.4 and Equation 2.5 and illustrated in Figure 2.2. Equation 2.4 presented the empirically based relationship between the ellipse axis ratio and the sensor spacing in terms of degrees of resonance. The resonance order was calculated from the sensor spacing using Equation 2.5.

A range of SNR were presented in Table 5.3 for the 72EO responses. The worst case result was an SNR of 27% for the 3mm blade's 72EO first bending mode response at 286RPM. This 27% would correspond with an EO error of +/-19EO. The best case result was an SNR of 6% for the 2mm blade's 72EO first torsional mode response at 617RPM. This would translate into an error of +/-4EO. On the other hand, the SNR for the 16EO response was shown to be 3%, which would correspond with an EO error of +/-0.5.

6.4.4 Sources of Uncertainty in the 2PP Calculation

As discussed in Section 6.4.1 and Section 6.4.2, good results were obtained from the 16EO data. This was particularly true for the 30% PSR case, where the EO result was within an error band of +/- 1EO, as shown in Table 5.8. From the results, it appeared that the accuarcy of the EO calculation improved with an increased PSR setting. However, this could not be investigated fully since the PSR range was limited when sampling the 16EO data. This was discussed in Section 5.3.2.

The results from the 72EO data were very poor in comparison. Table 5.8 presents average errors from the 72EO data which, ranged from +/- 21EO for a PSR of 25% to +/- 4EO for a PSR

of 98%. As discussed in Section 6.4.3, the main source of error was attributed to the sparseness of the data sampled during the phase change of the 72EO resonant response. As a result of this, the influence of parameters such as SNR and PSR on the EO calculation could not be evaluated for the 72EO case.

6.5 Replacement of the Strain Gauge Method

6.5.1 Comparison of Tip Deflection Measurement

The conventional method for measuring the blade response during an engine test was described in Section 2.2. Strain gauges are attached to the blade surface at optimum positions, which are established with the use of FEA. The gauge output is evaluated whilst the engine is run through its operating speed range. The strain gauge output is converted to tip deflection using strain to tip deflection correlation factors. The blade tip deflection is then related back to the amplitude associated with the blade's fatigue limits.

Strain to tip deflection correlation factors are evaluated through the use of bench tests, where the blade is secured on a shaker table and is excited at its resonant frequencies. The blade strain is measured using strain gauges, whilst the tip deflection is measured using a non-contact device such as an Electronic Speckle Pattern Interferometry system. This type of system was discussed in Section 4.3, where it was shown that large errors can be associated with strain to tip deflection correlation factors. For example, errors ranging from 12% to 33% were recorded in this work. A summary of the correlation factors and errors were shown in Table 4.8 and Table 4.9.

The error associated with the tip-timing deflection measurement was first discussed in Section 4.6, where it was shown that the tip-timing probes could detect the position of the blade tip within +/-0.03mm. This was found to be equivalent to the state-of-the-art, when compared with error values quoted in other published work. SNR values, which represented the ratio of the tip-timing instrumentation error to the magnitude of the response amplitude were summarised in Table 5.3, where it was shown that the percentage error associated with the tip deflection measurement system varied from 3% to 27%.

The tip deflection measurement capabilities of both systems in this work were comparable, with similar percentage errors presented in both cases. However, this was not the case when considering the calculation of the blade's frequency response.

6.5.2 Comparison of Frequency Measurement

The measurement of the blade vibration frequency using strain gauges during this work was discussed in Section 3.3.3. The gauge output data was continuously sampled during each EO response, which was then processed off-line using the Matlab signal processing toolbox in order to evaluate the spectrum of the signal. The calculated frequencies correlated well with the numerical model frequency results, as shown in Table 4.3, Table 4.4, Table 4.10, and Table 4.11.

The tip-timing methods were less effective in evaluating the blade frequency response. The results from the two tip-timing algorithms were discussed extensively in Section 6.3 and Section 6.4. The 2PP results were discussed in Section 6.4, where it was shown that there were large errors in the calculated EO at the higher 72EO responses. Although in this case, the evaluation was hindered by the poor sampling density of the blade's resonance. The AR and ARIV results

were discussed in Section 6.3. Acceptable results were achieved at low blade tip velocity values (high Δt). However, the accuracy of the frequency calculation deteriorated significantly for higher tip velocities.

At present, the tip-timing method is viewed as a complementary technique, used in addition to the conventional strain gauge method. For the tip-timing method to be considered as a replacement to the conventional strain gauge method, the issues associated with the frequency measurement must be remedied.

7. Conclusions

7.1 The Aims

This chapter sets out to draw conclusions from the work carried out in this thesis. This is done primarily by answering the objectives set out in Section 1.3, which included:

1. Development of a test facility with tip-timing instrumentation and a data acquisition system.
2. Construction of the algorithm code and integration with the data acquisition system.
3. Test the algorithms under real engine conditions, evaluate the results, and compare with previously published numerical results.
4. Evaluate the results in terms of their prospect as a replacement for the conventional technique using strain gauges.

Section 7.2 concludes the first two objectives, providing an overview of the tip-timing system and its performance. Section 7.3 concludes the third objective, presenting the main findings from the experimental tests of the two tip-timing algorithms. Section 7.4 concludes the fourth objective, where an overview of the tip-timing method and the algorithms are presented in a more general context. The original contributions from this work are then summarised in Section 7.5, the publications list is presented in Section 7.6, and the recommendations for further work is given in Section 7.7.

7.2 The Tip-Timing Test Facility

A low speed tip-timing test facility was successfully built up in order to test the tip-timing algorithms using representative engine conditions. This facility included the Cranfield University one and a half stage compressor test rig, a purpose-built optical tip-timing measurement system, and a data acquisition and post processing system.

Two specially built test blades were substituted for conventional blades on the rotating test facility in order that a range of EO responses could be excited. The engine order response was evaluated through the use of numerical modelling and engine strain gauge tests. Blade tip deflections, representative of the those experienced in gas turbines, were achieved.

Optical tip-timing instrumentation was successfully built and used to sample the blade tip response. The performance of the tip-timing instrumentation was evaluated through a series of tests from which, it was shown that the position of the blade could be detected to within +/- 0.03mm. This performance was shown to be comparable to the state-of-the-art, as quoted in other published work.

A data acquisition system was built for the purpose of acquiring blade tip time of arrival data and measuring the blade tip deflection from this data. Five channels were used to sample the OPR signal and the four tip-timing probe signals. The deflection data was sampled during the traverse of each the known critical operating speeds and shown to be representative of the two test blade's resonant responses.

The tip-timing algorithms, the AR method and the 2PP method, were coded using PV-Wave software according to the theory presented in Section 2.5 and Section 2.6. In the case of the 2PP method, an external procedure for fitting the tip deflection data to an ellipse had to be incorporated into the existing method. The method was taken from published work on the least squares fitting of data to a general ellipse. The algorithm results were evaluated and compared to previously published numerical work.

7.3 Tip-Timing Results

7.3.1 The AR and ARIV Results

The AR and ARIV methods were experimentally tested using tip-timing data sampled at each of the compressor critical operating speeds. The two parameters, PSR and SNR, were initially used to evaluate the algorithms. These parameters were specified by previously published simulation work in [8] and [21] as being critical when evaluating the performance of both the AR method and the ARIV method.

Two PSR settings of 30% and 72% were available in this work. A range of SNR values, evaluated from the blade tip response amplitude and the known tip-timing instrumentation error, were calculated for each of the critical speed responses. The calculated autoregressive parameter was evaluated. No correlation between the level of SNR or PSR and the accuracy of the calculated autoregressive parameter was established. The error in the autoregressive parameter appeared to be random and did not degrade with the lower PSR setting. This was also shown by the simulation results published in [8] and [21], where the AR output was evaluated for a range of PSR and SNR values using numerical tip-timing data.

However, in the experimental results reported in this thesis, a significant variation in the accuracy of the calculated frequency was shown. The frequency was calculated from the autoregressive parameter and Δt. A correlation between the accuracy of the calculated frequency and the $1/\Delta t$ factor was established. The parameter, Δt, represented the time taken for the blade tip to pass between each of the four tip-timing probes and was dependent on the blade tip velocity and the physical probe spacing on the casing. This sensitivity was not highlighted in the previous published work.

There was no improvement in the results when comparing the ARIV and the AR methods. The numerical work published in [21] also illustrated this. However, the simulation work published in [8] presented significant improvements in the results when applying the GARIV method. The GARIV method was a global variant of the ARIV approach, where a number of revolutions could be used to calculate the autoregressive parameter. The GARIV theory was discussed, where it was shown that its success was due to the multiplication of uncorrelated noise components from many revolutions of data. Such an approach may be useful in reducing the random error associated with the autoregressive parameter.

However, the success of the GARIV method would depend on the extent of the reduction in the random error, since any error is magnified by the $1/\Delta t$ factor.

7.3.2 The 2PP Results

The 2PP method was experimentally tested using tip-timing data sampled during the traverse of each of the critical operating speeds. The calculated EO was evaluated using data sampled from the 16EO response and the 72EO response for a range of PSR settings. A limited PSR range of

10% to 30% was available for the 16EO response, while a larger PSR range of 25% to 98% was achieved for the 72EO response.

Considering the 16EO results only, it was found that a significant improvement in the results were achieved as the PSR was increased from 10% to 30%. At the PSR of 30%, the results were within 1EO of the correct value. The improvement in the EO calculation was in good agreement with the published numerical results in [21], where it was shown that improved EO results could be achieved above a PSR of 22%. The improved results, shown for the 30% PSR, were attributed to the effect of the probe spacing, $\Delta\theta$, on the geometry of the ellipse. It was illustrated that for an increased probe spacing within the 10% to 30% PSR range, the length of the minor axis was increased. As a consequence, the influence of the data scatter on the axis ratio calculation error was reduced. However, the effect of the probe spacing could not be evaluated for the full PSR range using the 16EO response data. Therefore, the result was inconclusive.

A full PSR range (25% to 98%) was achieved for the 72EO response data. However, the results were poor in this case, with errors as large as 30EO being recorded in one case. There were two factors which may have caused this. The first of which, was the poor sampling density of the 72EO resonant characteristics. Control of the compressor's RPM speed was coarse, with a resolution of 1RPM. Therefore, the peak response and phase shift, which are associated with a resonance and are the basis of the elliptical polar plot, were not represented well by the sampled data. The 72EO response was found to be weaker than the 16EO response as a result of the 72EO bending modes being excited at the lower RPM speeds and the 72EO torsional mode response being inherently weaker than the bending mode response. As a consequence, the RPM range, over which the 72EO resonance was excited, was limited. This was shown when comparing the fitted ellipse plots from the 72EO tests to those from the 16EO tests, where it was clear that the data from the 72EO tests formed a smaller proportion of the ellipse than in the case of the 16EO results. The second reason for the poor 72EO data was attributed to the linear relationship between the percentage error in the response amplitude calculation and the percentage error in the calculated EO. Percentage errors up to 27% were experienced in these tip-timing measurements. Therefore, for the 72EO response, an error of 20EO could be experienced. Errors of this type were not highlighted in previously published work.

Overall, the 16EO results appeared promising, with a significant improvement at the 30% PSR setting, which appeared to be due to the magnitude of the minor axis. However, the improvement with PSR could not be evaluated fully in this case. Although the 72EO data had a wider range of PSR, the influence of this could not be evaluated. This was mainly as a result of the poor sampling density of the 72EO resonance characteristics and therefore, the random nature of the measured minor axis. The other issue highlighted from the results was the inherent larger errors associated with the larger EO values. However, this again could not be investigated thoroughly as a consequence of the poorly sampled data.

7.4 Tip-Timing Prospects

The potential for replacing the conventional strain gauge method with tip-timing was discussed. This was done by evaluating the effectiveness of both the strain gauge method and the tip-timing method in measuring tip deflection and response frequency.

The tip deflection measurement capabilities of both systems were found to be comparable. The strain gauge method used strain to tip deflection correlation factors in order to evaluate the blade response amplitude from strain. In this work, such correlation factors were found to have errors ranging from 12% to 33%. The errors associated with the tip-timing tip deflection measurement were approximated from the ratio of the tip-timing instrumentation error to the magnitude of the blade response amplitude. Such errors ranged from 3% to 27%.

However, the two methods were not found to be comparable when evaluating the frequency response. The strain gauge method is inherently very effective in measuring the vibration frequency, where multiple frequency responses can be evaluated from the continuously sampled data using well developed FFT algorithms.

The tip-timing algorithms, on the other hand, were less effective in evaluating the blade frequency response and were limited to measuring SDOF responses. For example, the 2PP method was shown to produce errors as large as 34EO for the 72EO data. The AR and ARIV methods produced more acceptable frequency results at low blade tip velocity values, with a typical deviation of 16Hz being recorded for one of the cases at 205RPM. However, the accuracy in the calculated frequency was found to deteriorate with higher tip velocities (lower Δt), with a deviation of 88Hz being recorded at the speed of 857RPM. This sensitivity to Δt may have significant implications in a gas turbine, where the tip velocities can be an order of magnitude higher than the tip velocities experienced by the test facility used in this work. The test blades experienced a tip velocity of around 60m/s at the highest critical operating speed of 941RPM.

At present, the tip-timing method is viewed as a technique, which is used parallel to the strain gauge method. For this to change however, the issues associated with frequency measurement must be remedied and scope for measuring multiple frequency responses is required.

7.5 Original Contributions

The work discussed in this thesis has led to reported findings that were not available in previously published literature.

An experimental optical tip-timing low speed test facility was built. This included purpose-built optical tip-timing instrumentation, and a tip-timing data acquisition and post processing system, which were incorporated on to the Cranfield University low speed test facility.

The remaining original contributions are grouped according to the tip-timing algorithms.

7.5.1 The AR and ARIV Algorithms

1. Experimental testing of the AR and ARIV methods using a controlled test environment representative of a real engine, using real optical tip-timing probes.

2. Analysis of AR and ARIV frequency results from data sampled over a range of frequencies and RPM speeds.

3. From the analysis, it was established that the accuracy of the calculated frequency was sensitive to tip velocity and the physical probe spacing on the casing. This may have implications when using the AR and ARIV techniques on higher speed engines.

7.5.2 The 2PP Algorithm

4. Experimental testing of the 2PP method using a controlled engine test environment.

5. Comparison of 2PP experimental results taken from data sampled at a low EO (16) response and a high EO (72EO) response using a range of PSR settings.

6. From the analysis, it was illustrated that the accuracy of the result deteriorated when using the larger EO response data. This was partially attributed to the linear relationship between the percentage error associated with measured response amplitude and the calculated EO.

7. It was shown that the success of the 2PP method may also correspond with the sensitivity of the frequency response to RPM speed. It was found that for the weaker response with an inherent limited RPM range, the ellipse fits were under-sampled and consequently less accurate results were produced.

7.6 Publications List

Grant, K.R., Ivey, P.C., 2002, "The Experimental Validation of Tip-Timing Techniques for Condition Monitoring of HCF in Gas Turbine Aero-Engines". 38th AIAA/ASME/SAE/ASEE Joint Propulsion Conference & Exhibit, 7-10 July. Indianapolis.

Grant, K.R., Ivey, P.C., 2002, "Investigation into the use of Tip-Timing for Blade Condition Monitoring". COMADEM 2002, 2-4 September. University of Birmingham.

Ivey, P.C., Grant, K.R., 2002, "The New Potential for Joint US/UK Studies in Sensor Technology for HCF Failure in Gas Turbine Aero-Engines". AIAA Aerodynamic Measurement Technology and Ground Testing Conference. St. Louis.

Ivey, P.C., Grant, K.R., Lawson, C.P., 2002, "Tip-Timing Techniques for Turbomachinery HCF Condition Monitoring". The 16th Symposium on Measuring Techniques in Transonic and Supersonic Flow in Cascades and Turbomachines". Cambridge.

7.7 Further Work

The work in this thesis provided an experimental analysis of two recently published tip-timing algorithms and evaluated them in terms of their potential as a replacement of the conventional strain gauge method. From the conclusions presented in this work, further work is recommended.

7.7.1 The 2PP Method

It was found through the course of this work that the 2PP output results may improve with an increased PSR. However, a more extensive PSR range is required in order to evaluate this fully. The test facility used during the course of this work could be modified in order to carry out this work. This would involve increasing the length of the cassette in order to capture a larger percentage of the 16EO response. The relationship between the cassette length and PSR was discussed in Section 5.3.1 and Section 5.3.2.

It was also highlighted that the impact of SNR on the EO calculation may worsen for higher EO values. The work in this project was unable to evaluate this since large errors were incurred in the EO calculation due to the sampled 72EO data sparsely covering the resonant response. This was discussed in Section 6.4.3 and Section 6.4.4. In order to evaluate the performance of the 2PP Method for higher EO values, a test facility with finer speed control is required to sample the EO data over a very finite speed range.

7.7.2 The AR and ARIV Methods

The effect of noise on the AR calculated frequency was found to be amplified with blade tip velocity. In this work, the ARIV method did not provide improved results. However, it was highlighted that a global variant of the ARIV method, known as the GARIV method, may further reduce the influence of noise. This GARIV method should be incorporated onto the Cranfield University tip-timing test facility in order that an experimental evaluation of the method can be carried out.

It was also highlighted that the AR and ARIV methods were restricted to measuring an SDOF response. However, with the development of more advanced engines there are more complex and multiple mode conditions experienced. As a consequence, tip-timing methods for measuring an MDOF response should be explored.

7.7.3 High Speed Testing

The algorithms presented in this work were tested using a low speed test facility, where the blade tip velocities were at least an order of magnitude smaller than those experienced on gas turbine engines. The AR and ARIV algorithms, in particular, were established as being sensitive to the blade velocity parameter. As a consequence, the algorithms should be tested using a higher speed facility in order to complete the experimental analysis.

7.7.4 Optical Probe Performance

The optical tip-timing probes in this work were evaluated to be able to detect the position of the probe to within +/-0.03mm. Improving the performance of the probes should be investigated, as this would reduce the degree of noise in the measured tip deflection data.

This may involve the use of lenses on the probe tip in order to generate a smaller light spot at the blade tip. A smaller light spot would provide a smaller and steeper signal rise at the photodetector, minimising the influence on noise on pretriggering. This was discussed in more detail in Section 3.3.1.

More sophisticated photodetectors with a lower degree of noise may be also used. This would also minimise the influence of noise on pretriggering, as discussed in Section 3.3.1.

References

[1] R. E. Kielb, H. D. Chiang. "Recent Advancements in Turbomachinery Forced Response Analyses". AIAA 92-0012. 1992.

[2] T. H. Fransson. "Dynamic Aeroelasticity". *Von Karman Institute for Fluid Dynamics Lecture Series on Aeroelasticity in Axial-Flow Turbomachines.* 1999-2005.

[3] M. Baumgartner, F. Kameier, J. Hourmouziadis. "Non-Engine Order Blade Vibration in a High Pressure Compressor". *ISABE Twelth International Symposium on Airbreathing Engines.* 1995.

[4] Y. EL - Aini, R. deLaneuville, A. Stoner. "High Cycle Fatigue of Turbomachinery Components - Industry Perspective". AIAA 97-3365. 1997

[5] T. Nicholas. "High Cycle Fatigue Life Management in Gas Turbine Engines". *Proceedings of the 5th National Turbine Engine High Cycle Fatigue Conference.* 2000.

[6] S. M. Bagnall, D. L. Shaw, J. C. Mason-Flucke. "Implications of 'Power by the Hour' on Turbine Blade Lifing". *Proceedings of the 5th National Turbine Engine High Cycle Fatigue Conference.* 2000

[7] R. Friend. "Turbine Engine Research in the United States Air Force". *IEEE Aerospace Conference Proceedings.* Vol. 7, pp 73165 - 73178, 2001.

[8] I. B. Carrington, J. R. Wright, J. E. Cooper, G. Dimitriadis. "A Comparison of Blade Tip Timing Data Analysis Methods". *Proc. Instn. Mech. Engrs.* Vol. 215. Part G. 2001.

[9] S. Heath. "A New Technique for Identifying Synchronous Resonances Using Tip-Timing". *ASME Journal of Engineering for Gas Turbines and Power.* Vol. 122, No. 2. April 2000.

[10] I. Fradley. "Improved Methods of determining Turbine Blade Vibration Levels". *Cranfield University M.Sc. Thesis.* 1995.

[11] R. Hohenberg. "Detection and Study of Compressor-blade Vibration". *Journal of the Society for Experimental Stress Analysis. Experimental Mechanics.* Vol. 7, No. 6, June 1967.

[12] S. Heath, M. Imregun. "A Review of Analysis Techniques for Blade Tip-Timing Measurements". *Transactions of the ASME.* 97-GT-213. June 1997.

[13] P. E. McCarty. "Development of a non-interference technique for measurement of turbine engine compressor blade stress". Report AEDC/TR-79/78. 1978

[14] P. E. McCarty, J. W. Thompson, R. S. Ballard. "Noninterference Technique for Measurement of Turbine Engine Compressor Blade Stress". *Journal of Aircraft.* Vol. 19, No. 1. January 1982.

[15] W. W. Robinson, R. S. Washburn. "A Real Time Non-Interference Stress Measurement System for Determining Aero Engine Blade Stresses". *Transactions of the ISA.* Paper #91-103. 1991.

[16] H. Jones. "A Nonintrusive Rotor Blade Vibration Monitoring System". *Transactions of the ASME.* 96-GT-84. June 1996.

[17] W. B. Watkins, R. M. Chi. "A Noninterference Blade Vibration Measurement System for Gas Turbine Engines". *Transanctions of the AIAA.* AIAA-87-1758. 1987.

[18] R. M. Chi, H. T. Jones. "Demonstration Testing of a Noninterference Technique for Measuring Turbine Engine Rotor Blade Stresses". *Transactions of the AIAA.* AIAA-88-3143. 1988.

[19] S. Heath, M. Imregun. "An Improved Single-Parameter Tip-Timing Method for Turbomachinery Blade Vibration Measurements using Optical Laser Probes". *International Journal of Mechanical Science.* Vol. 38. No. 10. 1996.

[20] M. Zielinski, G. Ziller. "Noncontact Vibration Measurements on Compressor Rotor Blades". *Measurement Science and Technology.* Vol. 11. No. 7. 2000.

[21] G. Dimitriadis, I. B. Carrington, J. R. Wright, J. E. Cooper. "Blade Tip Timing Measurement of Synchronous Vibrations of Rotating Bladed Assemblies". *Mechanical Systems and Signal Processing.* Vol. 16. No. 4. 2002.

[22] C. Lawson. "Capacitance Tip Timing Techniques in Gas Turbines". *Cranfield University PhD Thesis.* 2004.

[23] A. Fitzgibbon, M. Pilu, R. B. Fisher. "Direct Least Square Fitting of Ellipses". *IEEE Transactions on Pattern Analysis and Machine Intelligence,* Vol. 21. No. 5. 1999

[24] M. Petyt. "Introduction to Finite Element Vibration Analysis". Cambridge University Press. 1990.

[25] M. A. Dokainish, S. Rawtani. "Vibration Analysis of Rotating Cantilever Plates". *International Journal for Numerical Methods in Engineering,* Vol. 3. No. 2. 1971

[26] M. A. Lawry. *I-DEAS Master Series: Student Guide.* SDRC. 1999.

[27] P. N. James, P. Souter, D. C. Dixon. "A Comparison of Parameter Estimation Algorithms for Discrete Systems". *Chemical Engineering Science*, Vol. 29. 1974

[28] K. J. Astrom, P. Eykhoff. "System Identification-A Survey". *Automatica*, Vol. 7. 1971

Figures

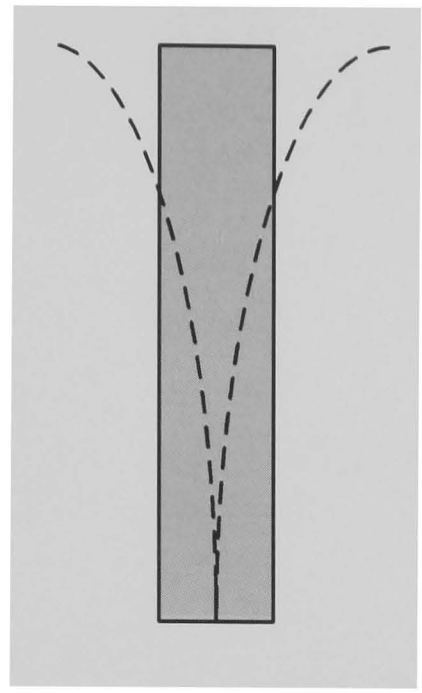

Figure 1.1 First Flap Mode

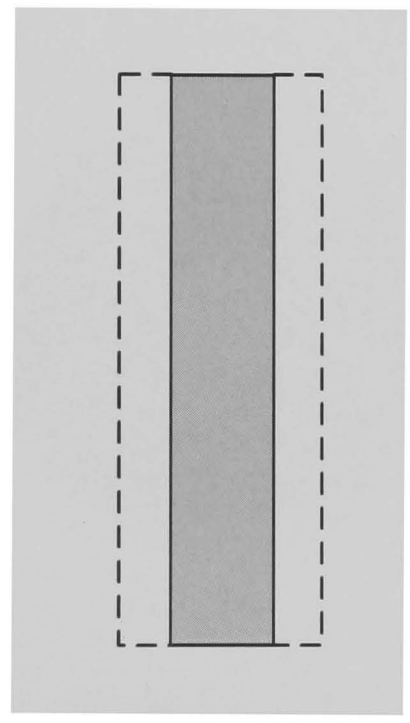

Figure 1.2 First Edgewise Mode

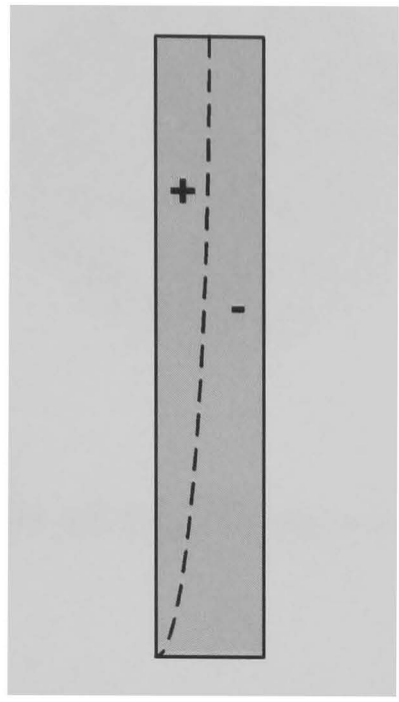

Figure 1.3 First Torsional Mode

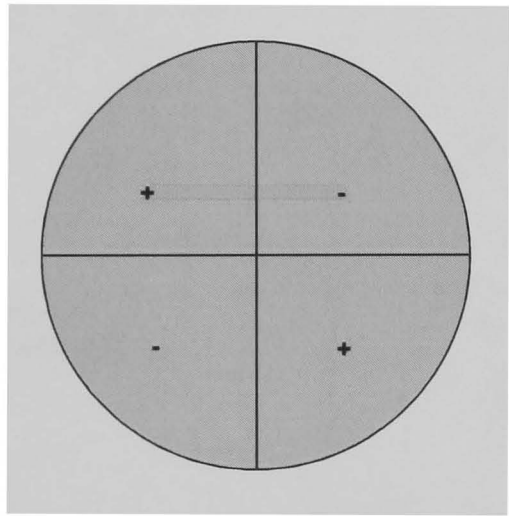

Figure 1.4 Two Diametral Mode

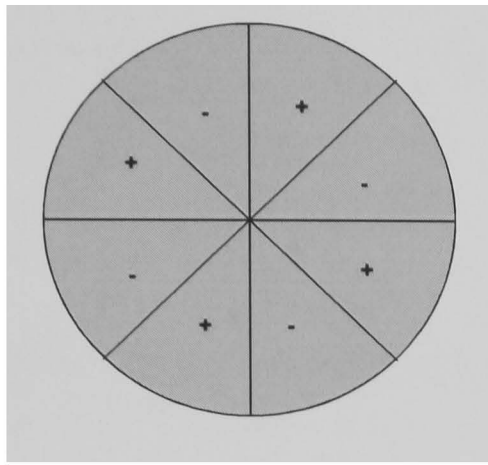

Figure 1.5 Four Diametral Mode

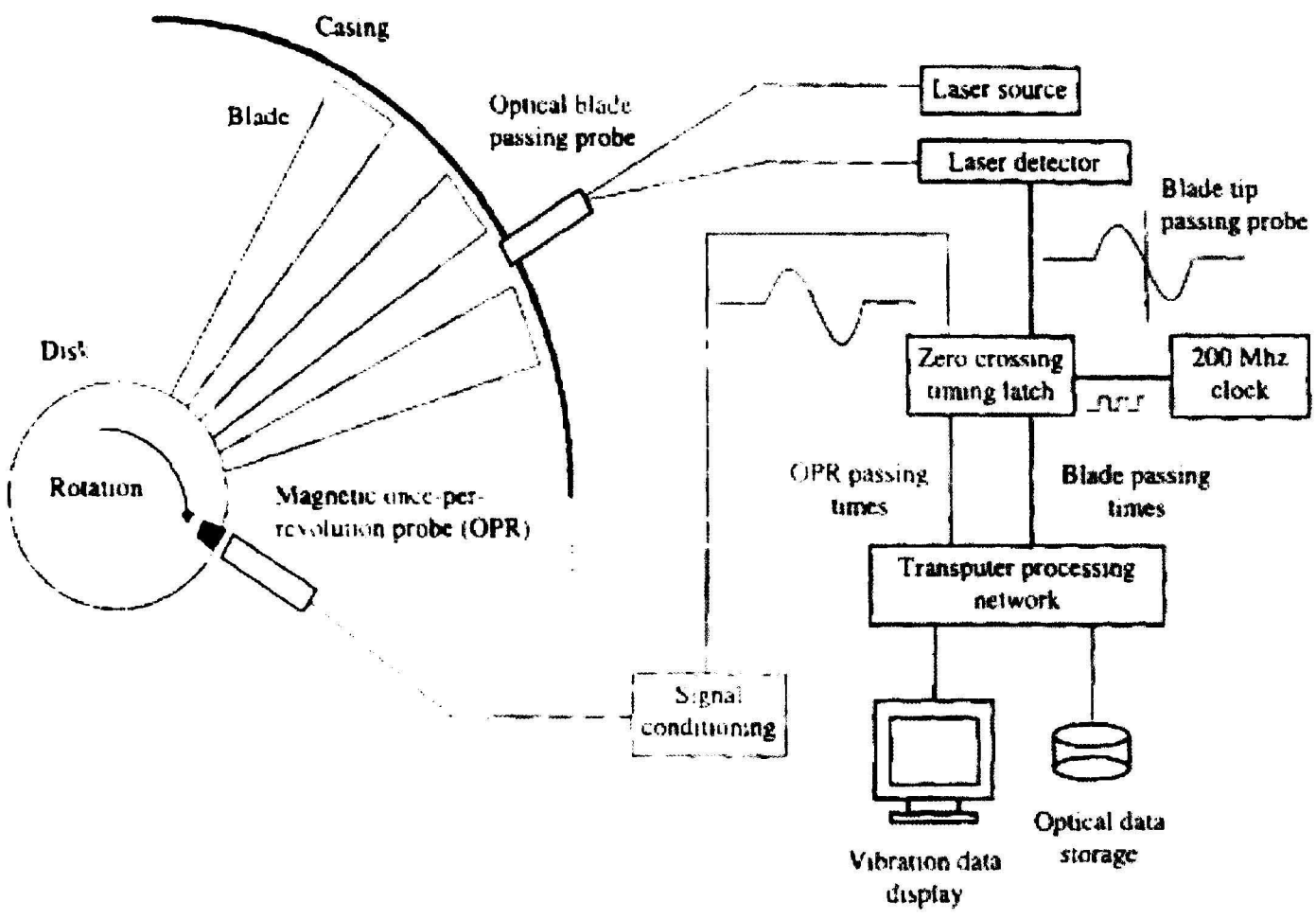

Figure 1.6 Tip-Timing System Diagram

Source [9]

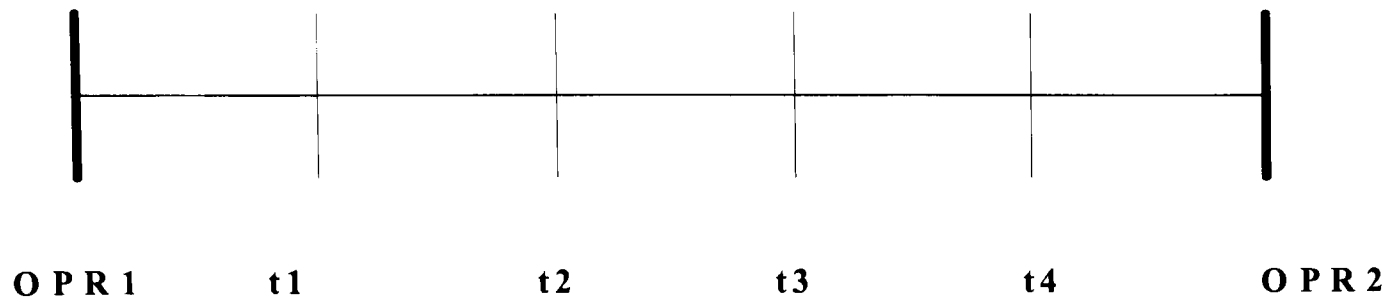

Figure 1.7 Time of Arrival Calculation

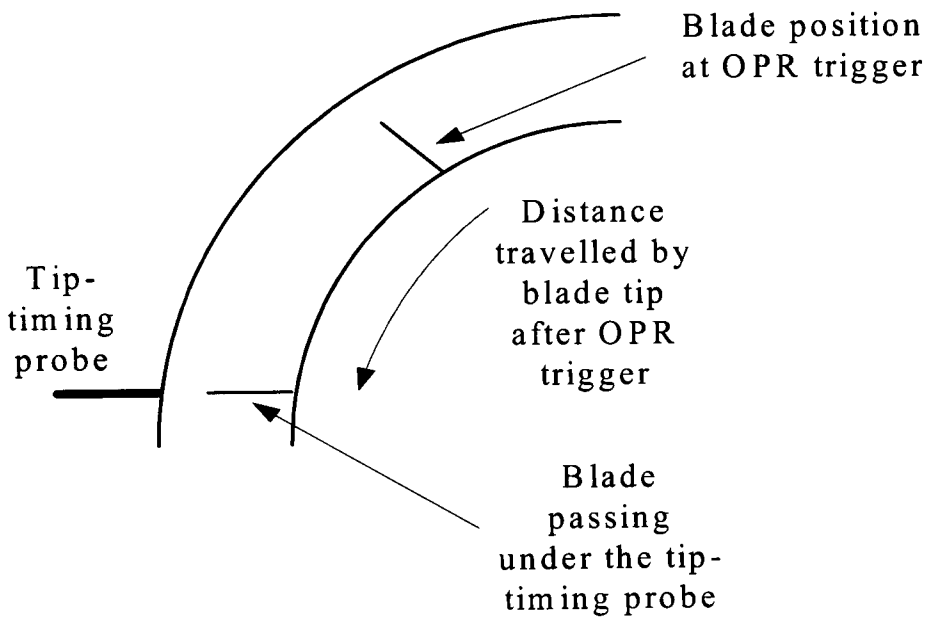

Figure 1.8 Illustration of Non-Vibrating Blade Tip Travel

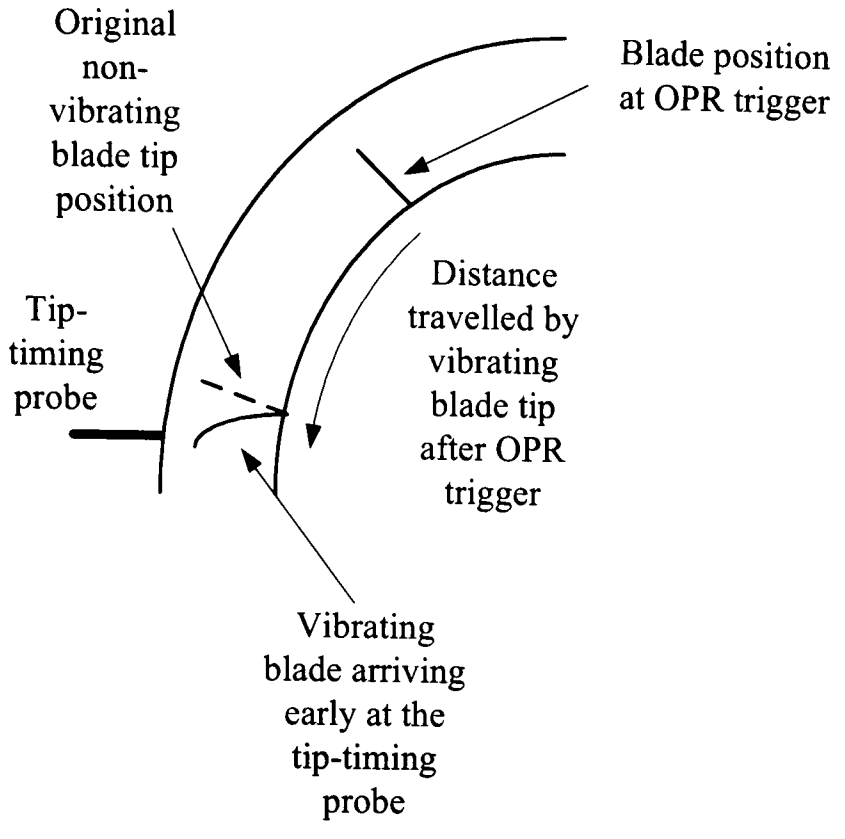

Figure 1.9 Illustration of Vibrating Blade Travel

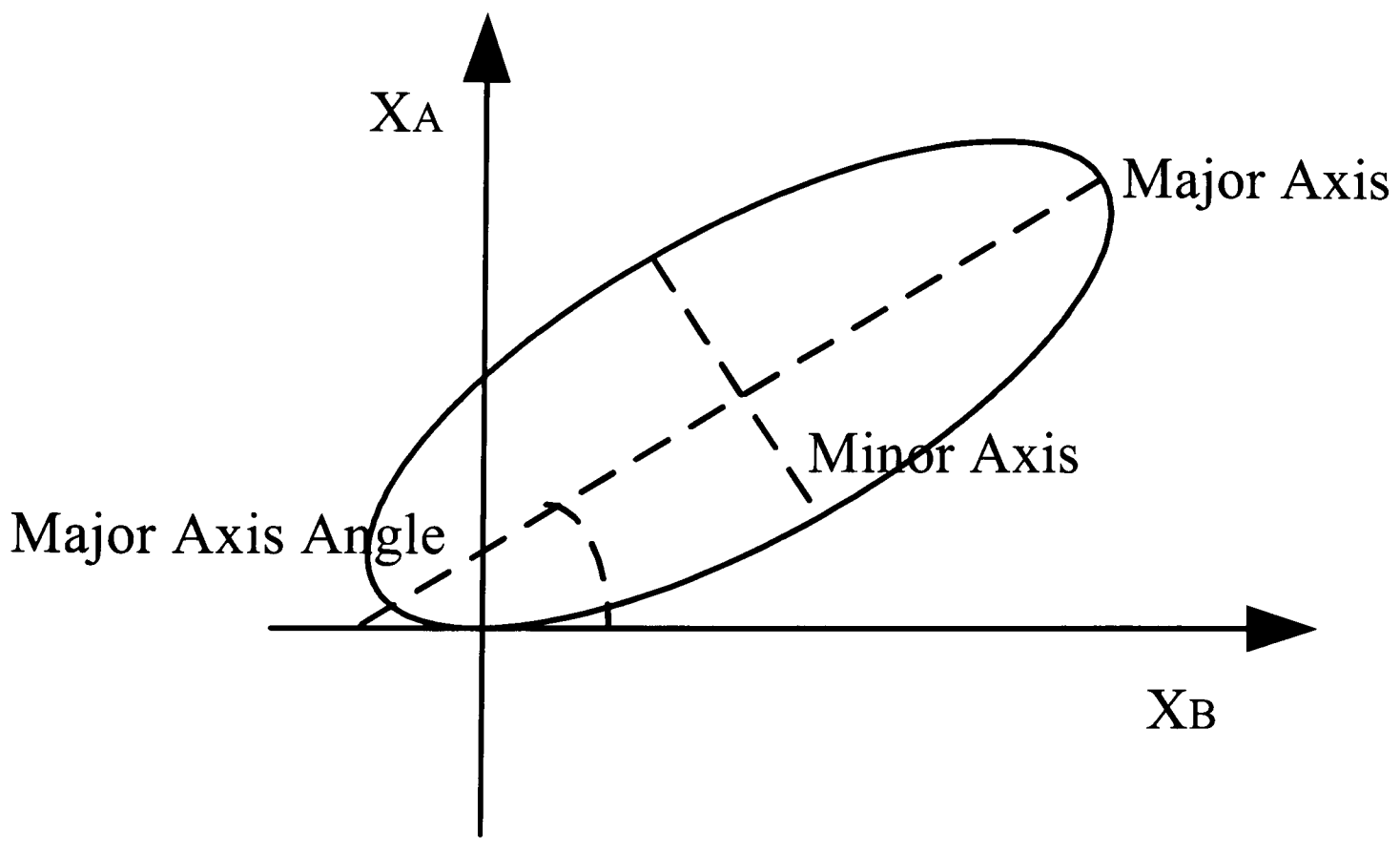

Figure 2.1 Illustration of Two Parameter Plot Parameters

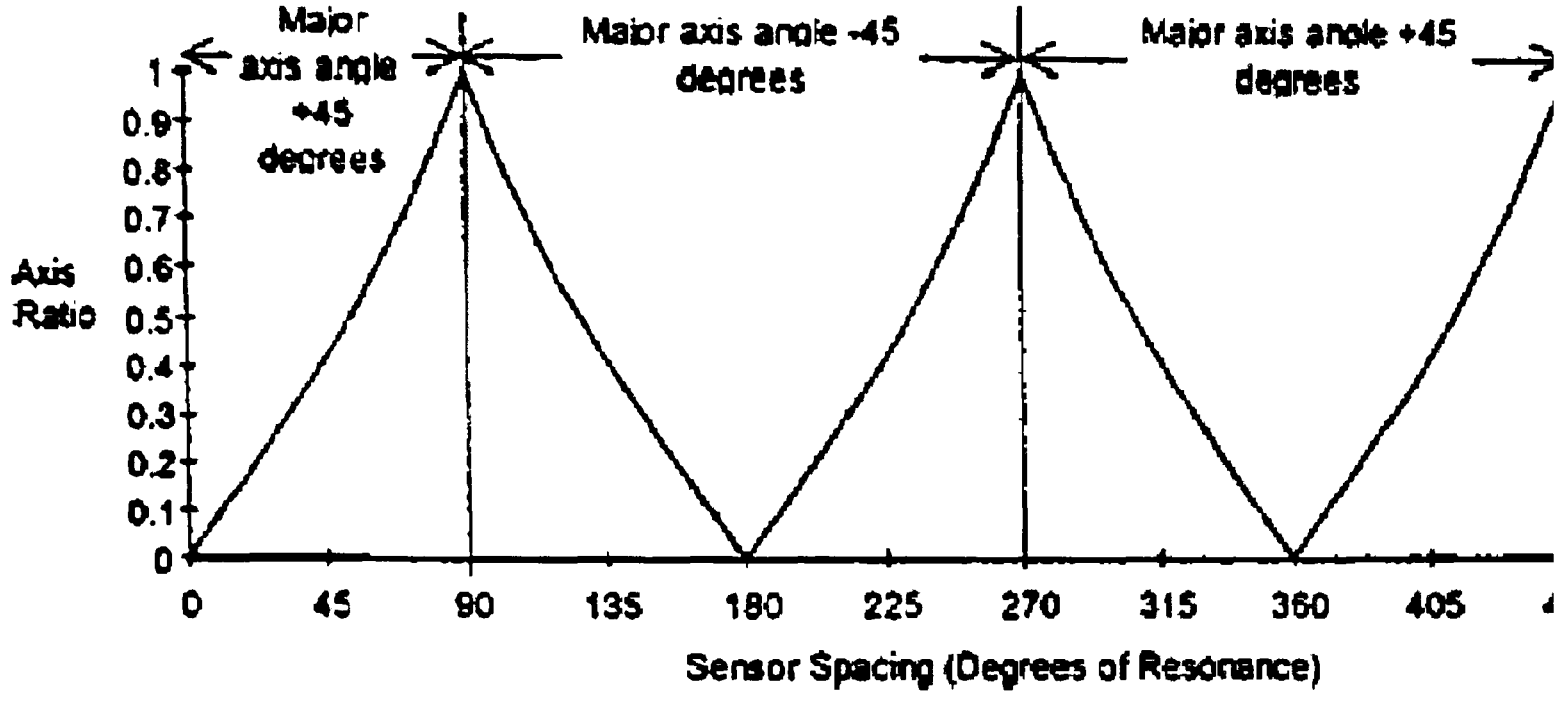

Figure 2.2 2PP Relationship between Axis Ratio, Major Axis Angle, and PSR

Source [9]

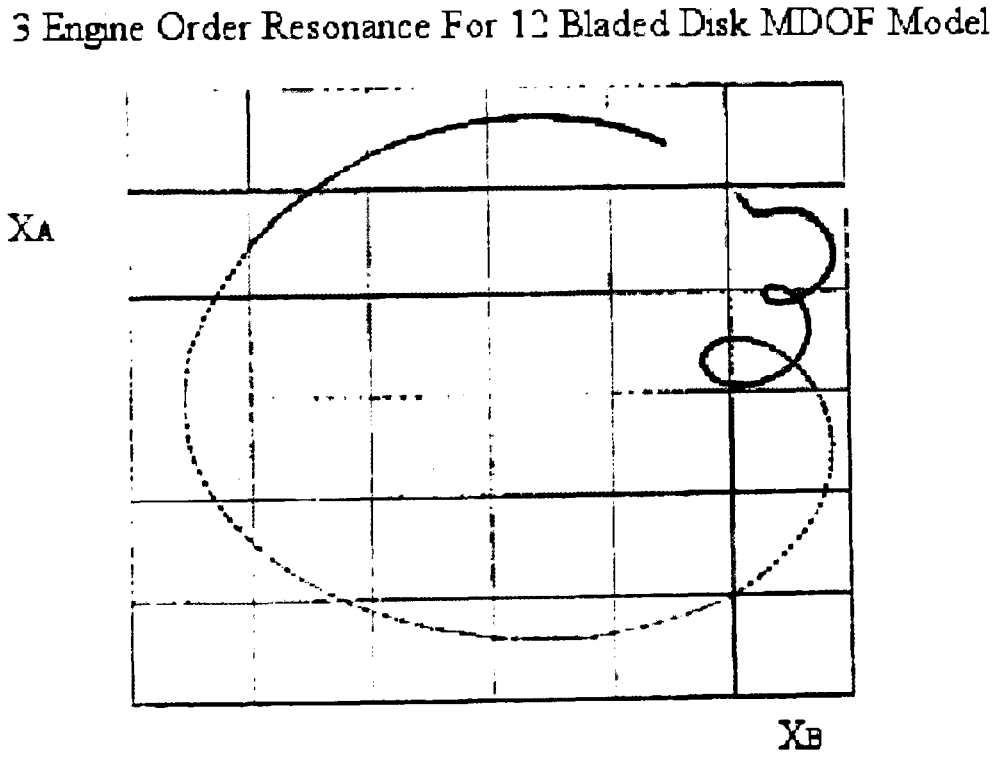

Figure 2.3 Illustration of Mistuning in the Two Parameter Plot

Source [9]

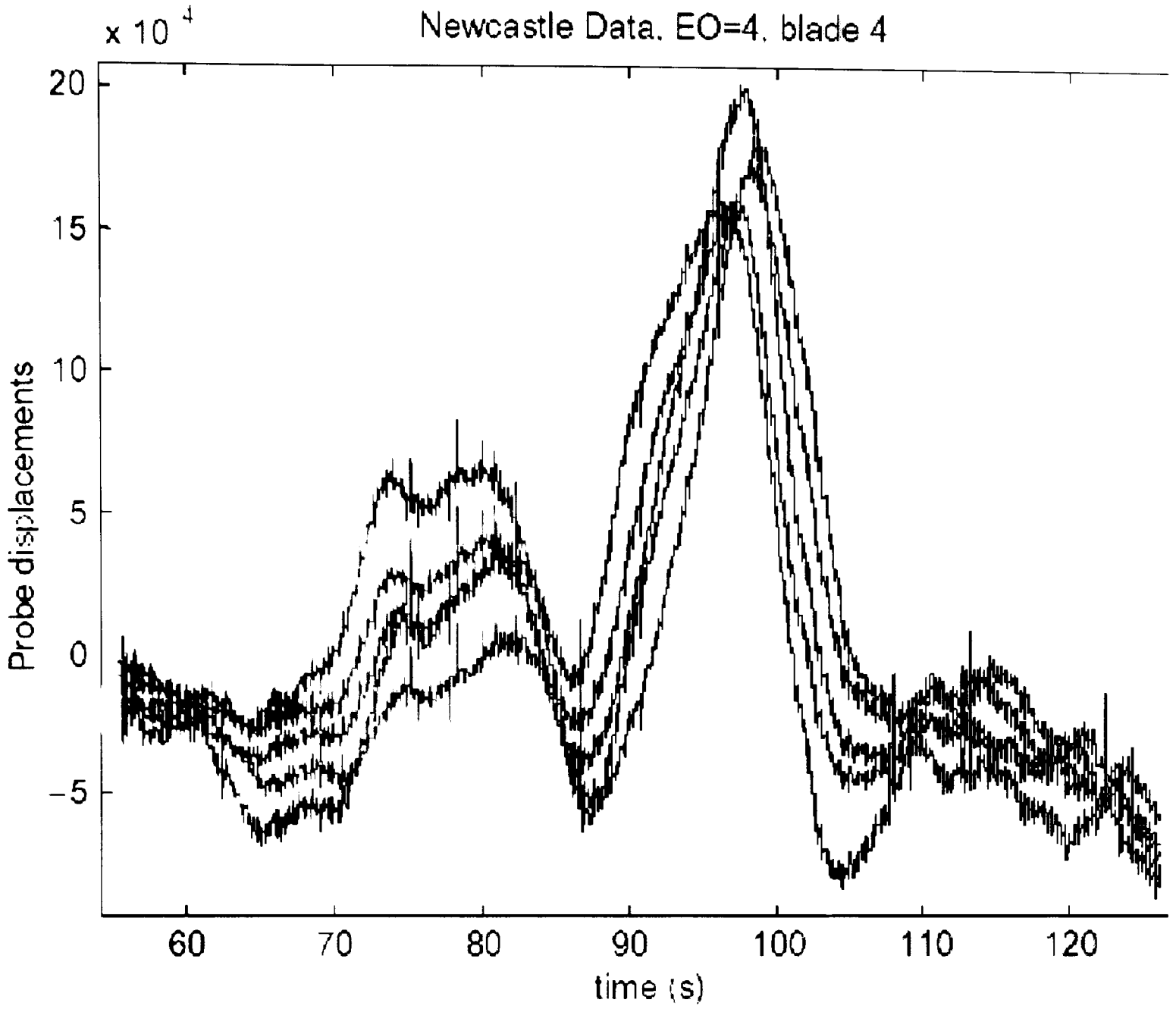

Figure 2.4 Example of Multiple Modes Excited by a Single Engine Order Forcing Function

Source [21]

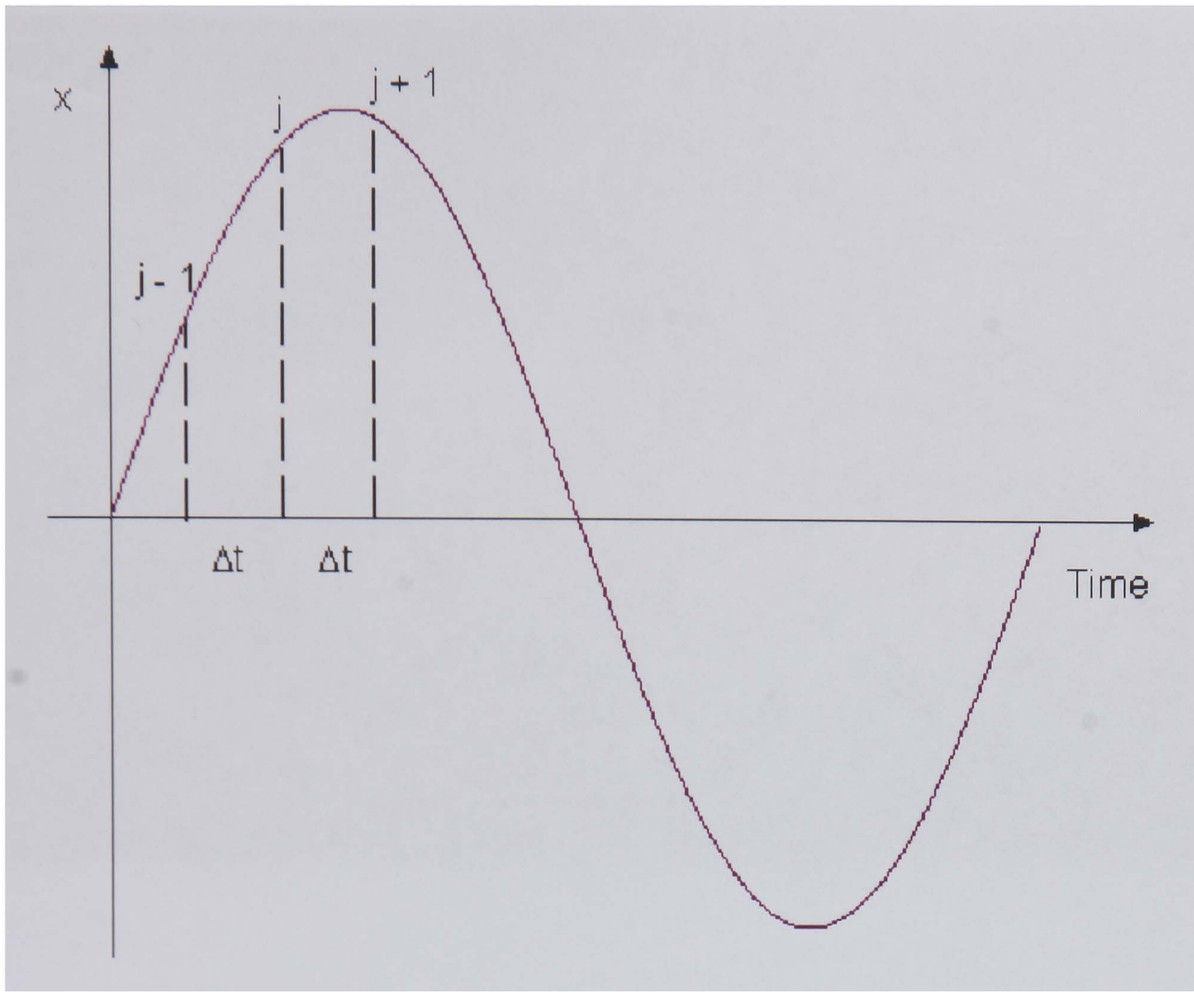

Figure 2.5 Probe Positioning on the Blade Vibration Cycle

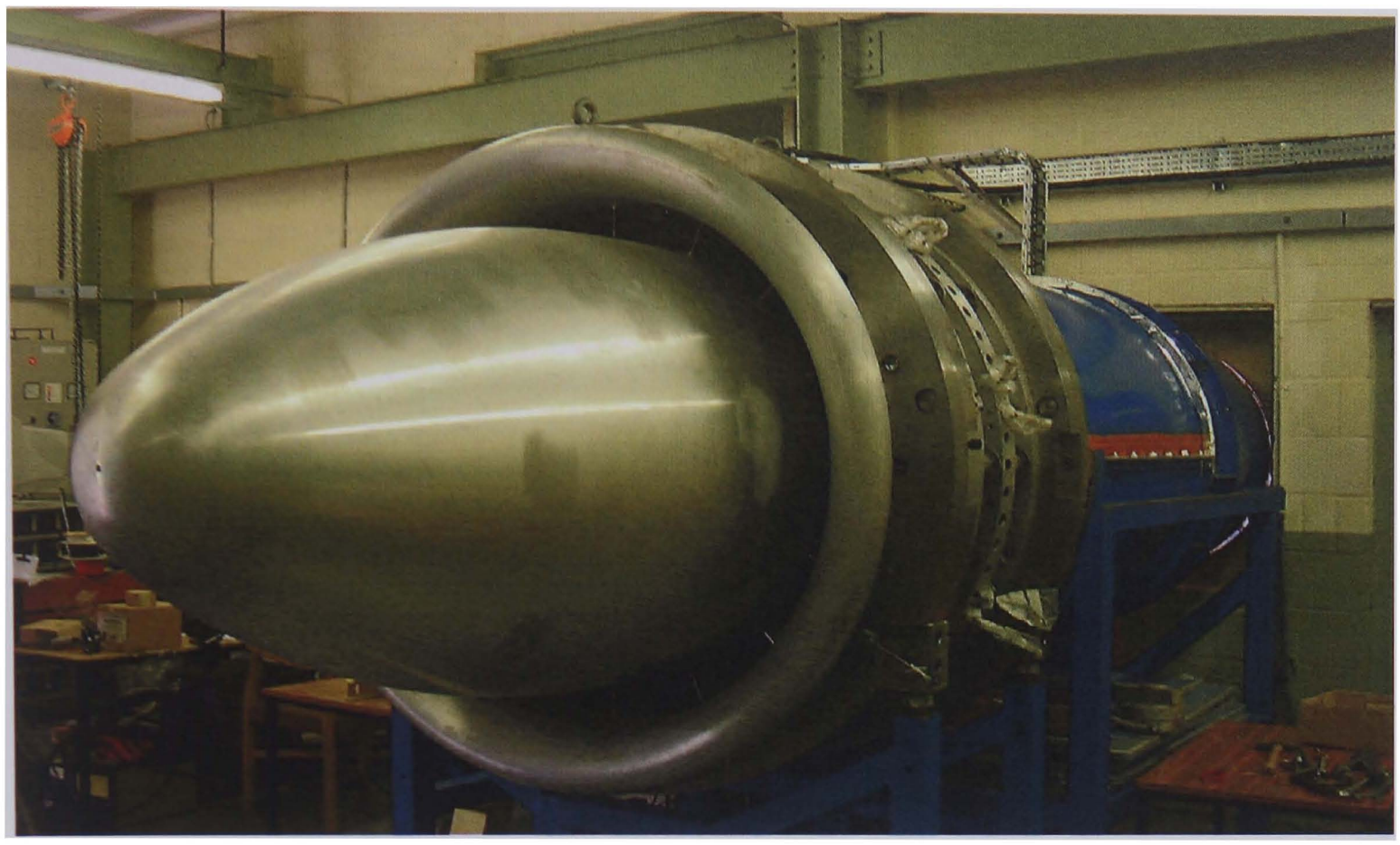

Figure 3.1 The One and a Half Stage Compressor Test Rig

Figure 3.2 The Compressor Intake

Figure 3.3 The Compressor Back Pressure Valve

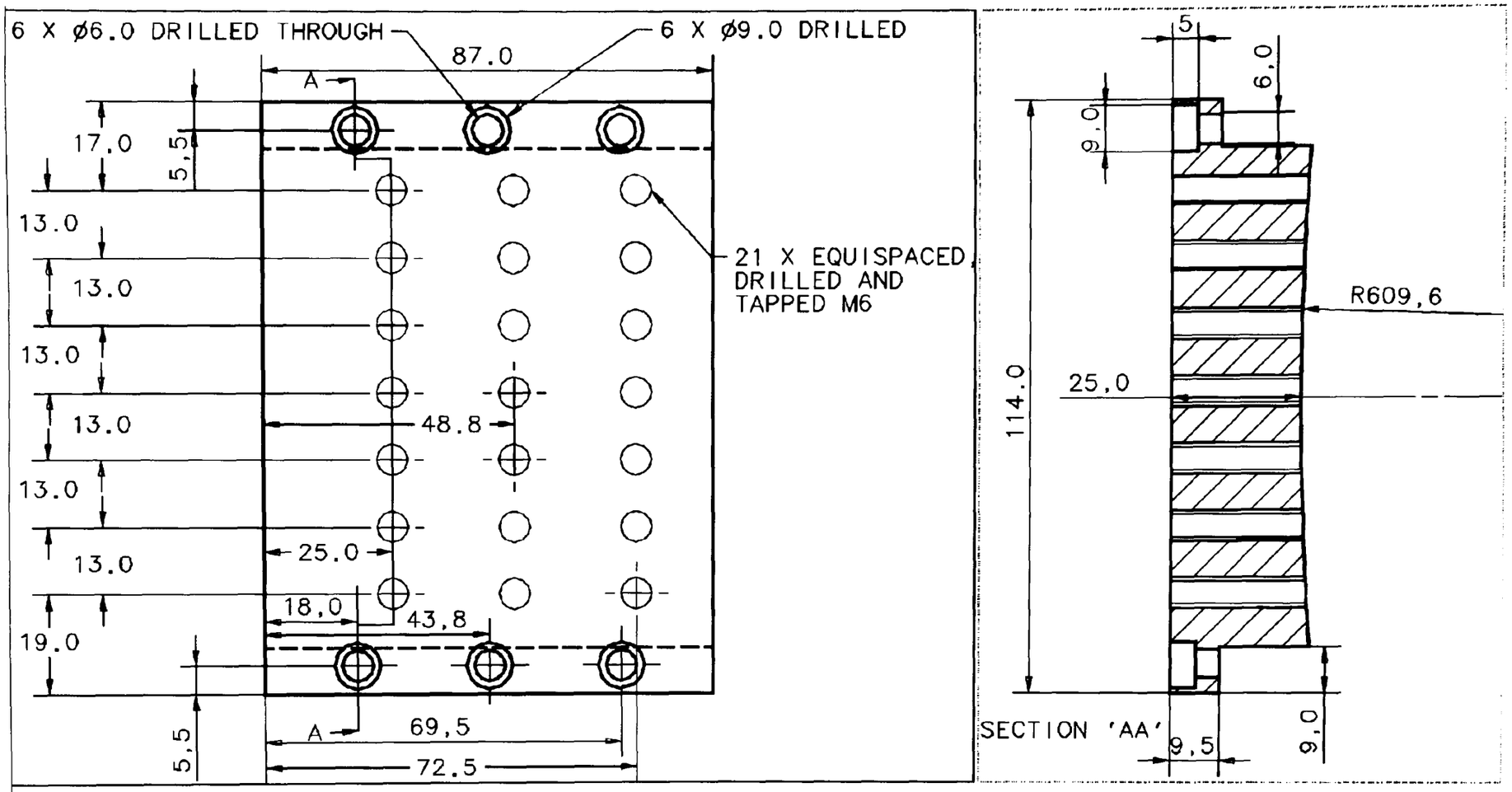

TITLE: 1.5 STAGE COMPRESSOR ROTOR CASSETTE – OPTICAL PROBE MOUNTING		
MATERIAL: ALUMINIUM ALLOY		
DRAWN BY:	DATE: 08-08-03	SIZE: A3
DIMENSIONS ARE IN MILLIMETERS UNLESS OTHERWISE SPECIFIED TOLERANCES ARE +/- 0.1 MM UNLESS OTHERWISE SPECIFIED		

Figure 3.4 The Optical Probe Cassette

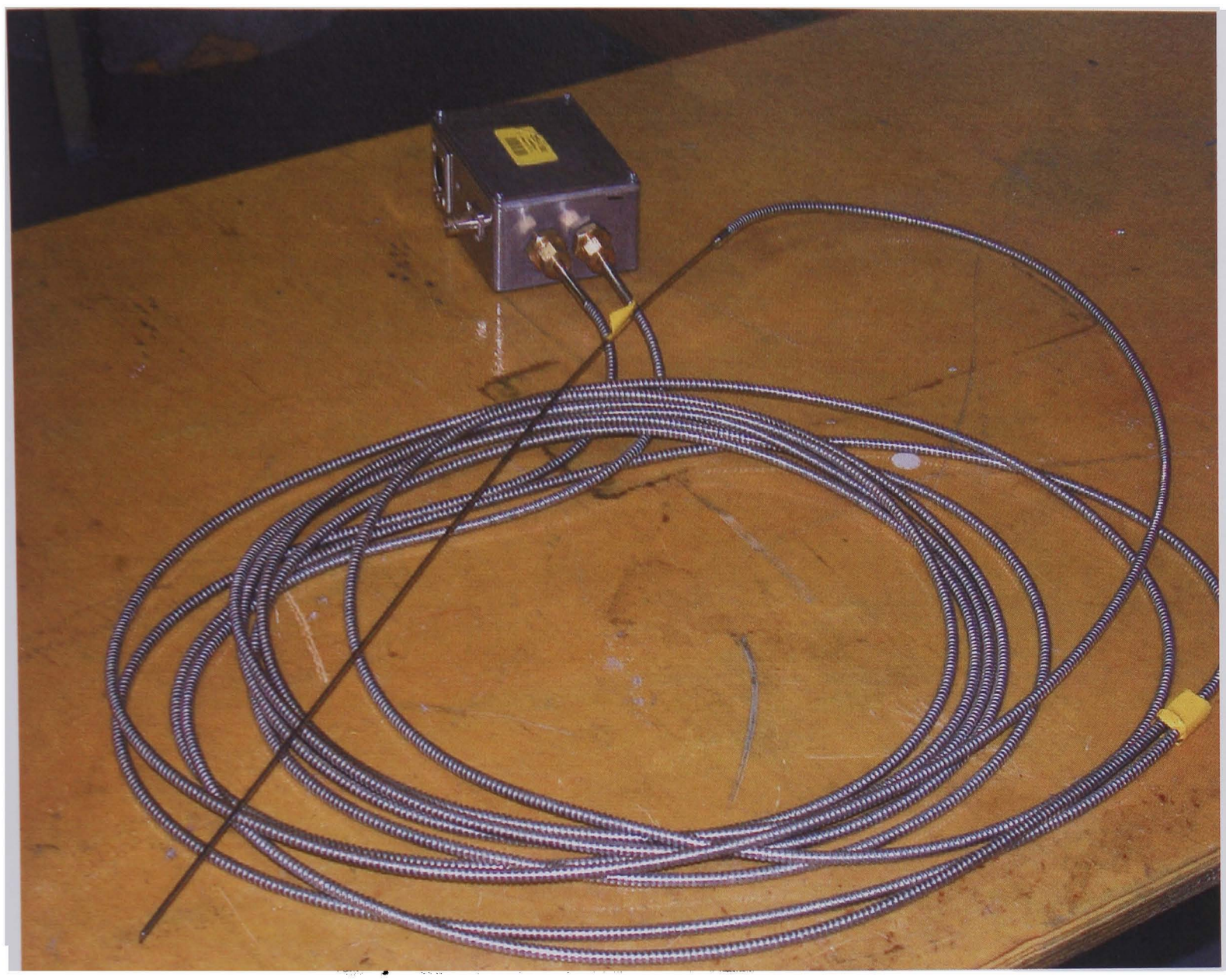

Figure 3.5 The Bifurcated Optical Probe

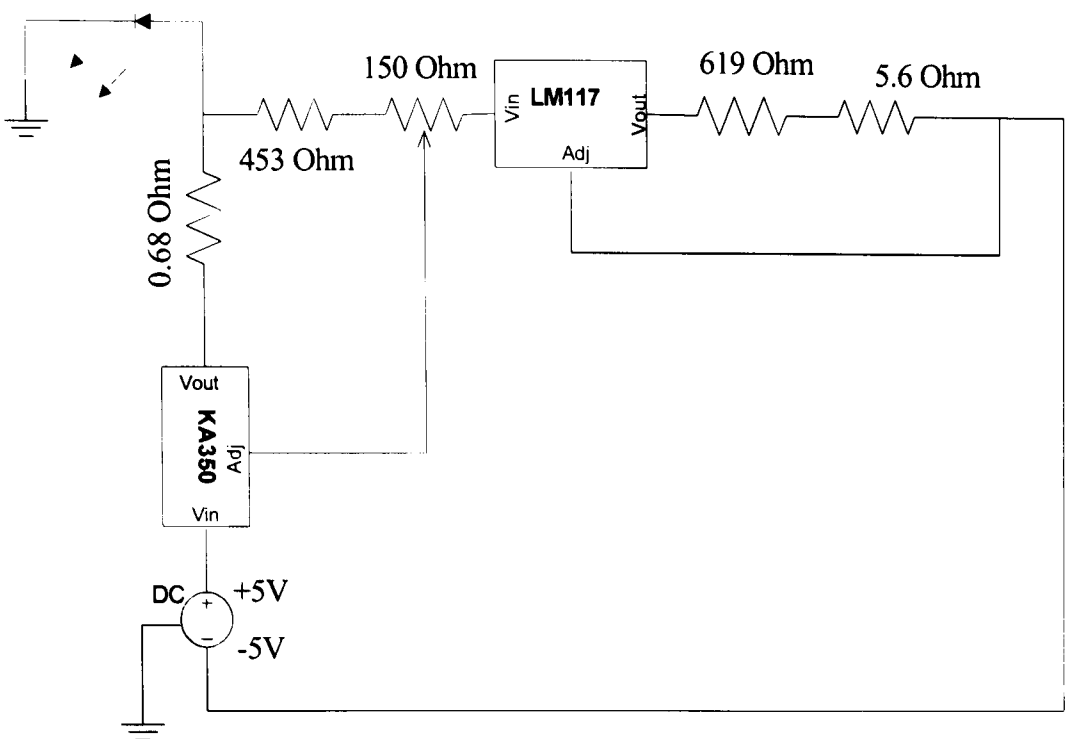

Figure 3.6 Optical Emitter Circuit Diagram

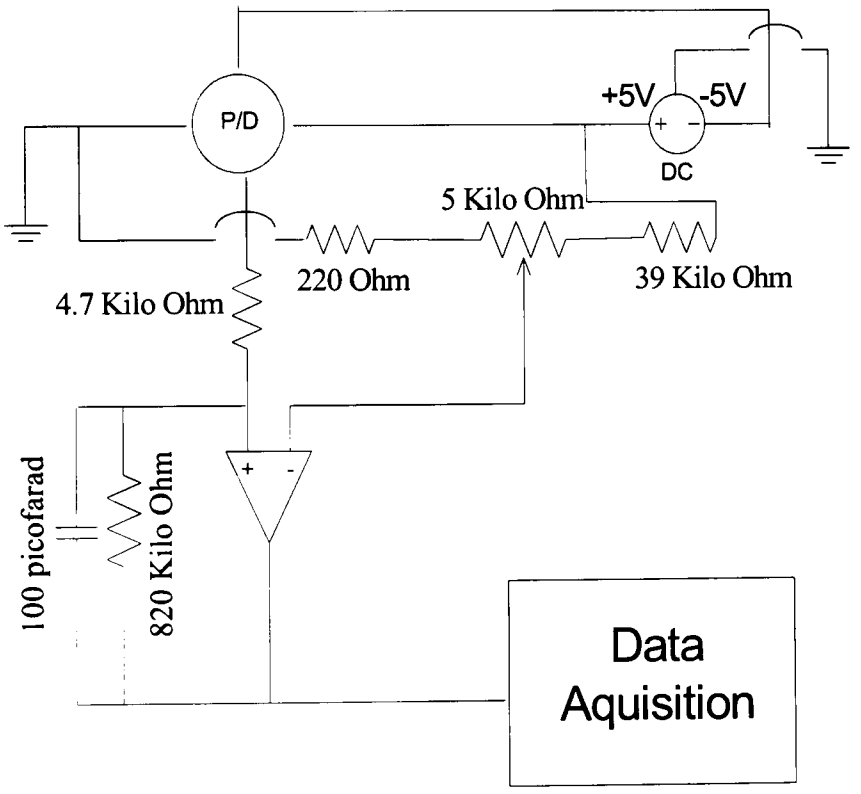

Figure 3.7 Photodetector, and Comparator Circuit Diagram

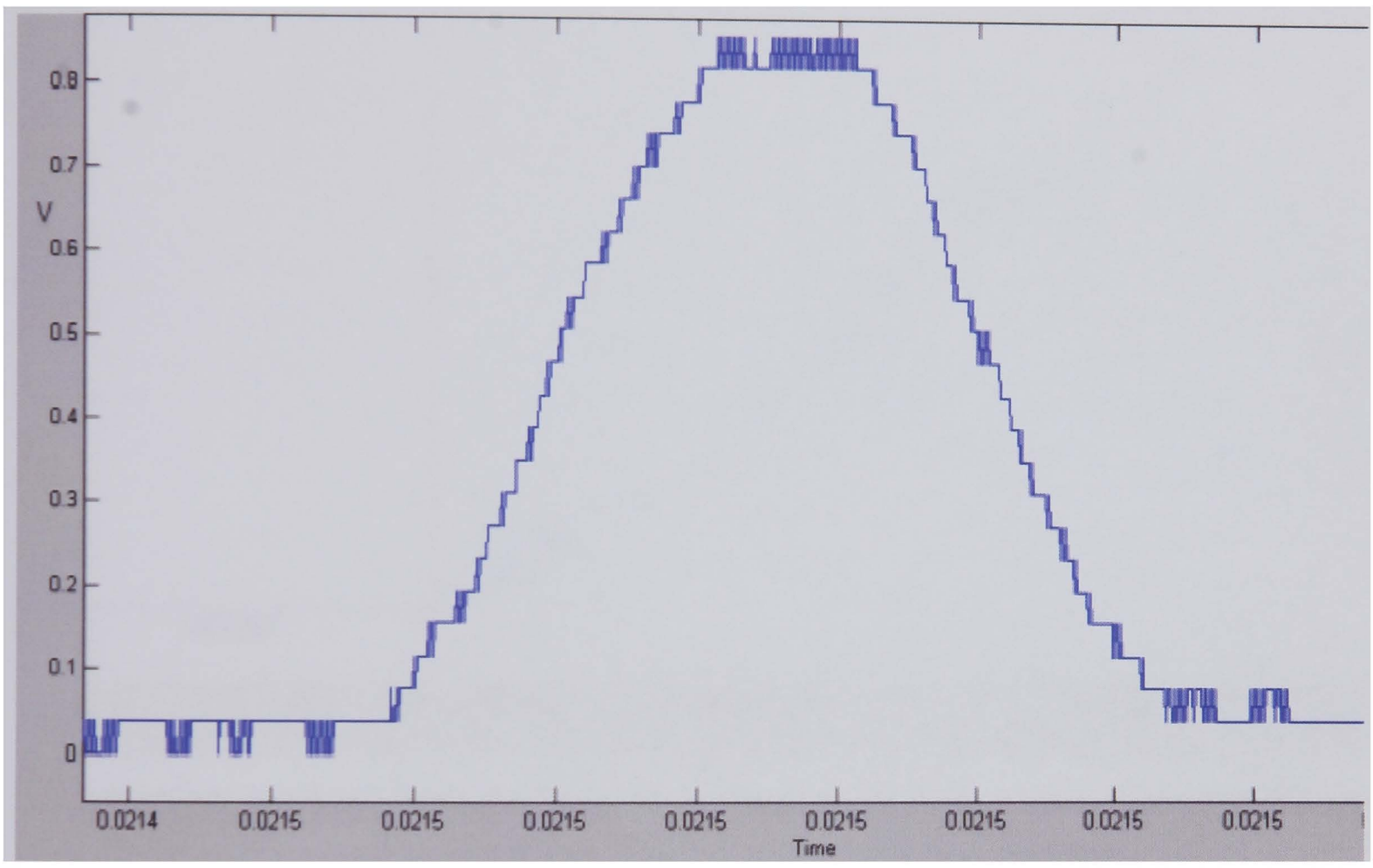

Figure 3.8 Photodetector Signal at 900RPM

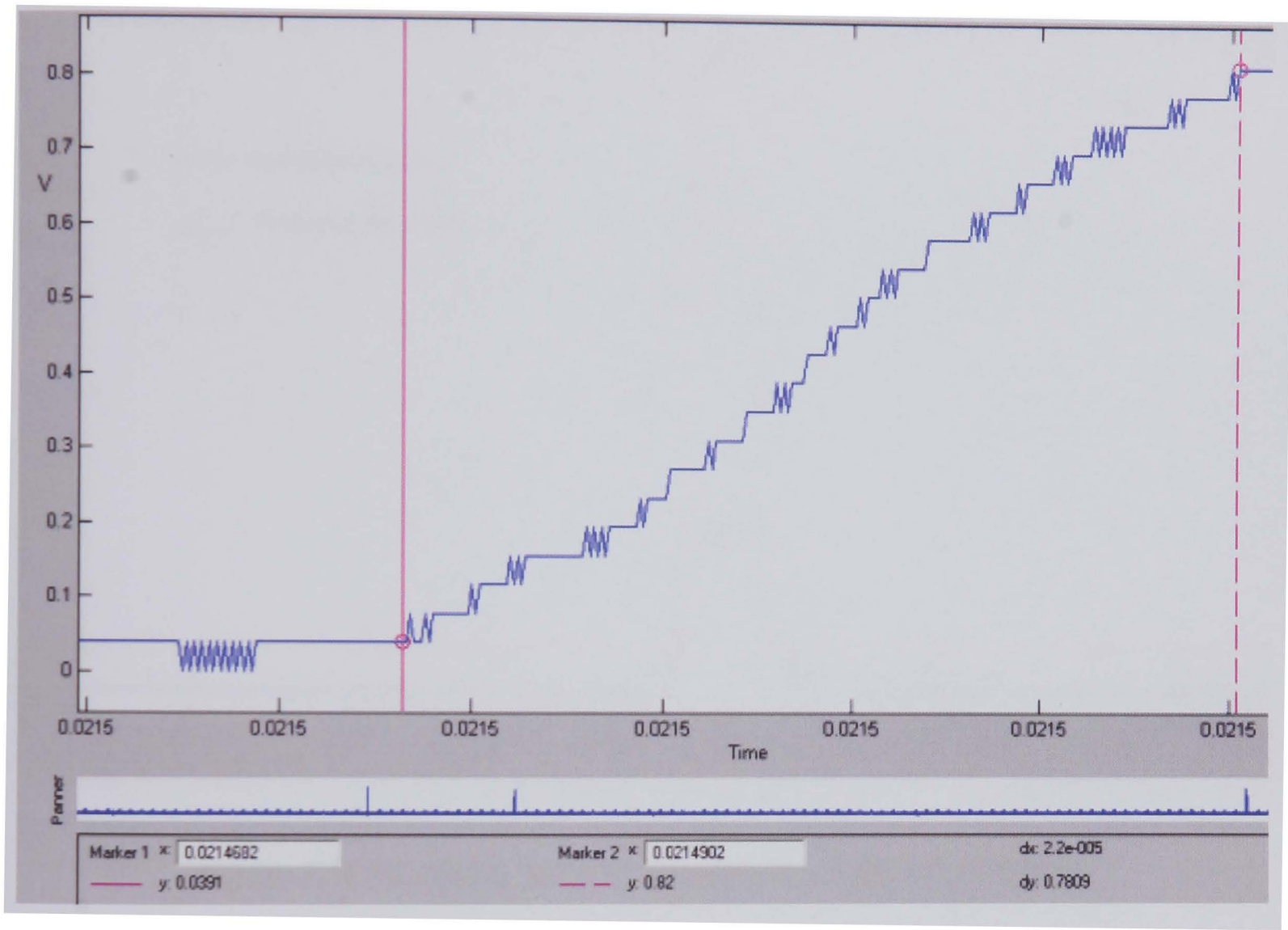

Figure 3.9 Photodetector Signal Rise Time at 900RPM

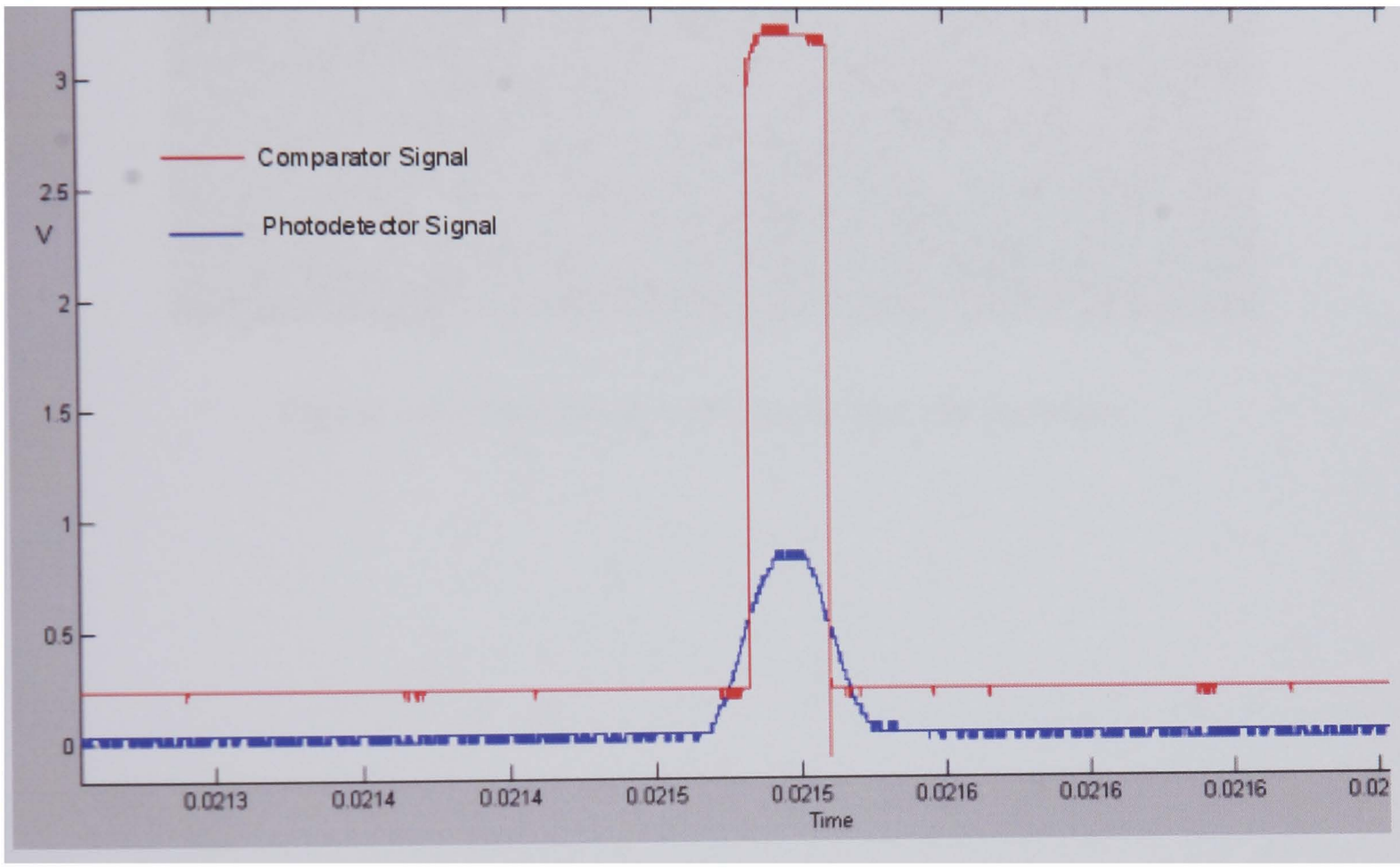

Figure 3.10 Photodetector, and Comparator Signals at 900RPM

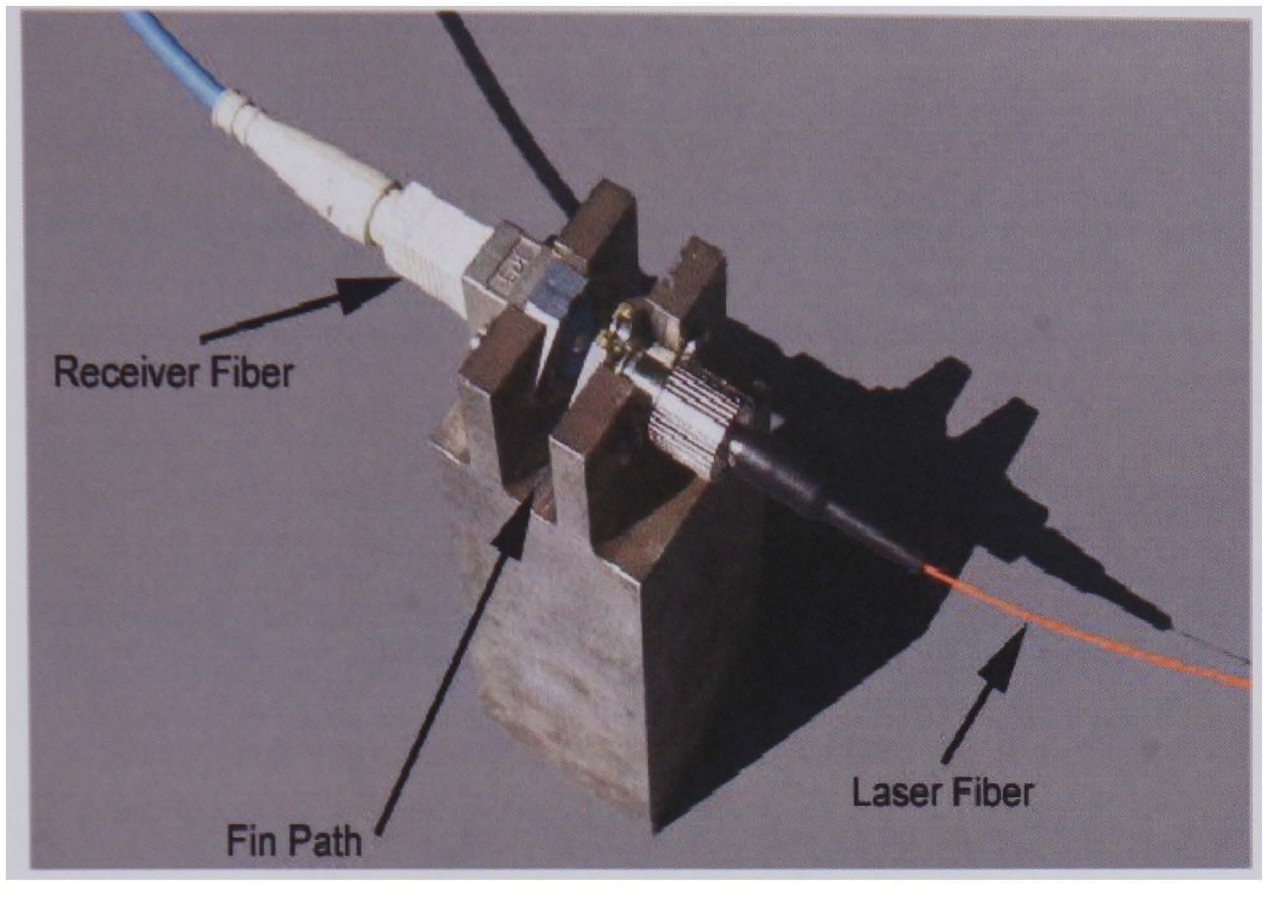

Figure 3.11 Once Per Revolution Sensor Arrangement

Figure 3.12 Test Blade with Affixed Strain Gauges

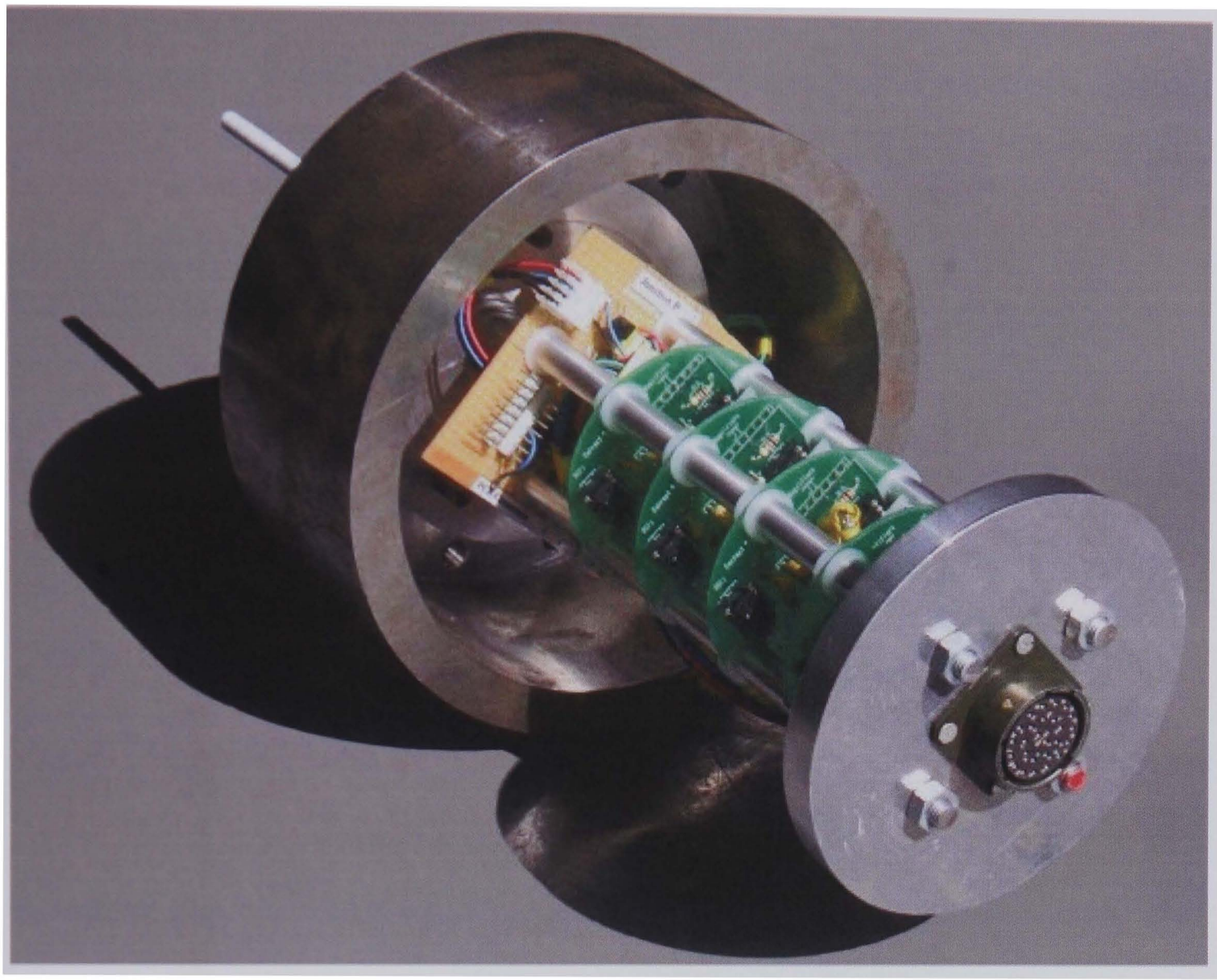

Figure 3.13 Strain Gauge Power, and Amplification Circuit Boards

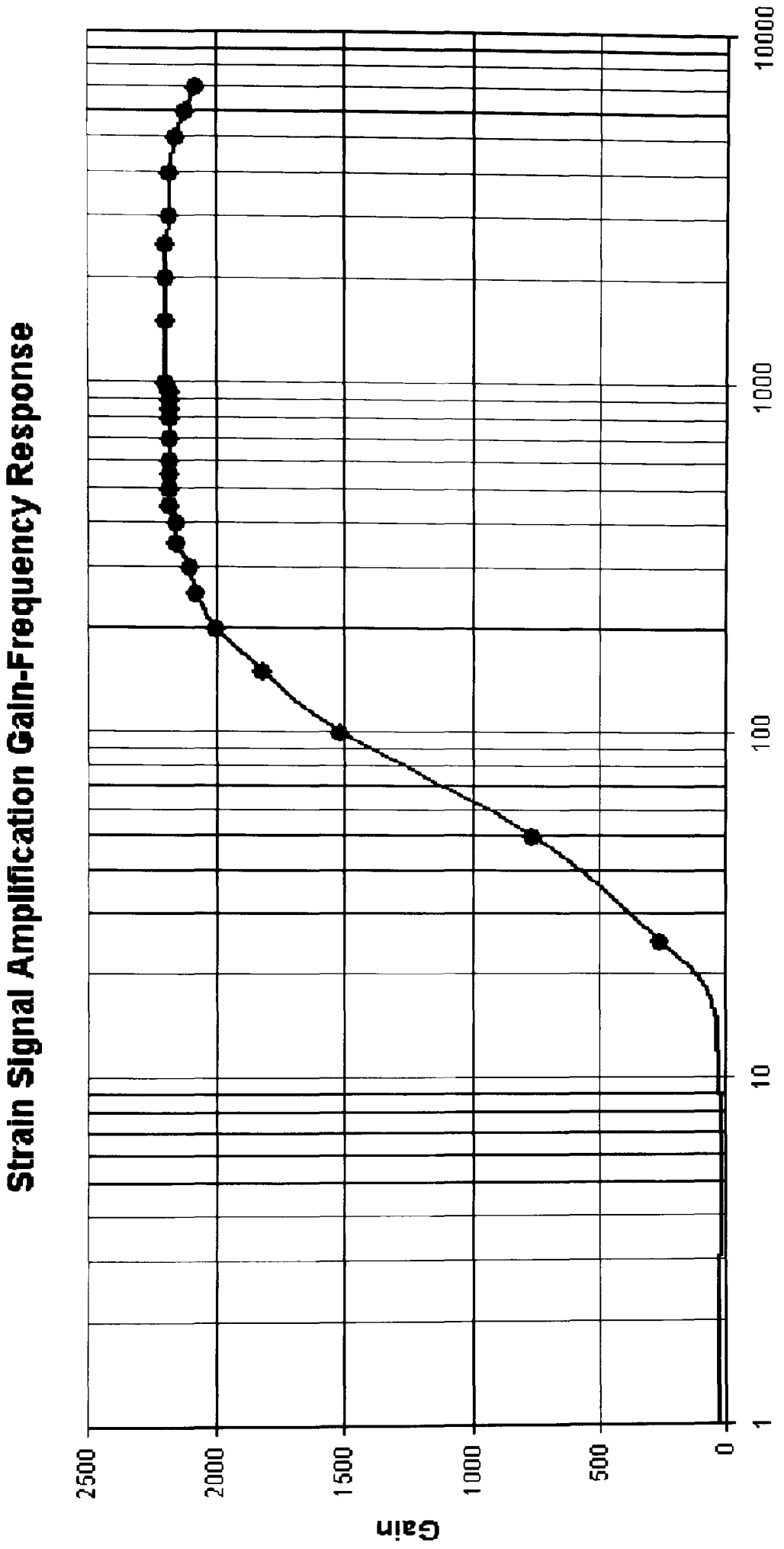

Figure 3.14 Strain Gauge Amplification Gain Frequency Response Characteristic

Source [22]

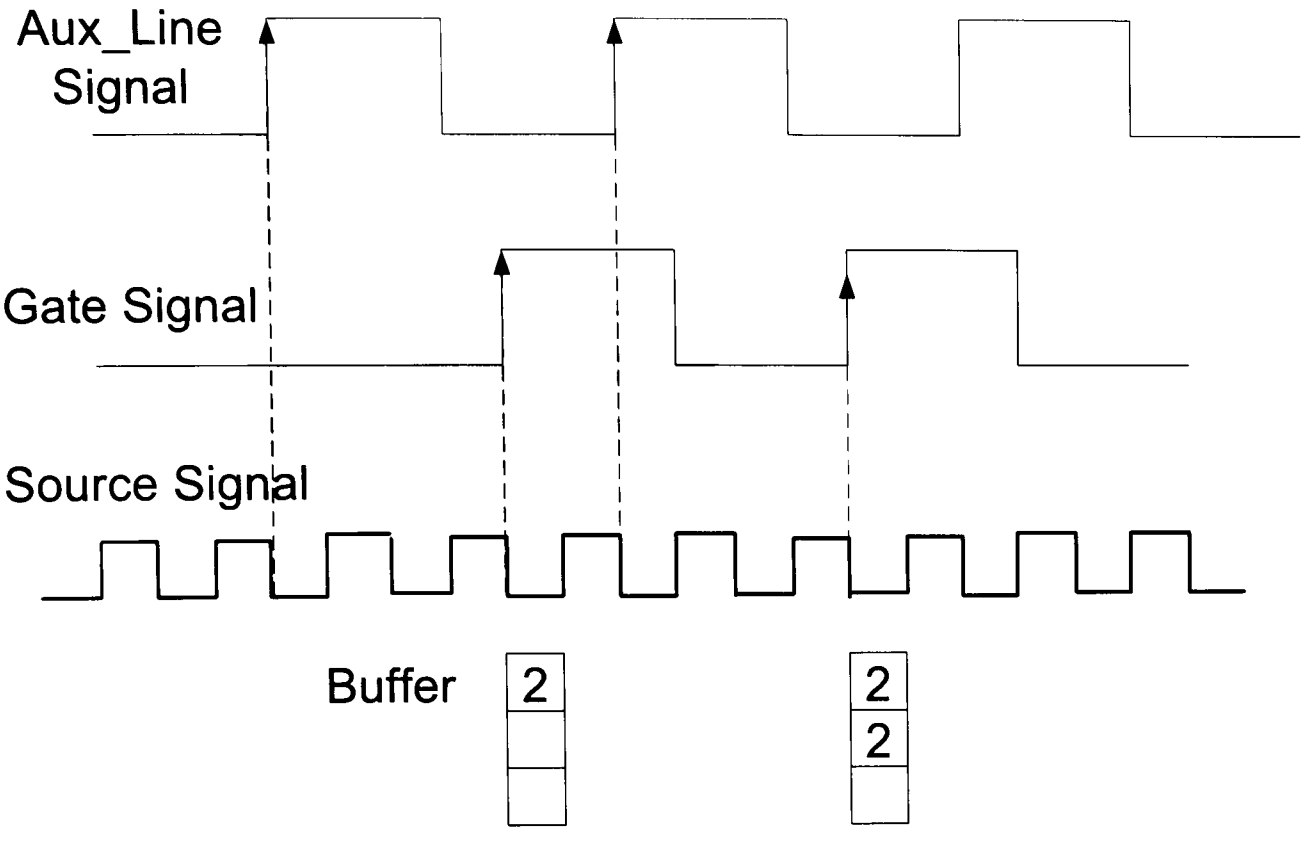

Figure 3.15 Buffered Two-Signal Edge-Separation Measurement

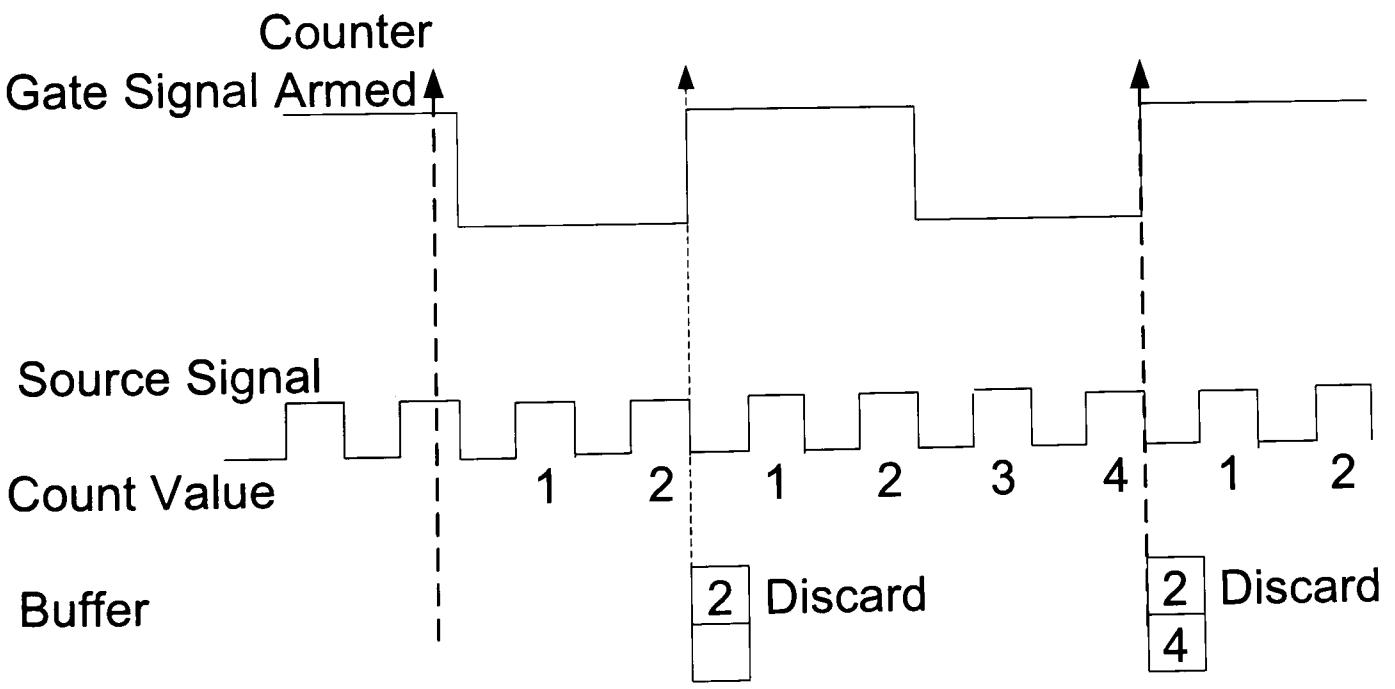

Figure 3.16 Buffered Period Measurement

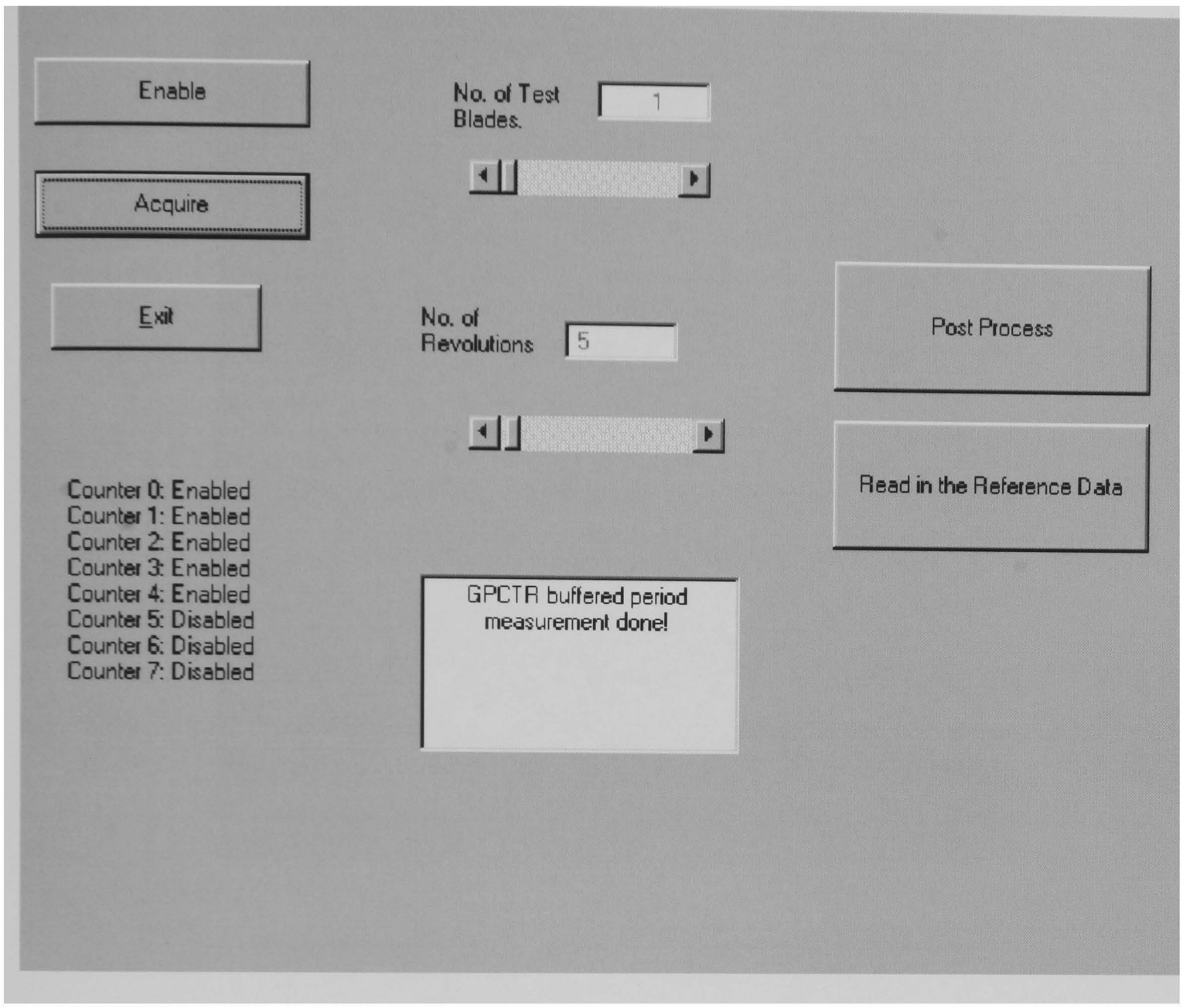

Figure 3.17 User Interface - The Main Form

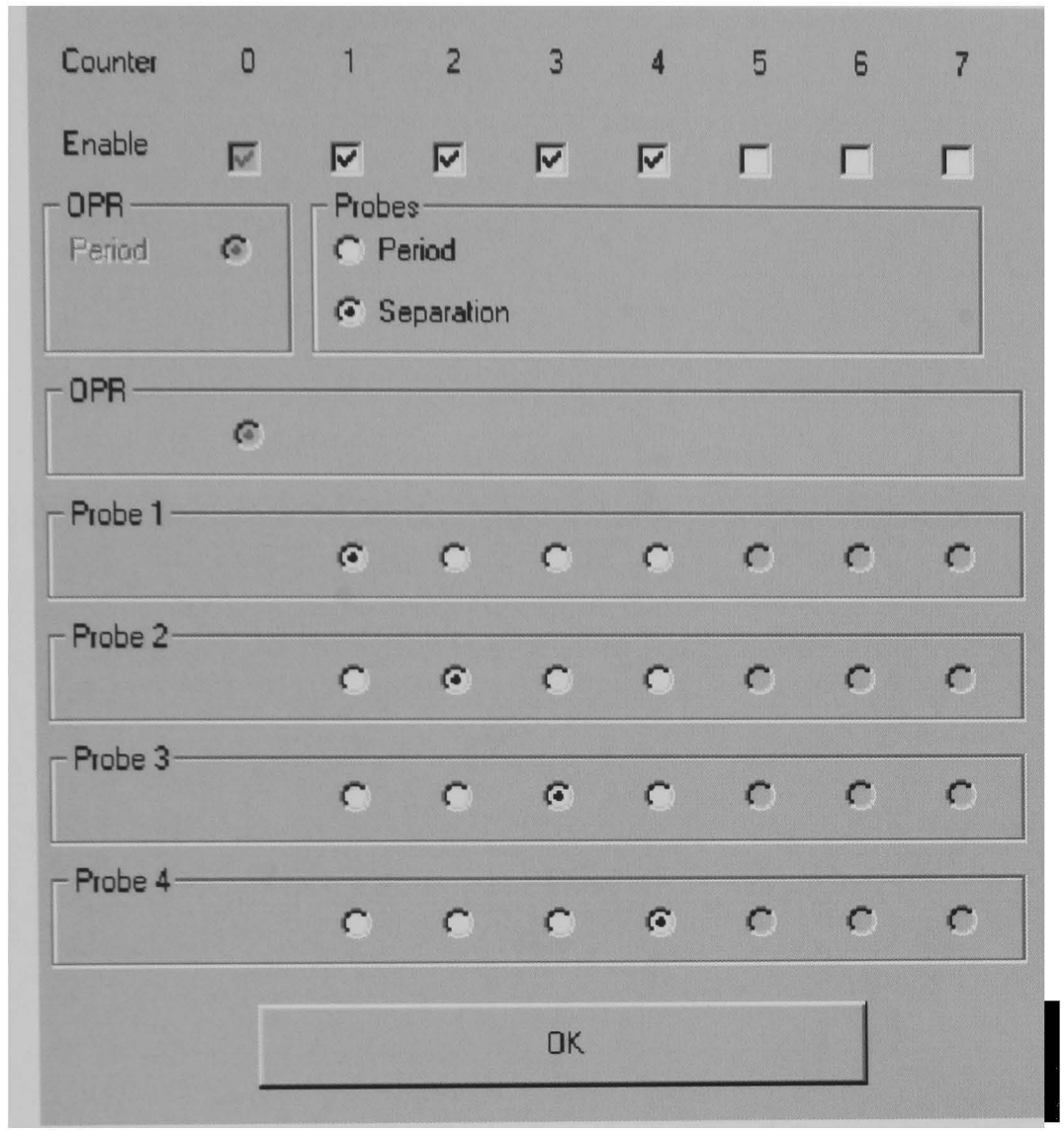

Figure 3.18 User Interface - Counter Selection Form

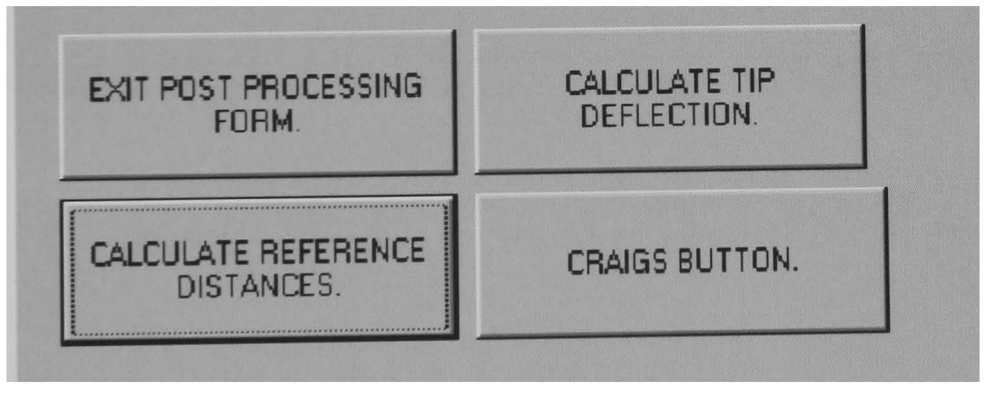

Figure 3.19 User Interface - Post Processing Form

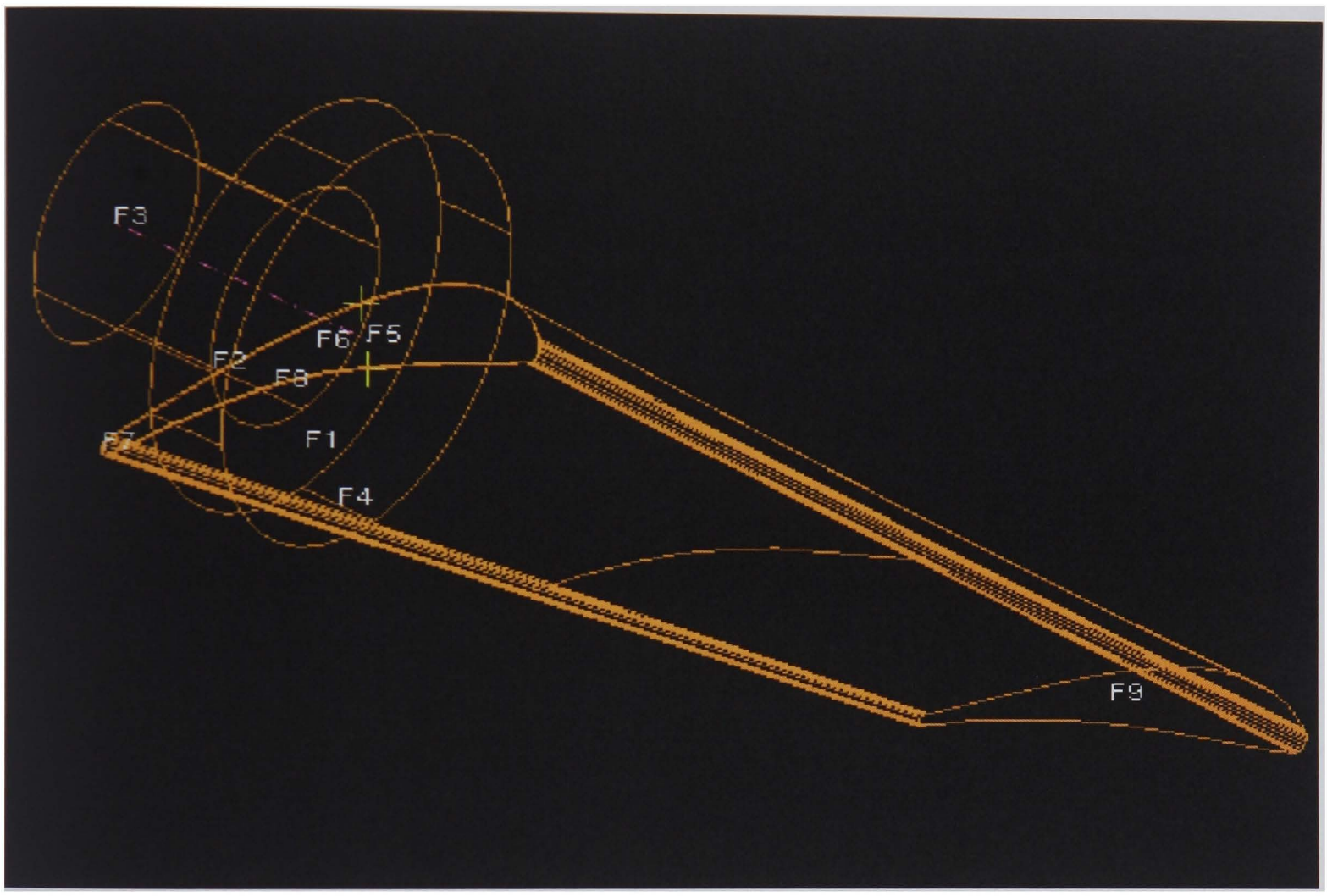

Figure 4.1 The Test Blade Solid Model

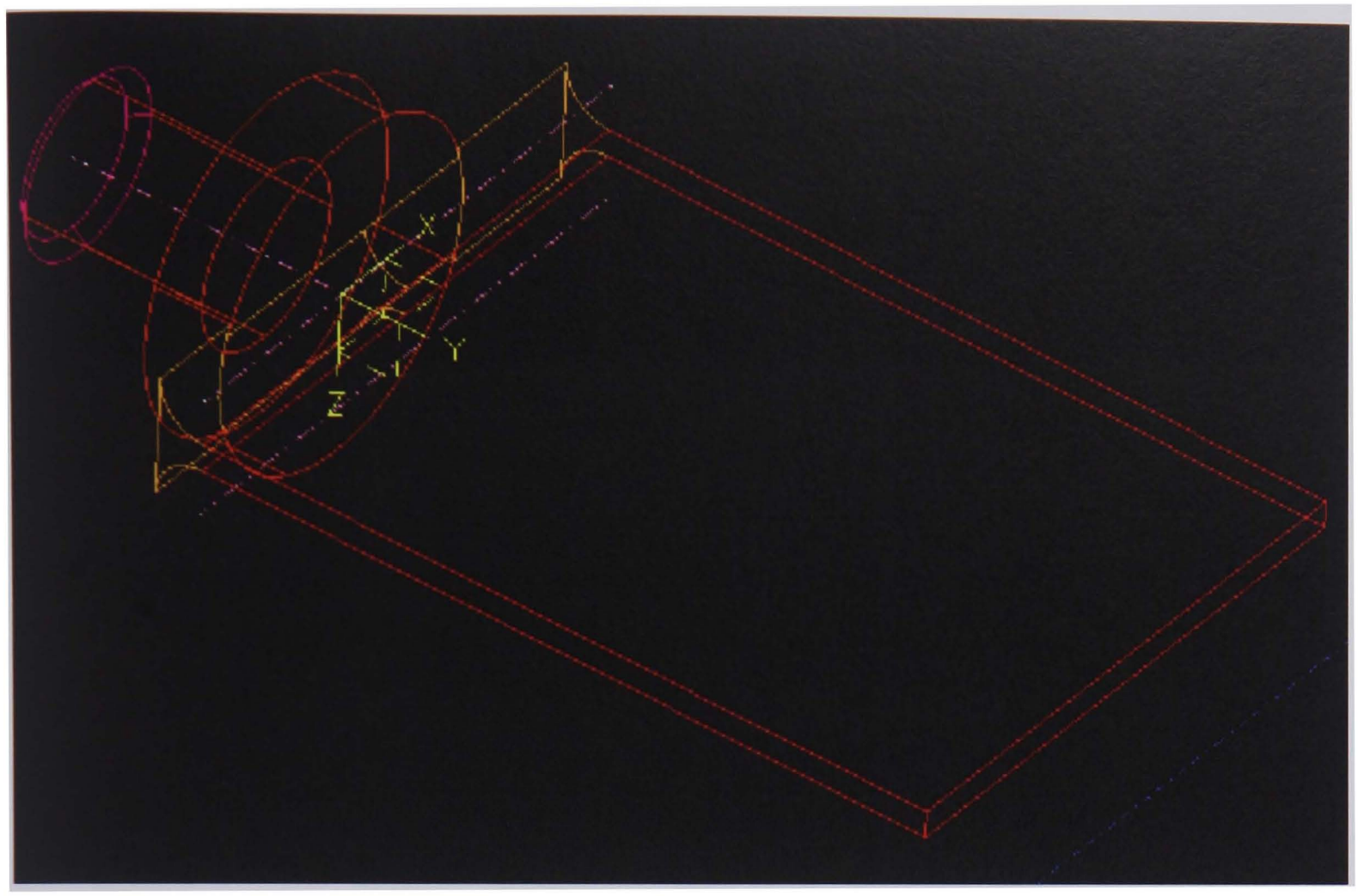

Figure 4.2 The Flat Blade Solid Model

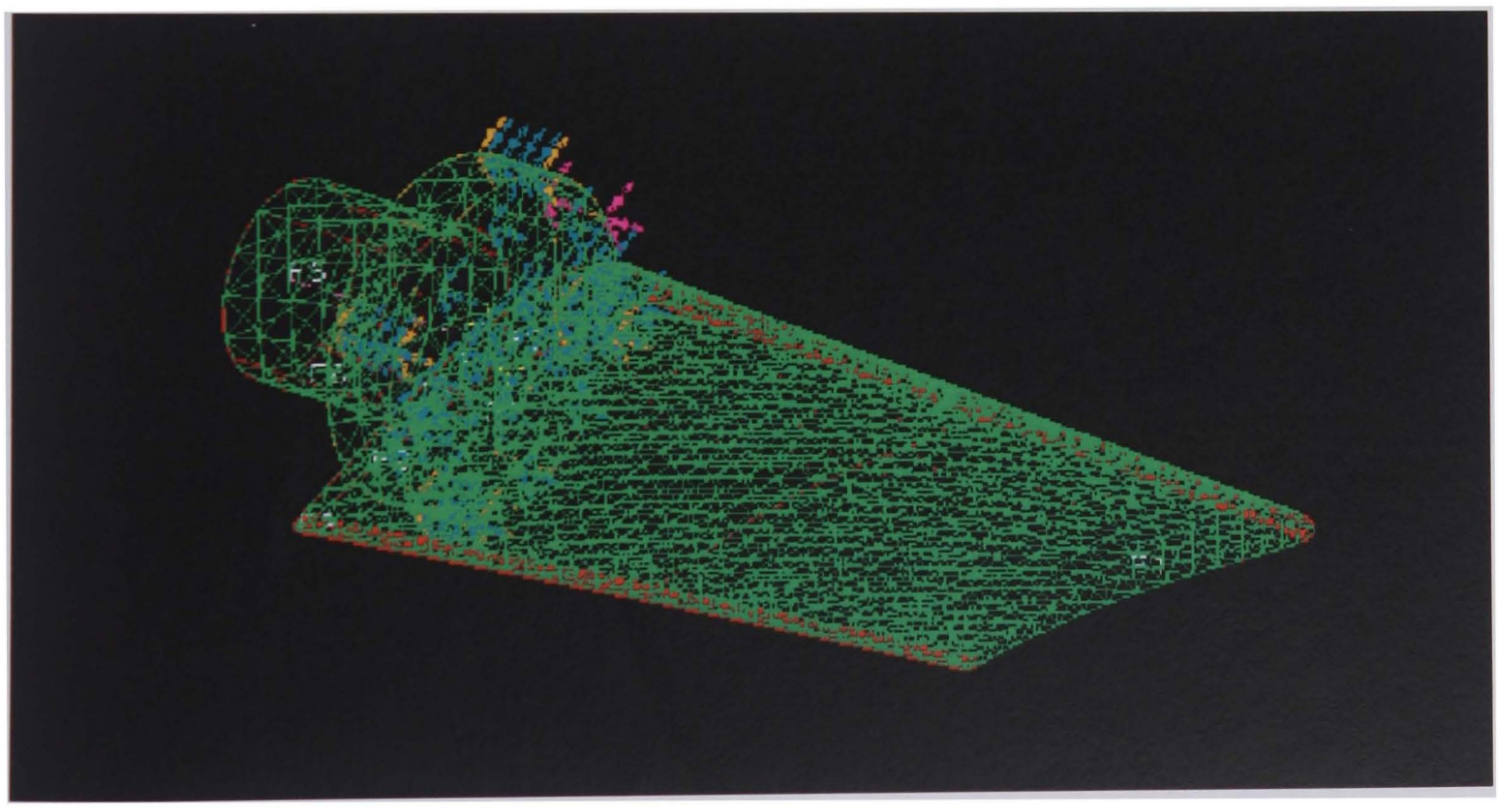

Figure 4.3 The Meshed Test Blade

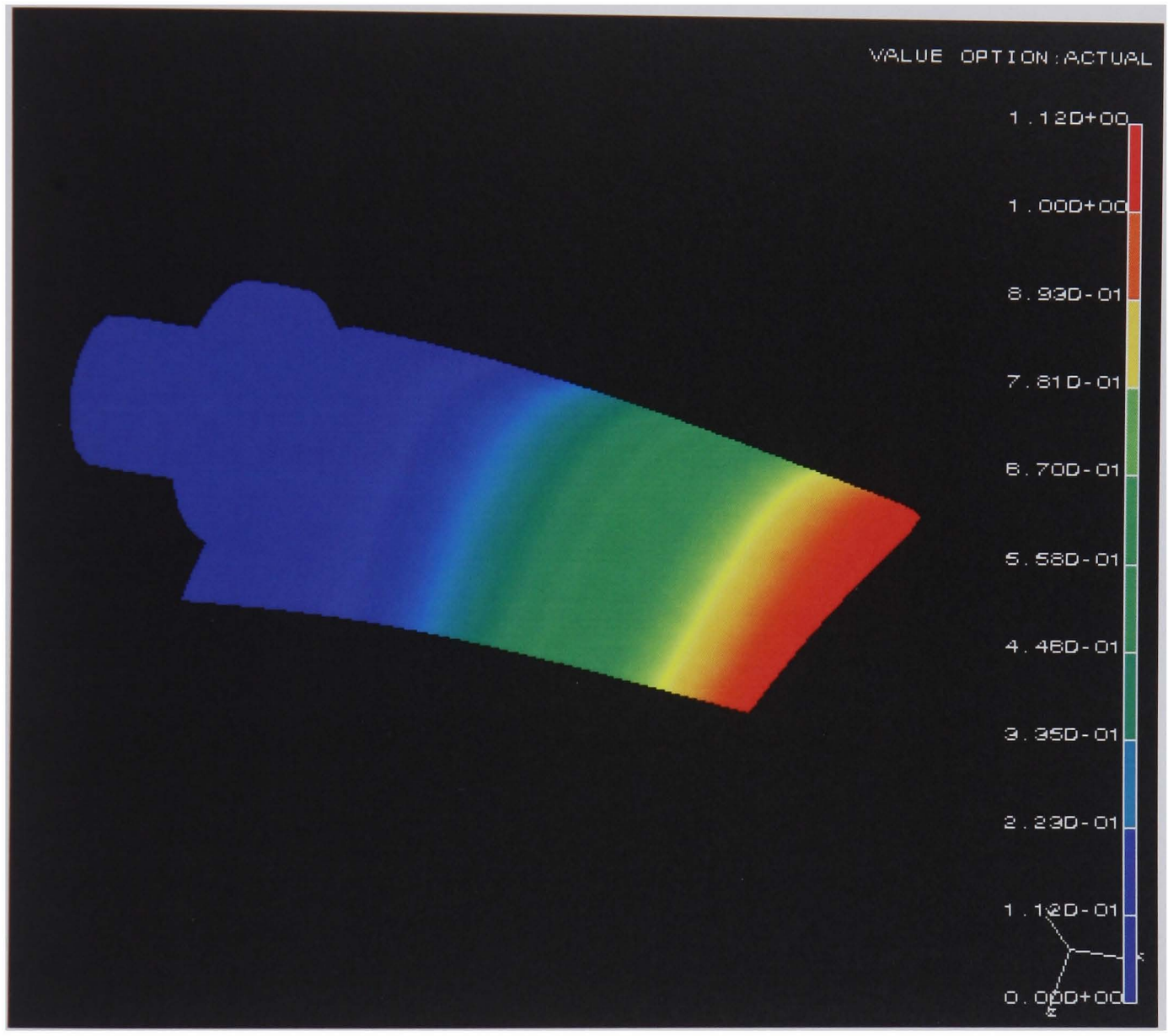

Figure 4.4 Test Blade Mode 1 Modal Displacement

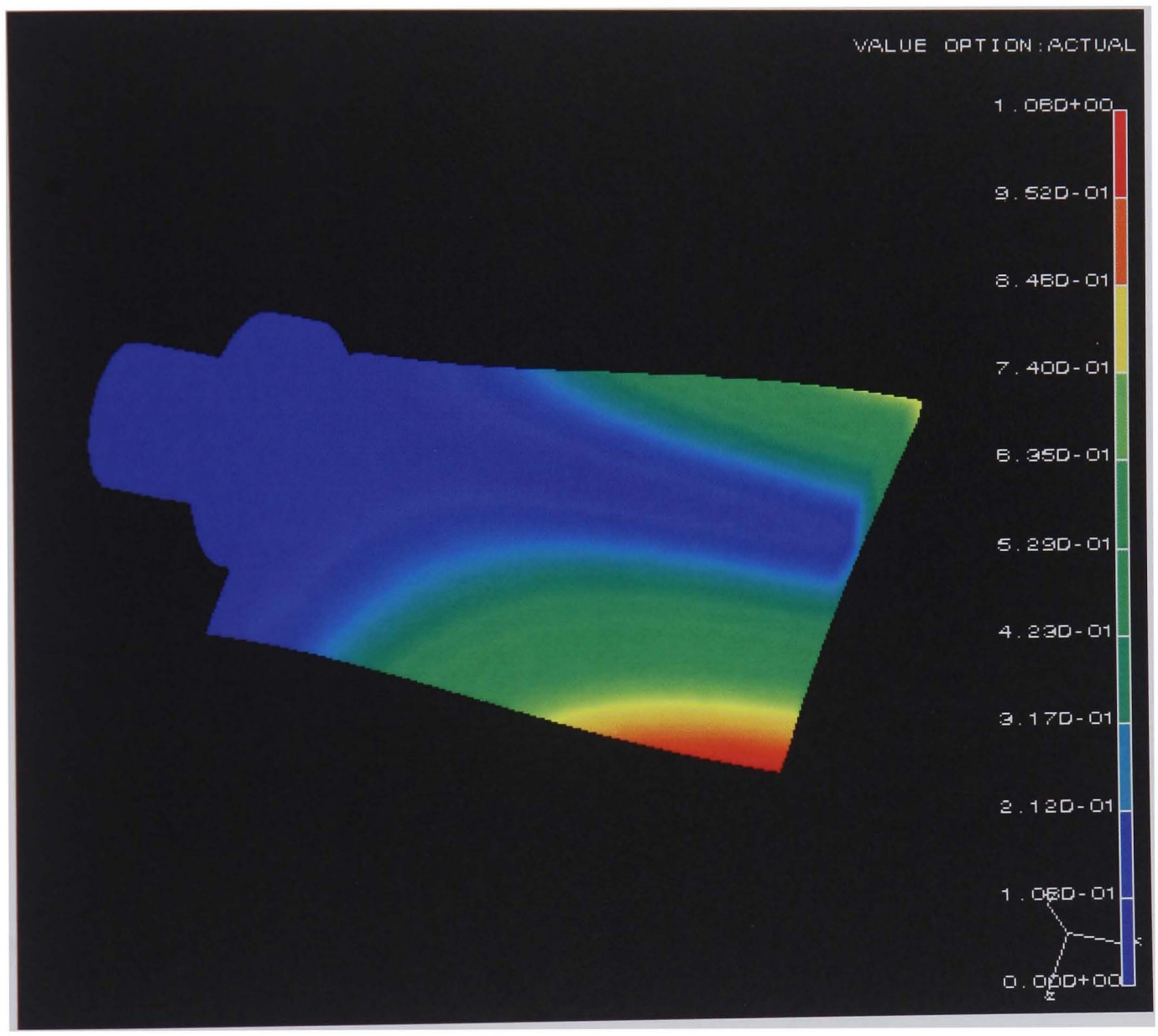

Figure 4.5 Test Blade Mode 2 Modal Displacement

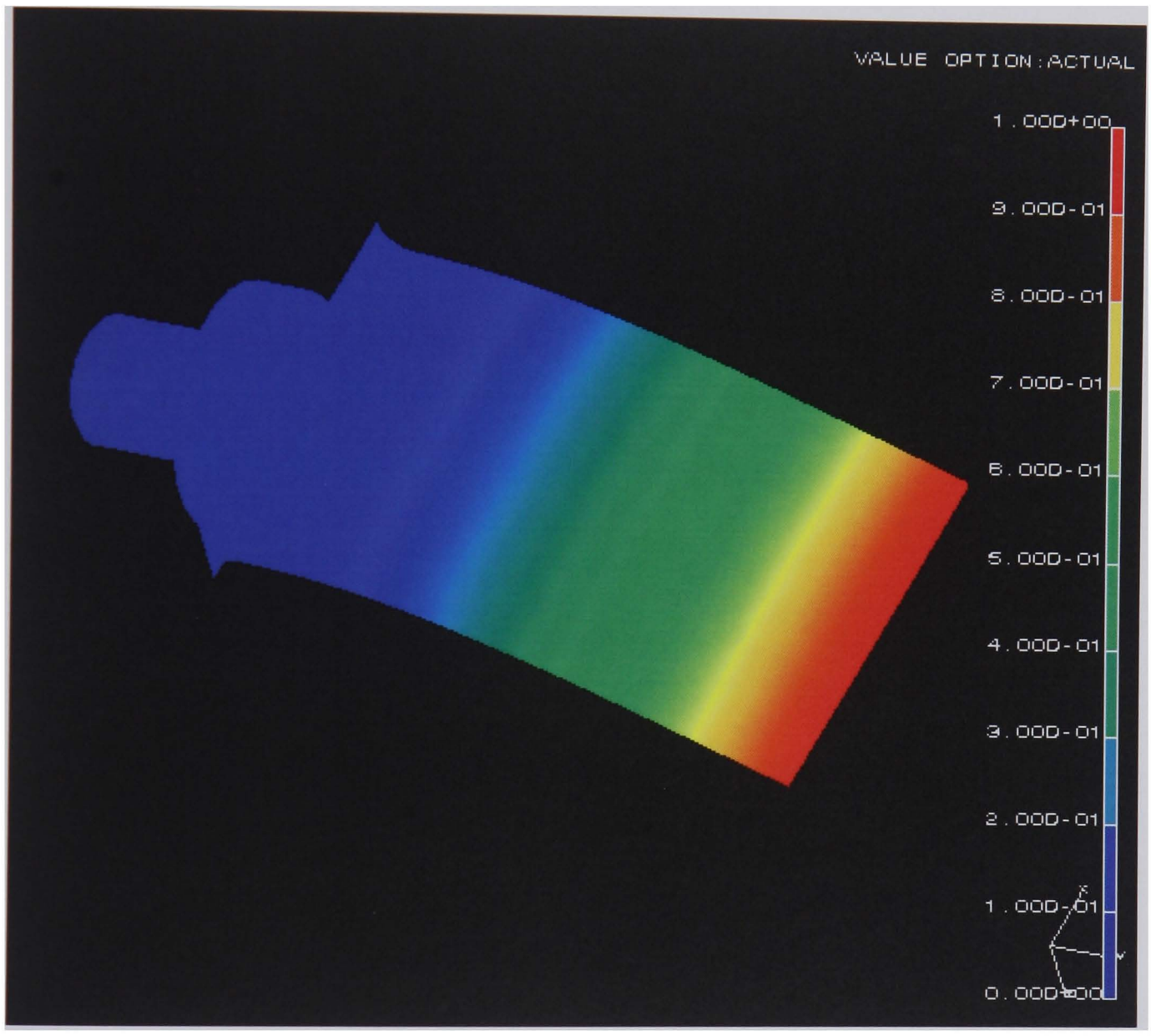

Figure 4.6 2mm Blade Mode 1 Modal Displacement

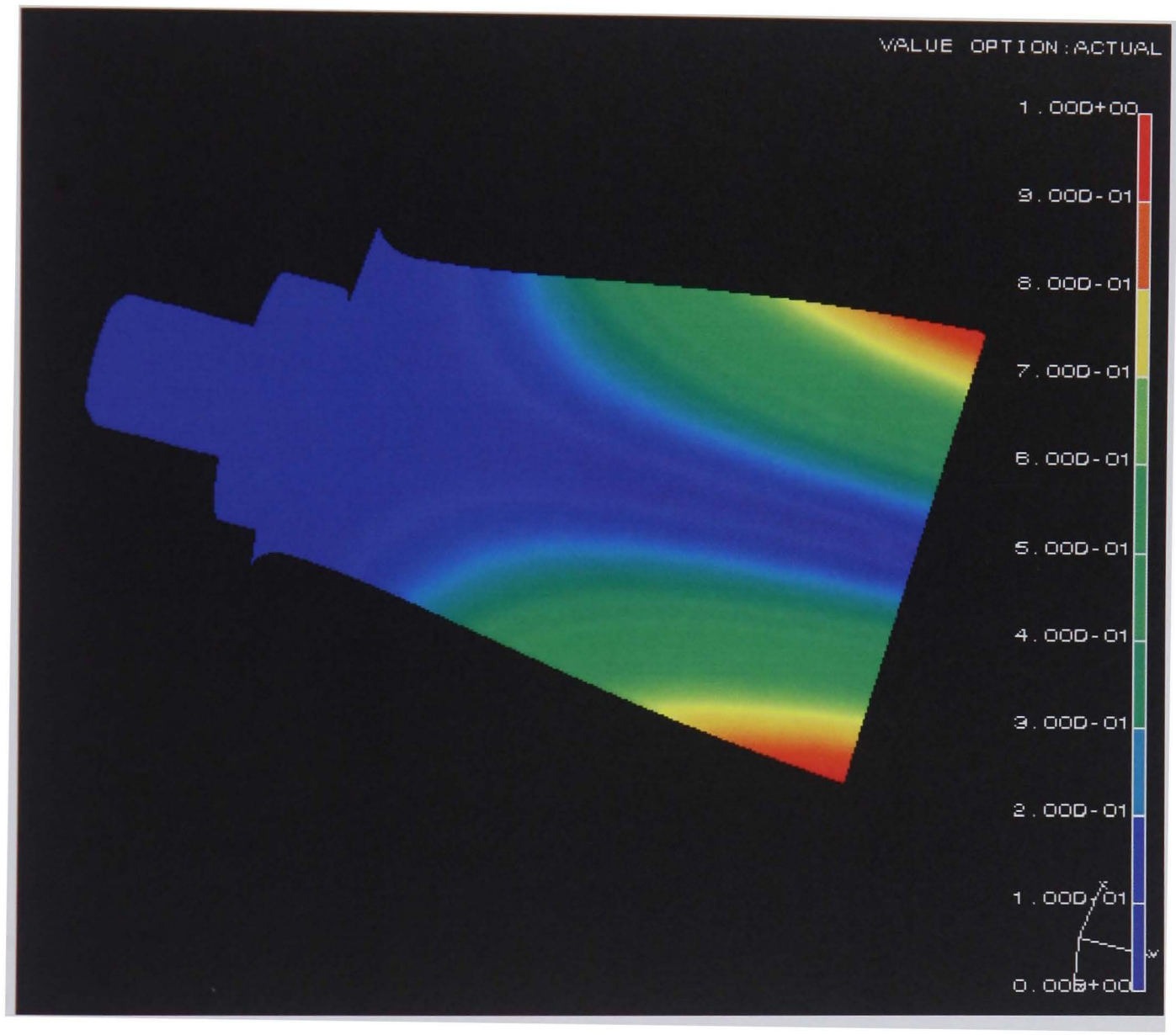

Figure 4.7 2mm Blade Mode 2 Modal Displacement

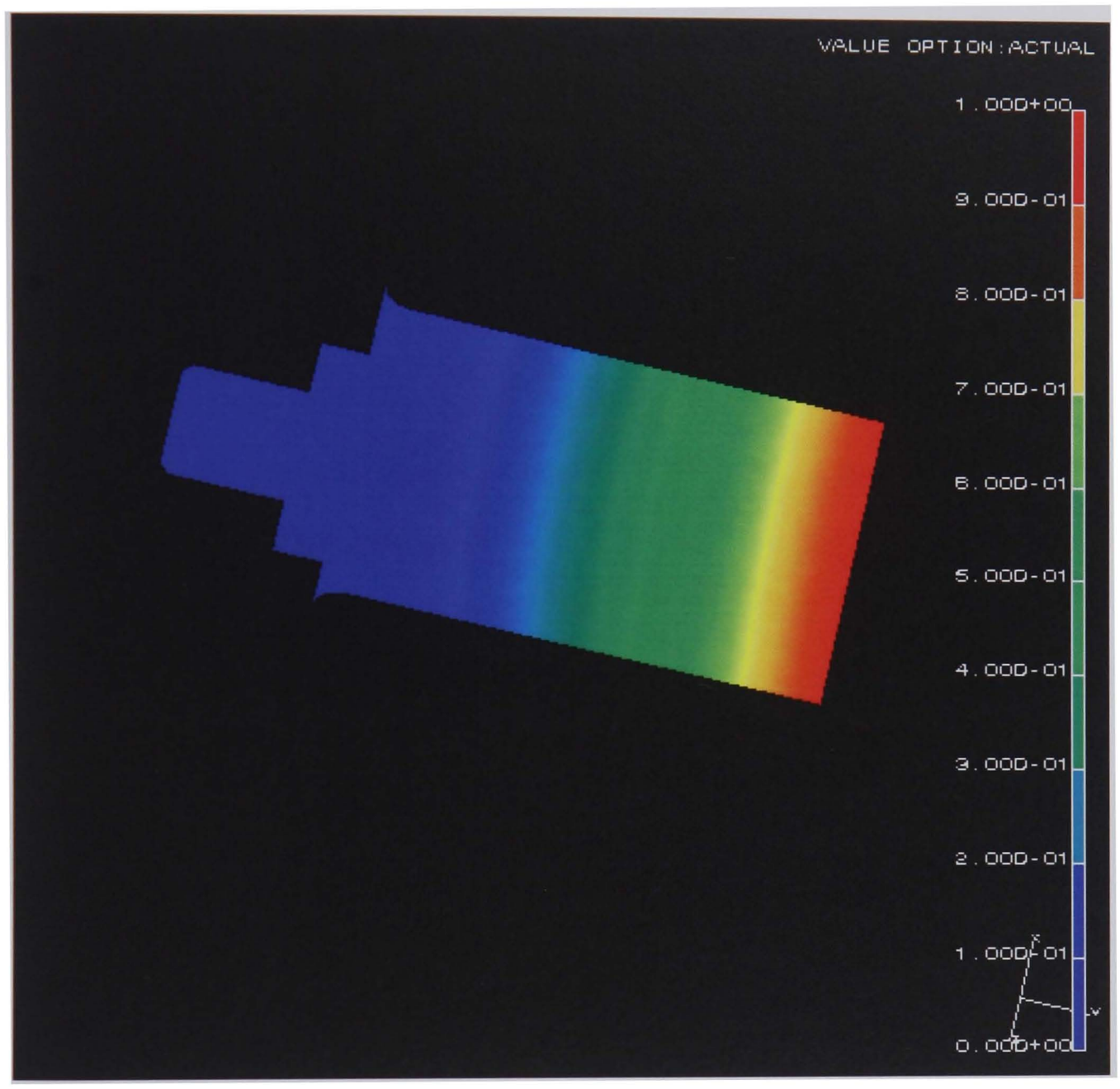

Figure 4.8 3mm Blade Mode 1 Modal Displacement

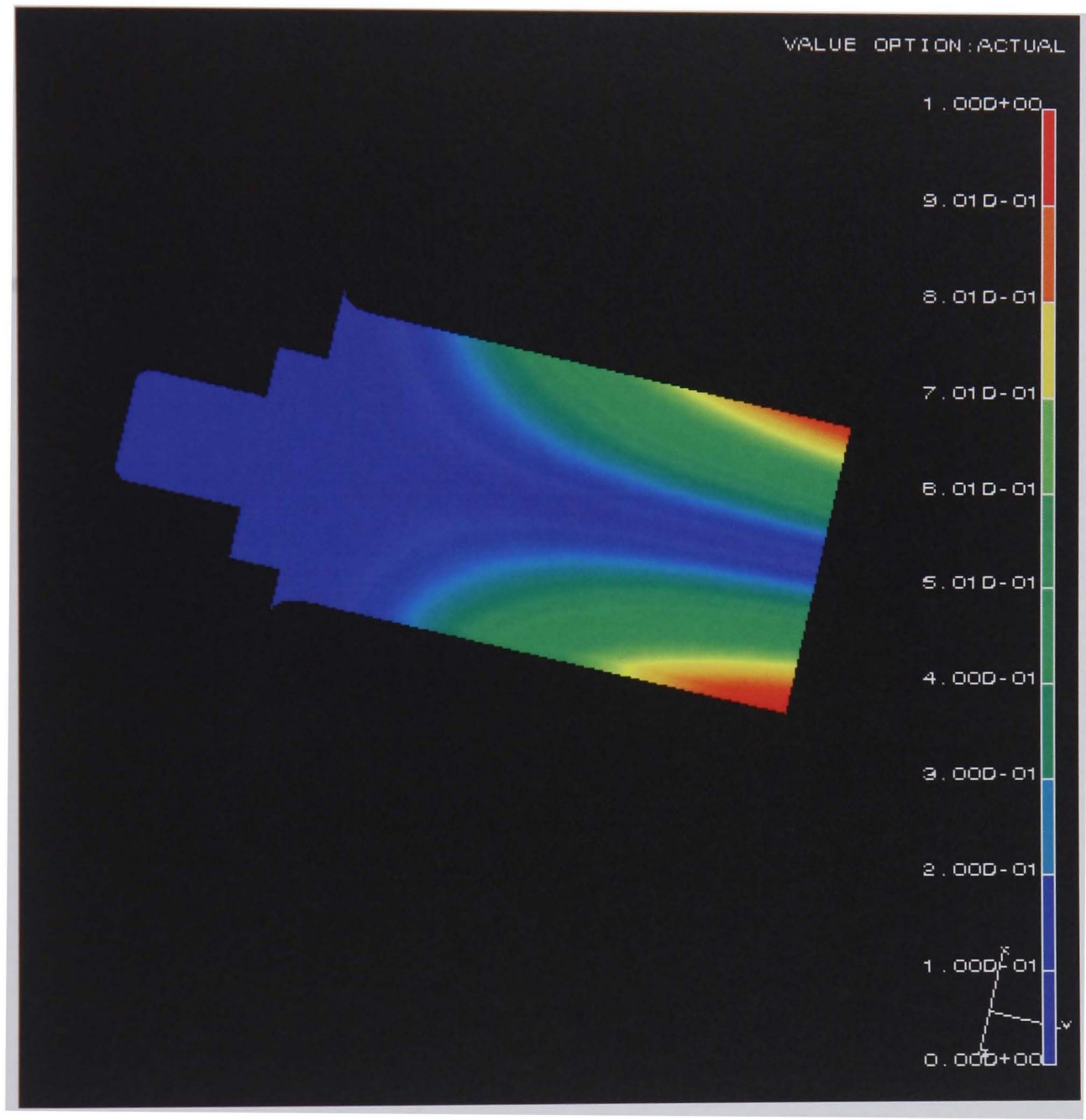

Figure 4.9 3mm Blade Mode 2 Modal Displacement

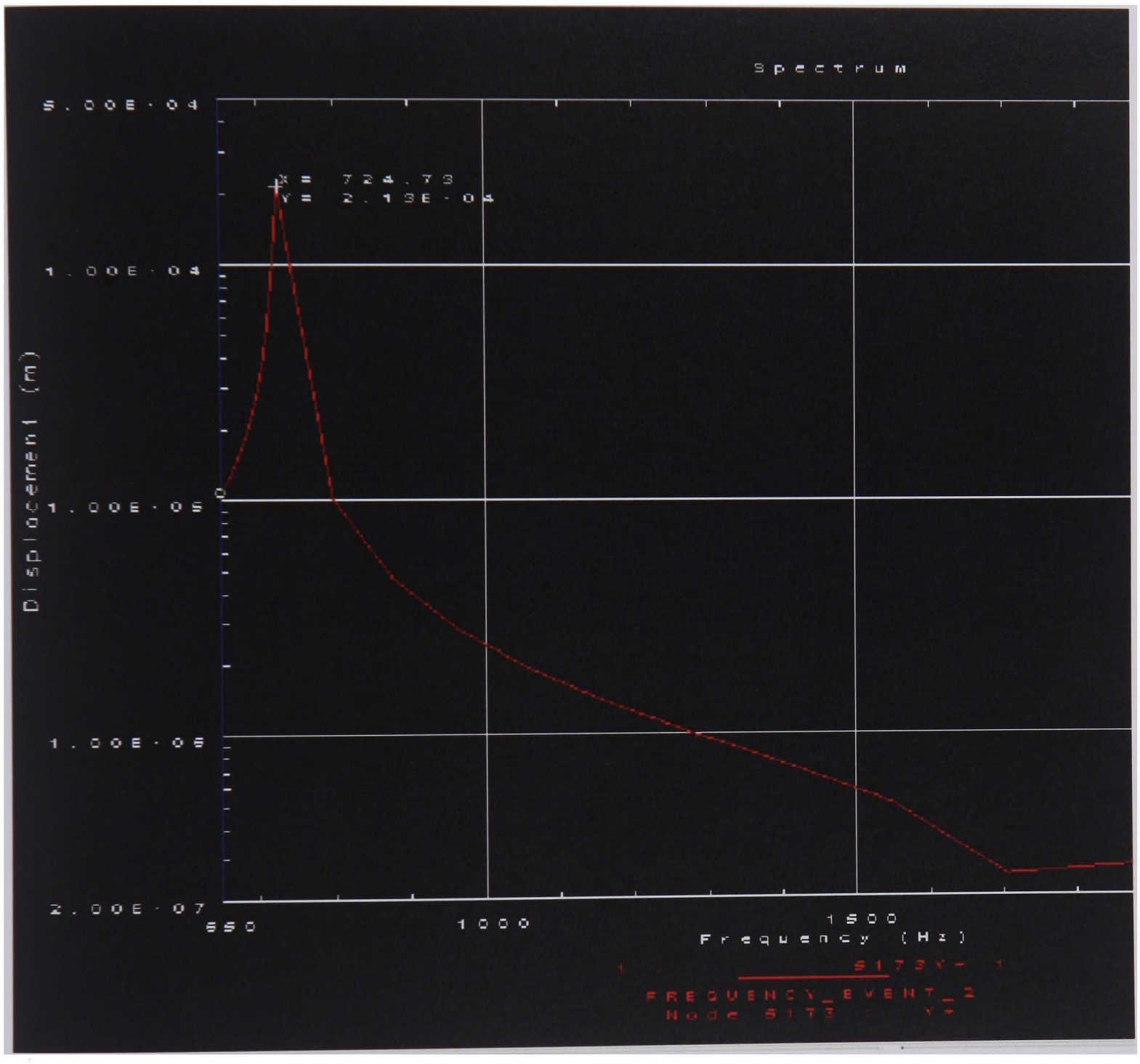

Figure 4.10 Test Blade Forced Frequency Response

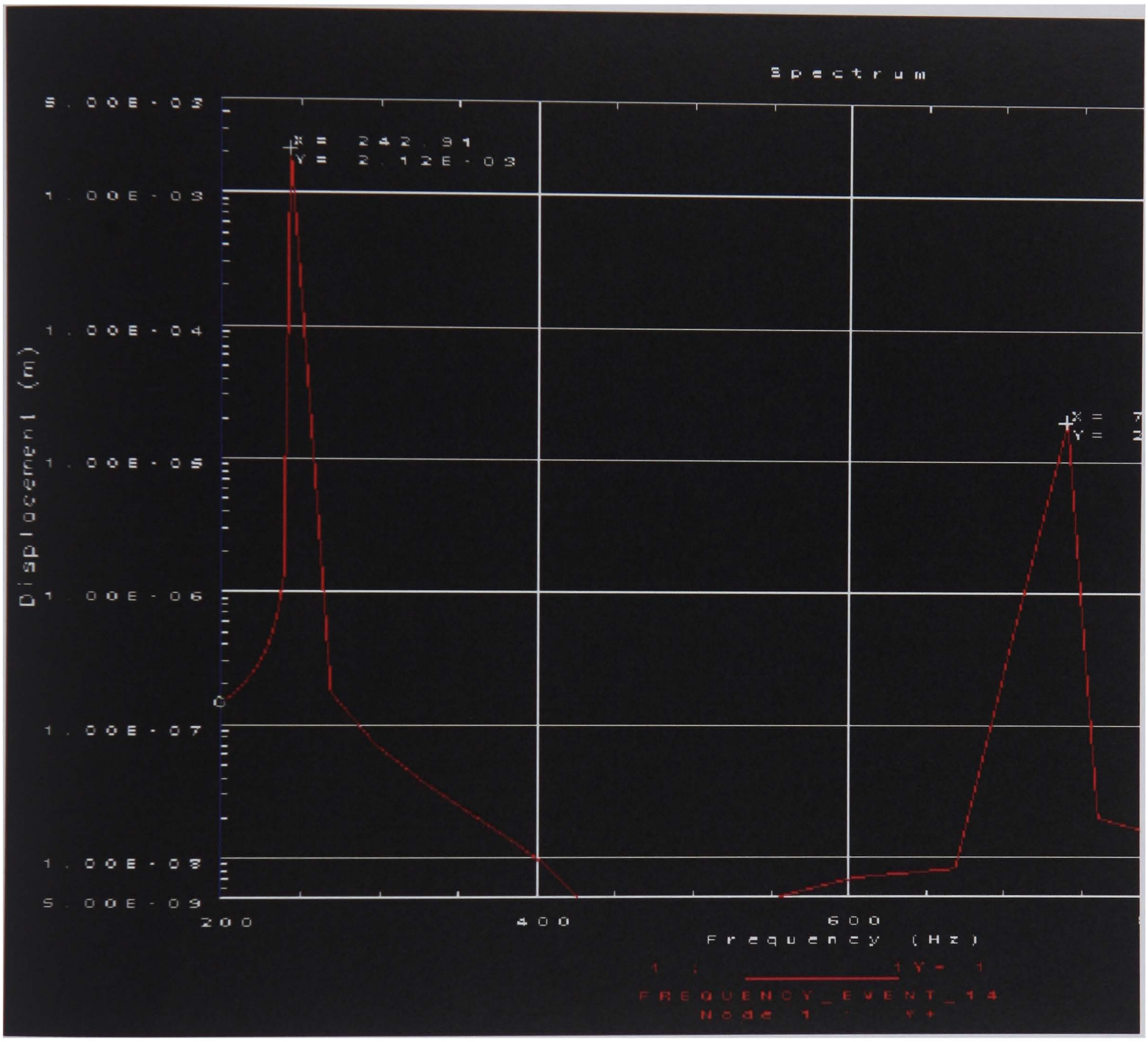

Figure 4.11 2mm Blade Forced Frequency Response

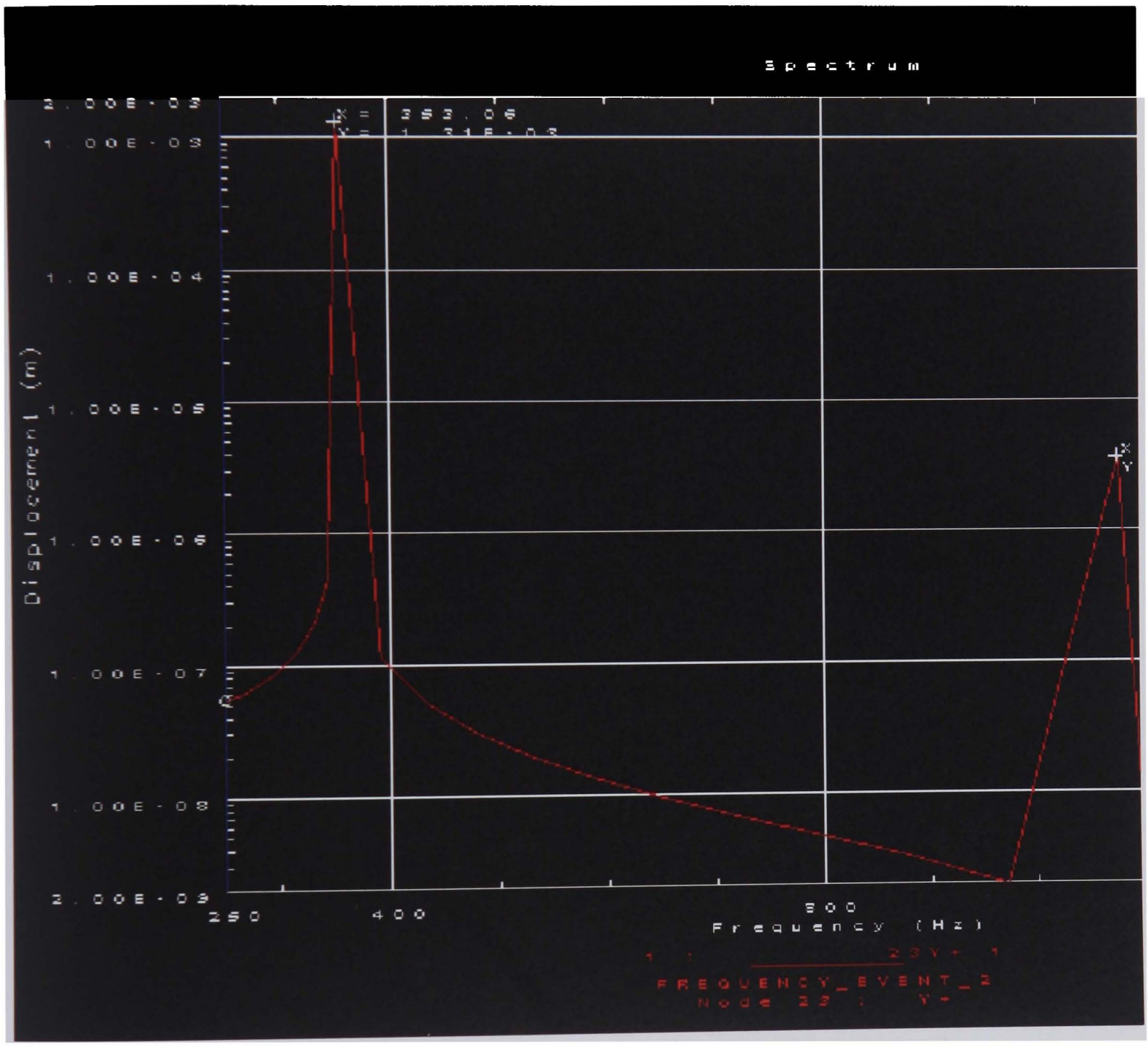

Figure 4.12 3mm Blade Forced Frequency Response

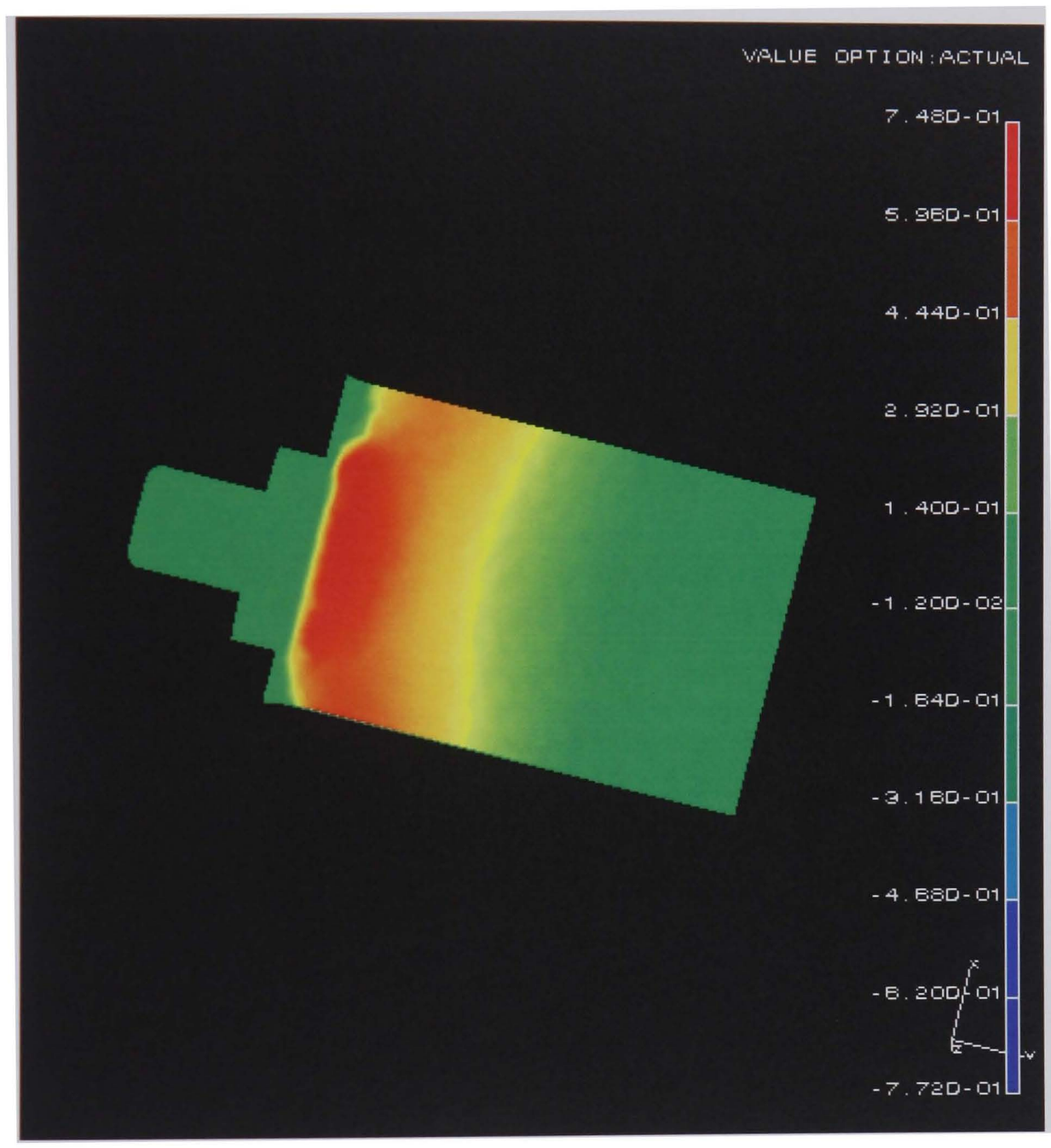

Figure 4.13 3mm Blade Mode 1 Modal Longitudinal Strain

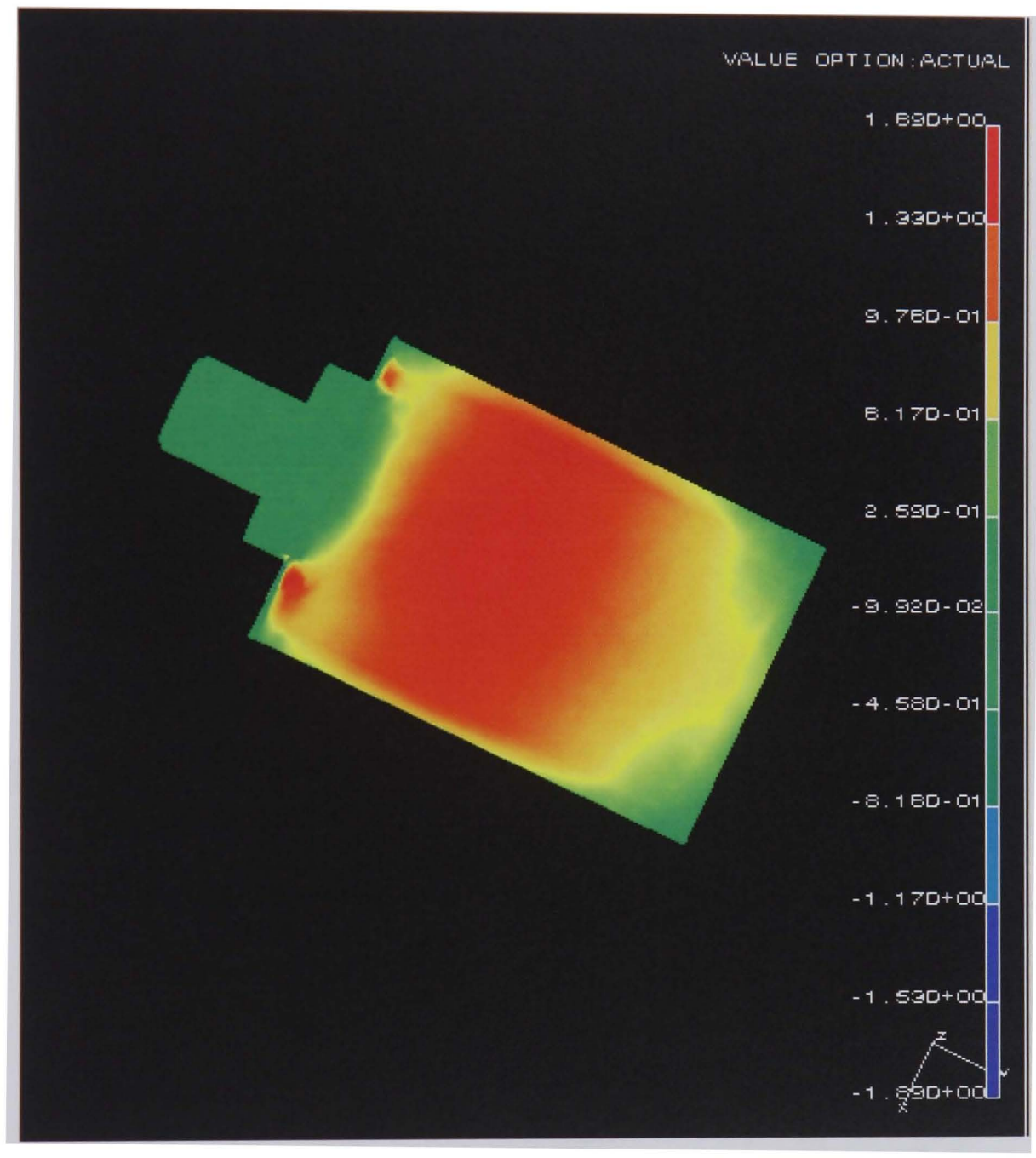

Figure 4.14 3mm Blade Mode 2 Modal Shear Strain

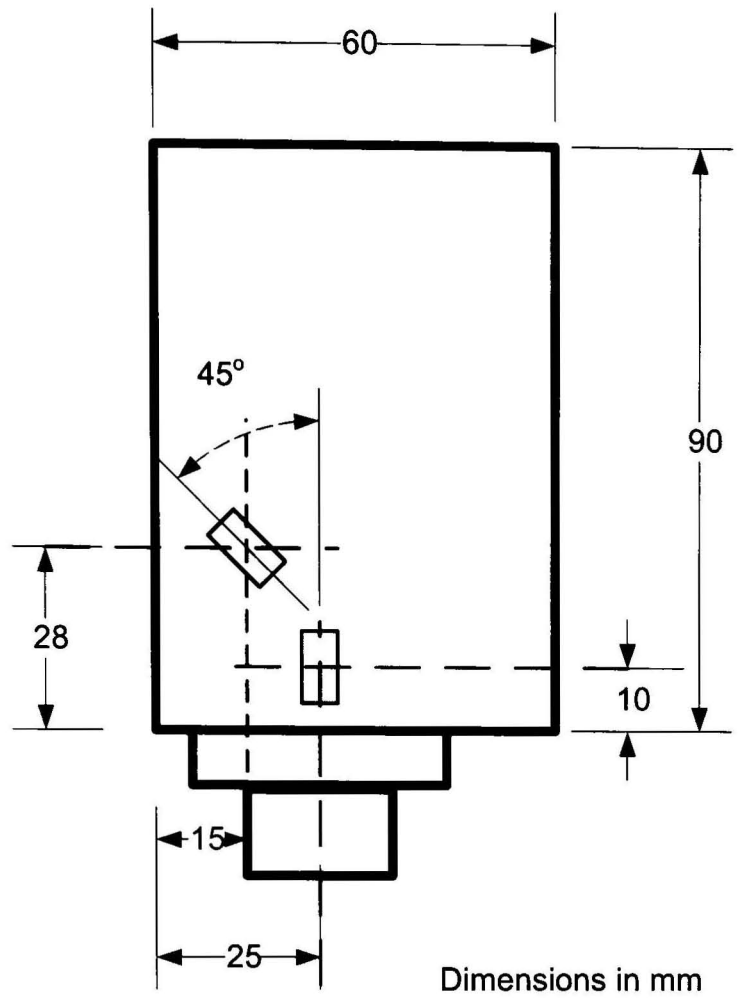

Figure 4.15 Strain Gauge Surface Locations

Source[22]

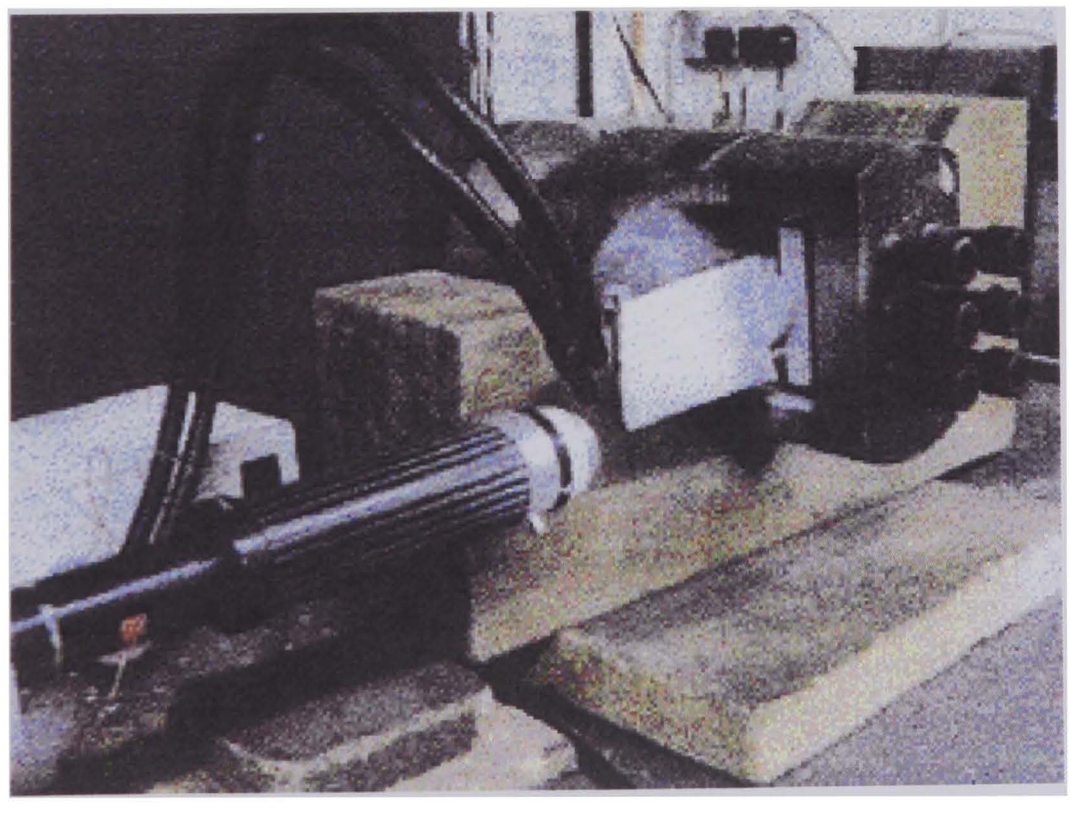

Figure 4.16 Bench Testing of the Blade using an ESPI system

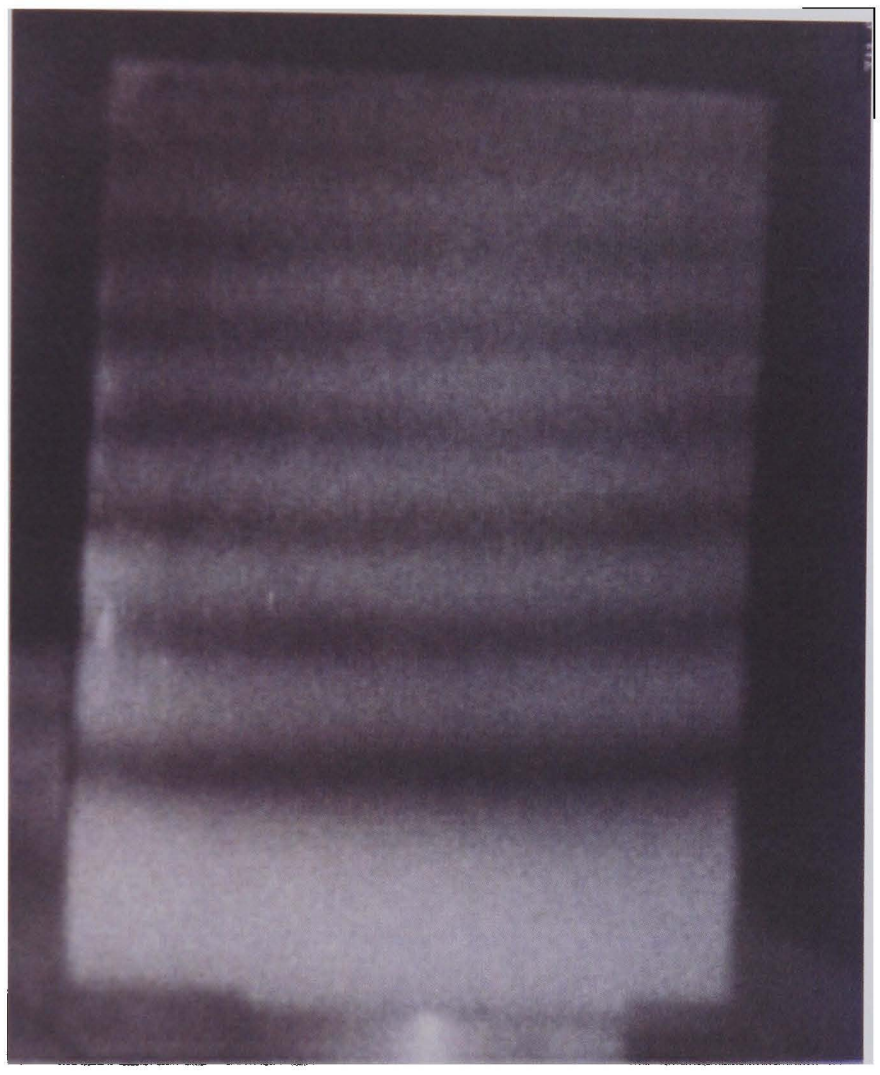

Figure 4.17 ESPI formation of the 2mm Blade First Mode Shape

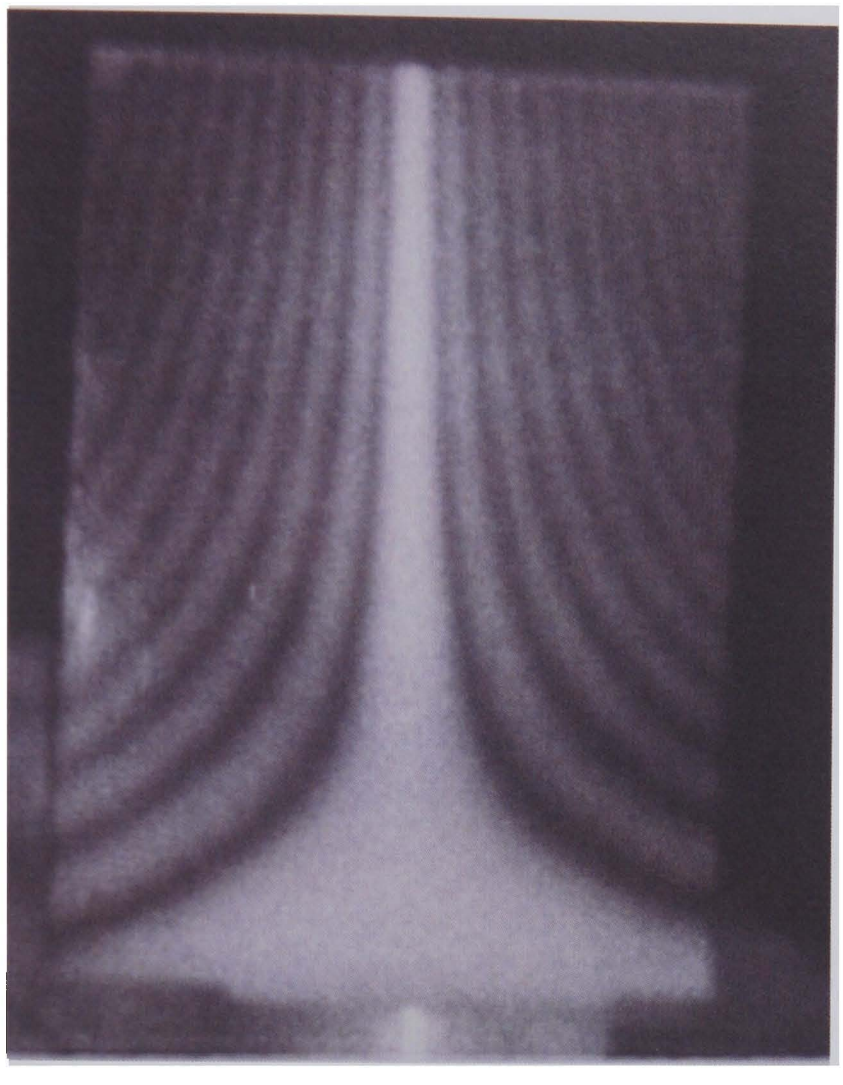

Figure 4.18 ESPI formation of the 2mm Blade Second Mode Shape

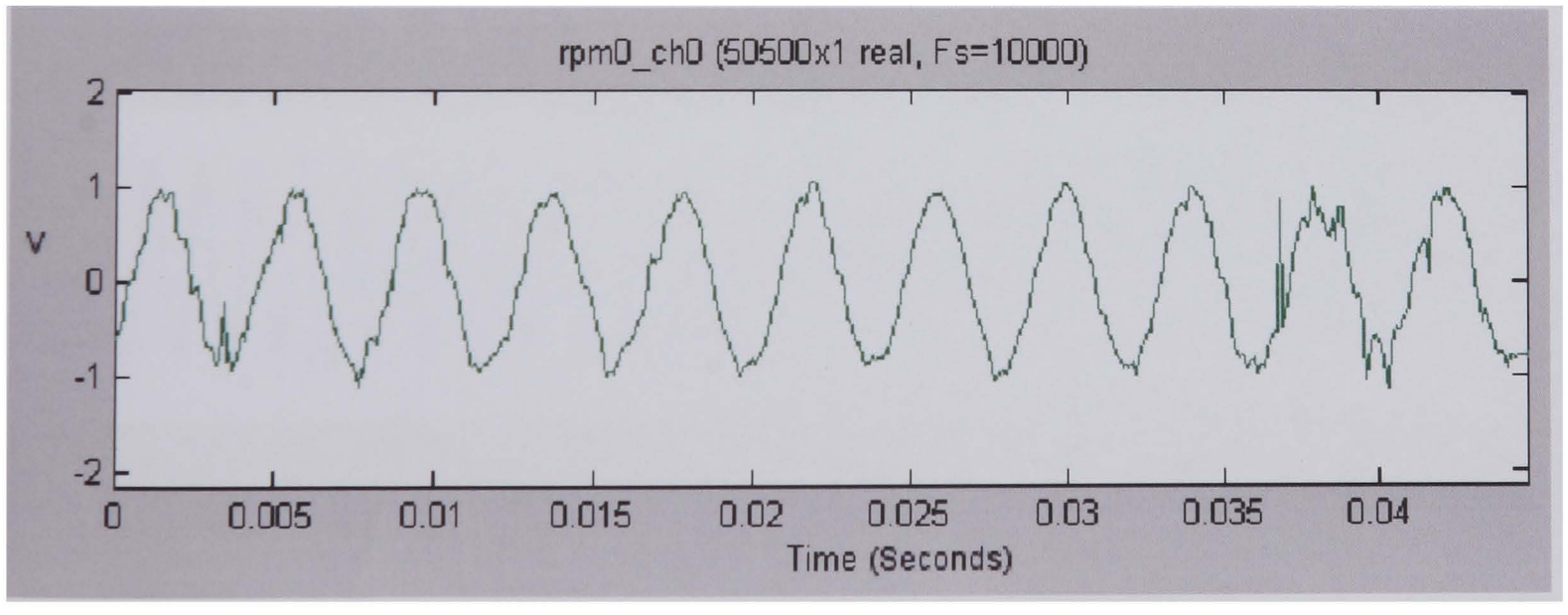

Figure 4.19 2mm Blade Strain Response at 205RPM

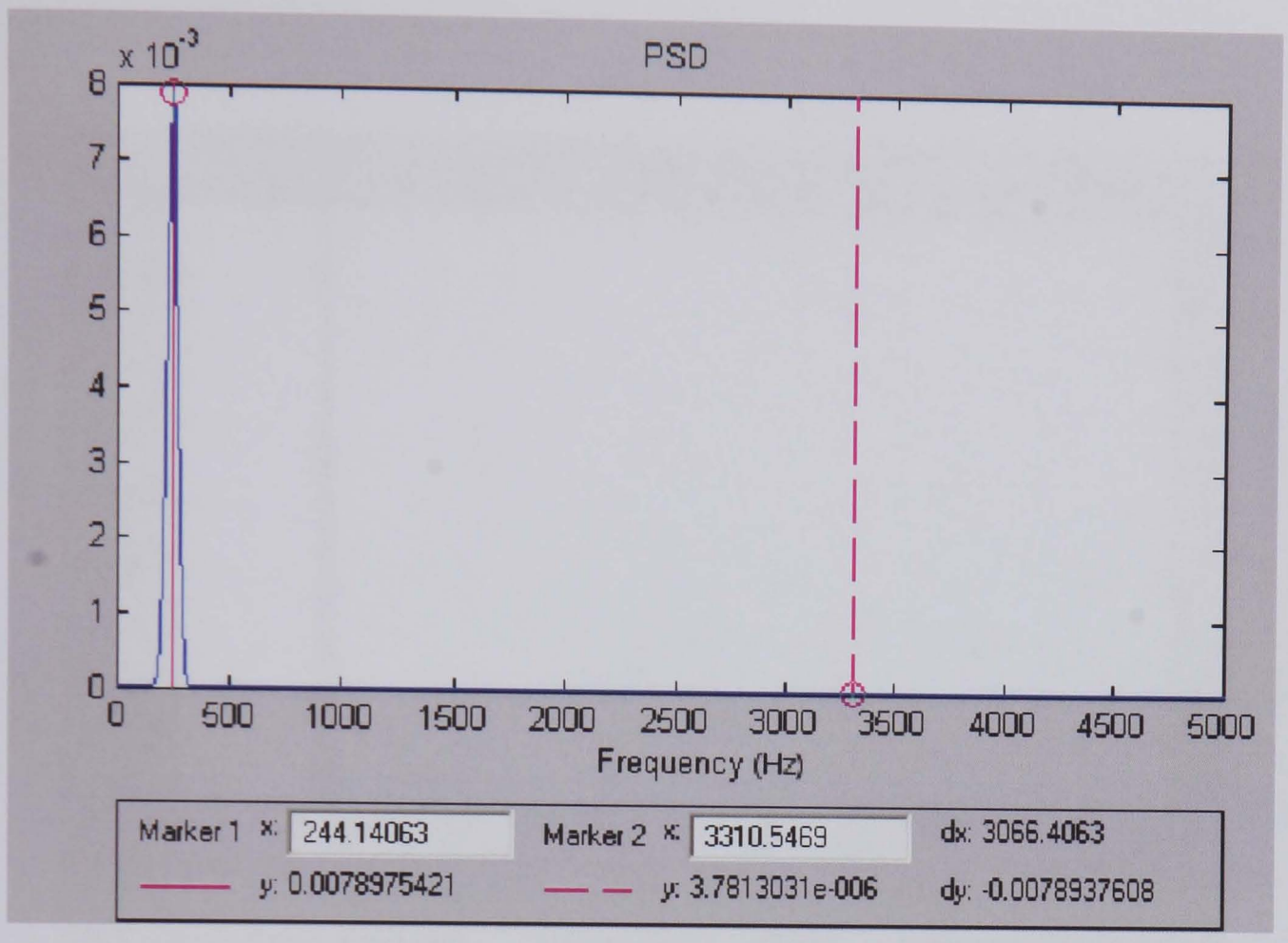

Figure 4.20 2mm Blade FFT of the Strain Response at 205RPM

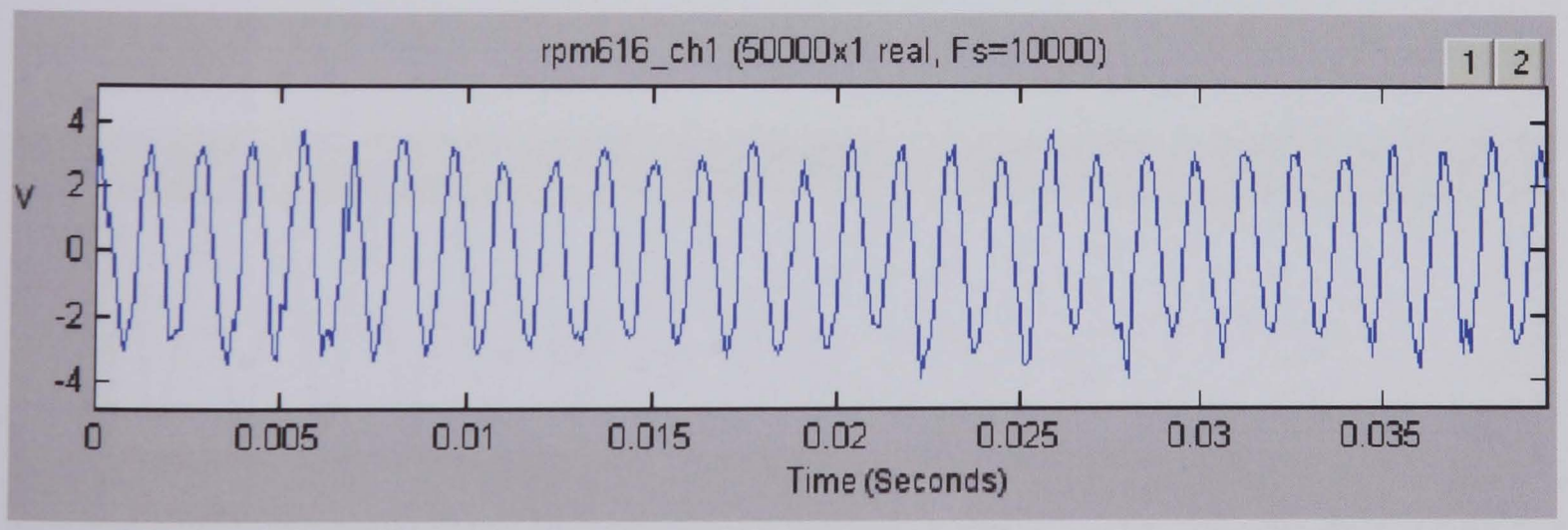

Figure 4.21 2mm Blade Strain Response at 617RPM

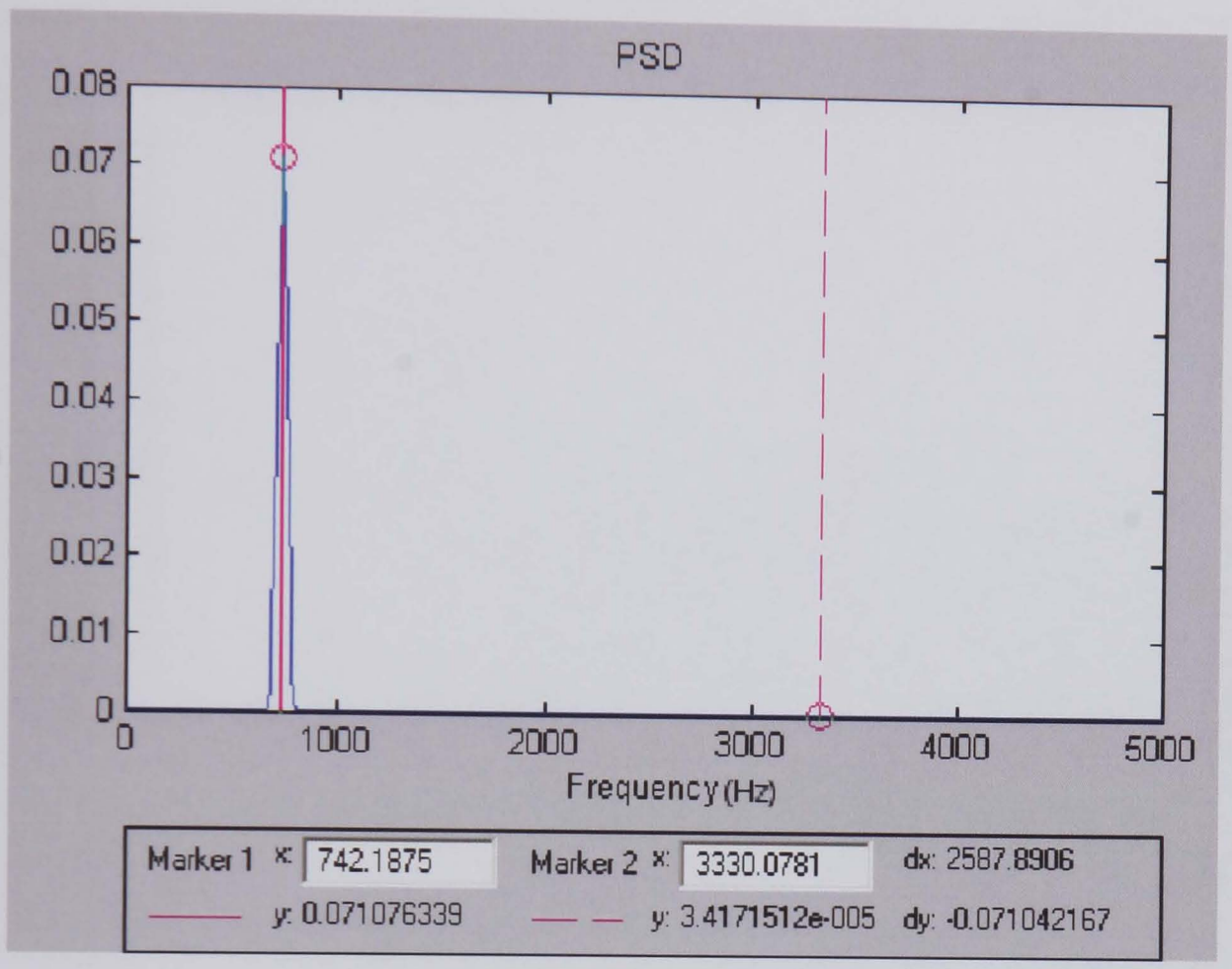

Figure 4.22 2mm Blade FFT of the Strain Response at 617RPM

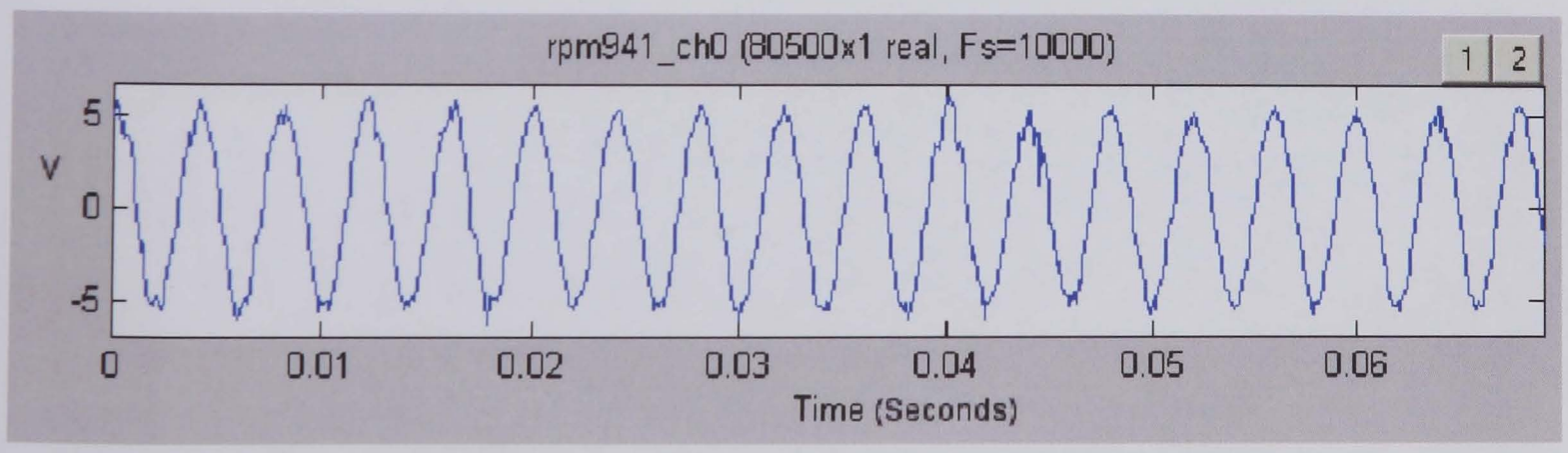

Figure 4.23 2mm Blade Strain Response at 941RPM

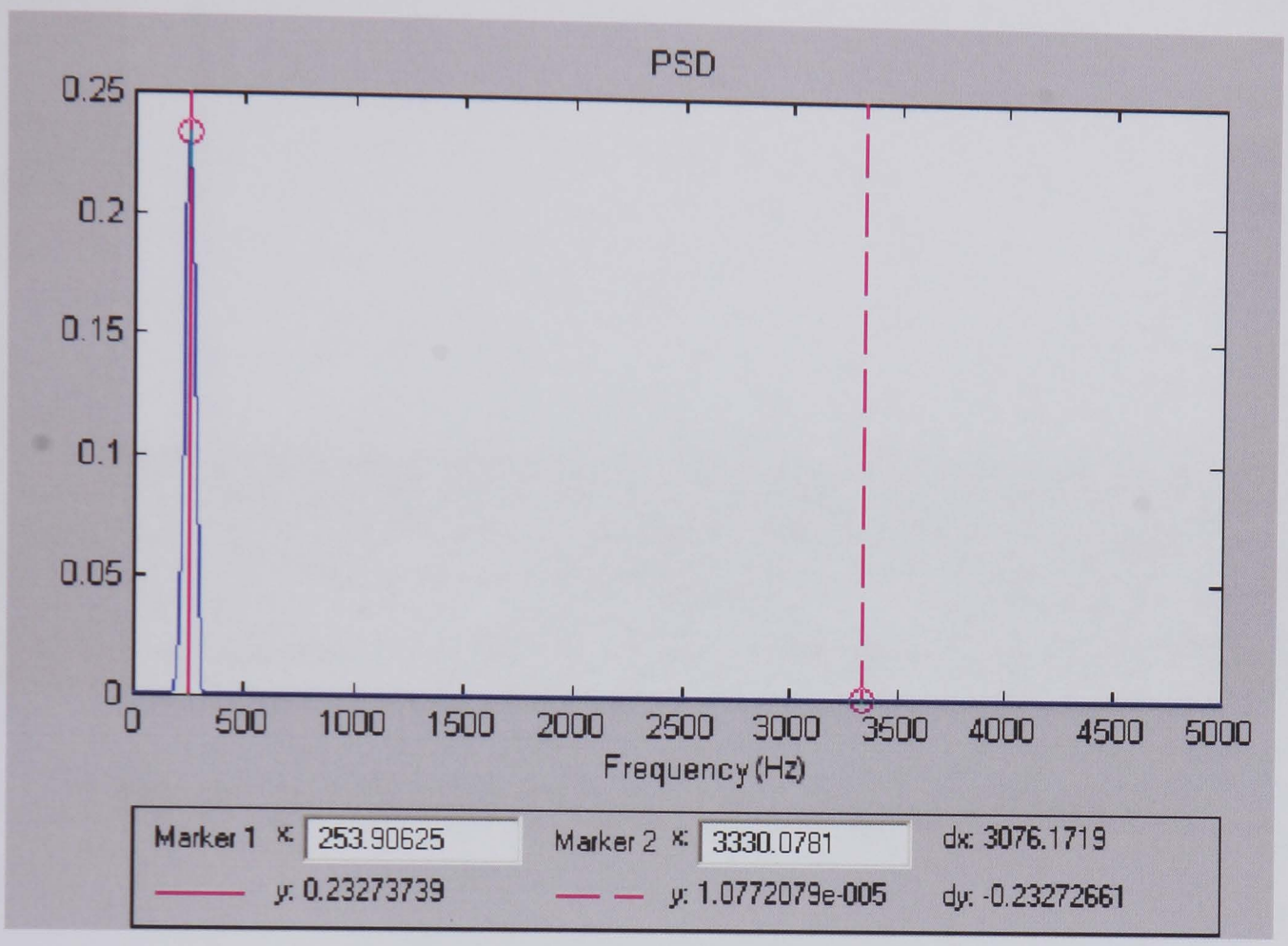

Figure 4.24 2mm Blade FFT of the Strain Response at 941RPM

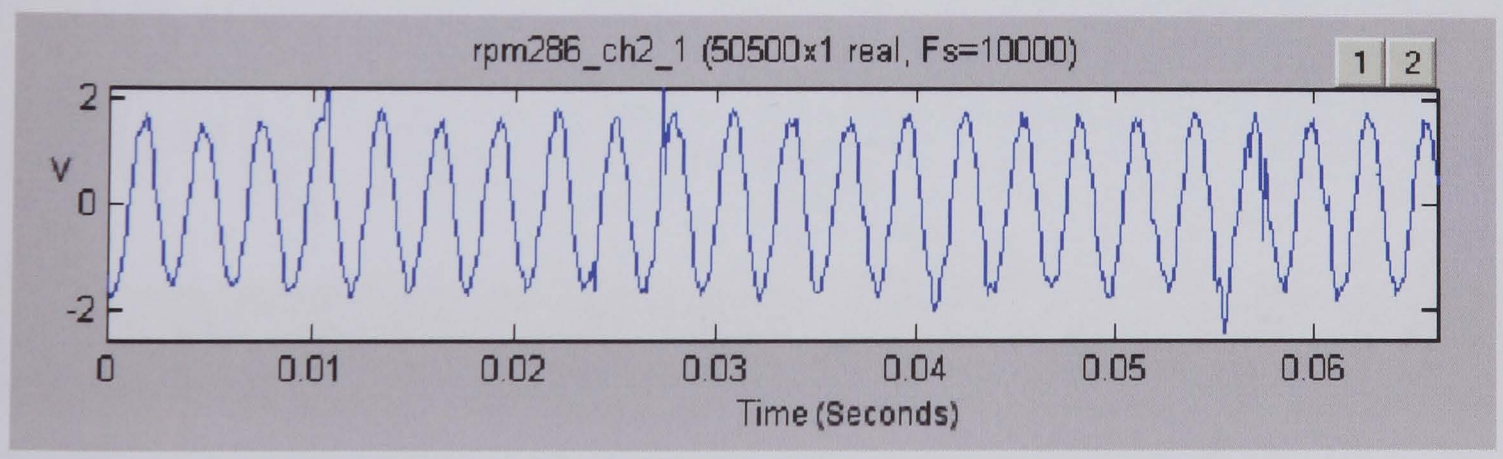

Figure 4.25 3mm Blade Strain Response at 286RPM

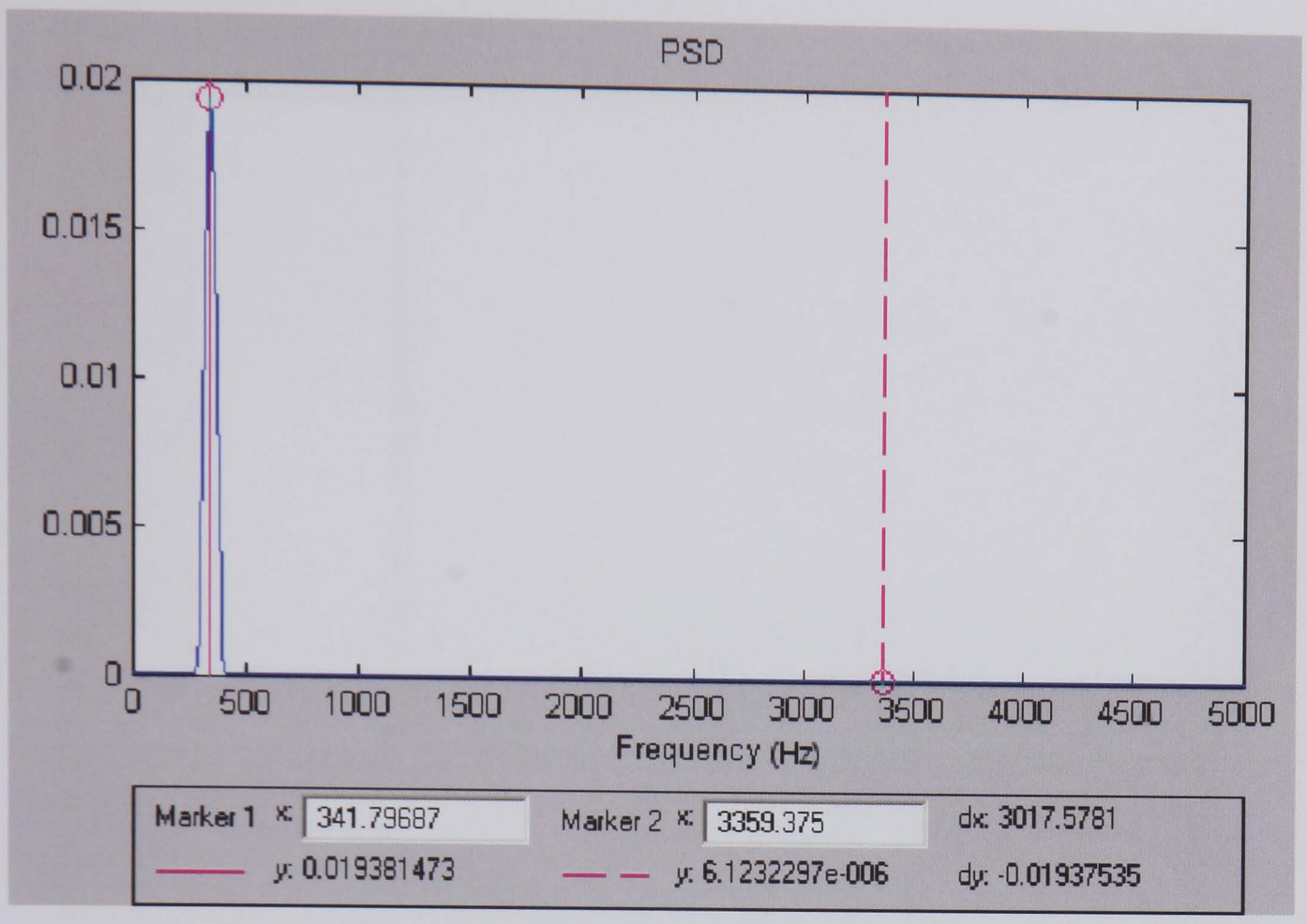

Figure 4.26 3mm Blade FFT of the Strain Response at 286RPM

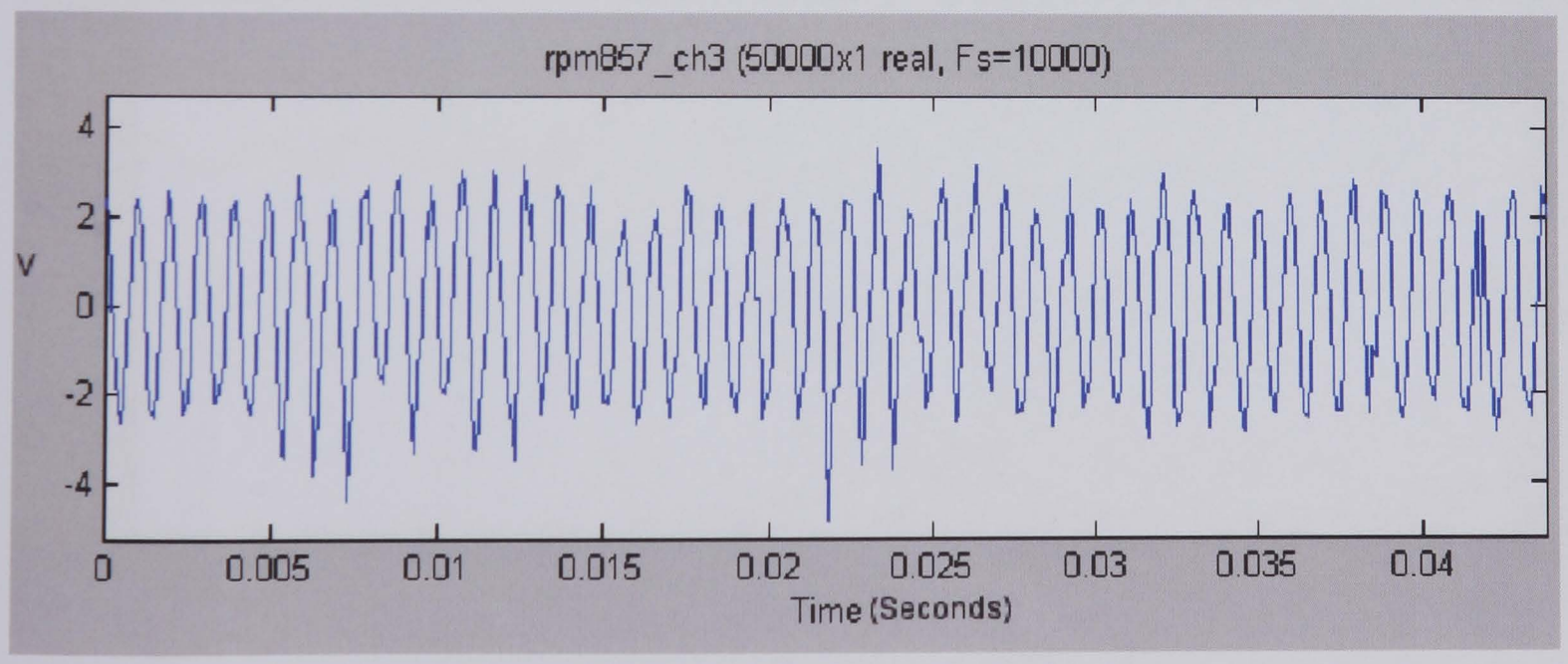

Figure 4.27 3mm Blade Strain Response at 857RPM

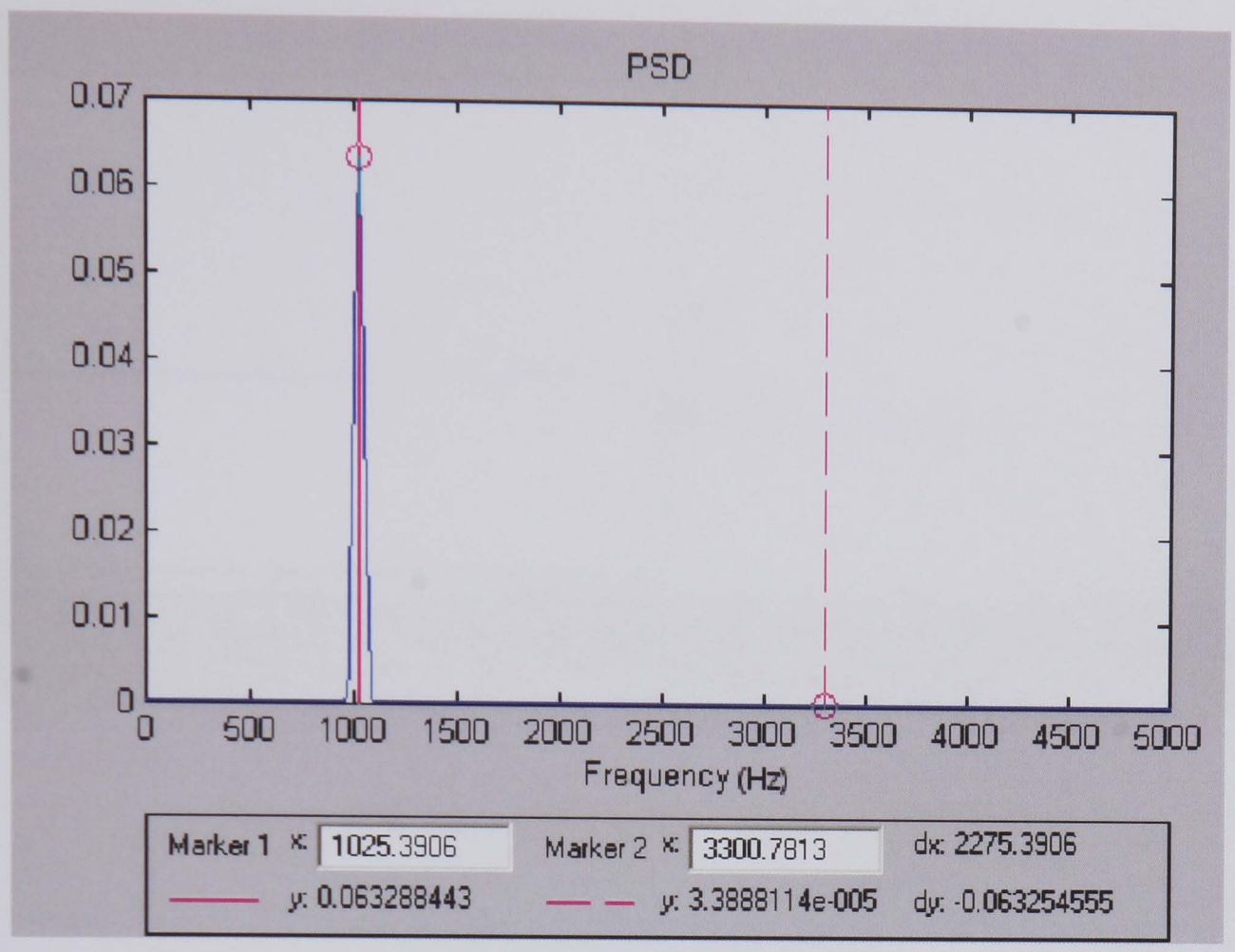

Figure 4.28 3mm Blade FFT of the Strain Response at 857RPM

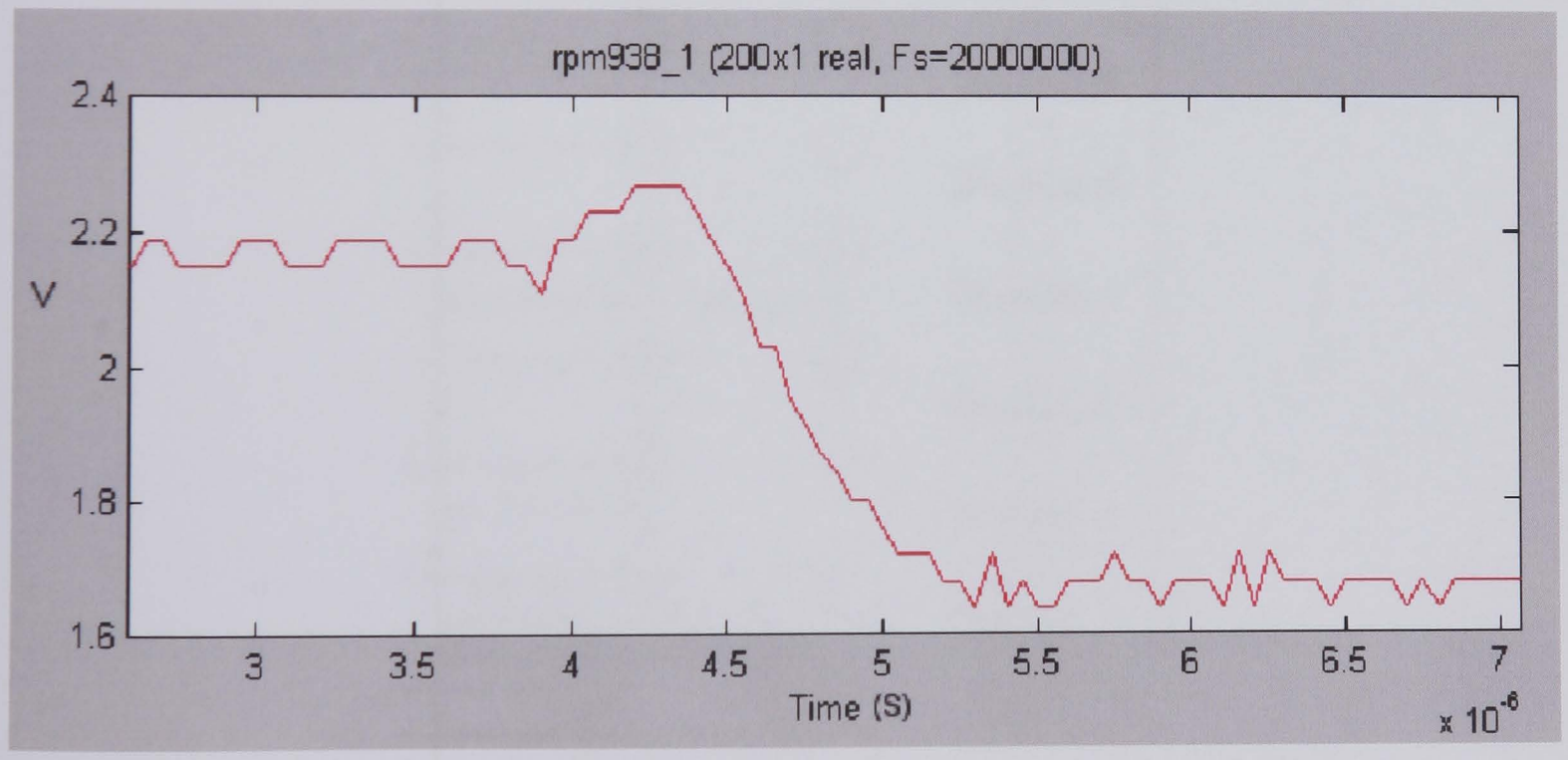

Figure 4.29 The OPR Analog Signal at 938RPM

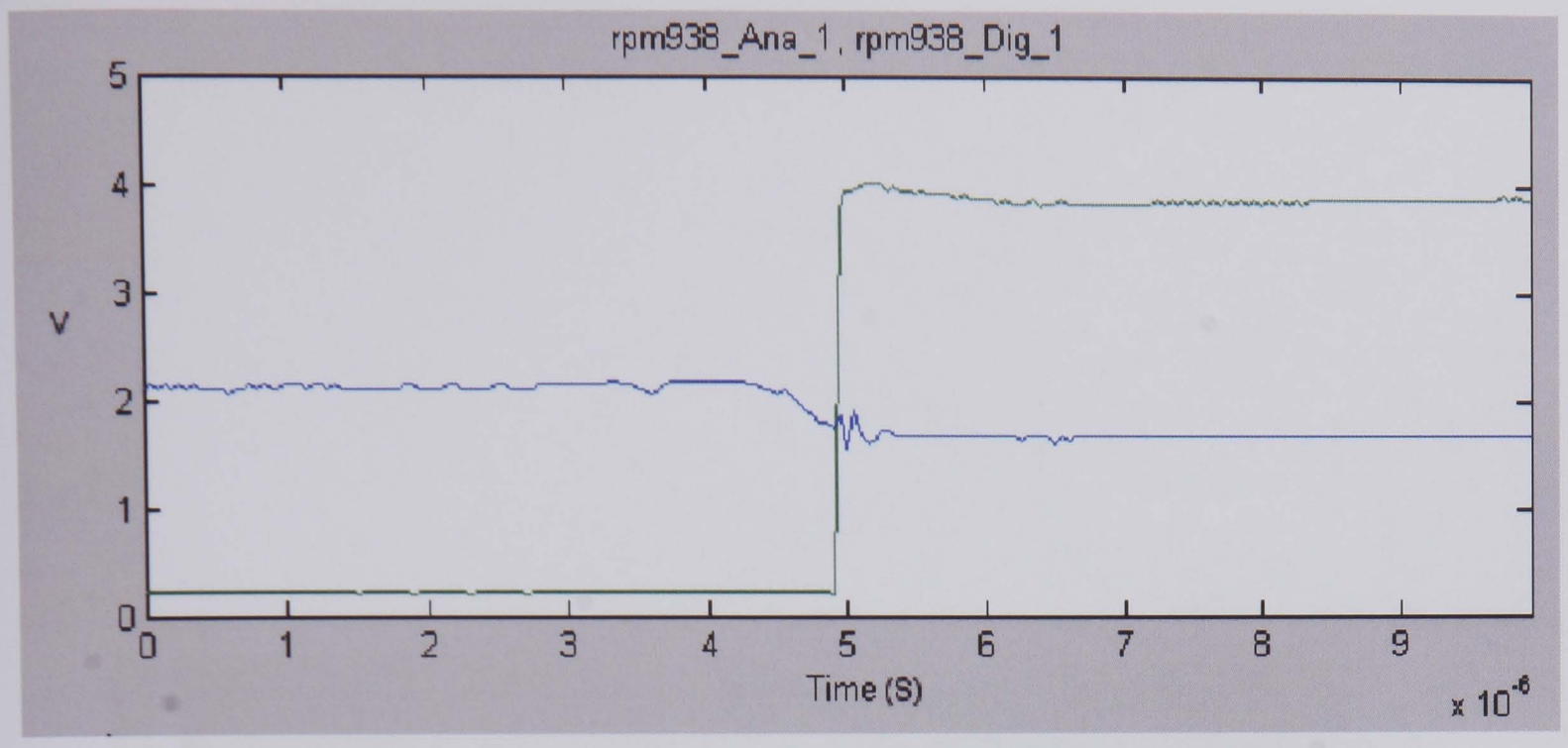

Figure 4.30 The OPR Digital Trigger at 938RPM

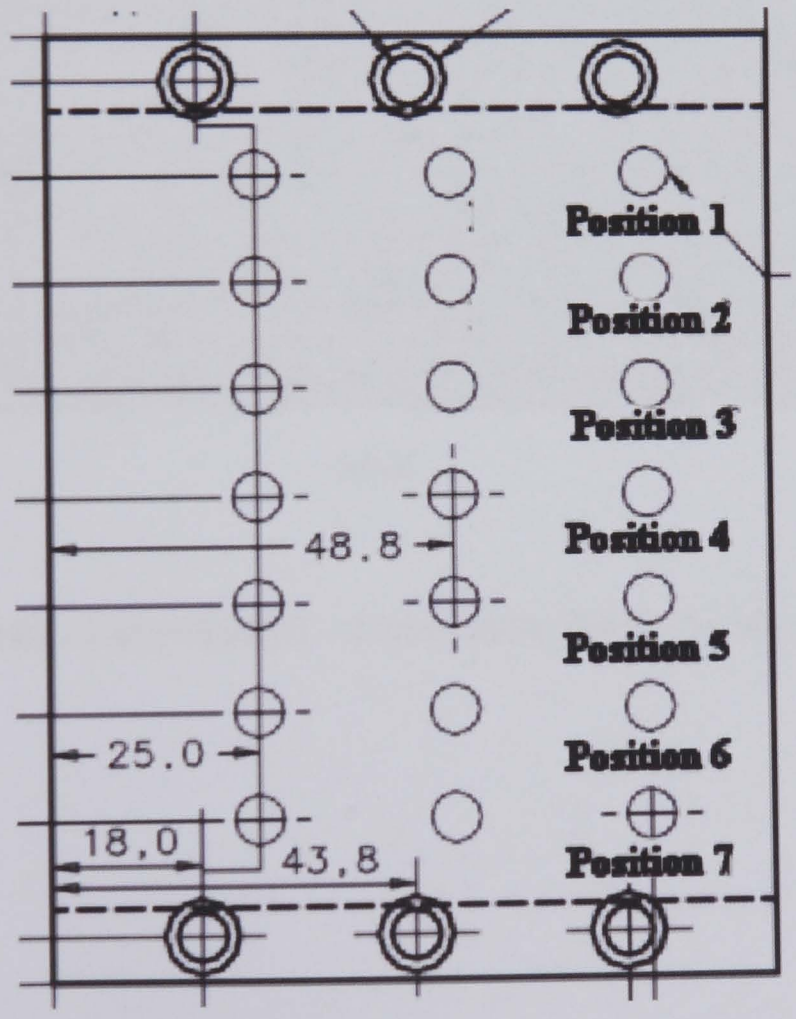

Figure 5.1 Illustration of Probe Position Numbering

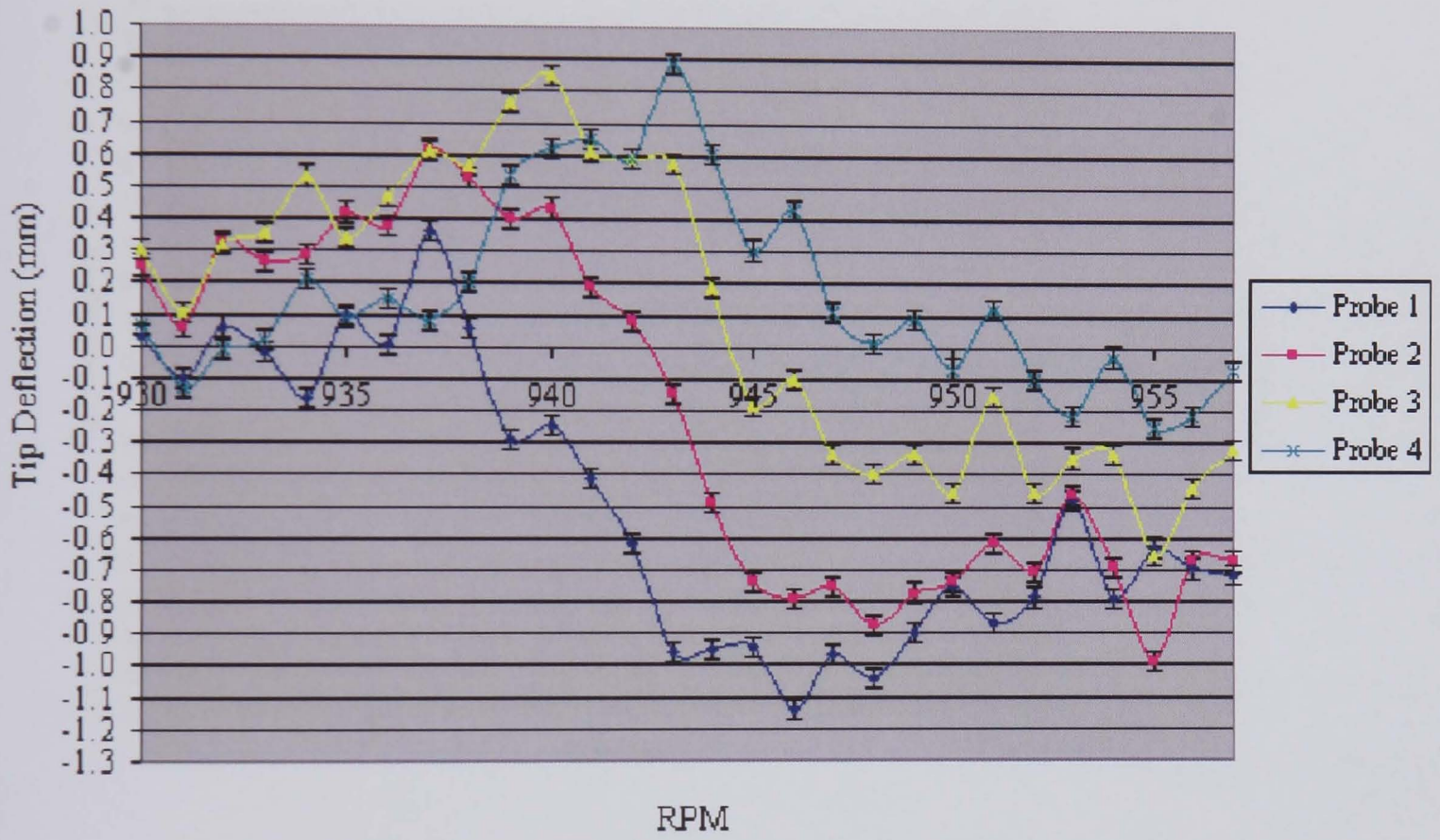

Figure 5.2 Setup 1 at 941RPM - 2mm Blade Tip Deflection Versus RPM

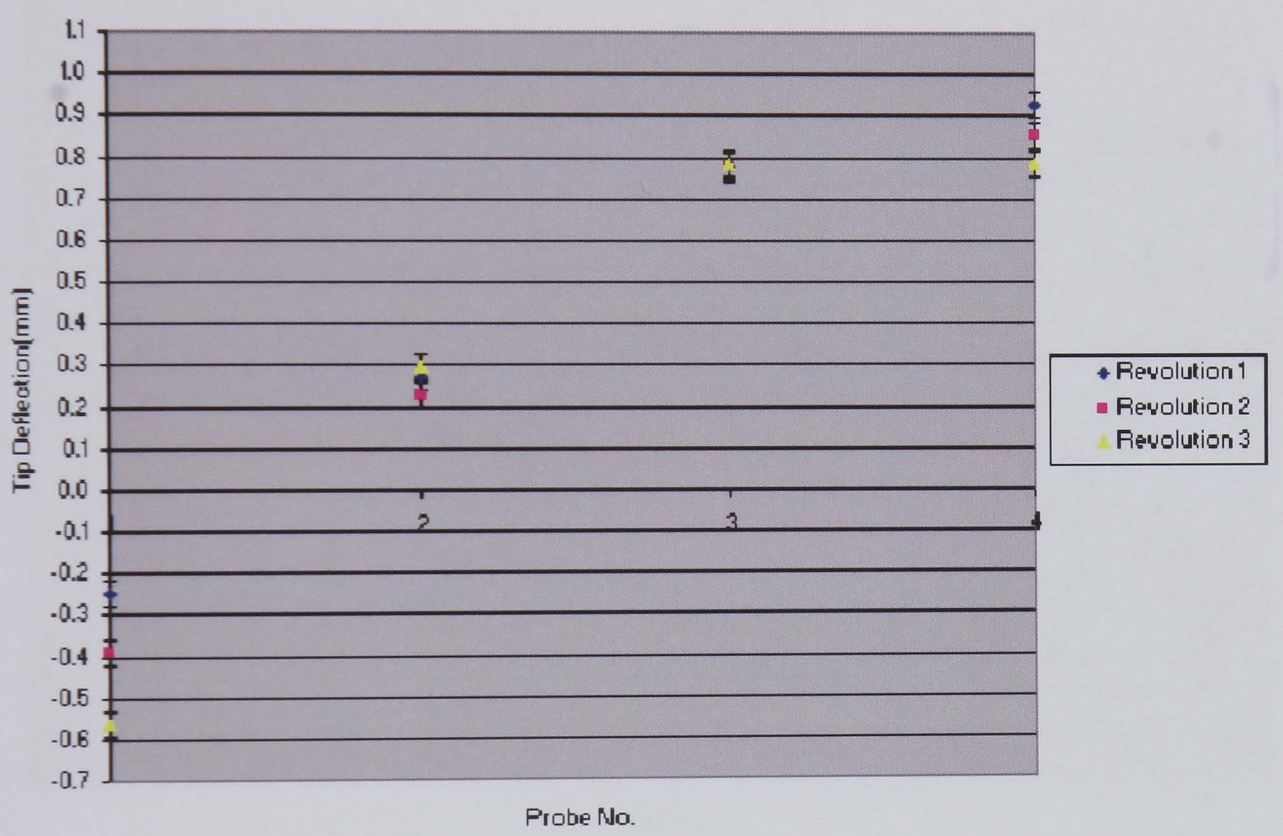

Figure 5.3 Setup 1 at 941RPM (30% PSR) - 2mm Blade Tip Deflection Versus Probe Number

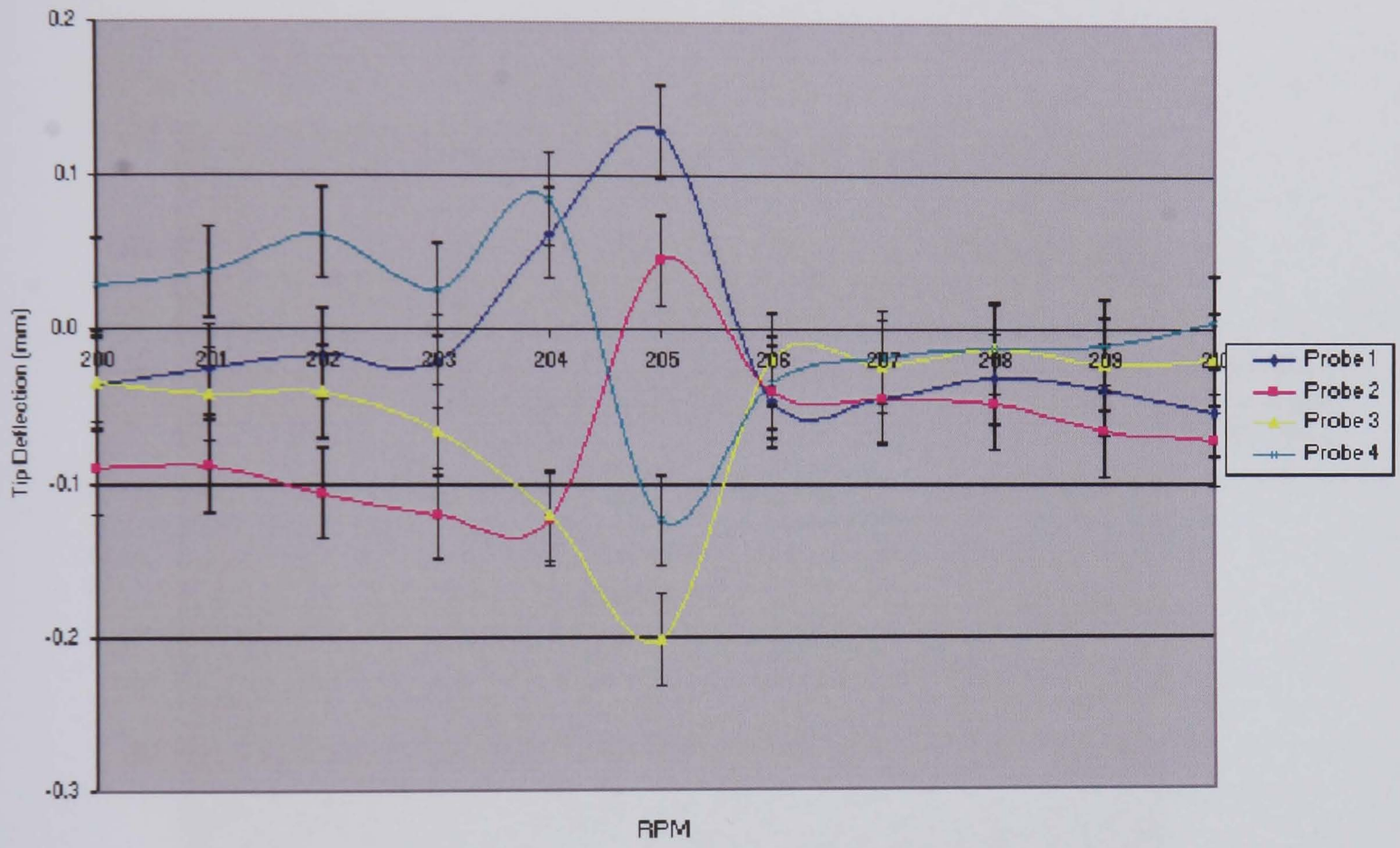

Figure 5.4 Setup 2 at 205RPM - 2mm Blade Tip Deflection Versus RPM

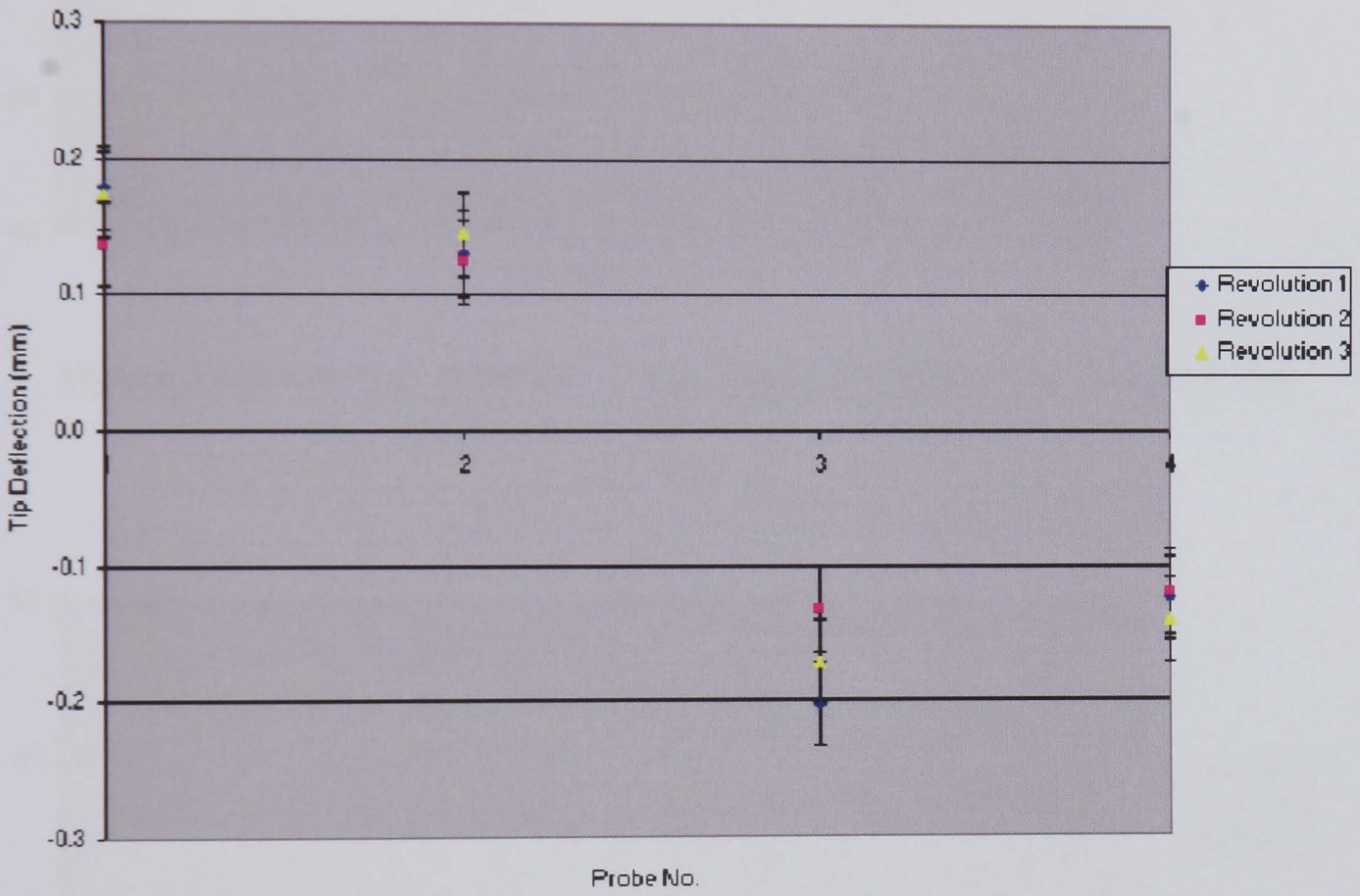

Figure 5.5 Setup 2 at 205RPM (72% PSR) - 2mm Blade Tip Deflection Versus Probe Number

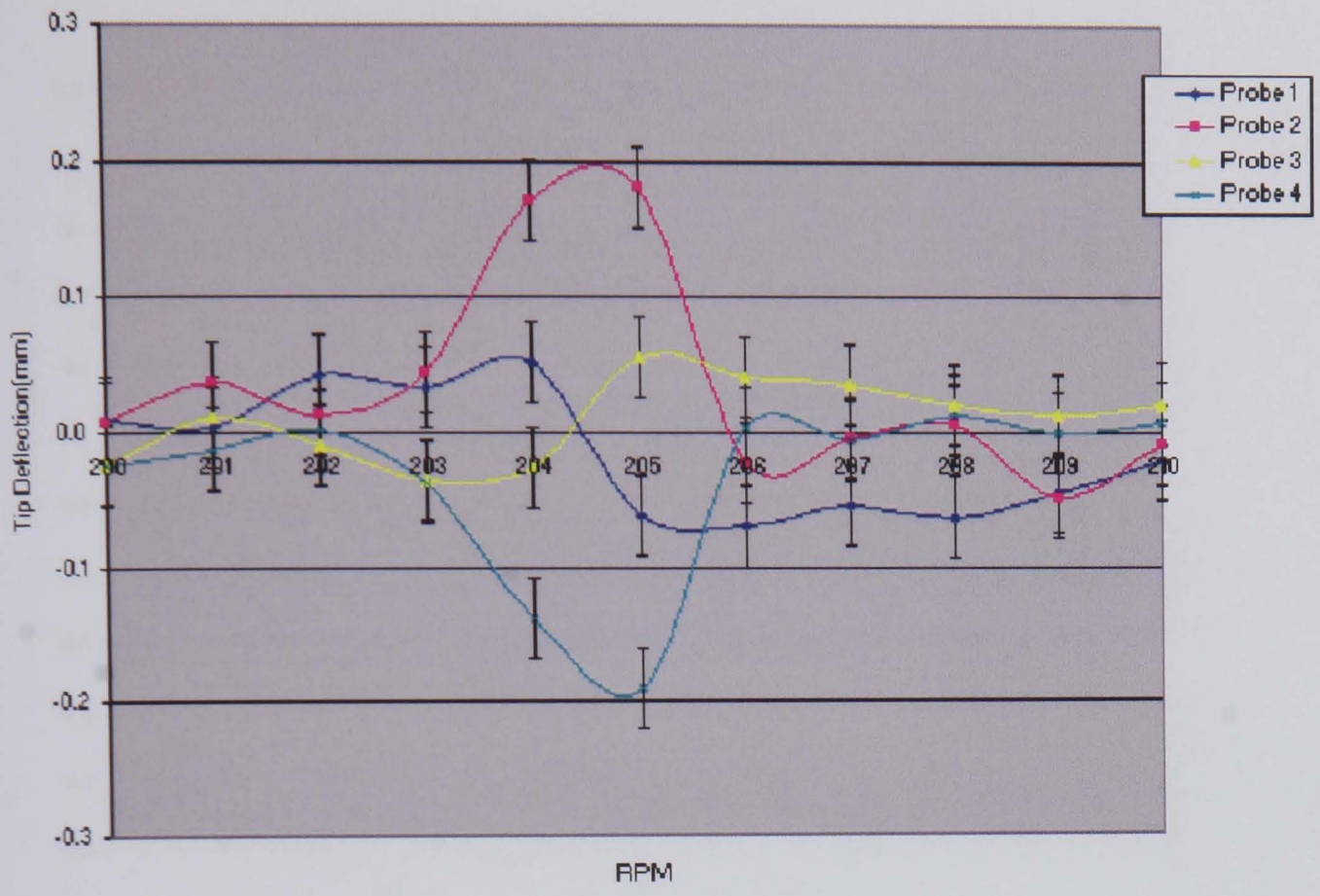

Figure 5.6 Setup 3 at 205RPM - 2mm Blade Tip Deflection Versus RPM

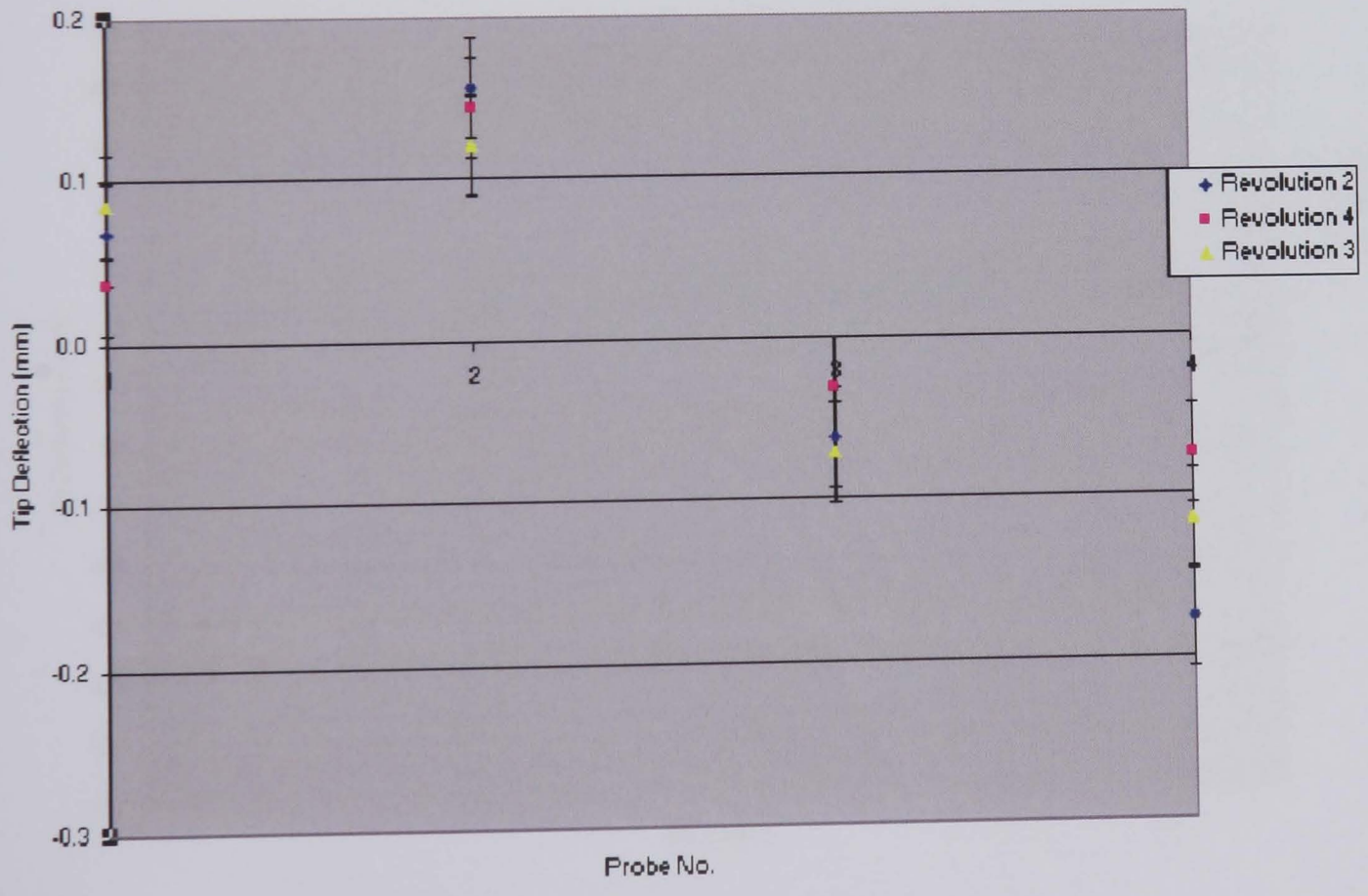

Figure 5.7 Setup 3 at 205RPM (72% PSR) - 2mm Blade Tip Deflection Versus Probe Number

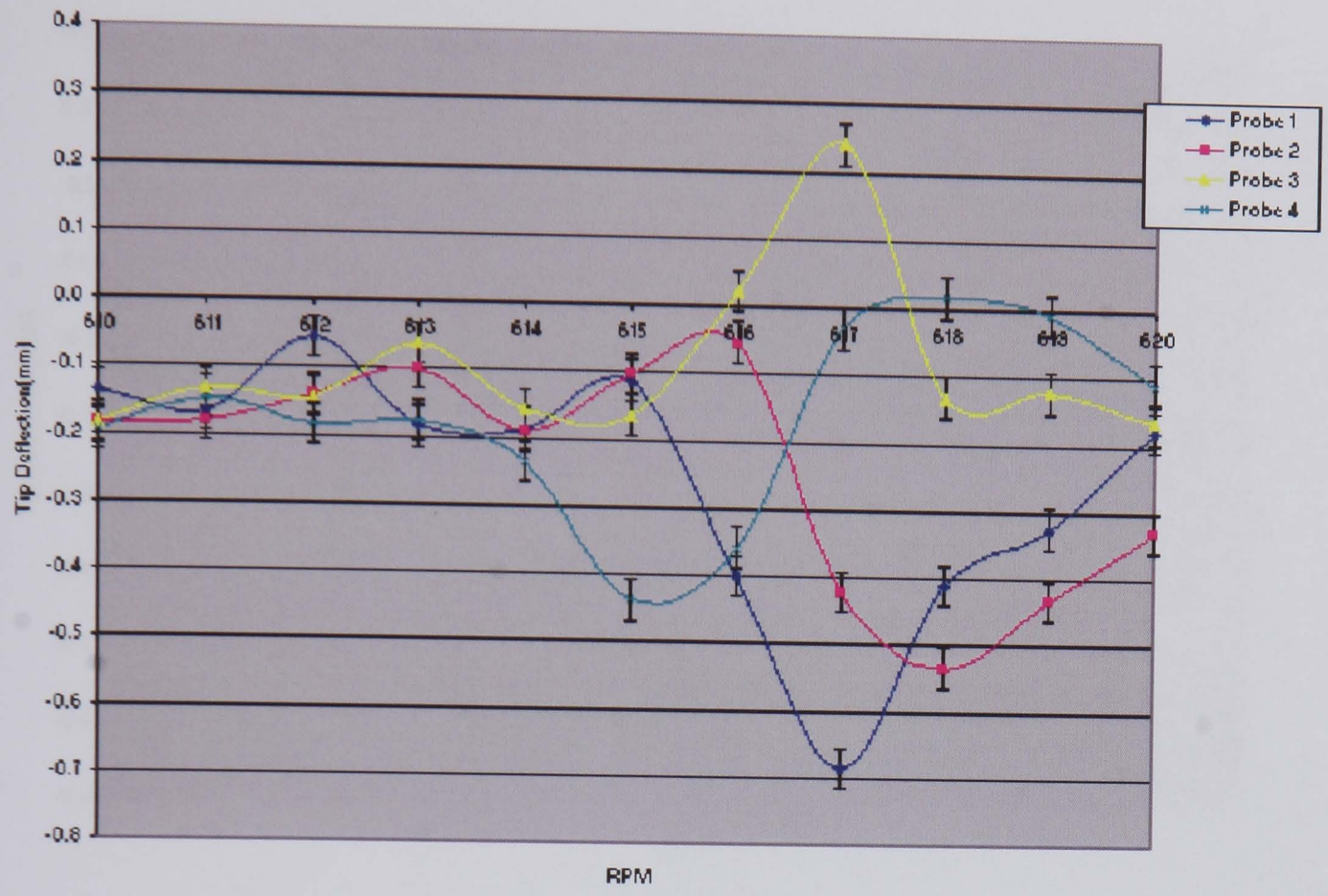

Figure 5.8 Setup 2 at 617RPM - 2mm Blade Tip Deflection Versus RPM

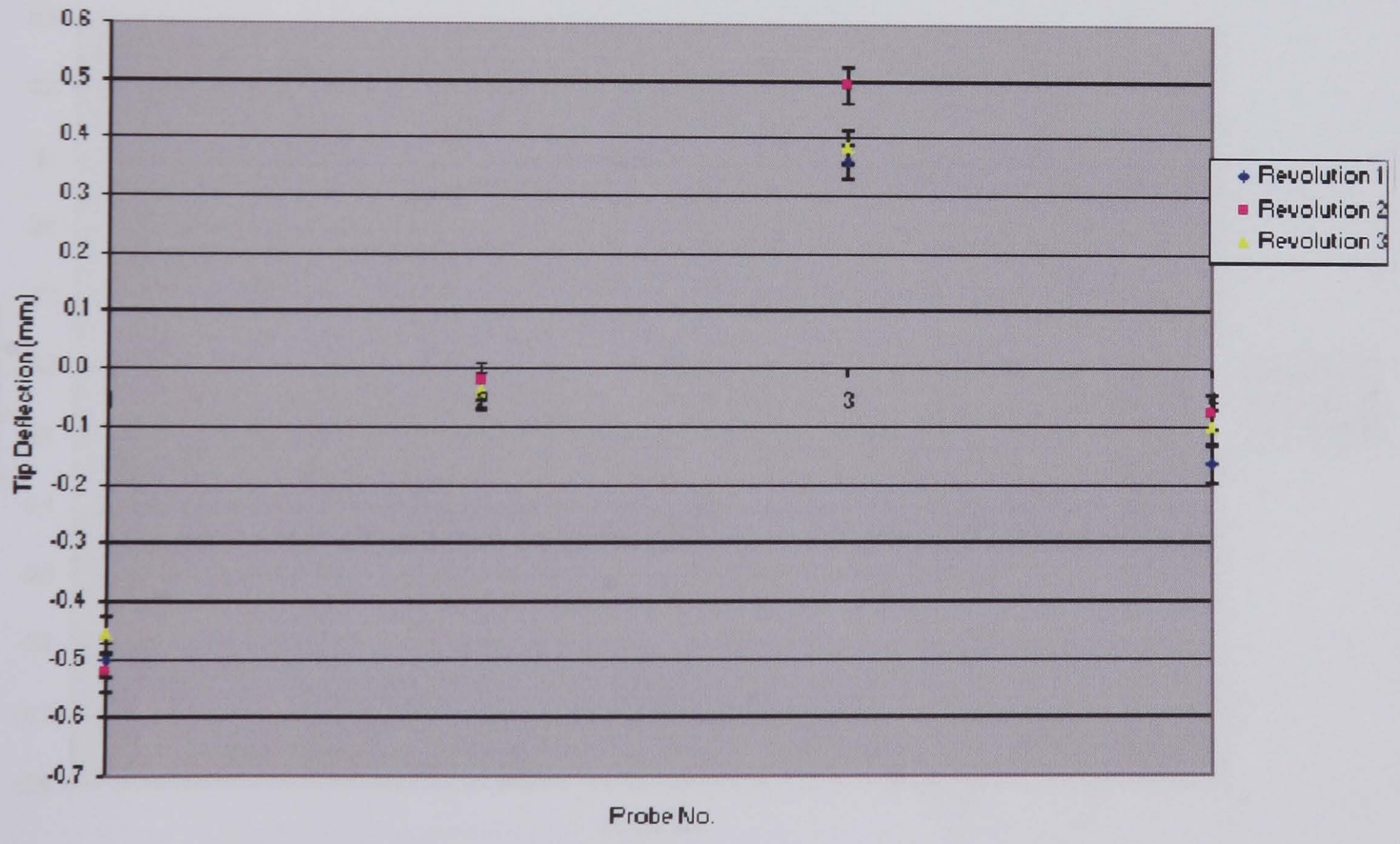

Figure 5.9 Setup 2 at 617RPM (72% PSR) - 2mm Blade Tip Deflection Versus Probe Number

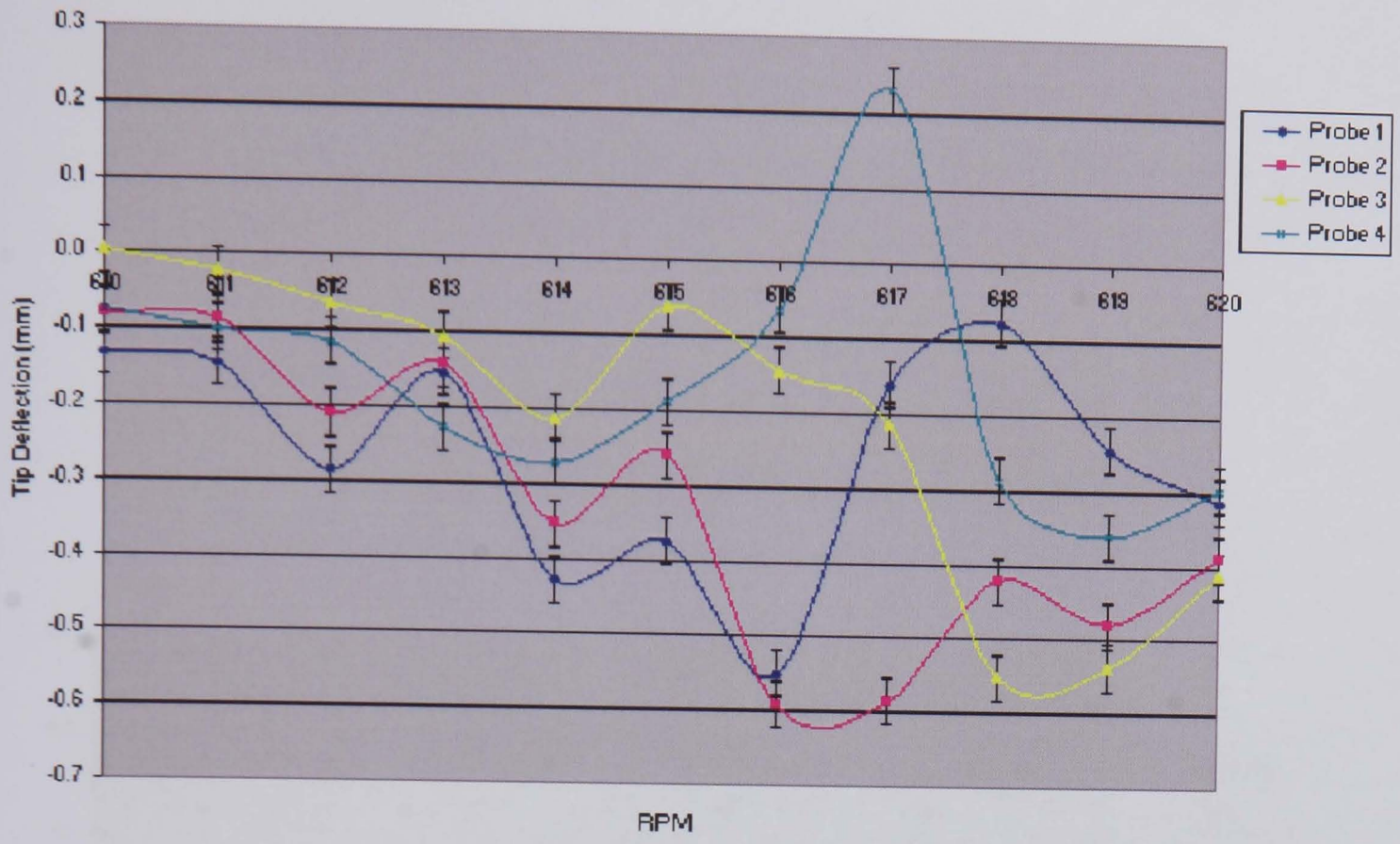

Figure 5.10 Setup 3 at 617RPM - 2mm Blade Tip Deflection Versus RPM

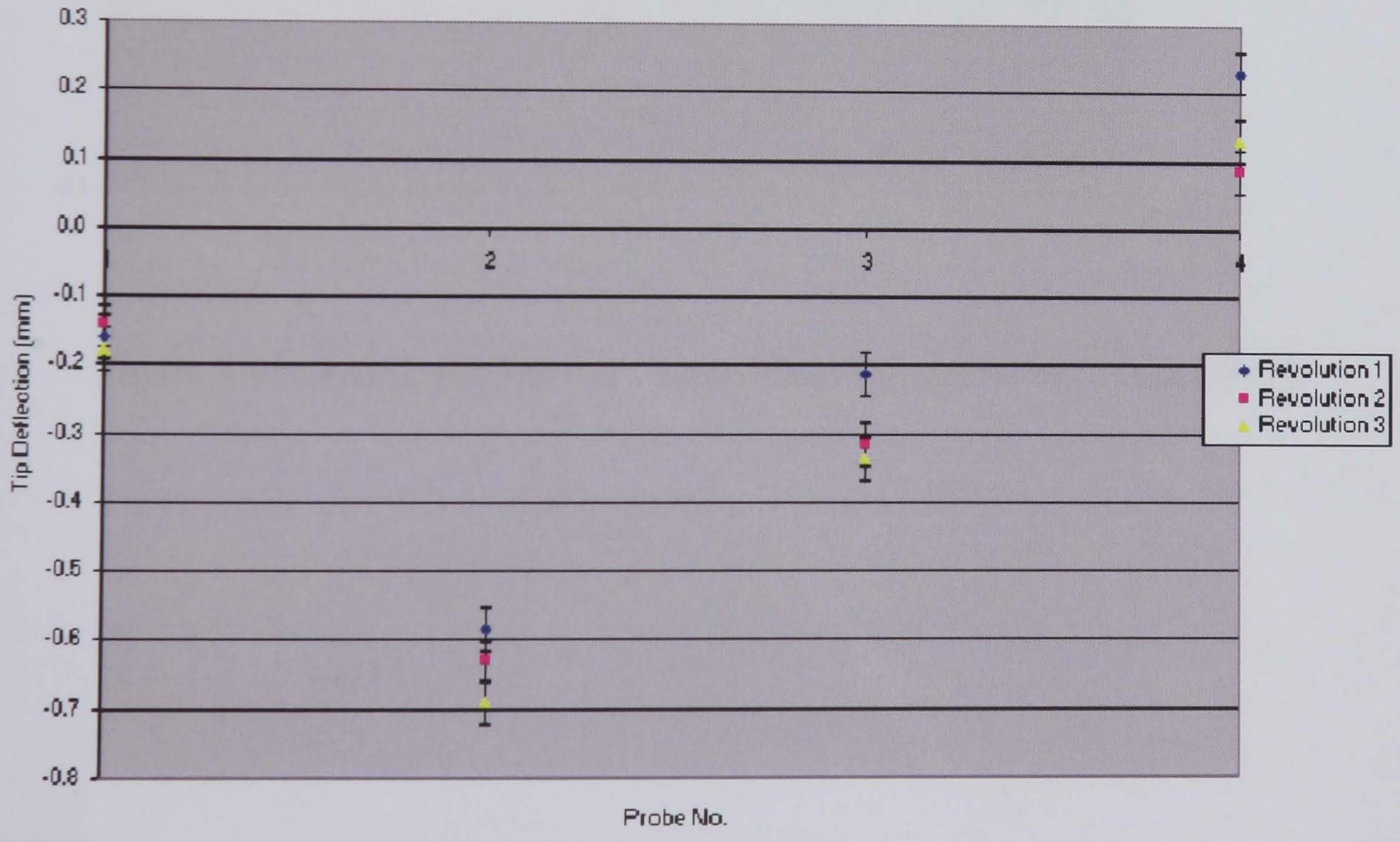

Figure 5.11 Setup 3 at 617RPM (72% PSR) - 2mm Blade Tip Deflection Versus Probe Number

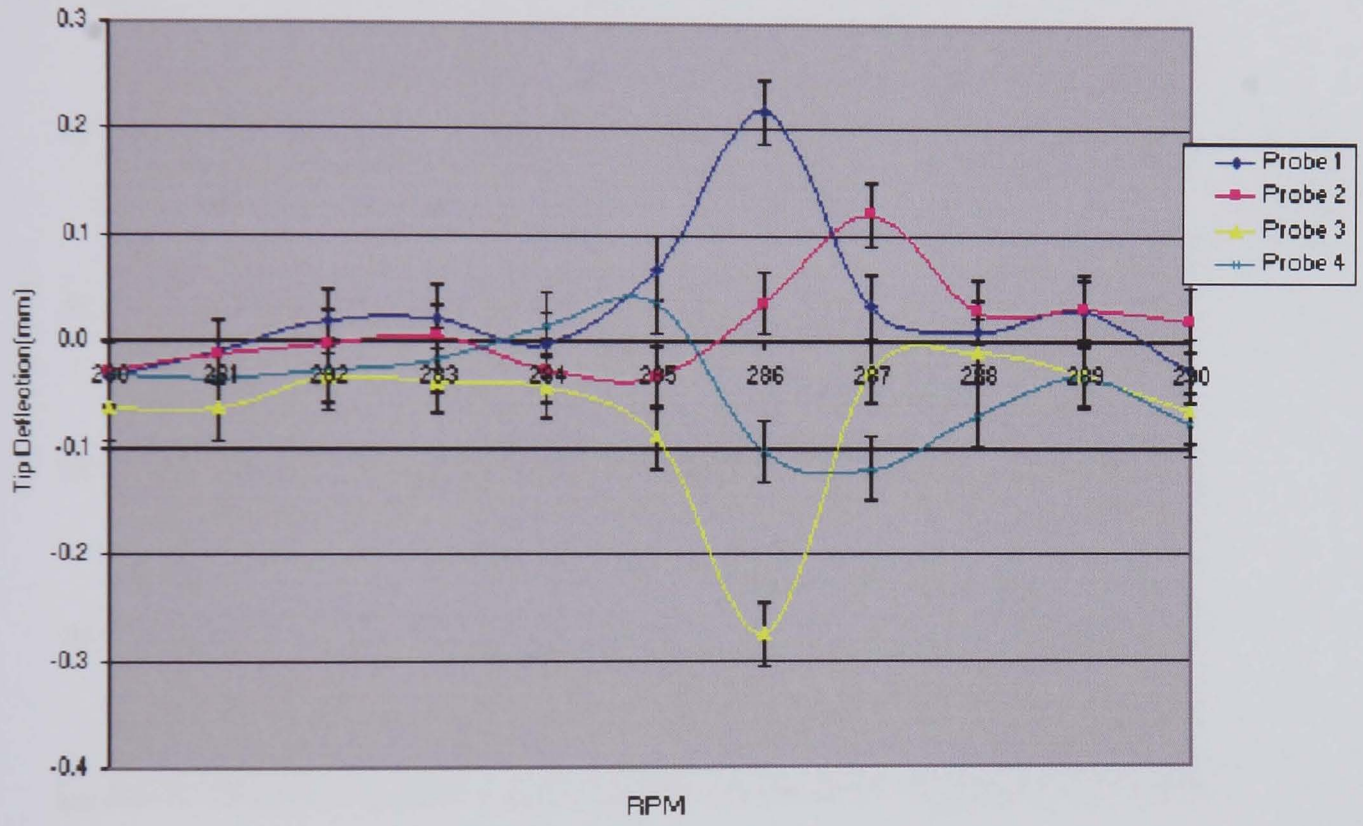

Figure 5.12 Setup 2 at 286RPM - 3mm Blade Tip Deflection Versus RPM

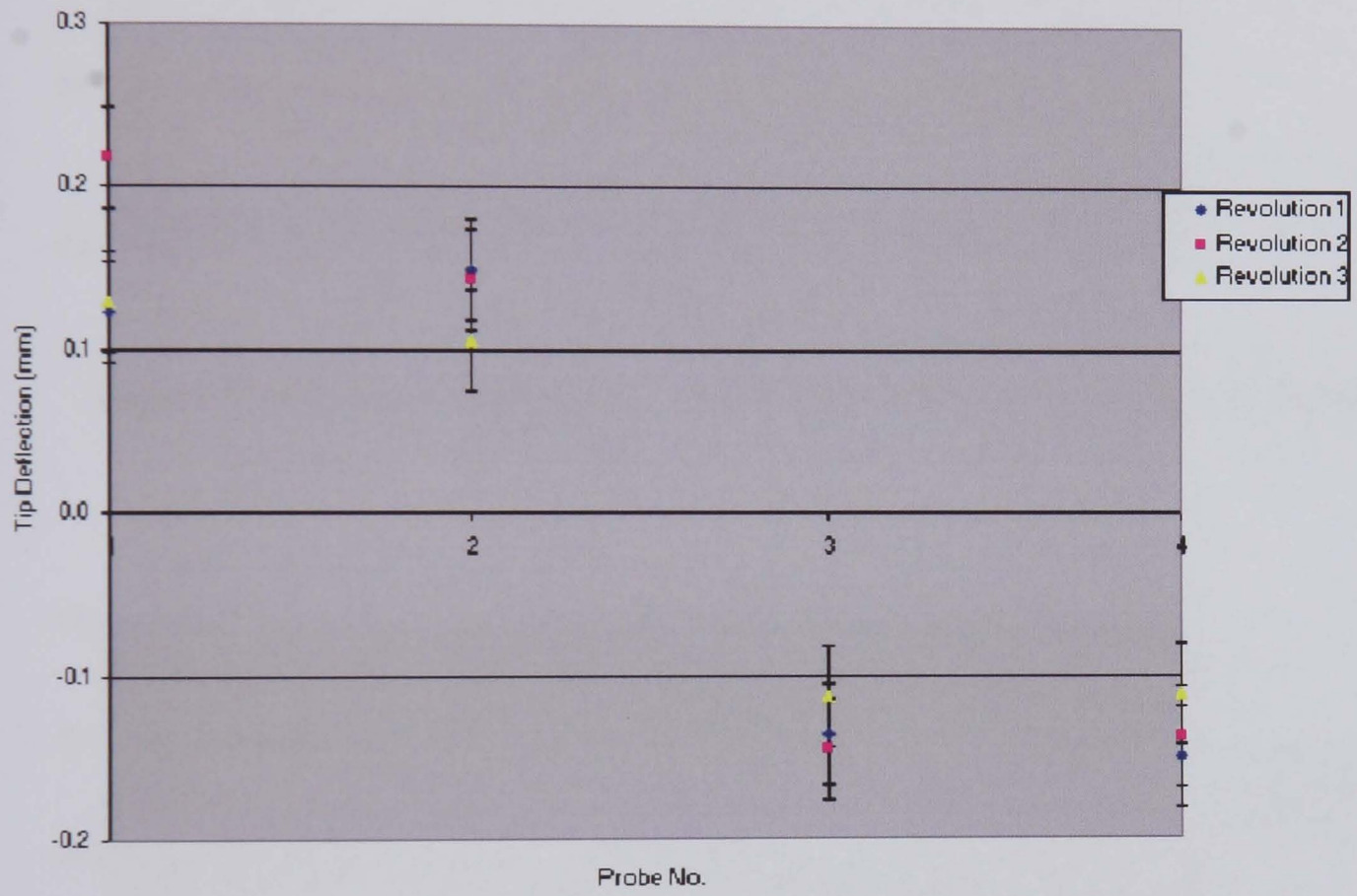

Figure 5.13 Setup 2 at 286RPM (72% PSR) - 3mm Blade Tip Deflection Versus Probe Number

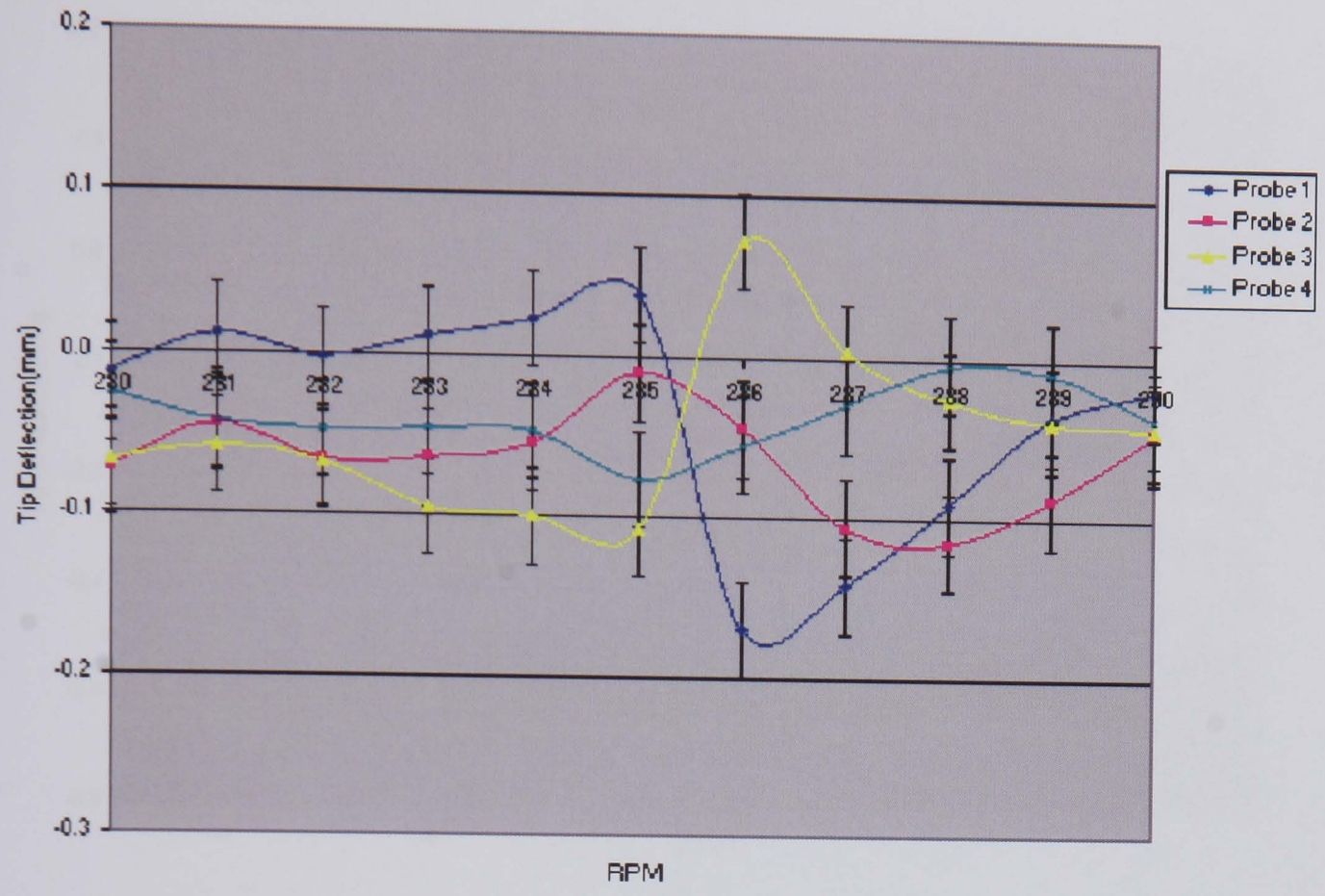

Figure 5.14 Setup 3 at 286RPM - 3mm Blade Tip Deflection Versus RPM

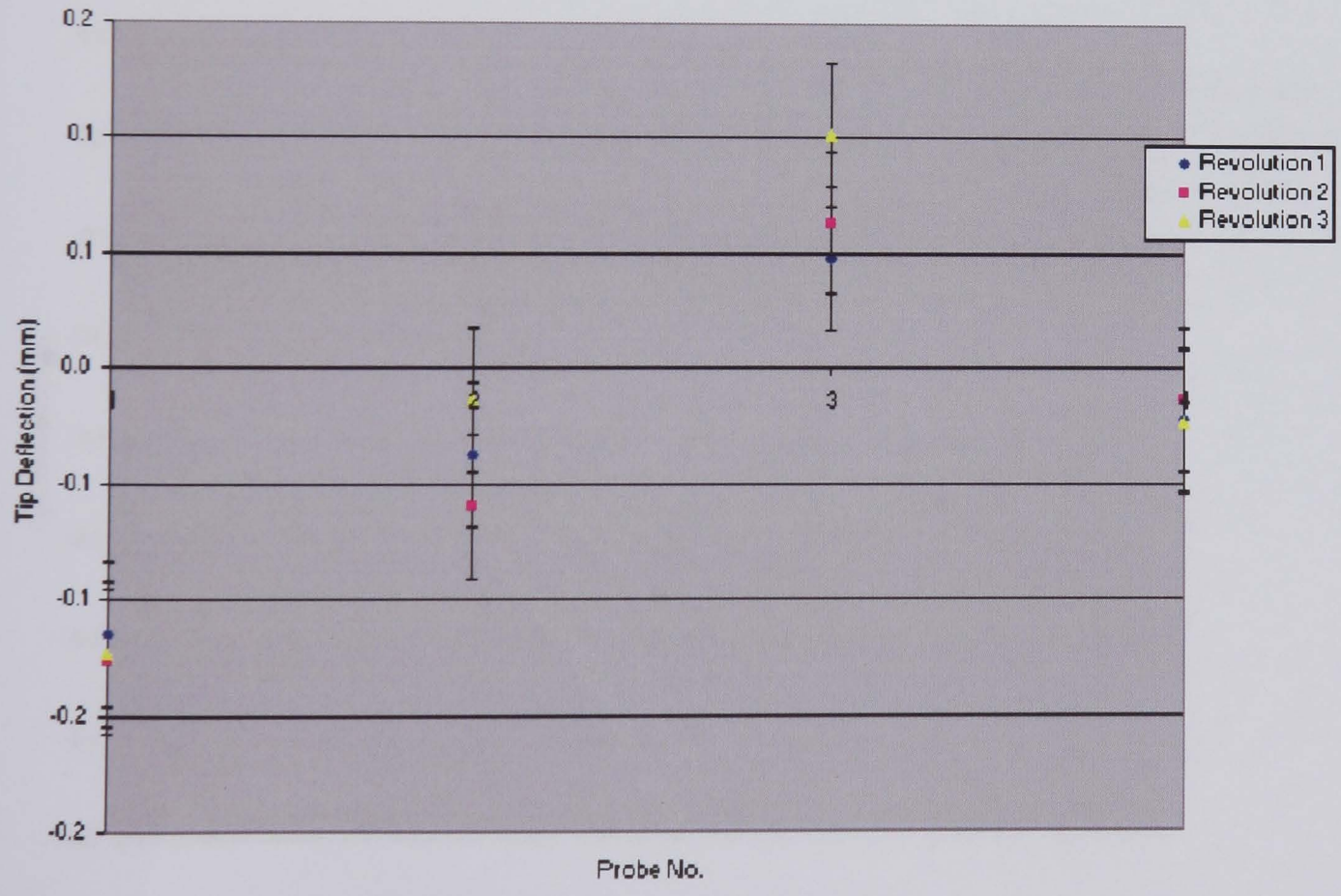

Figure 5.15 Setup 3 at 286RPM (72% PSR) - 3mm Blade Tip Deflection Versus Probe Number

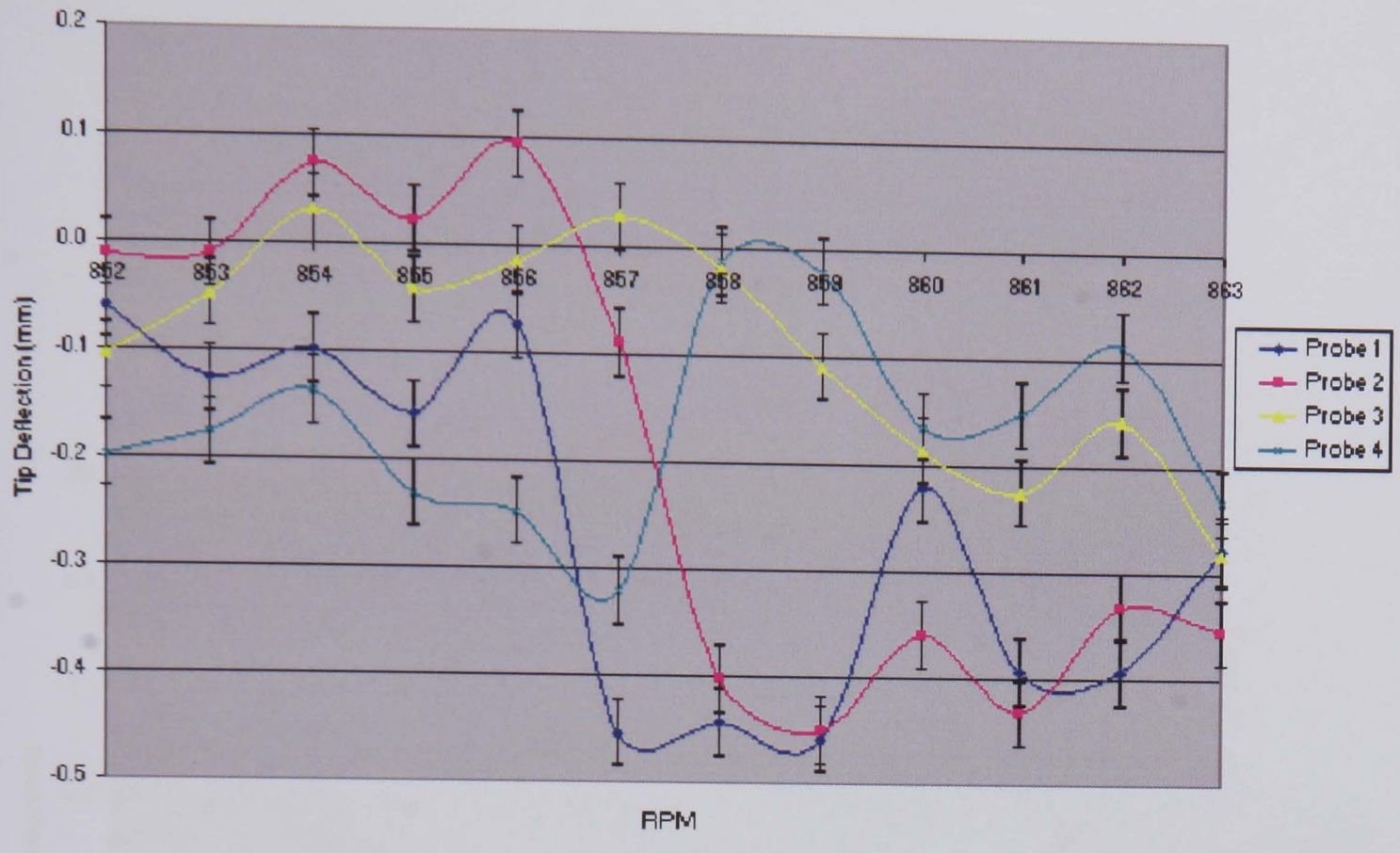

Figure 5.16 Setup 2 at 857RPM - 3mm Blade Tip Deflection Versus RPM

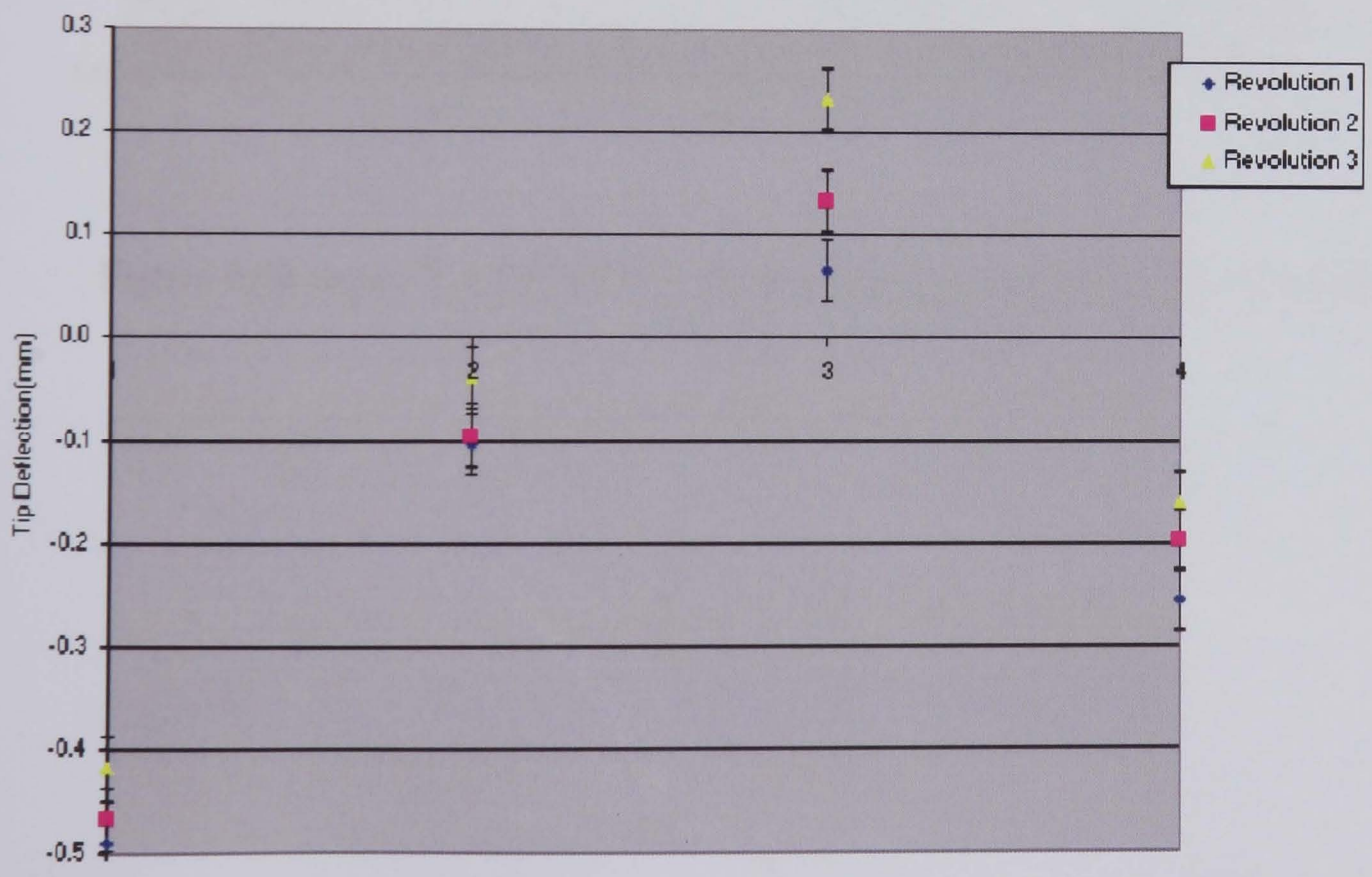

Figure 5.17 Setup 2 at 857RPM (72% PSR) - 3mm Blade Tip Deflection Versus Probe Number

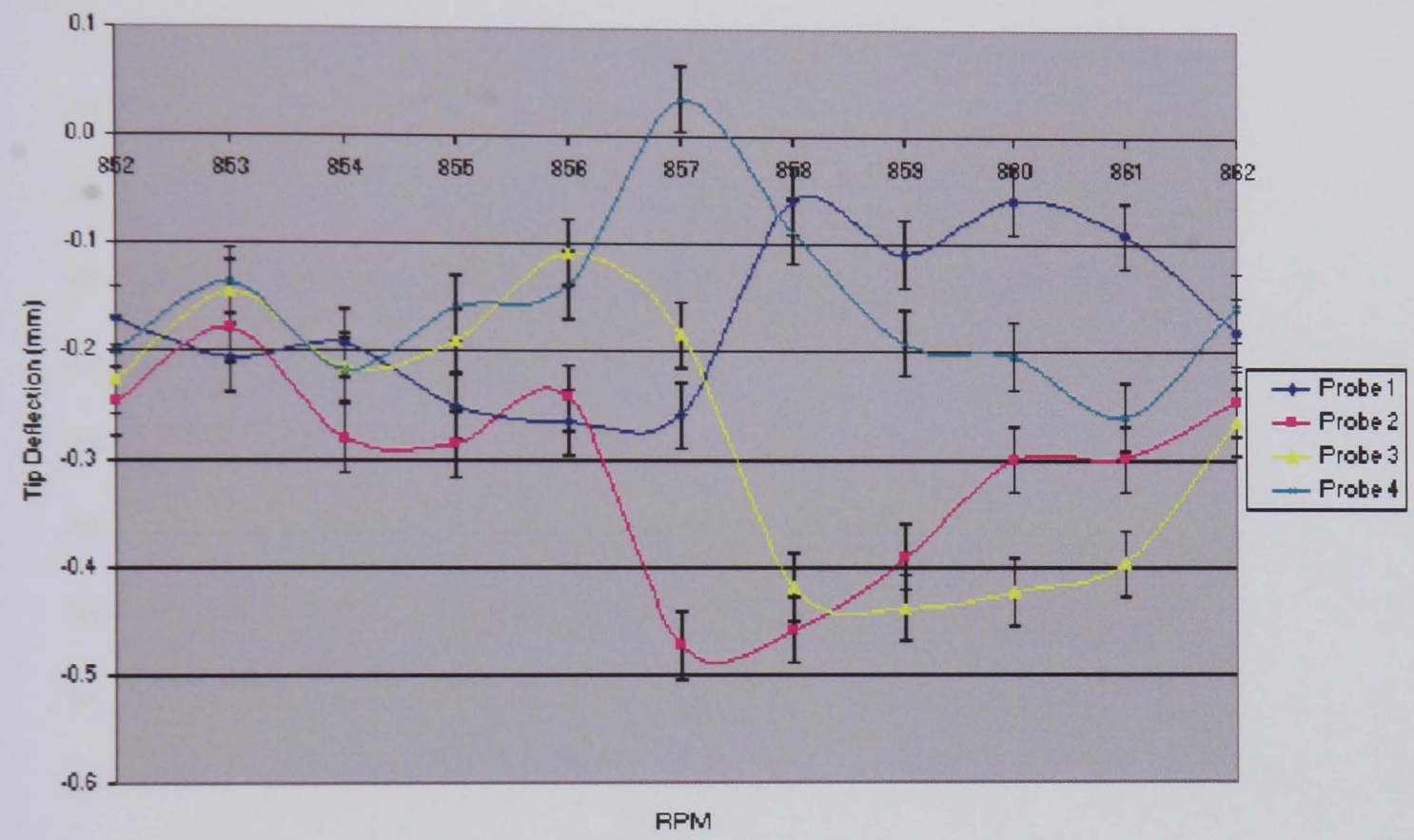

Figure 5.18 Setup 3 at 857RPM - 3mm Blade Tip Deflection Versus RPM

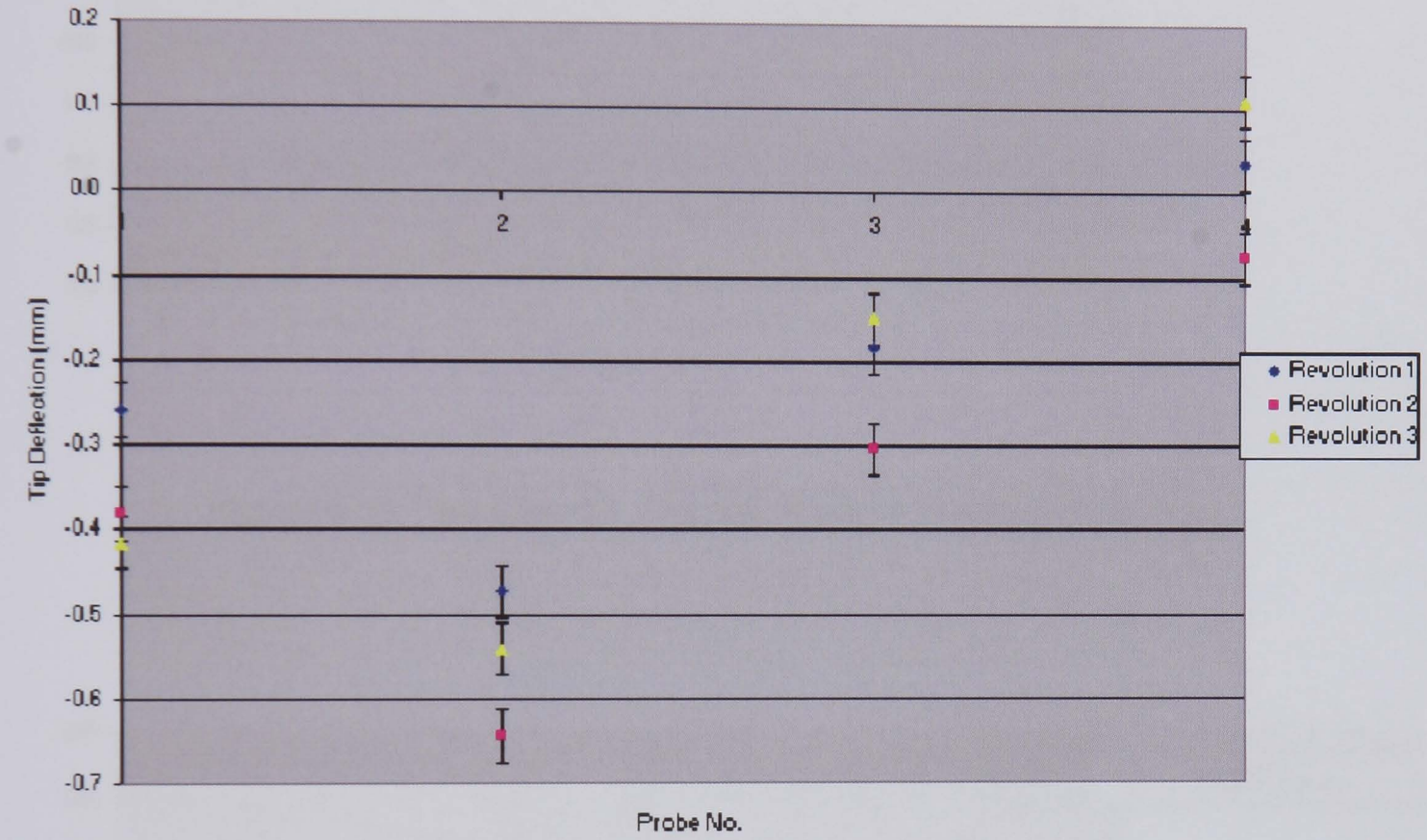

Figure 5.19 Setup 3 at 857RPM (72% PSR) - 3mm Blade Tip Deflection Versus Probe Number

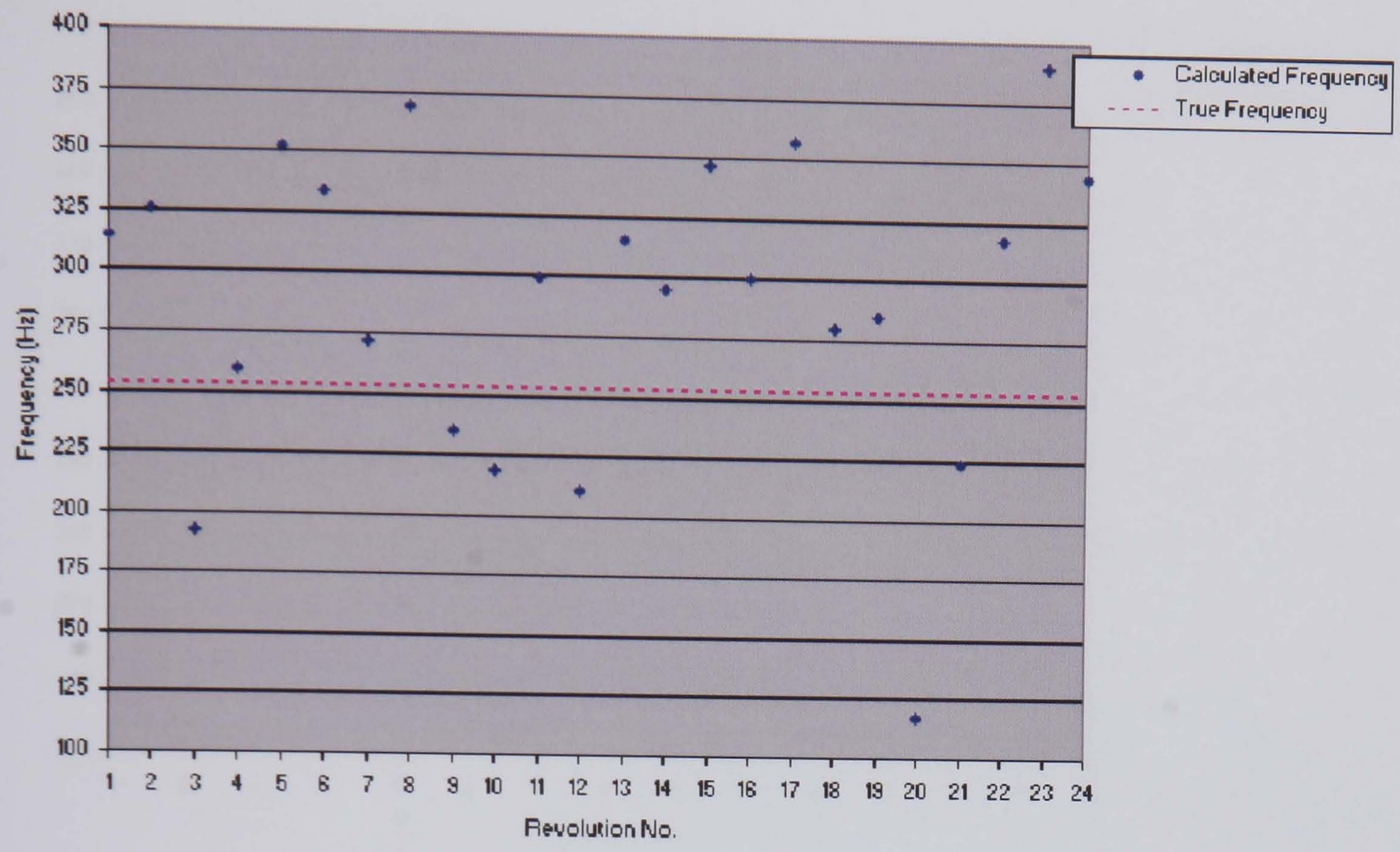

Figure 5.20 Test Case 1 - The AR Method Frequency Results

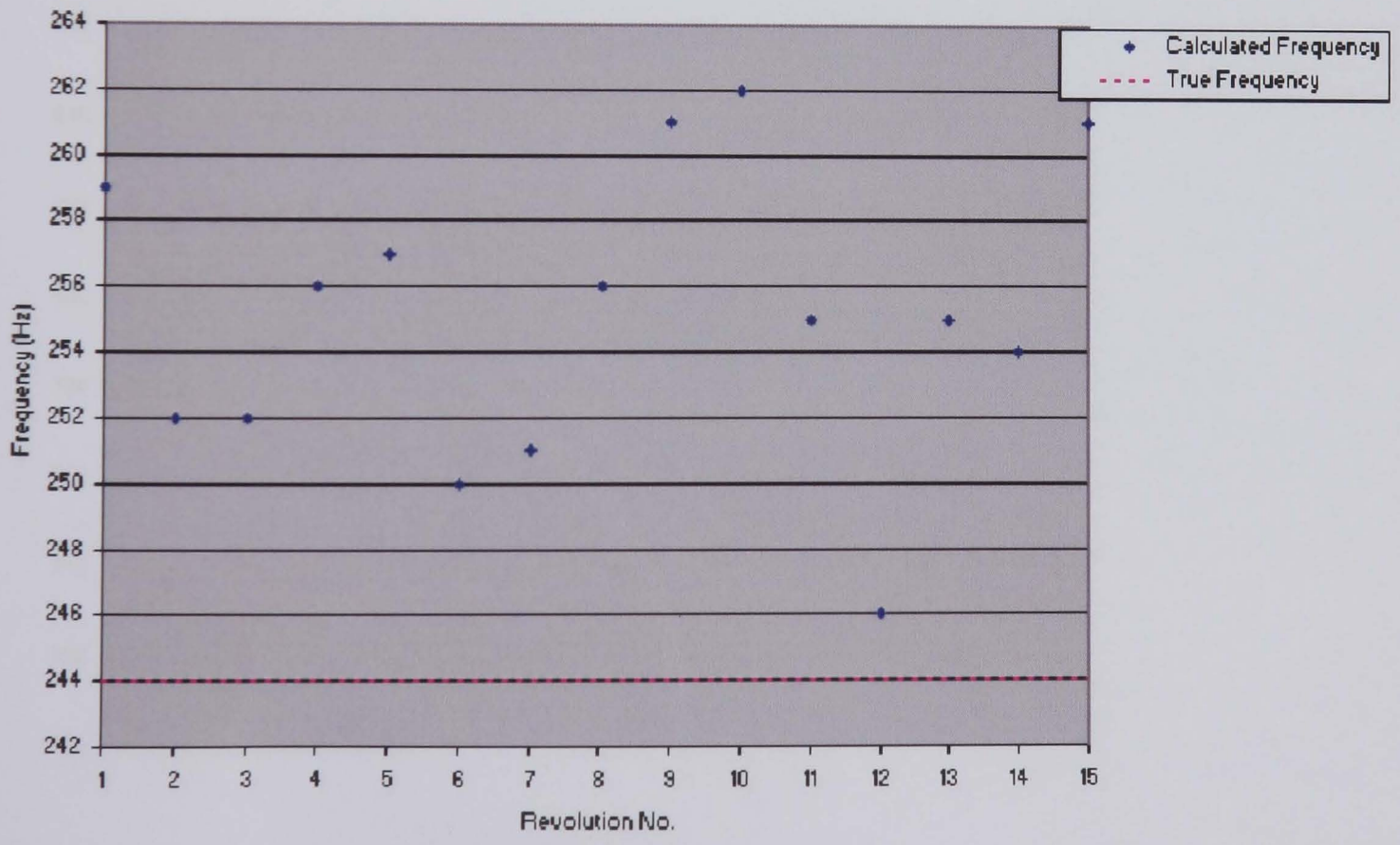

Figure 5.21 Test Case 2 - The AR Method Frequency Results

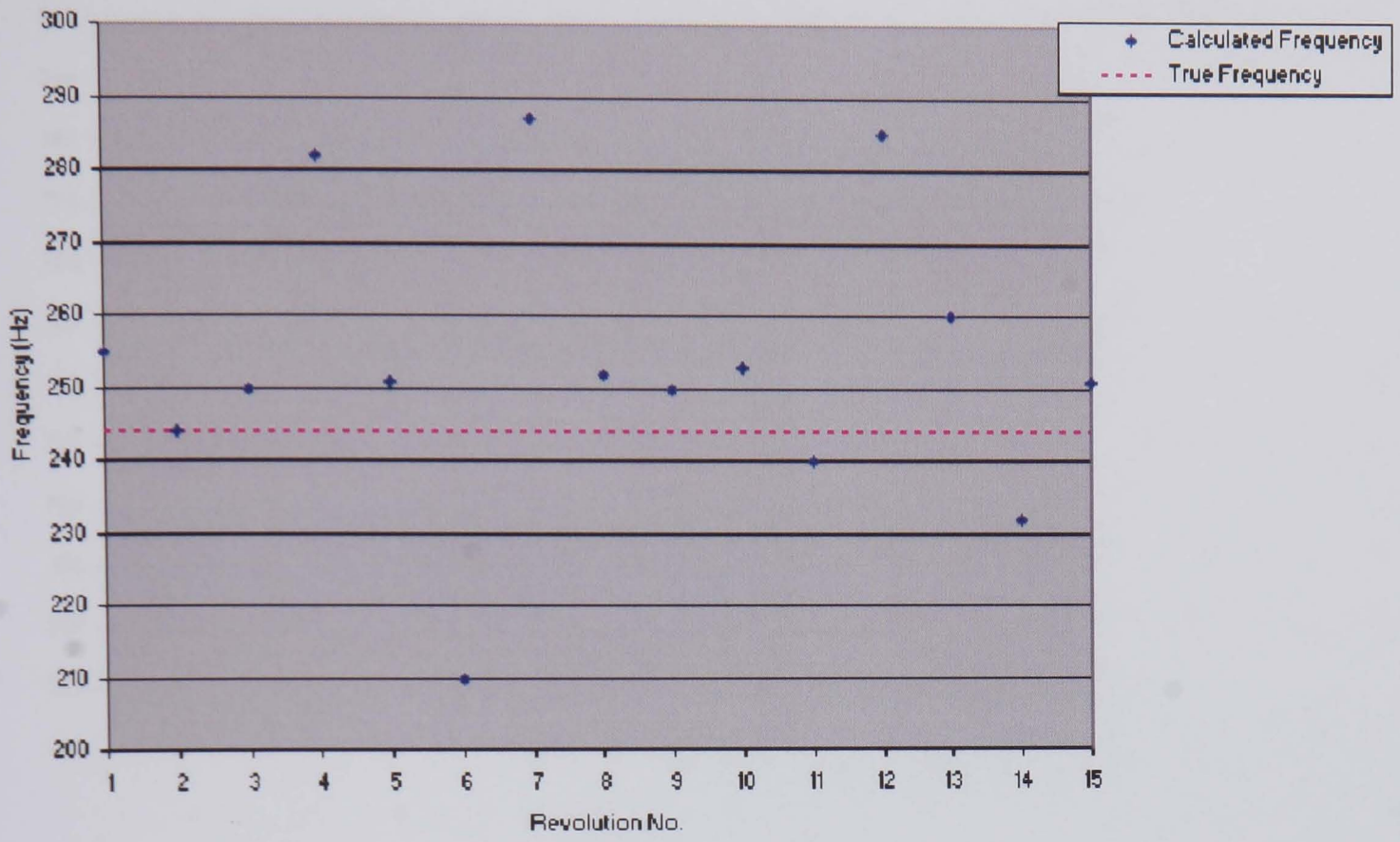

Figure 5.22 Test Case 3 - The AR Method Frequency Results

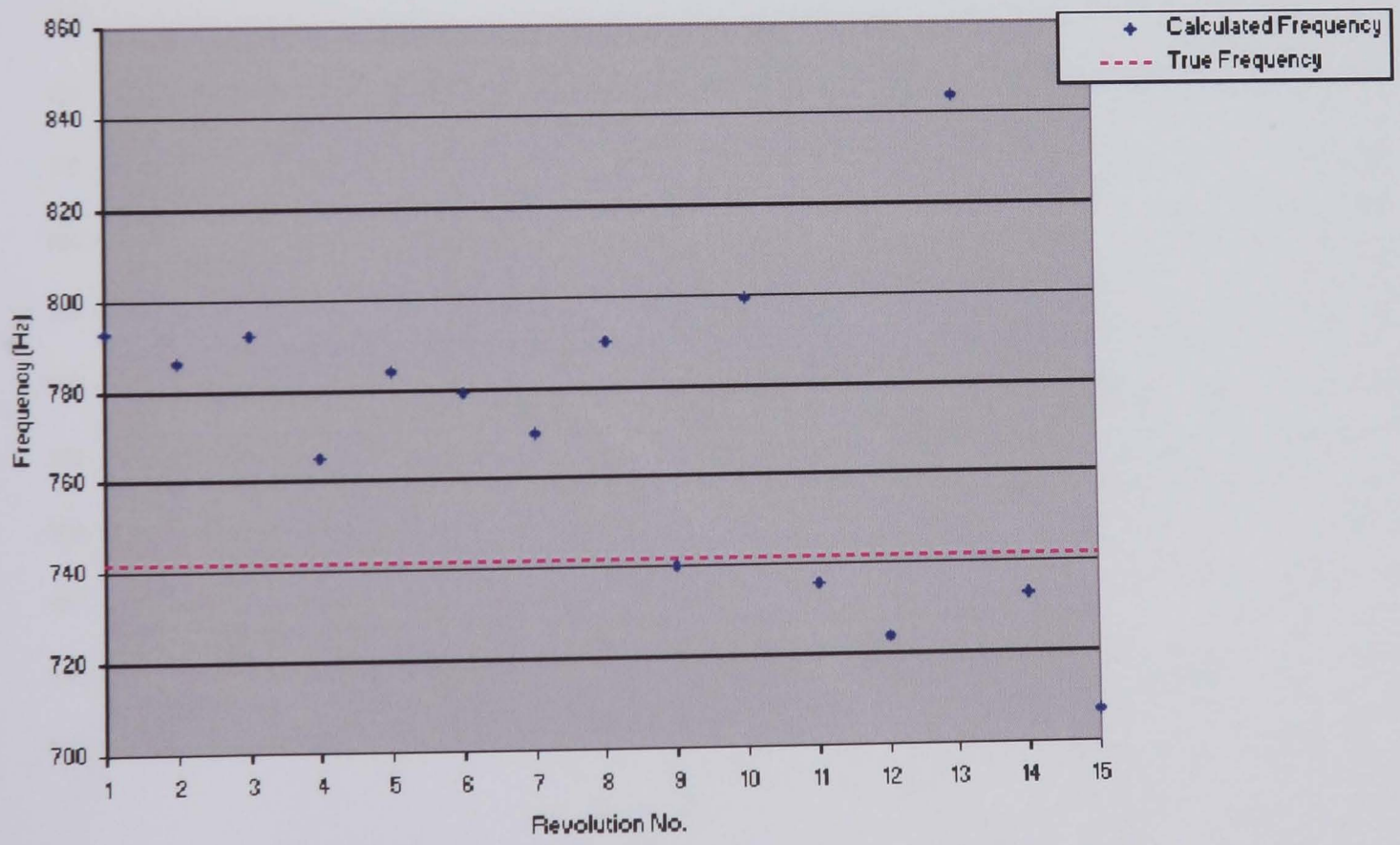

Figure 5.23 Test Case 4 - The AR Method Frequency Results

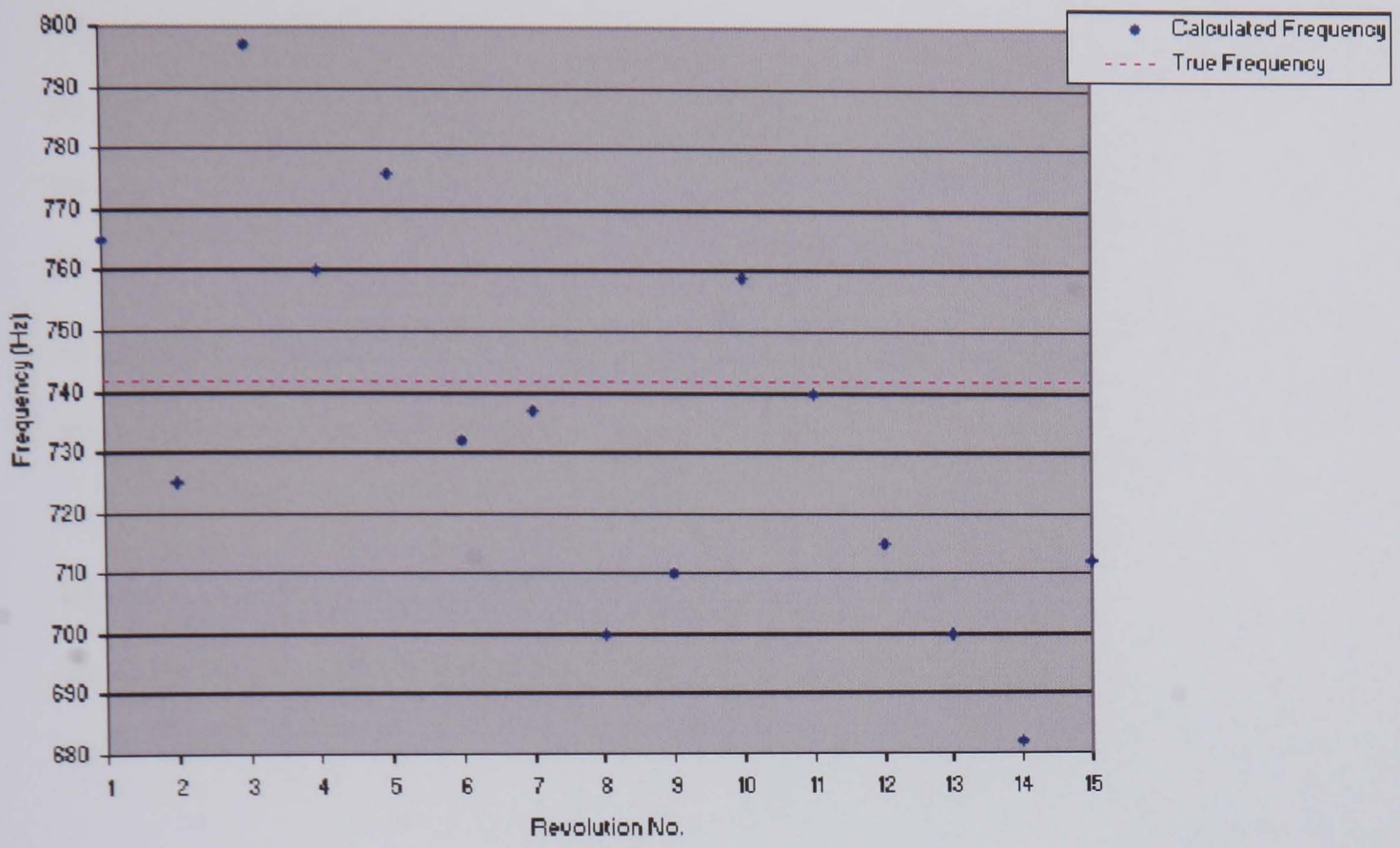

Figure 5.24 Test Case 5 - The AR Method Frequency Results

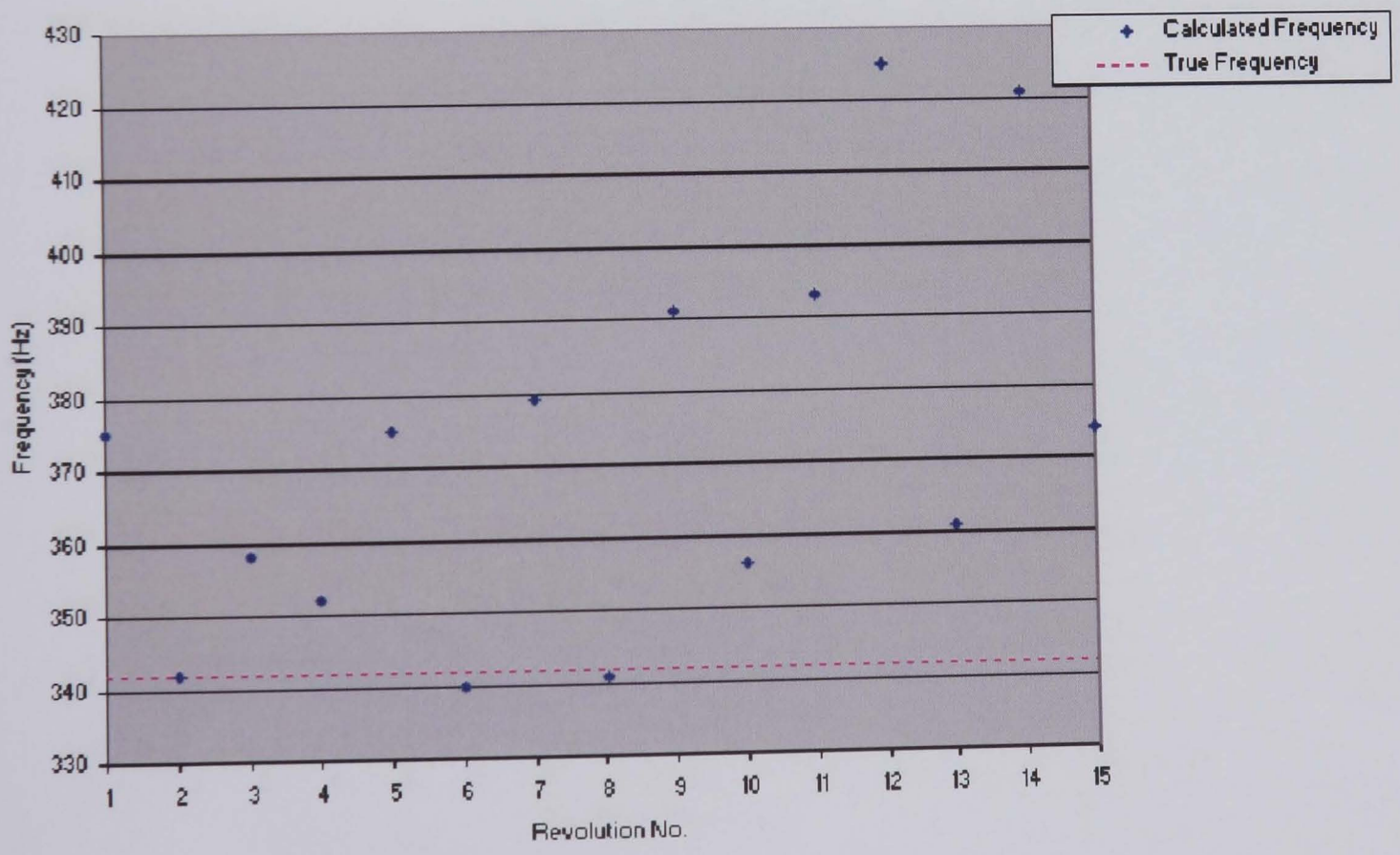

Figure 5.25 Test Case 6 - The AR Method Frequency Results

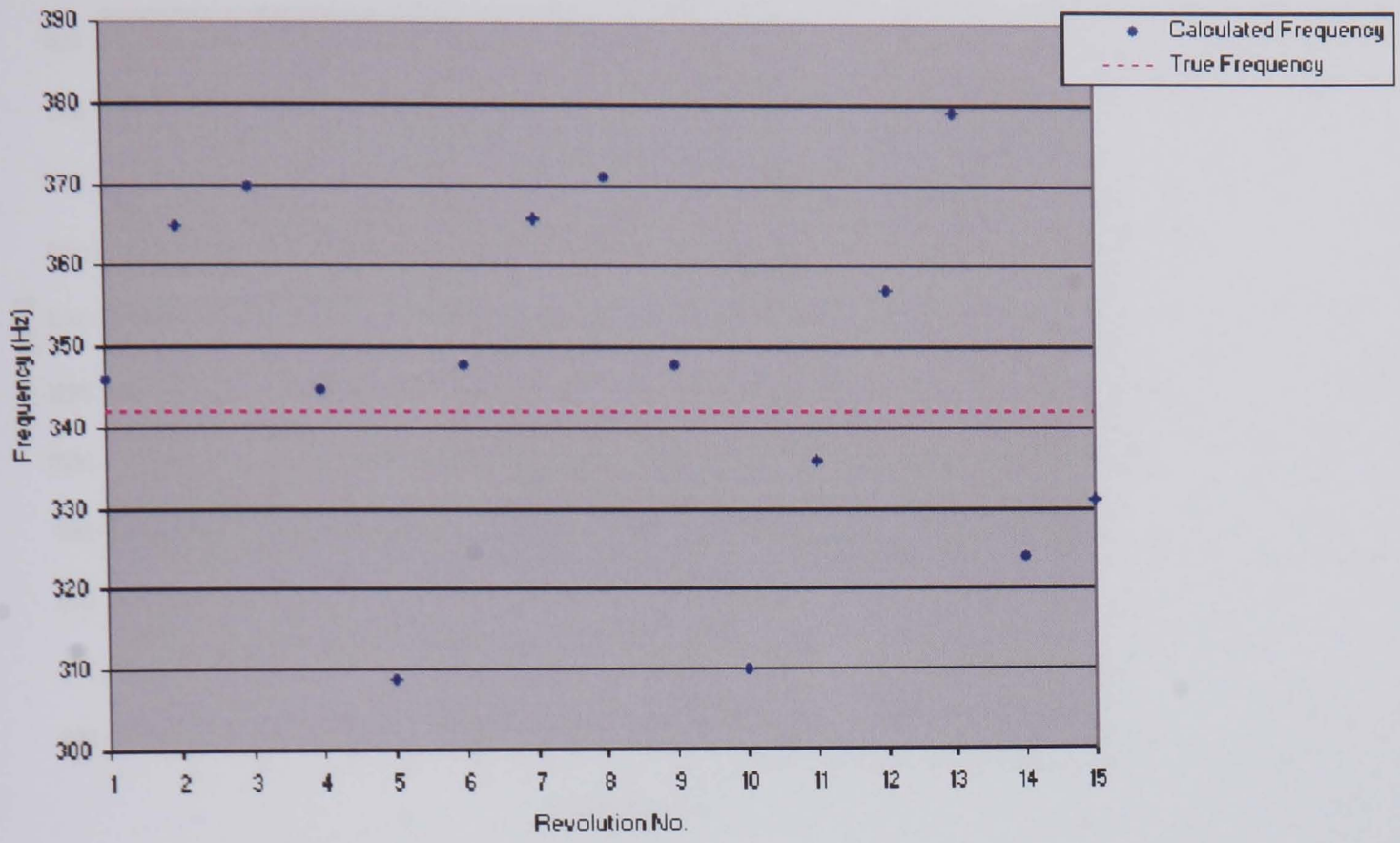

Figure 5.26 Test Case 7 - The AR Method Frequency Results

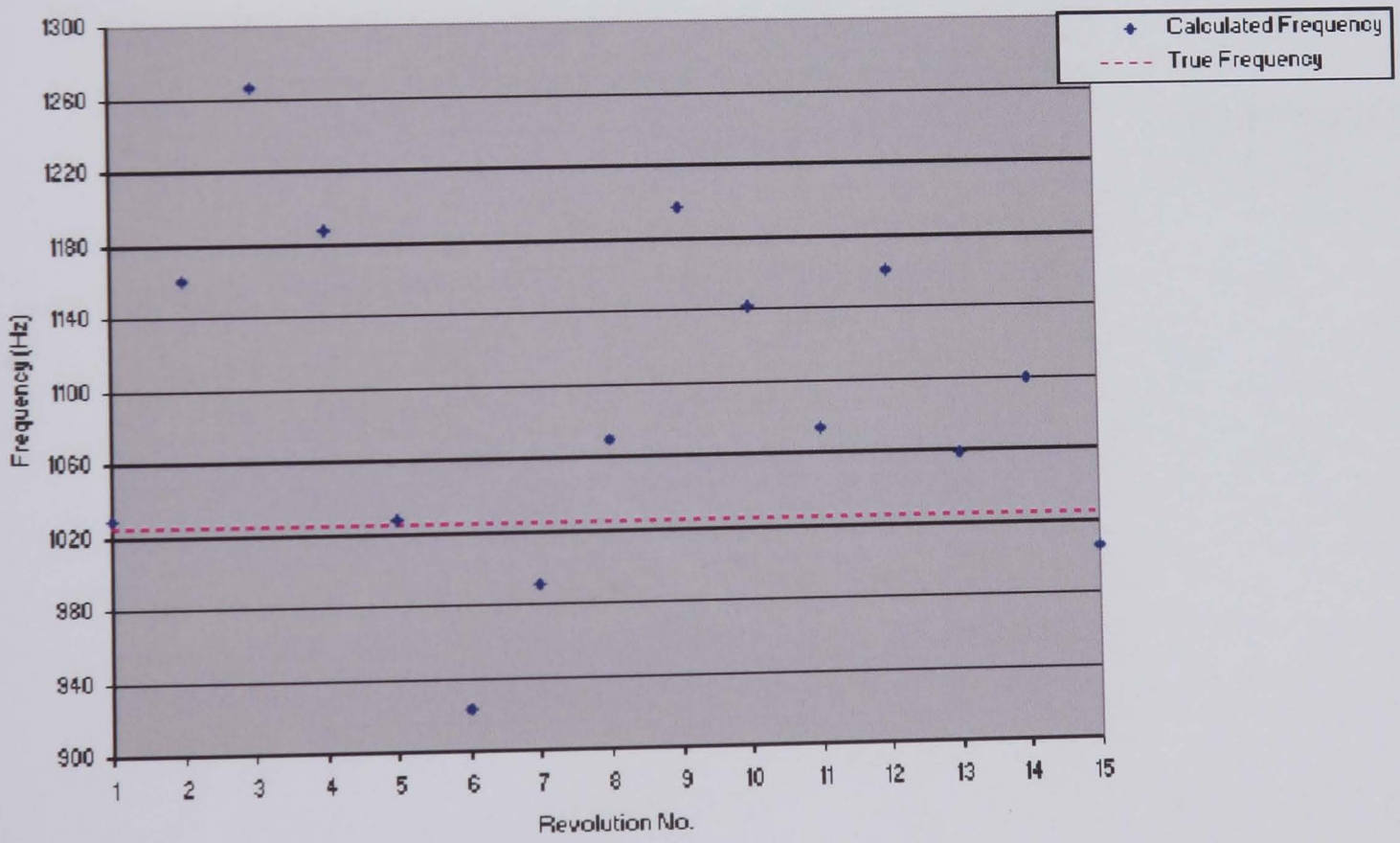

Figure 5.27 Test Case 8 - The AR Method Frequency Results

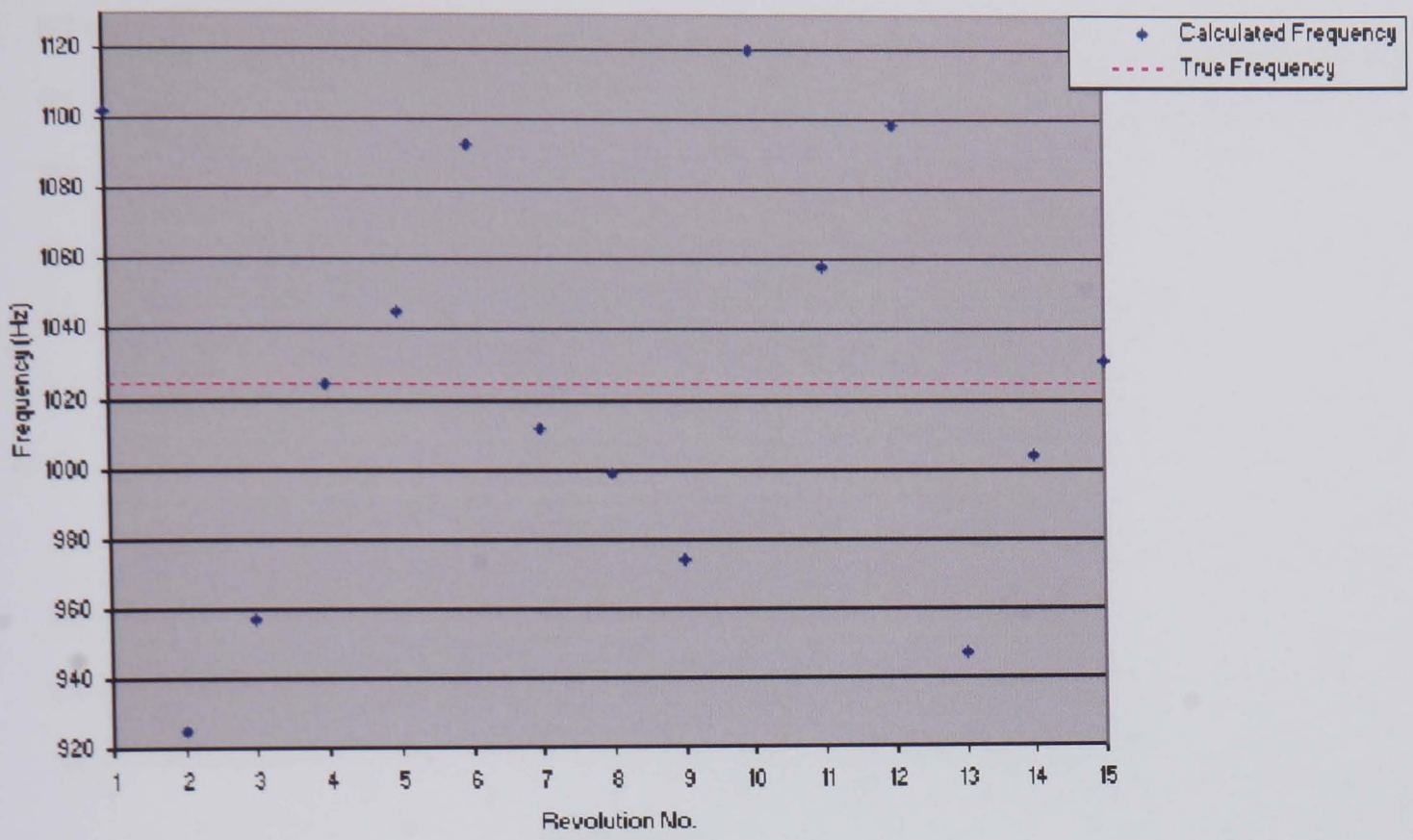

Figure 5.28 Test Case 9 - The AR Method Frequency Results

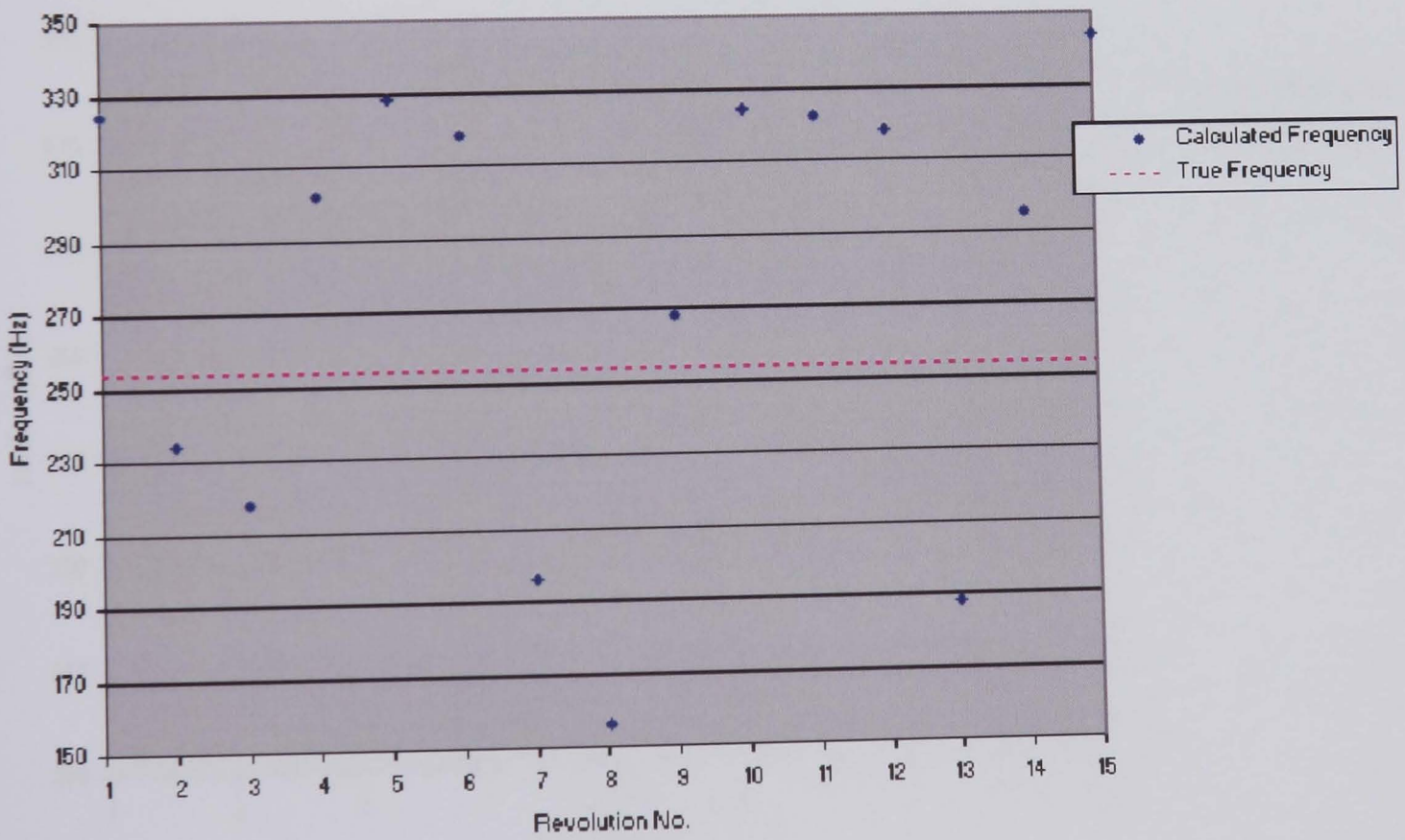

Figure 5.29 Test Case 1 - The ARIV Method Frequency Results

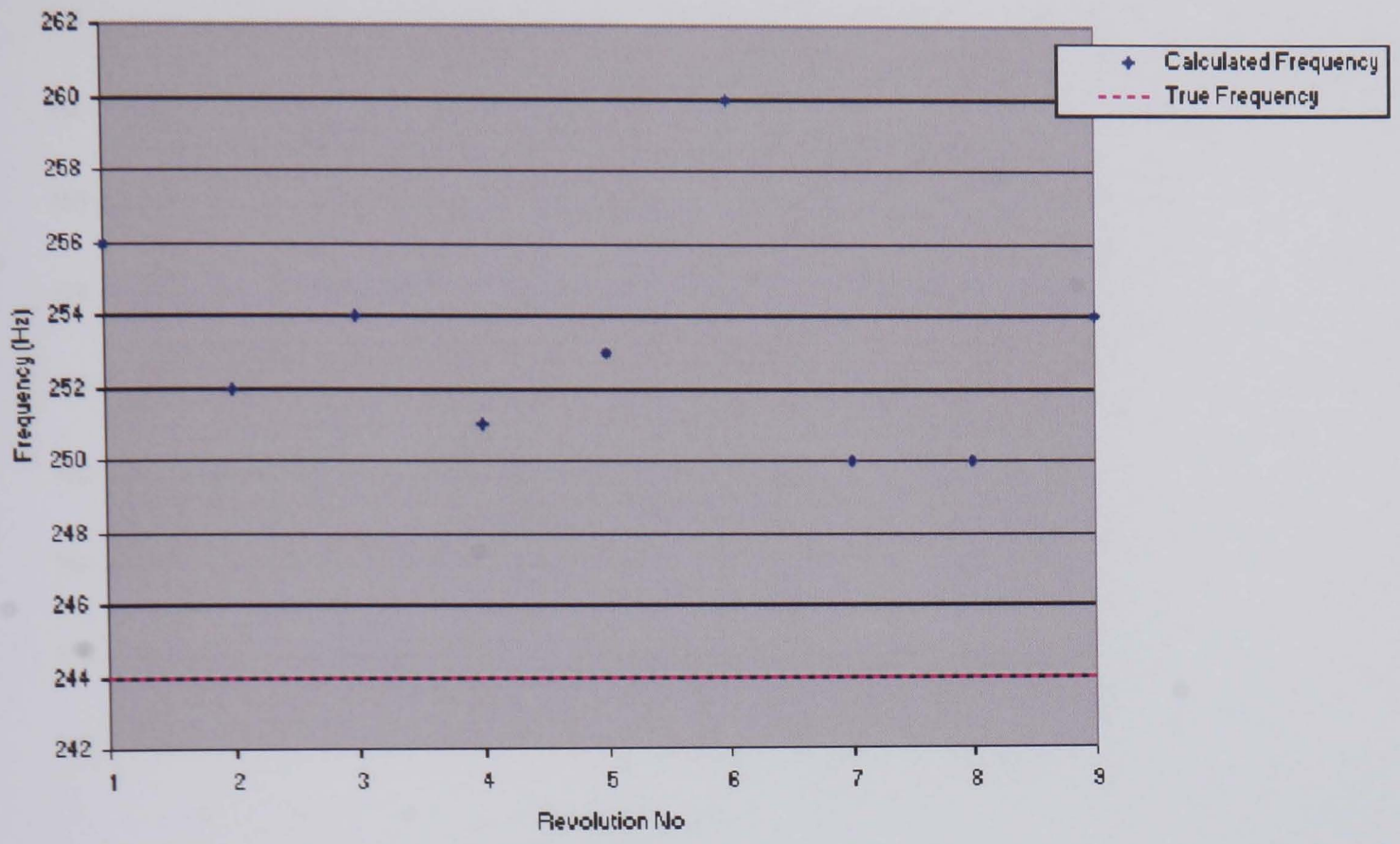

Figure 5.30 Test Case 2 - The ARIV Method Frequency Results

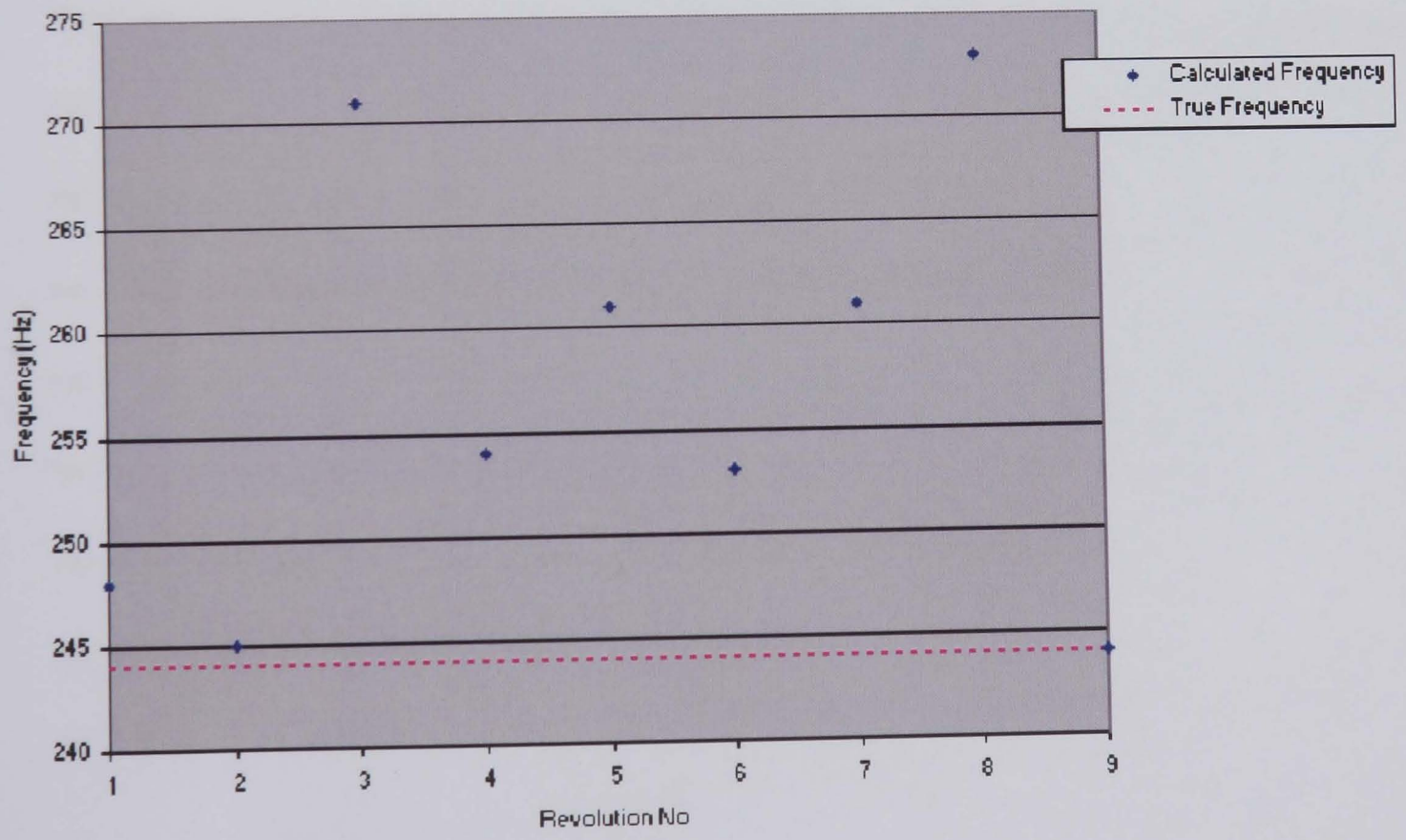

Figure 5.31 Test Case 3 - The ARIV Method Frequency Results

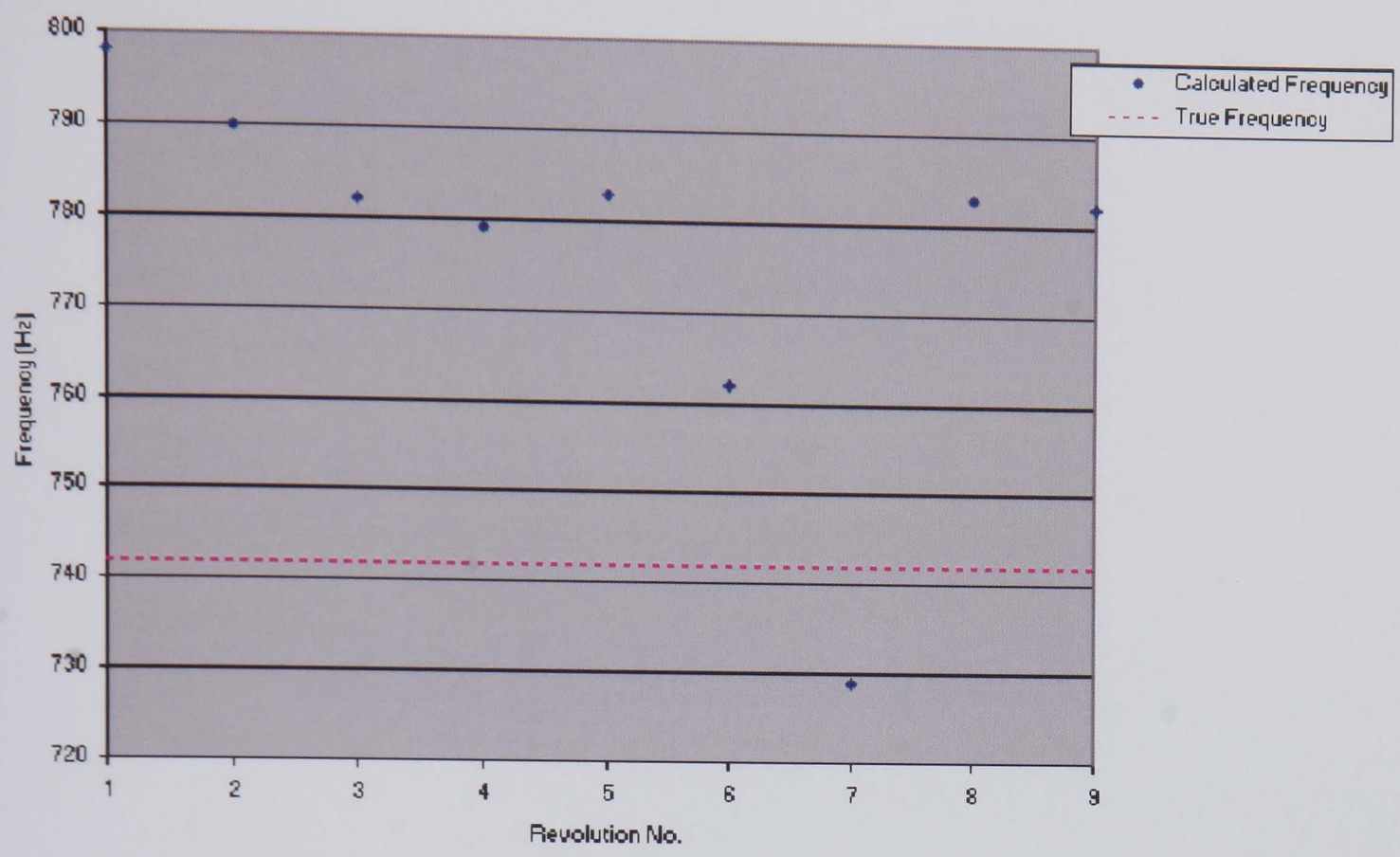

Figure 5.32 Test Case 4 - The ARIV Method Frequency Results

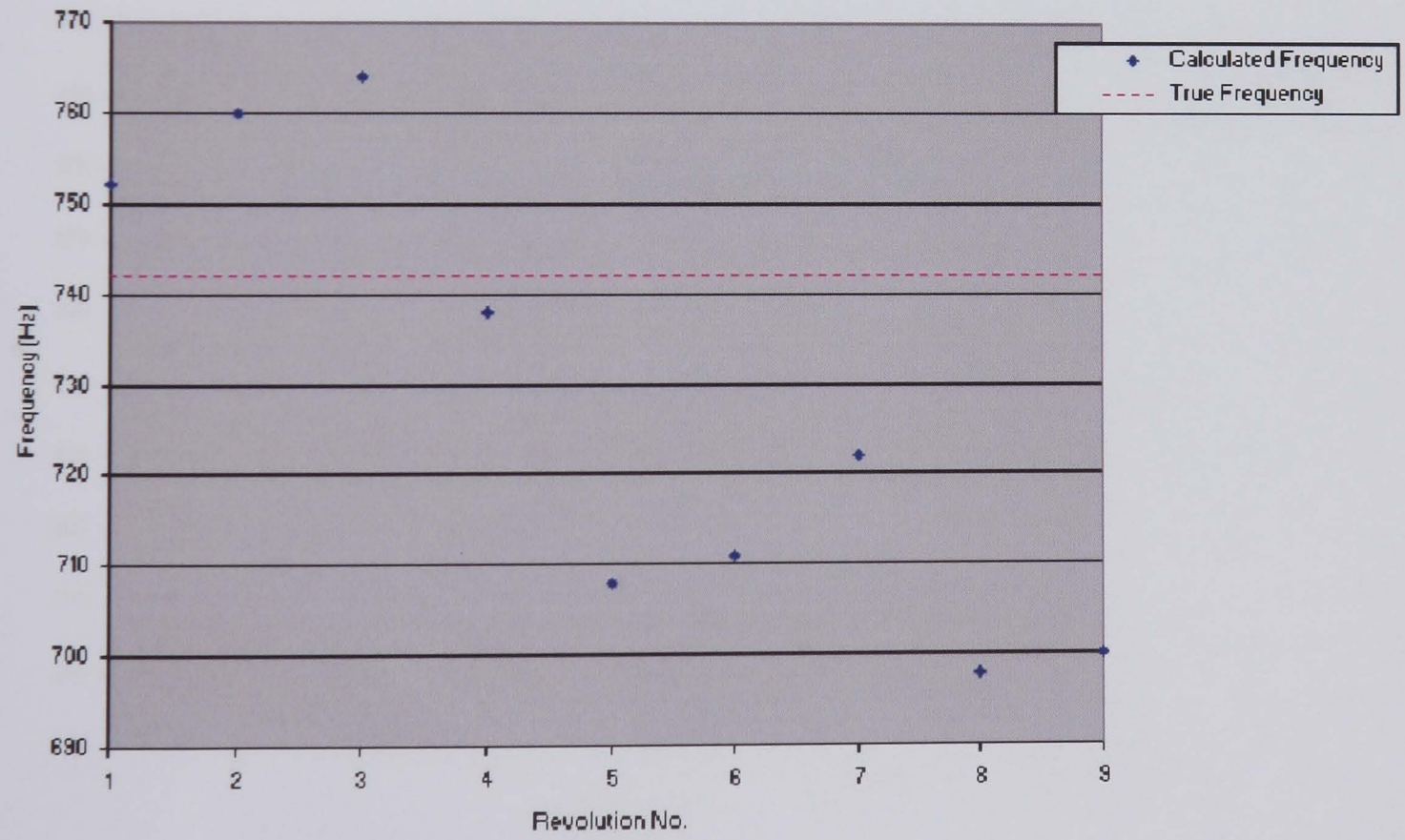

Figure 5.33 Test Case 5 - The ARIV Method Frequency Results

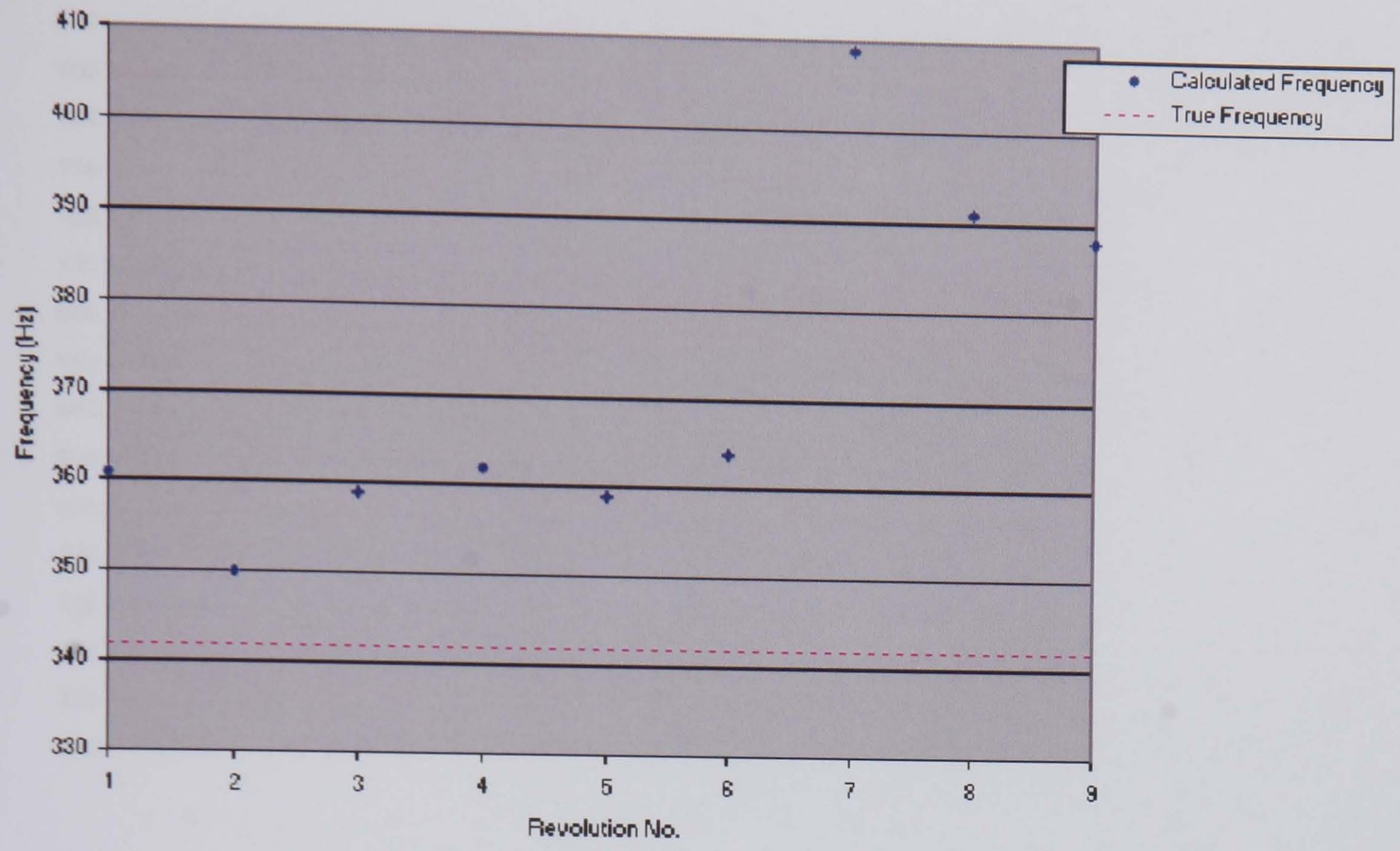

Figure 5.34 Test Case 6 - The ARIV Method Frequency Results

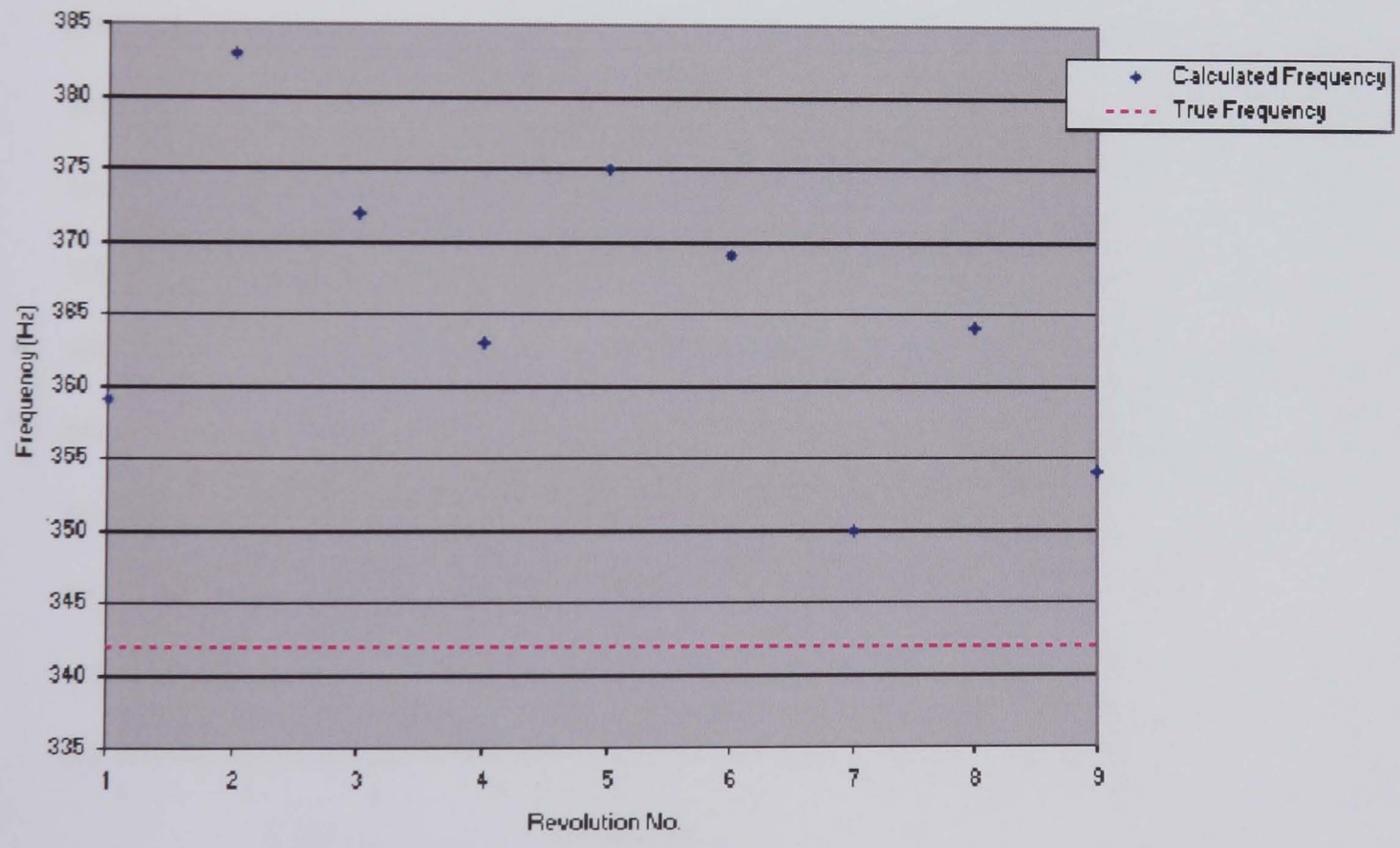

Figure 5.35 Test Case 7 - The ARIV Method Frequency Results

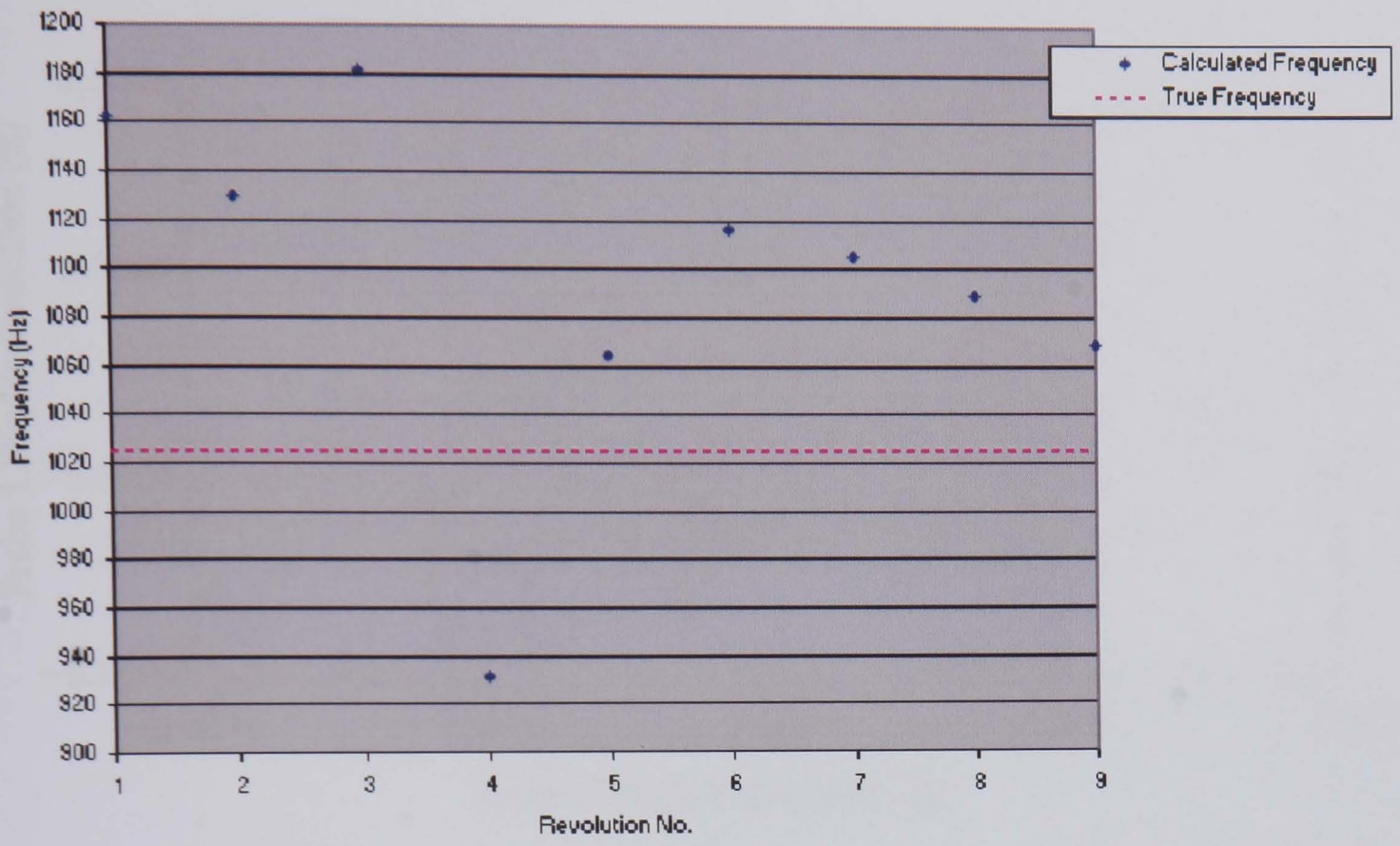

Figure 5.36 Test Case 8 - The ARIV Method Frequency Results

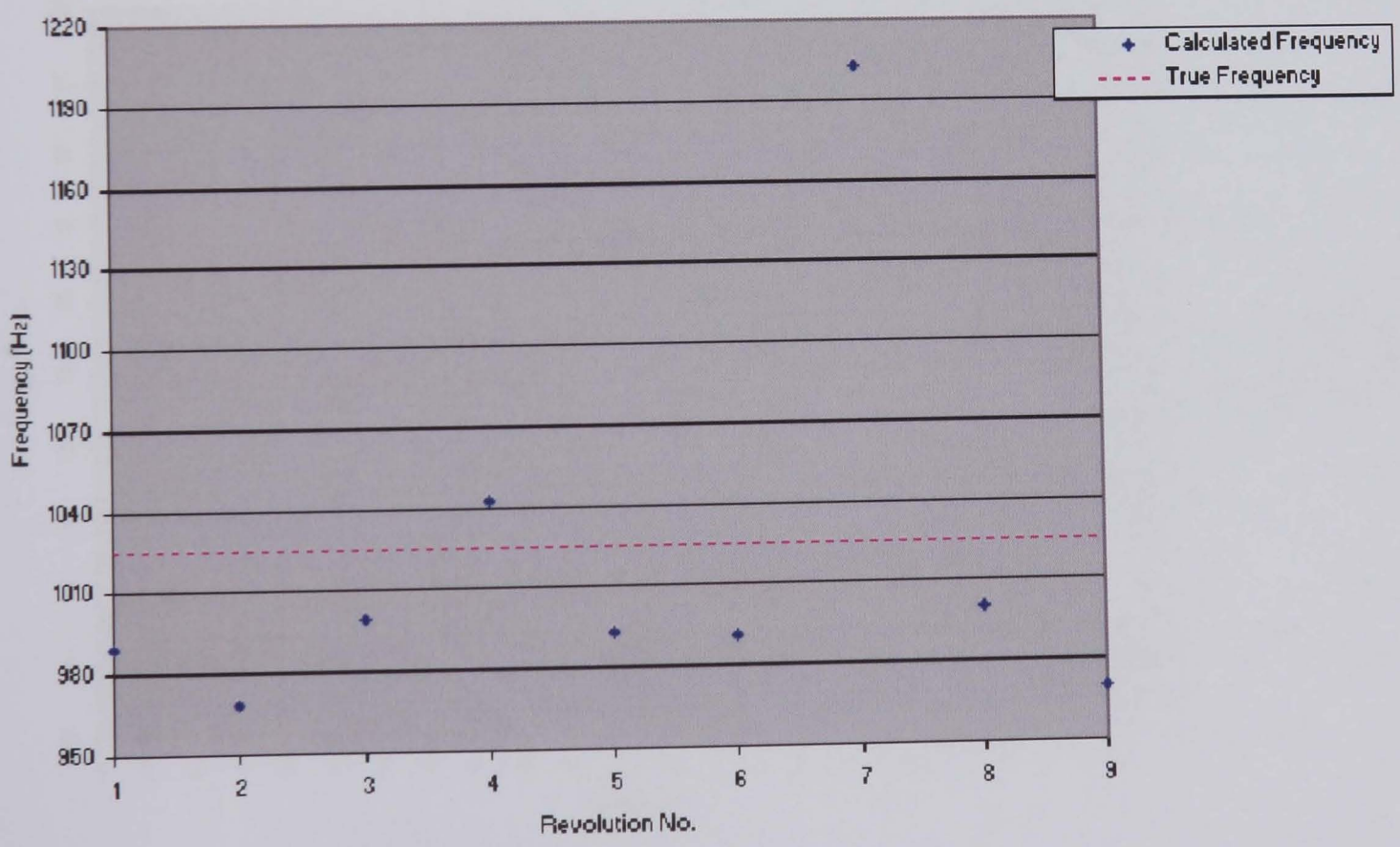

Figure 5.37 Test Case 9 - The ARIV Method Frequency Results

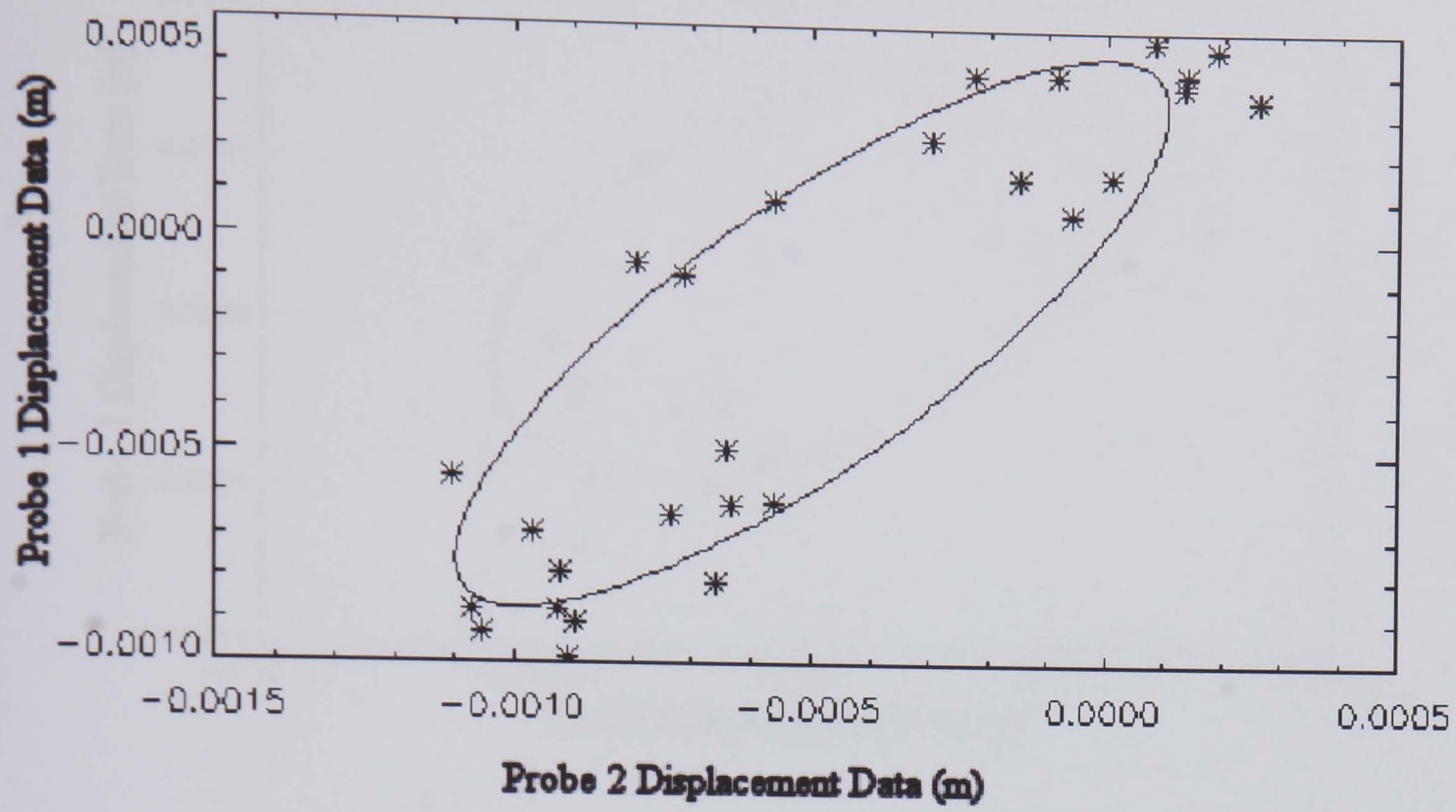

Figure 5.38 Test Case 1 (10% PSR) - The 2PP Ellipse Data Fit

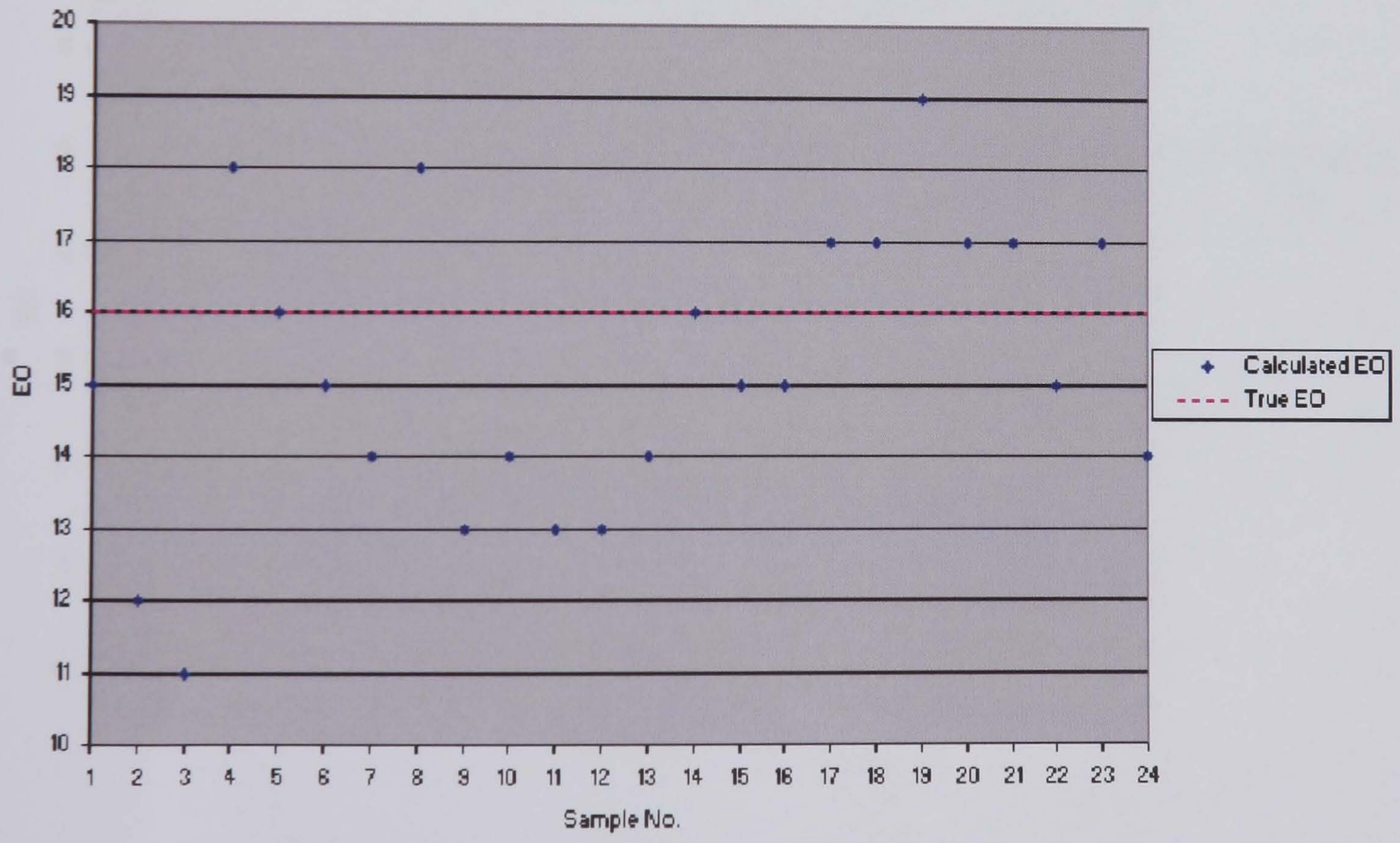

Figure 5.39 Test Case 1 (10% PSR) - The 2PP Calculated EO

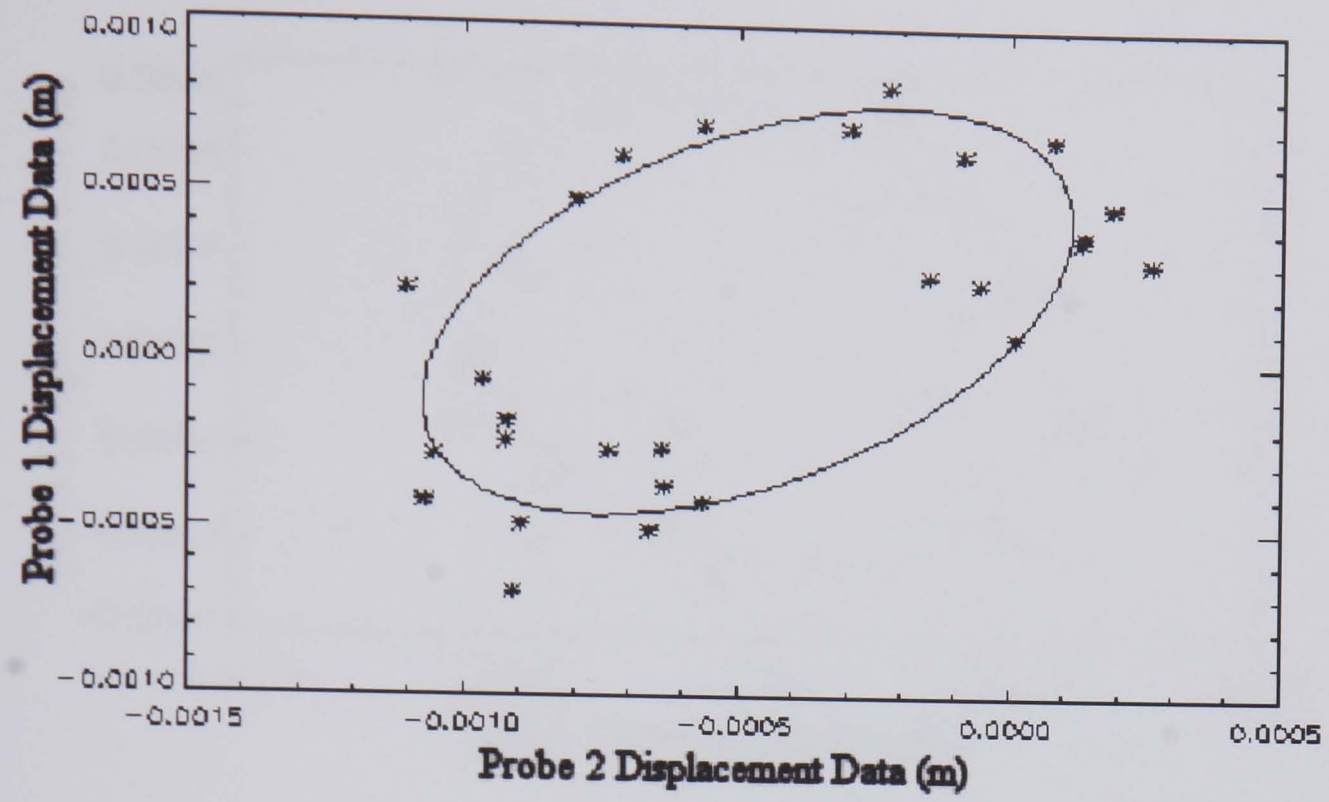

Figure 5.40 Test Case 2 (20% PSR) - The 2PP Ellipse Data Fit

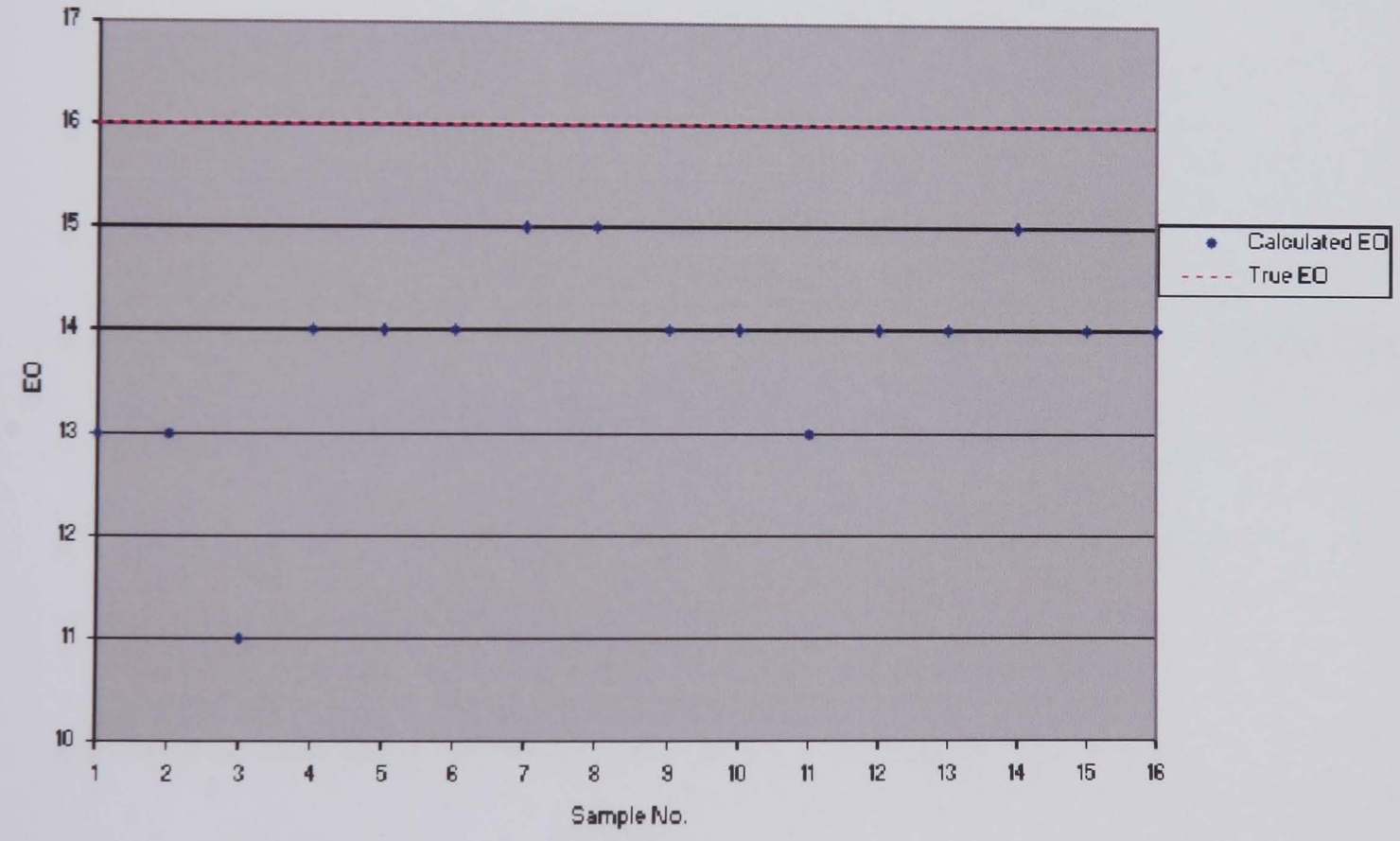

Figure 5.41 Test Case 2 (20% PSR) - The 2PP Calculated EO

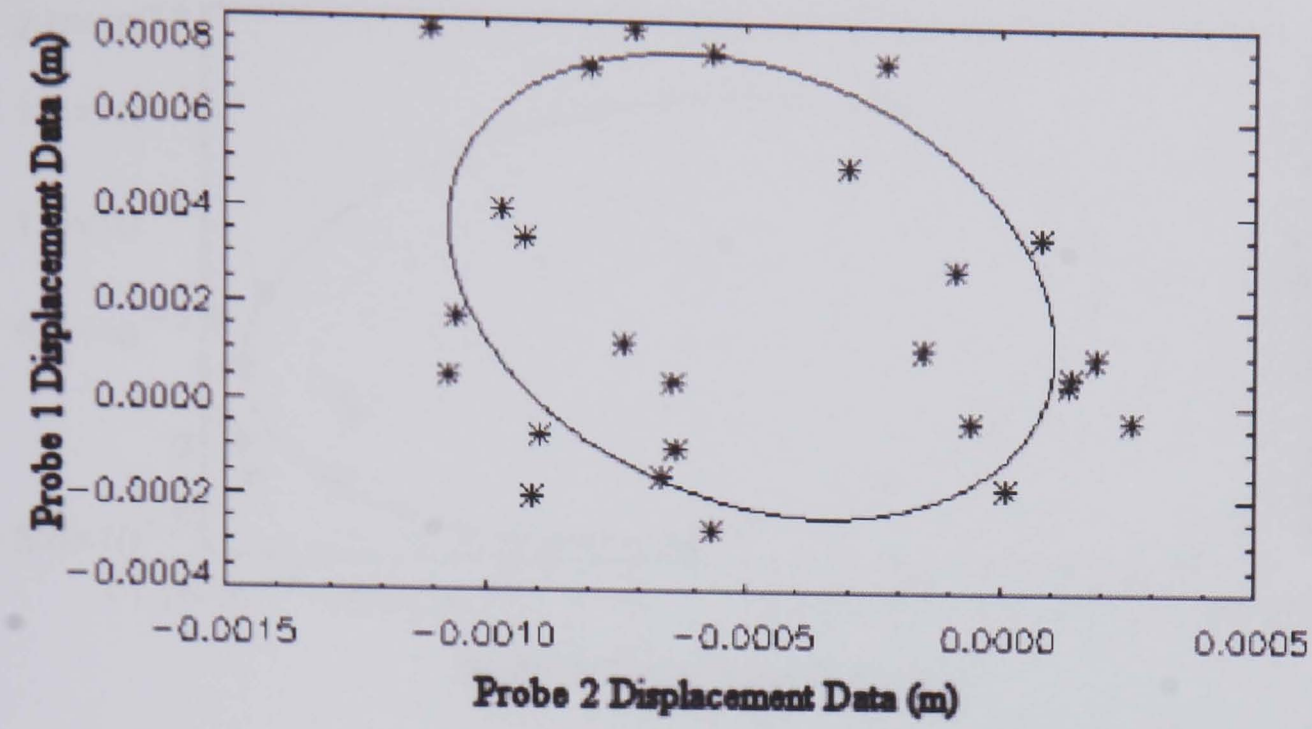

Figure 5.42 Test Case 3 (30% PSR) - The 2PP Ellipse Data Fit

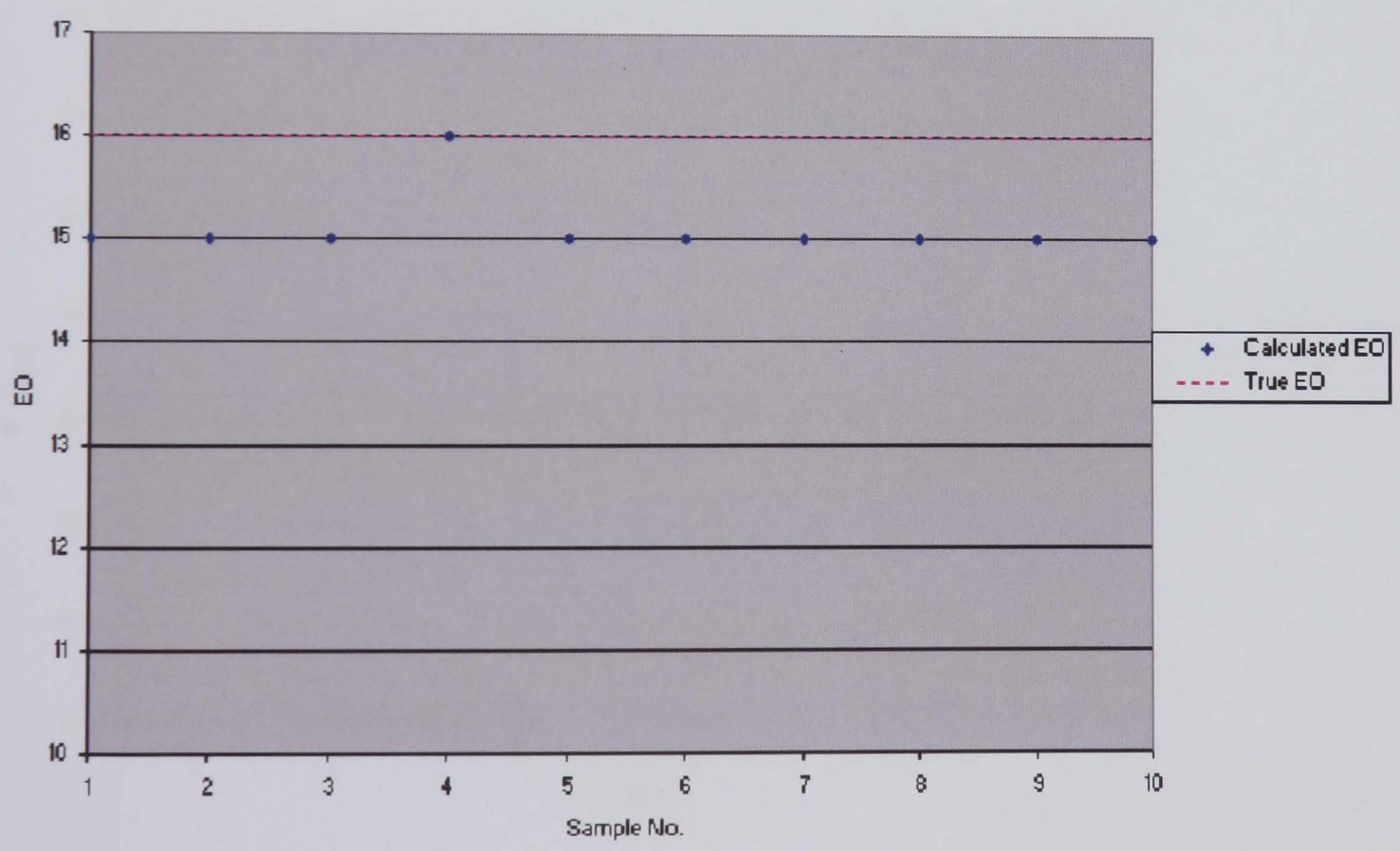

Figure 5.43 Test Case 3 (30% PSR) - The 2PP Calculated EO

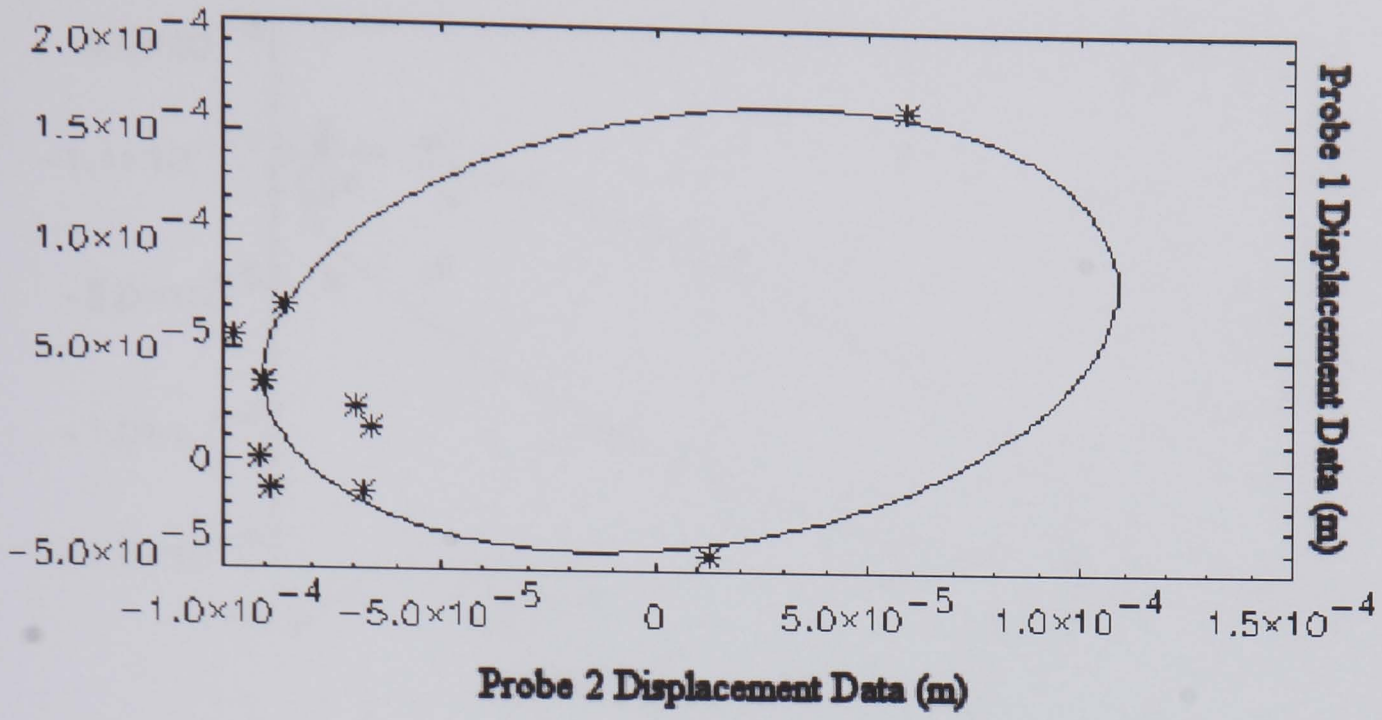

Figure 5.44 Test Case 4 (25% PSR) - The 2PP Ellipse Data Fit

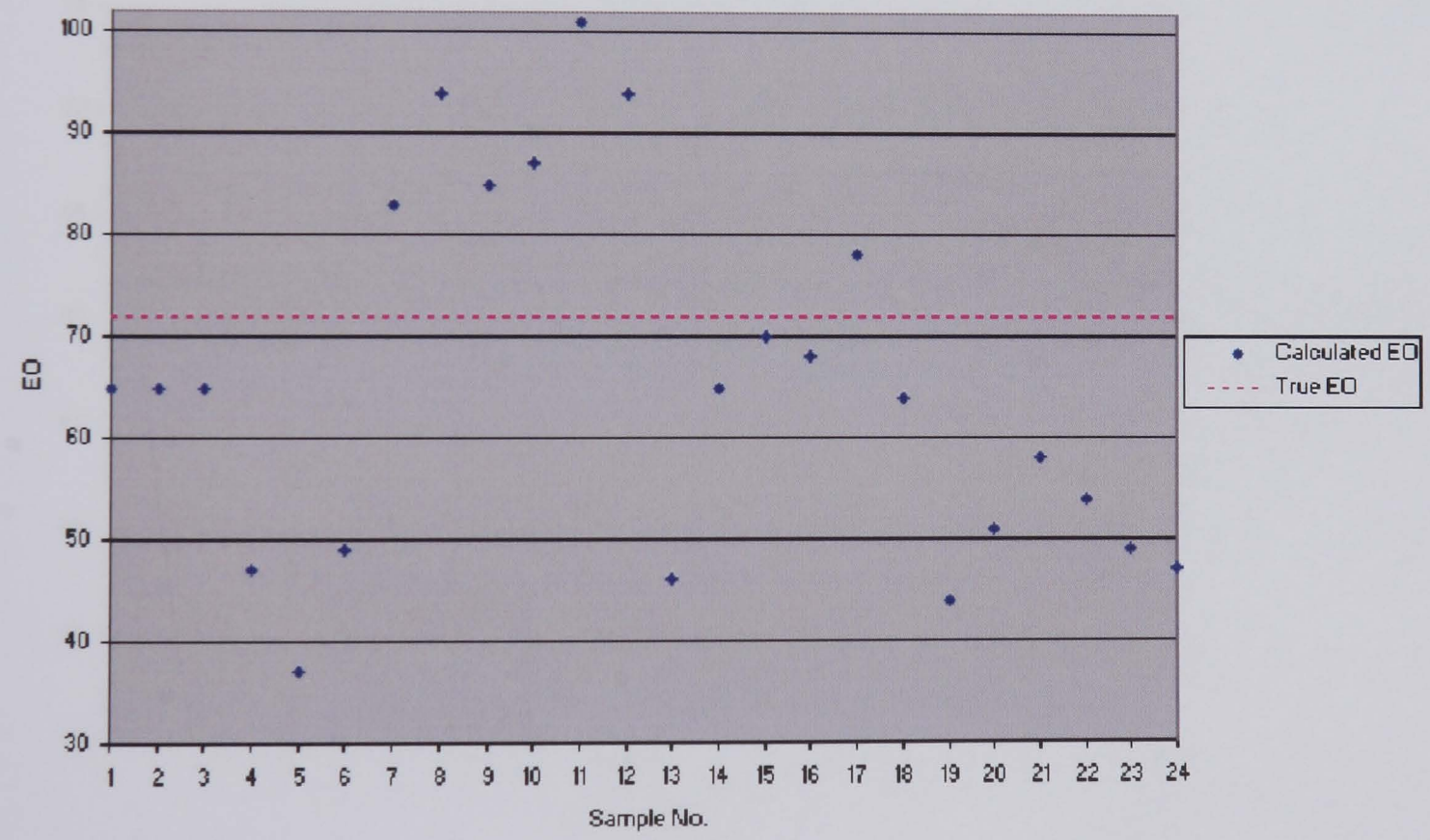

Figure 5.45 Test Case 4 (25% PSR) - The 2PP Calculated EO

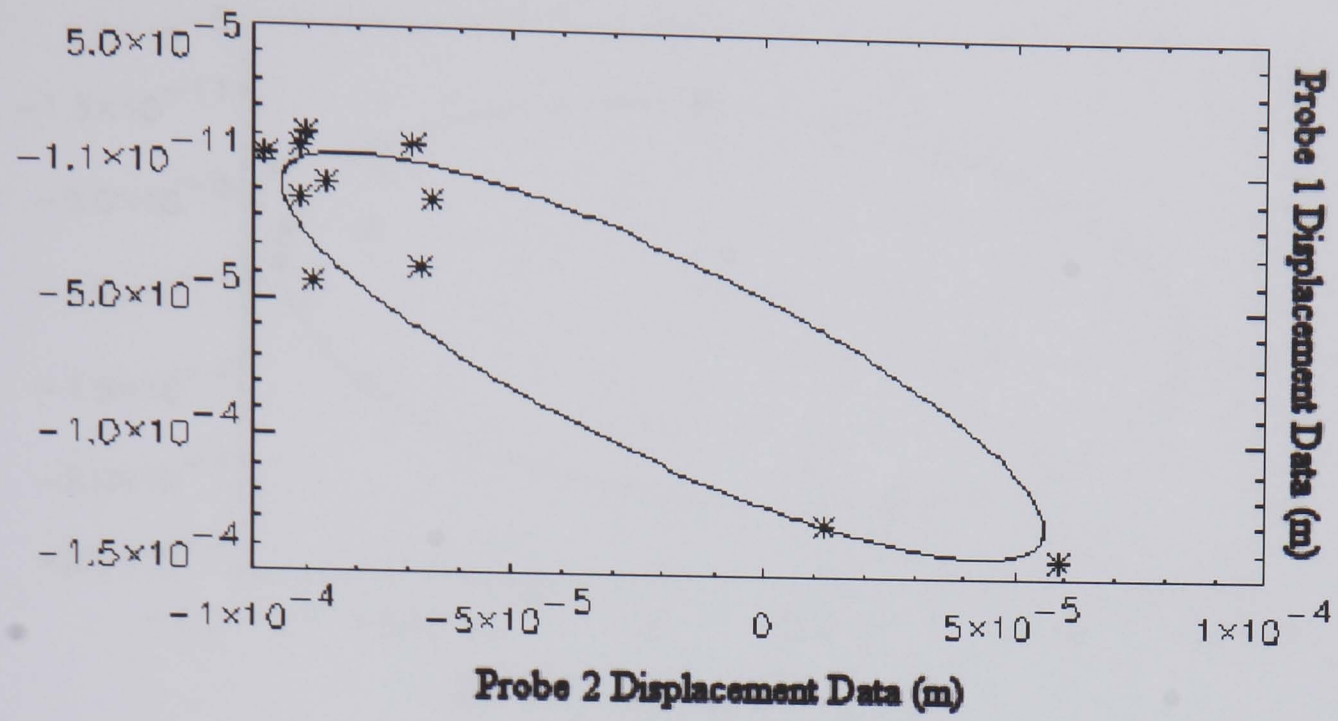

Figure 5.46 Test Case 5 (50% PSR) - The 2PP Ellipse Data Fit

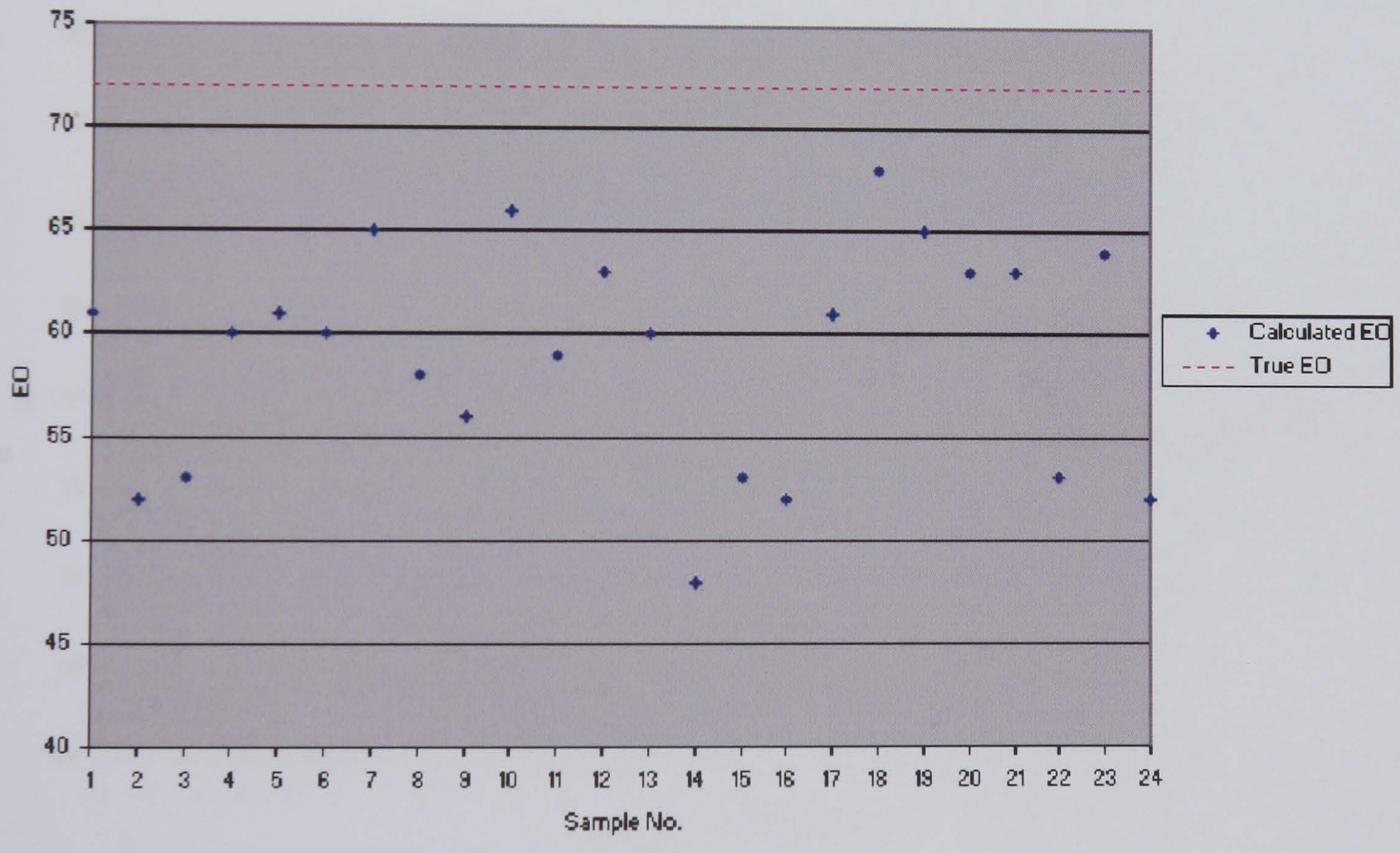

Figure 5.47 Test Case 5 (50% PSR) - The 2PP Calculated EO

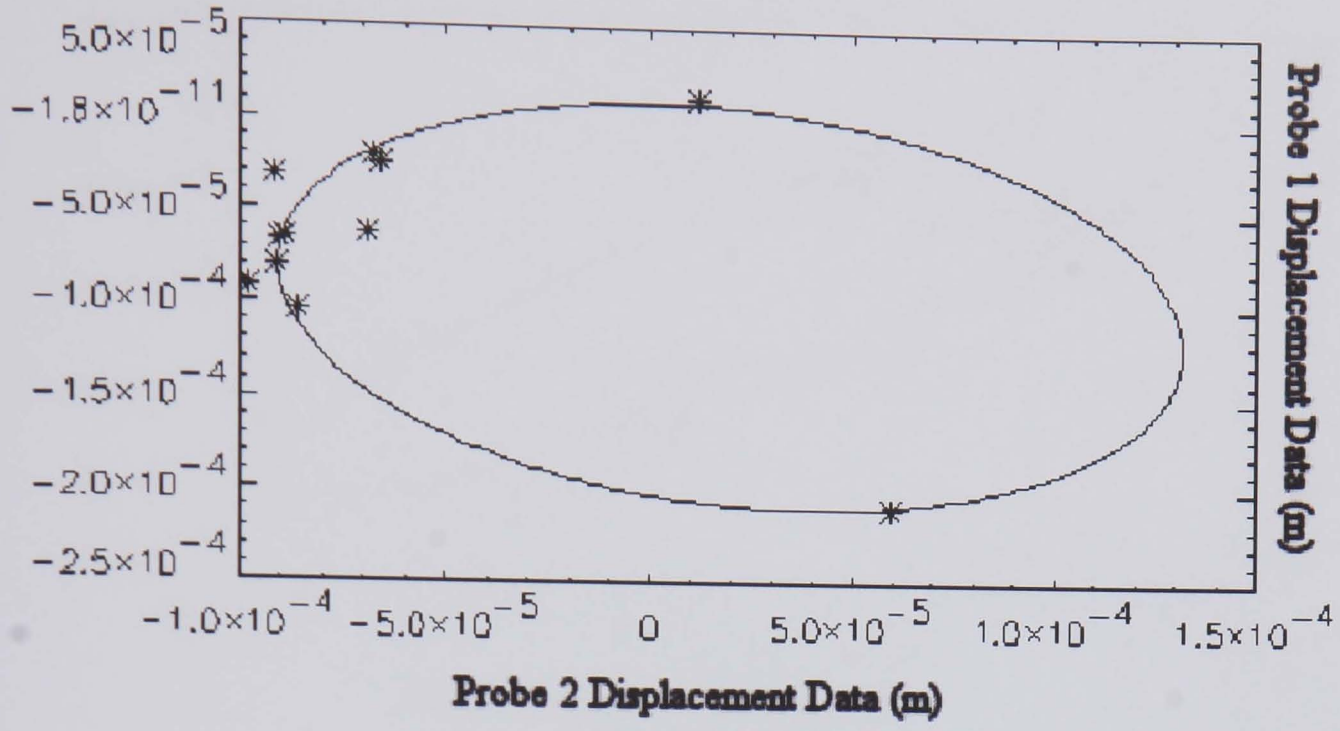

Figure 5.48 Test Case 6 (70% PSR) - The 2PP Ellipse Data Fit

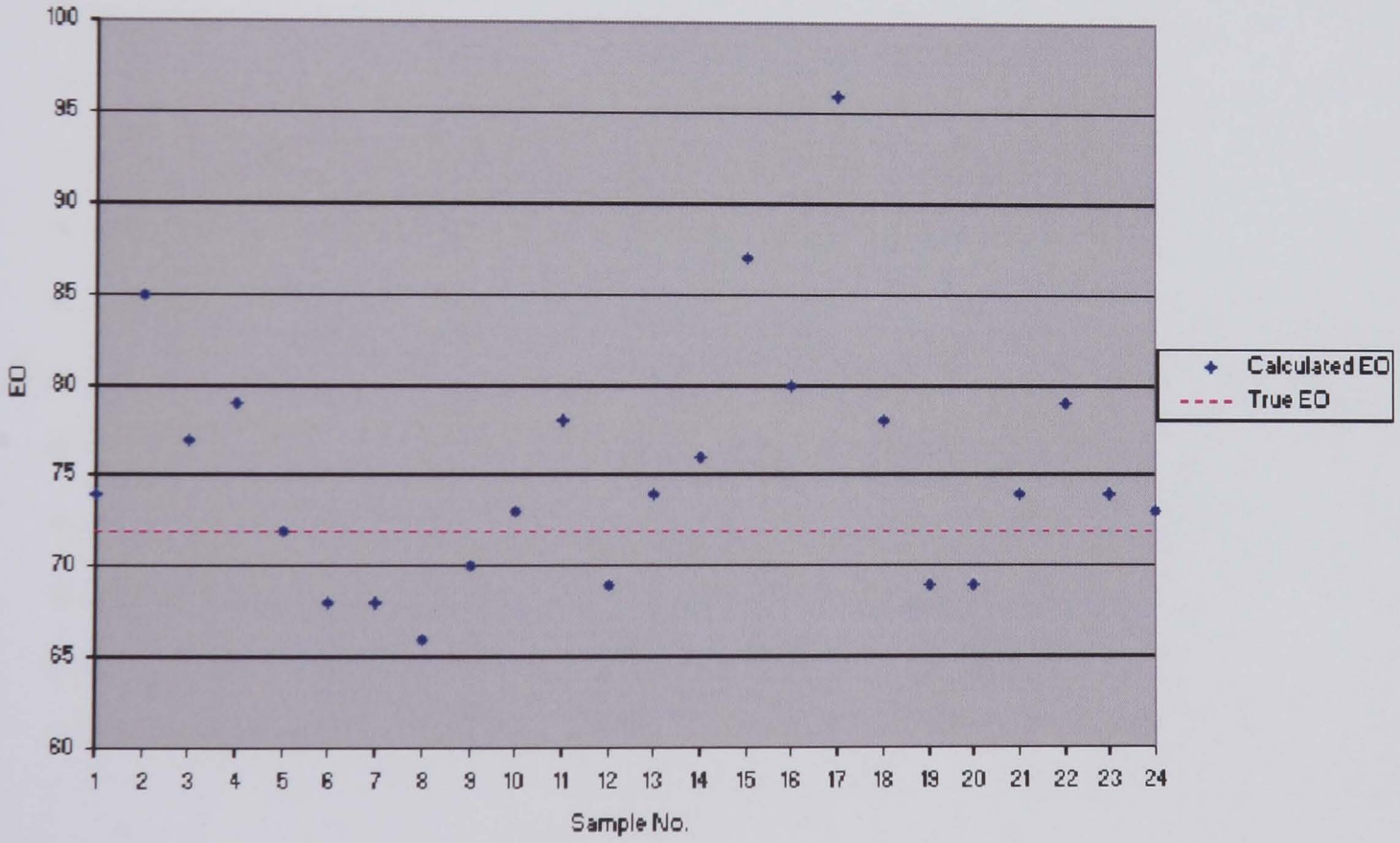

Figure 5.49 Test Case 6 (70% PSR) - The 2PP Calculated EO

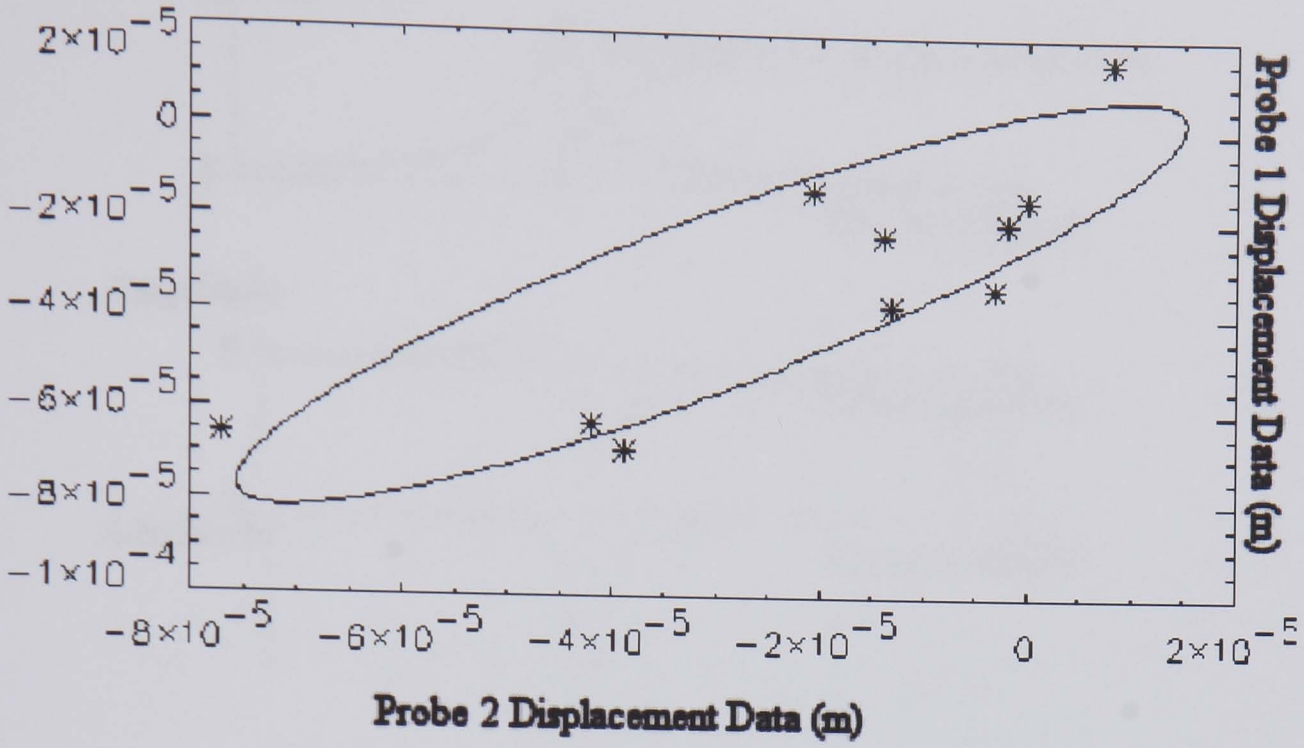

Figure 5.50 Test Case 7 (98% PSR) - The 2PP Ellipse Data Fit

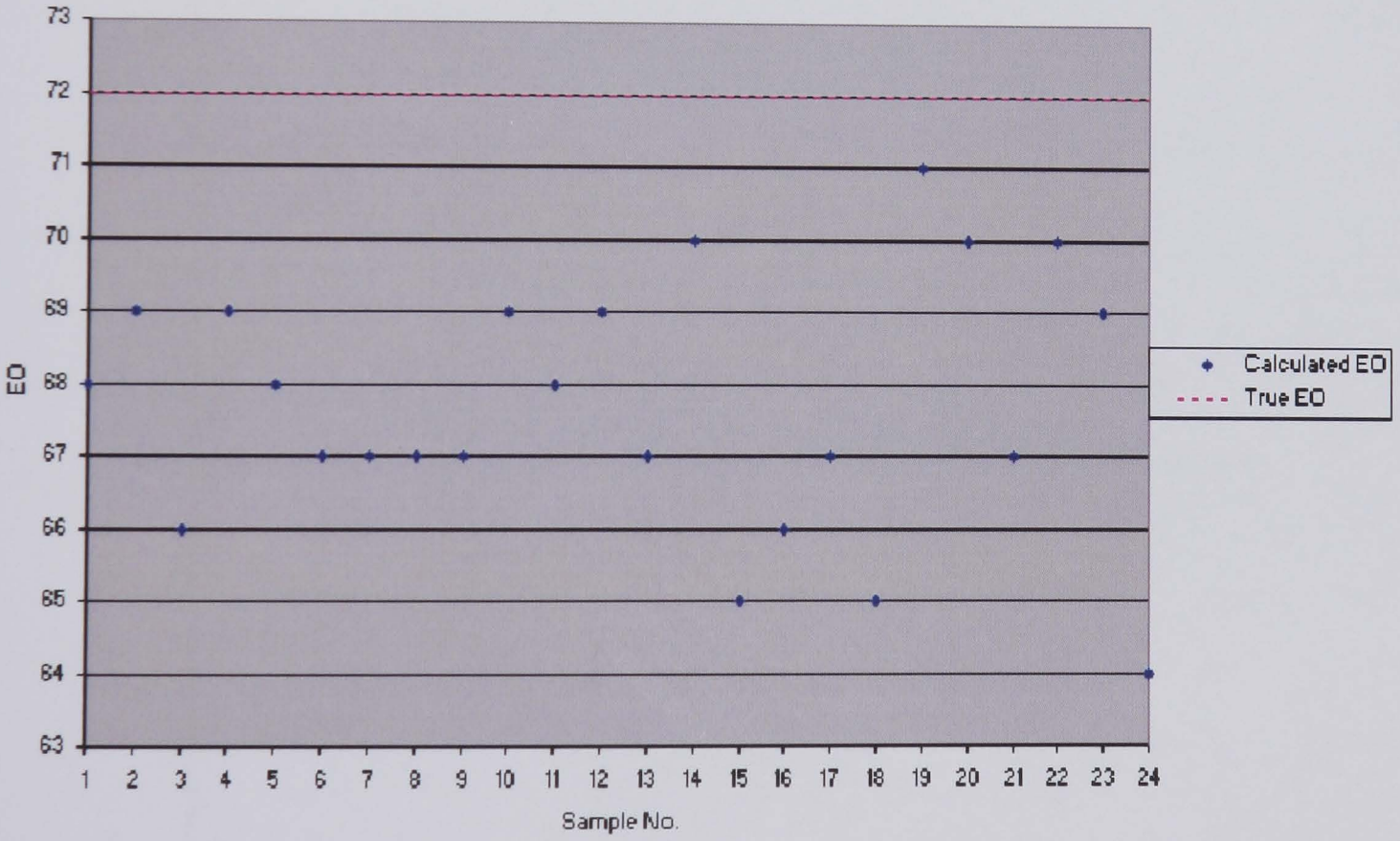

Figure 5.51 Test Case 7 (98% PSR) - The 2PP Calculated EO

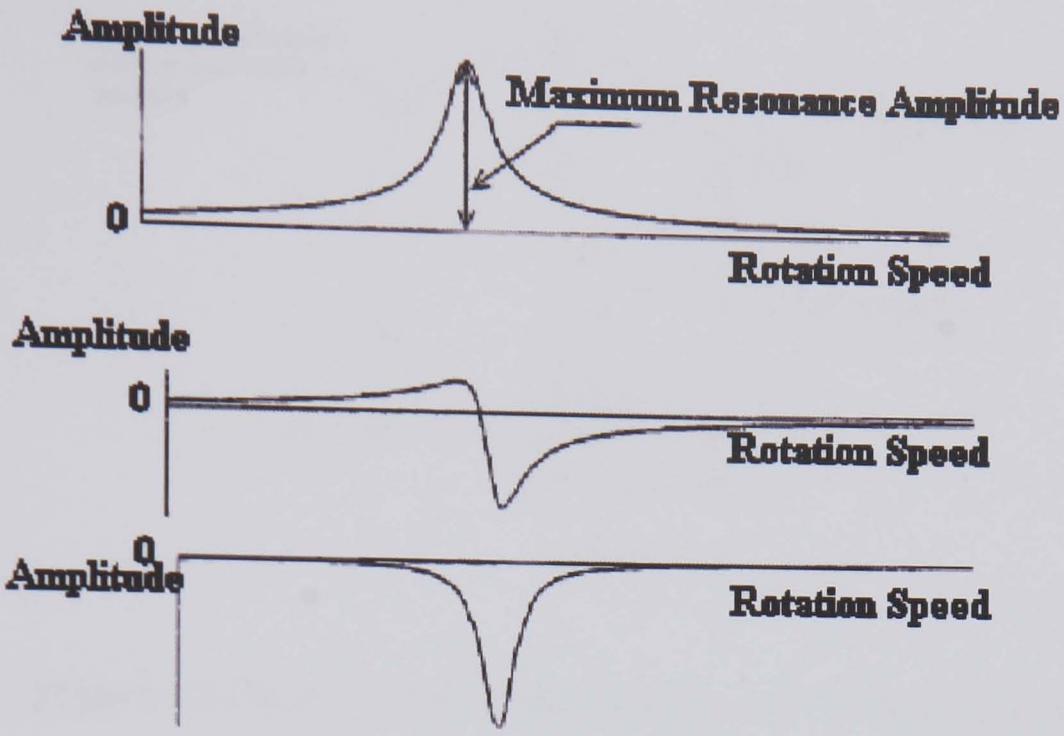

Figure 6.1 Illustration of the Response Amplitude for Different Measurement Positions

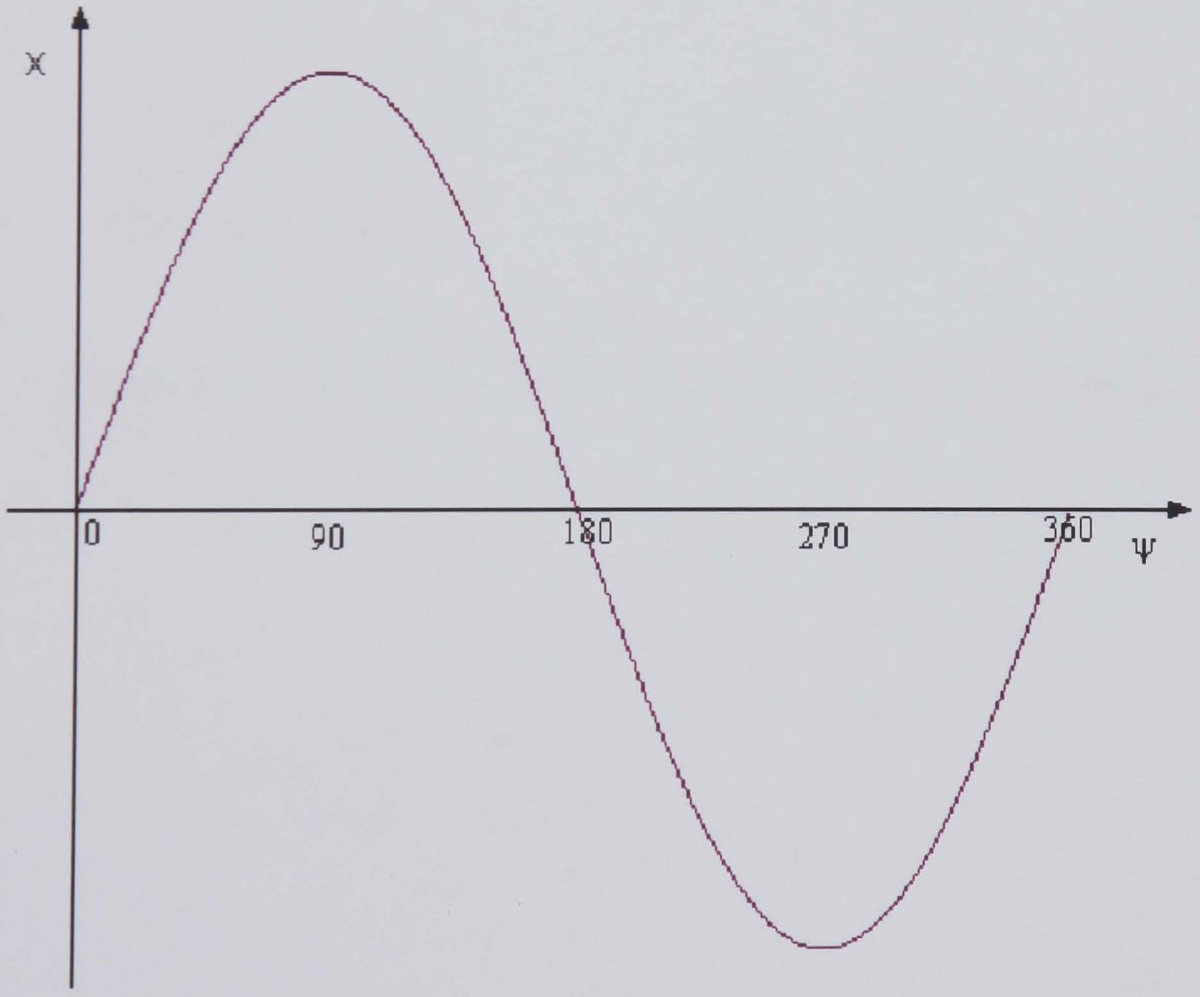

Figure 6.2 Illustration of the Angular Position on the Vibration Cycle

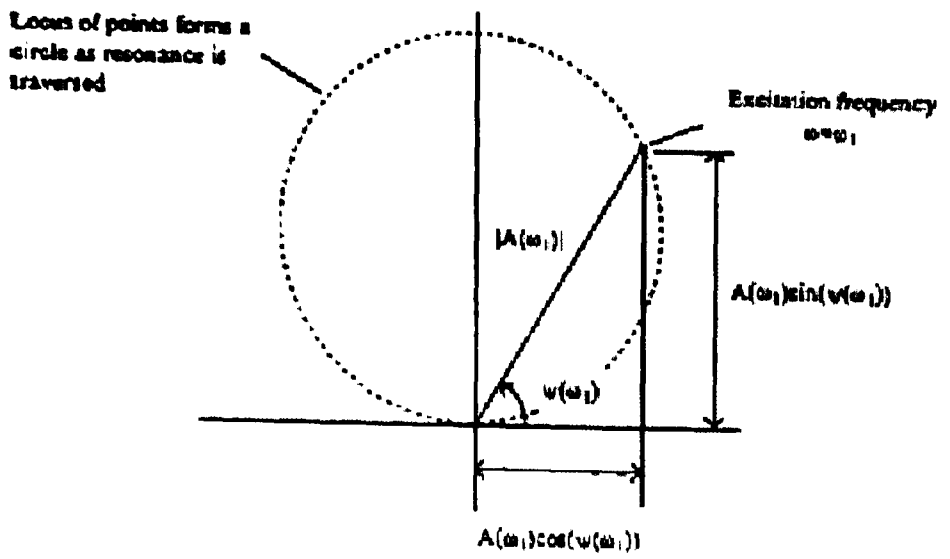

Figure 6.3 Polar Plot of a Single-Degree-of-Freedom-System

Source[9]

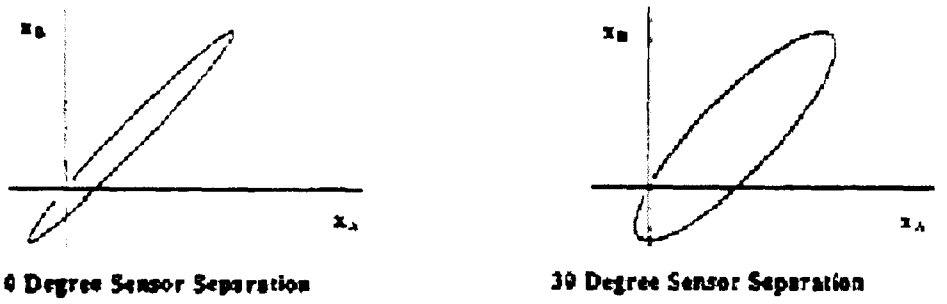

Figure 6.4 Examples of Ellipses from Different Probe Spacings

Source [9]

Tables

Region	P	Q	R	S
1	-7.22644	-21.82787	119.08946	-0.16976
2	7.27262	21.84211	-119.16418	180.17559
3	-7.28363	-21.82579	119.15622	179.82559
4	7.21876	21.84879	-119.10273	360.17127

Table 2.1 Polynomial Coefficients for Sensor Spacing Calculation

Density	2700kg/m^3
Young's Modulus	71GPa
Poisson's Ratio	0.33
1st Bending Aerodynamic Critical Damping Ratio	1%
1st Torsional Aerodynamic Critical Damping Ratio	0.5%

Table 4.1 Test Blade Material Properties

Mode	Mode Shape	Frequency(Hz)
1	Bending	725
2	Torsional	2081
3	Bending	3449

Table 4.2 Test Blade FEA Frequency Calculations

Mode	Mode Shape	Frequency(Hz)
1	Bending	243
2	Torsional	740
3	Bending	1486

Table 4.3 2mm Blade FEA Frequency Calculations

Mode	Mode Shape	Frequency(Hz)
1	Bending	353
2	Torsional	1075
3	Bending	2146

Table 4.4 3mm Blade FEA Frequency Calculations

Blade	1st Natural Frequency(Hz)	Tip Deflection(mm)
Test Blade	725	0.2
2mm Blade	243	2.1
3mm Blade	353	1.3

Table 4.5 Numerical Forced Response

Mode	Mode Shape	Frequency(Hz)
1	Bending	244
2	Torsional	736
3	Bending	1471

Table 4.6 2mm Blade Bench Test Frequency Results

Mode	Mode Shape	Frequency(Hz)
1	Bending	338
2	Torsional	1020
3	Bending	1994

Table 4.7 3mm Blade Bench Test Frequency Results

Mode	Gauge	Correlation Factor (MPa/mm)	Correlation Error (%)
1	A	16.9	29
1	B	5.1	33
2	A	13.5	29
2	B	30.4	28

Table 4.8 2mm Blade Strain Gauge Correlation Factors

Mode	Gauge	Correlation Factor (MPa/mm)	Correlation Error (%)
1	A	36.0	12
1	B	7.3	13
2	A	5.6	13
2	B	47.9	12

Table 4.9 3mm Blade Strain Gauge Correlation Factors

RPM	Engine Order	Response Frequency (Hz)	Mode
205	72	244	1st Bending
617	72	742	1st Torsional
941	16	254	1st Bending

Table 4.10 2mm Blade Engine Order Response

RPM	Engine Order	Response Frequency (Hz)	Mode
286	72	342	1st Bending
857	72	1025	1st Torsional

Table 4.11 3mm Blade Engine Order Response

RPM	Trigger Error (μsec)	Trigger Error (mm)
287	+/-0.08	+/-0.0015
650	+/-0.04	+/-0.0018
938	+/-0.02	+/-0.0013

Table 4.12 OPR Error Analysis Results

RPM	2mm Blade Error (mm)	3mm Blade Error (mm)
300	+/-0.047	+/-0.039
600	+/-0.050	+/-0.040
900	+/-0.052	+/-0.042

Table 4.13 Optical Probe 1 Analysis Results

RPM	2mm Blade Error (mm)	3mm Blade Error (mm)
300	+/-0.017	+/-0.011
600	+/-0.018	+/-0.011
900	+/-0.018	+/-0.011

Table 4.14 Optical Probe 2 Analysis Results

RPM	2mm Blade Error (mm)	3mm Blade Error (mm)
300	+/-0.020	+/-0.018
600	+/-0.021	+/-0.020
900	+/-0.021	+/-0.020

Table 4.15 Optical Probe 3 Analysis Results

RPM	2mm Blade Error (mm)	3mm Blade Error (mm)
300	+/-0.022	+/-0.030
600	+/-0.023	+/-0.031
900	+/-0.023	+/-0.031

Table 4.16 Optical Probe 4 Analysis Results

Probe Number	Tip Deflection Error (mm)
1	+/-0.052
2	+/-0.018
3	+/-0.021
4	+/-0.031

Table 4.17 Tip Deflection Measurement Errors

Probe Number	Measured Distance Error (mm)
1	+/-0.046
2	+/-0.025
3	+/-0.022
4	+/-0.021

Table 4.18 Blade Travelled Distance Errors

Case	Test Blade	RPM	Resonant Frequency (Hz)	True EO	Probe Setup	PSR (%)
1	2mm Blade	941	254	16	1	32
2	2mm Blade	205	244	72	2	72
3	2mm Blade	205	244	72	3	72
4	2mm Blade	617	742	72	2	72
5	2mm Blade	617	742	72	3	72
6	3mm Blade	286	342	72	2	72
7	3mm Blade	286	342	72	3	72
8	3mm Blade	857	1025	72	2	72
9	3mm Blade	857	1025	72	3	72

Table 5.1 AR, and ARIV Test Cases

Test Case	True EO	Probe Positions	PSR (%)
1	16	1 & 3	10
2	16	1 & 5	20
3	16	1 & 7	30
4	72	1 & 2	25
5	72	1 & 3	50
6	72	1 & 4	75
7	72	1 & 5	98

Table 5.2 The 2PP Test Cases

Test Blade	RPM	Resonant Frequency (Hz)	True EO	Blade Tip Amplitude (mm)	SNR (%)
2mm Blade	941	254	16	0.93	3
2mm Blade	205	244	72	0.17	17
2mm Blade	205	244	72	0.17	17
2mm Blade	617	742	72	0.51	6
2mm Blade	617	742	72	0.41	7
3mm Blade	286	342	72	0.18	17
3mm Blade	286	342	72	0.11	27
3mm Blade	857	1025	72	0.28	11
3mm Blade	857	1025	72	0.33	9

Table 5.3 SNR Values

Test Case	RPM	PSR	SNR	AR Parameter Error
1	941	32	3	0.223
2	205	72	16	0.114
3	205	72	18	0.202
4	617	72	6	0.155
5	617	72	8	0.111
6	286	73	20	0.259
7	286	73	27	0.151
8	857	73	11	0.235
9	857	73	9	0.143

Table 5.4 Autoregressive Parameter Errors for the AR Method

Test Case	RPM	Δt (seconds)	1/Δt (1/seconds)	AR Parameter Error	Average Frequency Error (Hz)
1	941	4.31E-04	2.32E+03	0.223	63
2	205	9.95E-04	1.00E+03	0.114	11
3	205	9.95E-04	1.00E+03	0.202	16
4	617	3.31E-04	3.02E+03	0.155	37
5	617	3.31E-04	3.02E+03	0.111	28
6	286	6.77E-04	1.48E+03	0.259	31
7	286	6.77E-04	1.48E+03	0.151	18
8	857	2.37E-04	4.22E+03	0.235	88
9	857	2.37E-04	4.22E+03	0.143	49

Table 5.5 Average Frequency Error Results for the AR Method

Test Case	RPM	SNR	AR Parameter Error
1	941	3	0.203
2	205	16	0.094
3	205	18	0.165
4	617	6	0.162
5	617	8	0.100
6	286	20	0.251
7	286	27	0.178
8	857	11	0.219
9	857	9	0.150

Table 5.6 Autoregressive Parameter Errors for the ARIV Method

Test Case	RPM	Δt (seconds)	1/Δt (1/seconds)	AR Parameter Error	Average Frequency Error (Hz)
1	941	4.31E-04	2.32E+03	0.203	59
2	205	9.95E-04	1.00E+03	0.094	9
3	205	9.95E-04	1.00E+03	0.165	13
4	617	3.31E-04	3.02E+03	0.162	37
5	617	3.31E-04	3.02E+03	0.100	25
6	286	6.77E-04	1.48E+03	0.251	29
7	286	6.77E-04	1.48E+03	0.178	23
8	857	2.37E-04	4.22E+03	0.219	90
9	857	2.37E-04	4.22E+03	0.150	51

Table 5.7 Average Frequency Error Results for the ARIV Method

Test Case	True EO	PSR	Average EO Error
1	16	10	2
2	16	20	2
3	16	30	1
4	72	25	21
5	72	50	16
6	72	70	6
7	72	98	4

Table 5.8 Average EO Error Results for the 2PP Method

PSR	Axis Ratio	Calculated EO
10	0.308	15
21	0.611	13
32	0.725	15
10	0.287	13
22	0.702	14
11	0.404	17

Table 6.1 Example of 16EO Ellipse Axis Ratios

Appendix A - Tip-Timing Code

Appendix A.1 - The Autoregressive Method

```
@math_startup
CD, 'C:\Data_Acquired\Blade_2mm\Vibration_Data\AutoregressiveTesting\Setup3'
no_probes = 4
no_blade = 1
no_revs = 5
no_windows = no_revs
no_revs_in_window = (no_revs/no_windows)
noarcoeffs = 2
neqb = no_probes - noarcoeffs
sol_size = no_probes*no_revs_in_window
data = FLTARR(no_probes, no_blades, no_revs)
deltatp = FLTARR(no_revs)
Freq_Array = FLTARR(no_blades, no_revs)
eoresult = FLTARR(no_blades, no_revs)
eoamp = FLTARR(no_blades, no_revs)
eophase = FLTARR(no_blades, no_revs)
lhs = FLTARR(neqb*no_revs_in_window)
rhs = FLTARR(neqb*no_revs_in_window, neqb*no_revs_in_window)
OPENR, 1, "rpm857_3_TIP_DISPLACEMENT.txt"
READF, 1, data
Close, 1
OPENR, 2, "rpm857_3_DELTATP.txt"
READF, 2, deltatp
Close, 2
;CONSTRUCT THE LHS AND RHS OF THE AUTOREGRESSIVE MATRICES USING
PROBE DATA
FOR loopblade = 0, no_blades-1 DO BEGIN
    FOR loopwindow = 0, no_windows-1 DO BEGIN
        lhs = lhs*0.0
        rhs = rhs*0.0
        startrev = loopwindow*no_revs_in_window
        FOR looprev = 0, no_revs_in_window-1 DO BEGIN
            delta_time = deltatp(looprev+startrev)
            FOR loopeqn = 0, neqb-1 DO BEGIN
                lhs(looprev*neqb+loopeqn) = data(loopeqn, loopblade, startrev+looprev) + $
                data(loopeqn+2, loopblade, startrev+looprev)
                rhs(looprev*neqb+loopeqn, 0) = data(loopeqn+1, loopblade, startrev+looprev)
                rhs(looprev*neqb+loopeqn, 1) = 1.0
            ENDFOR
        ENDFOR
```

```
;SOLVE FOR AUTOREGRESSIVE PARAMETER AND DC OFFSET USING LU
DECOMPOSITION PROCEDURE
        temp_solution = rhs
        solution = lhs
        LUDCMP, temp_solution, index, b
        LUBKSB, temp_solution, index, solution
        eoest = solution(0)
        IF eoest LT 2 AND eoest GT -2 THEN BEGIN
;CALCULATE THE BLADE FREQUENCY OF RESPONSE FROM THE CALCULATED
AUTOREGRESSIVE PARAMETER
            freqhz = (ACOS(eoest/2.0))/(delta_time*2.0*!PI)
CONSTRUCT THE LHS AND RHS OF THE BLADE RESPONSE MATRICES
            rhs2 = FLTARR(sol_size, sol_size)
            lhs2 = FLTARR(sol_size)
            delta_times = FINDGEN(no_probes)*delta_time
            freq_rad = freqhz*2.0*!PI*delta_times
            rhs2(*,0) = SIN(freq_rad)
            rhs2(*,1) = COS(freq_rad)
            temp = reform(data(*, loopblade, startrev:startrev+no_rev_in_window-1), sol_size)
            lhs2 = temp - solution(1)/(2-eoest)
            dc_offset = solution(1)/(2-eoest)
            temp_solution = rhs2
            solution = lhs2
;SOLVE FOR THE BLADE REPONSE AMPLITUDE AND PHASE USING THE LU
DECOMPOSITION PROCEDURE
            LUDCMP, temp_solution, index, b
            LUBKSB, temp_solution, index, solution
            Freq_Array(loopblade, loopwindow) = freqhz
            eoamp(loopblade, loopwindow) = SQRT(solution(0)^2 + solution(1)^2)
            eophase(loopblade, loopwindow) = ATAN(solution(1), solution(0))*180.0/!PI
        ENDIF ELSE BEGIN
            Print, "Error"
            Freq_Array(loopblade, loopwindow) = 0.0
            eoamp(loopblade, loopwindow) = 0.0
            eophase(loopblade, loopwindow) = 0.0
        ENDELSE
    ENDFOR
ENDFOR
```

Appendix A.2 - The Autoregressive Method with Instrumental Variables

```
@math_startup
CD, 'C:\Data_Acquired\Blade_2mm\Vibration_Data\AutoregressiveTesting\Setup3'
no_probes = 4
no_blade = 1
no_revs = 5
no_windows = 4
no_revs_in_window = 2
noarcoeffs = 2
neqb = no_probes - noarcoeffs
sol_size = no_probes
data = FLTARR(no_probes, no_blades, no_revs)
deltatp = FLTARR(no_windows)
Freq_Array = FLTARR(no_blades, no_windows)
eoresult = FLTARR(no_blades, no_windows)
eoamp = FLTARR(no_blades, no_windows)
eophase = FLTARR(no_blades, no_windows)
lhs = FLTARR(neqb*no_revs_in_window)
rhs = FLTARR(neqb*no_revs_in_window, 2)
OPENR, 1, "rpm857_3_TIP_DISPLACEMENT.txt"
READF, 1, data
Close, 1
OPENR, 2, "rpm857_3_DELTATP.txt"
READF, 2, deltatp
Close, 2
;CONSTRUCT THE LHS AND RHS OF THE AUTOREGRESSIVE MATRICES USING
PROBE DATA
FOR loopblade = 0, no_blades-1 DO BEGIN
    FOR loopwindow = 0, no_windows-1 DO BEGIN
        lhs = lhs*0.0
        rhs = rhs*0.0
        startrev = loopwindow
        FOR looprev = 0, no_revs_in_window-1 DO BEGIN
            delta_time = deltatp(startrev)
            FOR loopeqn = 0, neqb-1 DO BEGIN
                lhs(looprev*neqb+loopeqn) = data(loopeqn, loopblade, startrev+looprev) + $
                data(loopeqn+2, loopblade, startrev+looprev)
                rhs(looprev*neqb+loopeqn, 0) = data(loopeqn+1, loopblade, startrev+looprev)
                rhs(looprev*neqb+loopeqn, 1) = 1.0
            ENDFOR
        ENDFOR
;SET UP THE INSTRUMENTAL VARIABLES MATRIX
        instrument_var = rhs(neqb:no_revs_in_window*neqb-1, *)
;SOLVE FOR AUTOREGRESSIVE PARAMETER AND DC OFFSET USING LU
DECOMPOSITION PROCEDURE
      temp_solution = TRANSPOSE(instrument_var)#rhs(0:neqb*(no_revs_in_window-1)-
        1,*)
```

```
        solution = TRANSPOSE(instrument_var)#lhs(0:neqb*(no_revs_in_window)-1)
        LUDCMP, temp_solution, index, b
        LUBKSB, temp_solution, index, solution
        eoest = solution(0)
        IF eoest LT 2 AND eoest GT -2 THEN BEGIN
;CALCULATE THE BLADE FREQUENCY OF RESPONSE FROM THE CALCULATED
AUTOREGRESSIVE PARAMETER
            freqhz = (ACOS(eoest/2.0))/(delta_time*2.0*!PI)
CONSTRUCT THE LHS AND RHS OF THE BLADE RESPONSE MATRICES
            rhs2 = FLTARR(sol_size, sol_size)
            lhs2 = FLTARR(sol_size)
            delta_times = FINDGEN(no_probes)*delta_time
            freq_rad = freqhz*2.0*!PI*delta_times
            rhs2(*,0) = SIN(freq_rad)
            rhs2(*,1) = COS(freq_rad)
            temp = reform(data(*, loopblade, startrev), sol_size)
            lhs2 = temp - solution(1)/(2-eoest)
            dc_offset = solution(1)/(2-eoest)
            temp_solution = rhs2
            solution = lhs2
;SOLVE FOR THE BLADE REPONSE AMPLITUDE AND PHASE USING THE LU
DECOMPOSITION PROCEDURE
            LUDCMP, temp_solution, index, b
            LUBKSB, temp_solution, index, solution
            Freq_Array(loopblade, loopwindow) = freqhz
            eoamp(loopblade, loopwindow) = SQRT(solution(0)^2 + solution(1)^2)
            eophase(loopblade, loopwindow) = ATAN(solution(1), solution(0))*180.0/!PI
        ENDIF ELSE BEGIN
            Print, "Error"
            Freq_Array(loopblade, loopwindow) = 0.0
            eoamp(loopblade, loopwindow) = 0.0
            eophase(loopblade, loopwindow) = 0.0
        ENDELSE
    ENDFOR
ENDFOR
```

Appendix A.3 - The Two Parameter Plot Method

```
@math_startup
CD, 'C:\Data_Acquired\Blade_2mm\Vibration_Data\TwoParameterPlotTesting\Setup1'
no_revs = 11
no_probes = 4
data = FLTARR(no_revs*no_probes)
ProbeDistance = FLTARR(4.0*no_probes)
OPENR, 1, 'TPP_RPM205_Rev1.txt'
READF, 1, data
Close, 1
OPENR, 2, 'rpm335_1_REF_DISPLACEMENT.txt'
READF, 2, ProbeDistance
Close, 2
Position1 = 1
Position2 = 3
RPM = 205
sizes = SIZE(data)
xdata = FLTARR(sizes(1)/4)
ydata = FLTARR(sizes(1)/4)
For loopdatapoint = 0, (sizes(1)/4)-1 DO BEGIN
    xdata(loopdatapoint) = data((loopdatapoint*4)+1)
    ydata(loopdatapoint) = data((loopdatapoint*4)+3)
ENDFOR
sizesx = SIZE(xdata)
datasize = sizesx(1)
;DIRECT LEAST FITTING OF PROBE DATA TO AN ELLIPSE
design_matrix = FLTARR(6, datasize)
design_matrix(0, *) = xdata^2
design_matrix(1,*) = xdata*ydata
design_matrix(2,*) = ydata^2
design_matrix(3,*) = xdata
design_matrix(4,*) = ydata
design_matrix(5,*) FLTARR(datasize) + 1
design_matrix = TRANSPOSE(design_matrix)
scatter_matrix = TRANSPOSE(design_matrix)#design_matrix
constraint_matrix = FLTARR(6,6)
constraint_matrix(5,5) = 0.0
constraint_matrix(0,2) = 2.0
constraint_matrix(1,1) = -1.0
constraint_matrix(2,0) = 2.0
scatter_matrix = INV(scatter_matrix)#constraint_matrix
eigenvalue = EIG(scatter_matrix, Vectors = eigenvector)
eigenvalue = FLOAT(eigenvalue)
eigenvector = FLOAT(eigenvector)
index = WHERE(eigenvalue GT 0.0 AND FINITE(eigenvalue))
IF N_ELEMENTS(index) NE 1 THEN PRINT, "Error in eigen soln, index =", index
acoef = eigenvector(0, index)
```

```
bcoef = eigenvector(1, index)
ccoef = eigenvector(2, index)
dcoef = eigenvector(3, index)
ecoef = eigenvector(4, index)
fcoef = eigenvector(5, index)
acoef = acoef(0)
bcoef = bcoef(0)
ccoef = ccoef(0)
dcoef = dcoef(0)
ecoef = ecoef(0)
fcoef = fcoef(0)
residual = $
(acoef*xdata^2)+(bcoef*xdata*ydata)+(ccoef*ydata^2)+(dcoef*xdata)+(ecoef*ydata)+fcoef
p = (ccoef-acoef)/bcoef
p = p+SQRT(p^2+1)
q = SQRT(p^2+1)
xangle = ATAN(p)*180.0/!PI
PRINT, "xangle =", xangle
s = p/q
r = 1/q
g = (acoef*r^2)+(bcoef*r*s)+(ccoef*s^2)
h = (acoef*s^2)-(bcoef*r*s)+(ccoef*r^2)
u = (dcoef*r+ecoef*s)/(2*g)
v = (ecoef*r-dcoef*s)/(2*h)
w = (g*u^2)+(h*v^2)-fcoef
;CALCULATE THE ELLIPSE PARAMETERS
xcentre = s*v-r*u
ycentre = -s*u-r*v
majoraxis = SQRT(w/g)
minoraxis = SQRT(w/h)
npoints = 360.0
xangle = -xangle*!PI/180.0
theta = FINDGEN(npoints)*2.0*!PI/(npoints-1)
newx = majoraxis*COS(theta)
newy = minoraxis*SIN(theta)
xangle = -xangle
;FORM THE X AND Y AXIS OF THE ELLIPSE
tempx = xcentre+(newx*COS(xangle)-newy*SIN(xangle))
tempy = ycentre+(newx*SIN(xangle)+newy*COS(xangle))
maxx = MAX(tempx)
minx = MIN(tempx)
maxy = MAX(tempy)
miny = MIN(tempy)
xrange = [MIN(minx, miny), MAX(maxx, maxy)]
yrange = xrange
AxisRatio = minoraxis/majoraxis
;AxisRatio = 1/AxisRatio
;THE TWO PARAMETER PLOT PARAMETERS
;Region 1
P = -7.22644
```

```
Q = -21.82787
R = 119.08946
S = -0.16976
;Region 2
;P = 7.27262
;Q = 21.84211
;R = -119.16418
;S = 180.17559
;Region 3
;P = -7.28363
;Q = 21.82579
;R = 119.15622
;S = 179.82559
;Region 4
;P = 7.21876
;Q = 21.84879
;R = -119.10273
;S = 360.17127
;CALCULATION OF THE RESONANCE ORDER
SensorSpacing = (P*(AxisRatio^3))+(Q*(AxisRatio^2))+(R*(AxisRatio))+S
ProbeArc = ProbeDistance(position2)-ProbeDistance(position1)
ProbeAngularDistance = (ProbeArc/0.609)*(180.0/!PI)
ResonanceOrder = SensorSpacing/ProbeAngularDistance
FreqHz = (RPM/60.0)*ResonanceOrder
print, "ResonanceOrder =", ResonanceOrder
print, "FreqHz =", FreqHz
print, "AxisRatio =", AxisRatio
PLOT, tempx, tempy
END
```